ORNL/TM-2020/1570-R0
PPUP-101-TD0001-R0

Final Design Report
Proton Power Upgrade Project

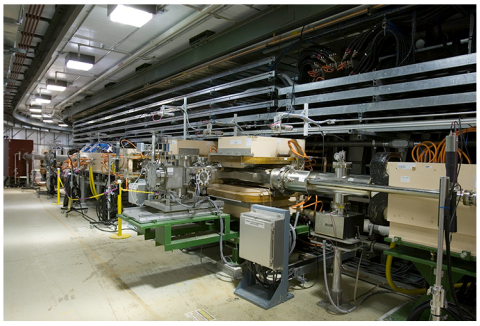

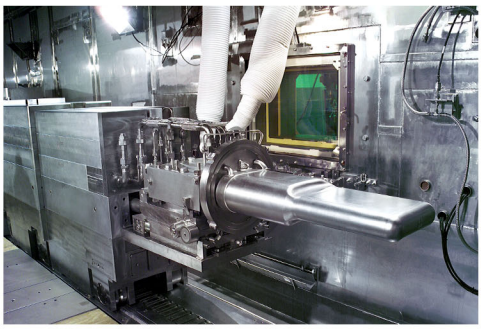

June 2020

Approved for public release.
Distribution is unlimited.

OAK RIDGE NATIONAL LABORATORY
MANAGED BY UT-BATTELLE FOR THE US DEPARTMENT OF ENERGY

ORNL/TM-2020/1570-R0
PPUP-101-TD0001-R0

Neutron Sciences Directorate

FINAL DESIGN REPORT
PROTON POWER UPGRADE PROJECT

John Galambos, Ralph Afanador, Erica Ahlschwede, David E. Anderson, Charlotte Barbier, William Barnett Jr., Kursat Bekar, Craig Bradley, Douglas Bunch, James Bullman Jr., Mark Buchanan, Amy Byrd, Gregory Capps, Mark Champion, Aaron Coleman, Richard Collins, Mark Connell, Sarah Cousineau, Mark Crofford, Douglas Curry, Edward Daly, Robert Dean, Brian Degraff, Craig Deibele, Marc Doleans, Bob Eason, James Eckroth, Nicholas Evans, Franz Gallmeier, Jim Goodpasture, Mandy Greenwood, Melissa Harvey, Kenneth Herwig, Jeffrey Holmes, Matthew Howell, Ahmad Ibrahim, Eric. B. Iverson, Lorelei Jacobs, Glen Johns, Kevin C. Johns, Larry Jones, Yoon Kang, Wylie Keener, Sang-Ho Kim, Brian Kolar, William Kravitz, John Kristy, Paul Langan, Geoffrey Laughon, Sung-Woo Lee, Wei Lu, Karoly Magda, Kelly Mahoney, John Mammosser, Oscar Martinez, Samuel P. Mckenzie, Thomas McManamy, Mark Middendorf, John Moss, Greg Norman, Kevin Norris, Ed O'Neal, Chris Pappas, Chip Piller, Michael Plum, Klent Pope, Jeremy Price, Bernie Riemer, Bryan Robertson III, Tom Roseberry Jr., Robert Saethre, Luke Santee, Jeffrey W. Saunders, James Schubert, Andrei Shishlo, Craig Smith, Dennis Solley, Zachary Sorrell, Jared Spradling, R. Wayne Steffey, Gregory Stephens, Christopher Stone, Barbara Thibadeau, Rod Thomas, George Toby, Steven Trotter, Lisa Turvin, Zhijun Wang, Mark Wezensky, Austin Wheat, Karen White, Derrick Williams, Matthew D. Williamson, Drew Winder, Angela Woody

Date Published: June 2020

Prepared by
OAK RIDGE NATIONAL LABORATORY
Oak Ridge, TN 37831-6283
managed by
UT-BATTELLE, LLC
for the
US DEPARTMENT OF ENERGY
under contract DE-AC05-00OR22725

CONTENTS

LIST OF FIGURES

LIST OF TABLES

ABBREVIATIONS, ACRONYMS, AND INITIALISMS

2D	2-dimensional
3D	3-dimensional
AC	alternating current
ACL	acceptance criteria listing
ADC	analog-to-digital converter
AFF	adaptive feed-forward
AIP	Accelerator Improvement Project
APS	Advanced Photon Source
ARR	accelerator readiness review
ASCE	American Society of Civil Engineers
ASE	Accelerator Safety Envelope
ASME	American Society of Mechanical Engineers
ASQ	American Society for Quality
ATM	alternate topology modulator
ATS	automatic transfer switch
AWG	American wire gauge
B&PV	Boiler and Pressure Vessel
BCP	buffered chemical polishing
BLI	beam line interface
BPLS	beam power limiting system
BTF	Beam Test Facility
CAD	computer-aid design
CAR	carbon adsorber room
CAS	Contractor Assurance System
CCL	coupled-cavity linac
CD	Critical Decision
CD-1	Critical Decision 1
CF	Conventional Facilities
CFD	computational fluid dynamics
CLO	Central Lab and Office (Building)
CMS	cryogenic moderator system
CPI	Communications and Power Industries
CV	core vessel
CVI	core vessel insert
CW	continuous wave
DAC	design and analysis calculation or digital-to-analog converter
DC	direct current
DIWS	deionized water system
DOE	Department of Energy
DPA	displacements per atom
DTL	drift-tube linac
EIS	environmental impact statement
EL	event link

EMS	Environmental Management System
EOS	equation of state
EP	electropolishing
EPICS	Experimental Physics and Industrial Control System
ESH&Q	environment, safety, health, and quality
FCM	field control module
FCT	fast current transformer
FEB	Front End Building
FHA	fire hazards analysis
FPC	fundamental power coupler
FPGA	field-programmable gate array
FSAD	Final Safety Assessment Document
FSAD-PF	Final Safety Assessment Document for Proton Facilities
FSAD-NF	Final Safety Assessment Document for Neutron Facilities
FSD	functional system design
FTS	First Target Station
GAR	gold amalgamation room
GI3	gas injection initial implementation
GLS	gas-liquid separation/separator
gpm	gallons per minute
G-WaLE	gas-wall-layer experiments
HAR	Hazard Analysis Report
HEBT	high-energy beam transport line
HEDP	high-energy differential pumping
HOM	higher-order mode
hp	horsepower
HP	high pressure
HPM	high-power protection module
HPRF	high-power radio frequency
HUR	hydrogen utility room
HVAC	heating, ventilation, and air-conditioning
HVCM	high-voltage converter modulator
IBC	International Building Code
ICD	Interface Control Document
ICS	Integrated Control System
ID	inner diameter
IEEE	Institute of Electrical and Electronics Engineers
IGBT	insulated gate bipolar transistor
IO	input/output
IOB	inlet orifice bubbler
IOC	input-output controller
IRP	inner reflector plug
ISM	Integrated Safety Management
ISO	International Organization for Standardization
J-PARC	Japan Proton Accelerator Research Complex
JSNS	Japan Spallation Neutron Source

JT	Joule-Thomson
LANL	Los Alamos National Laboratory
LBB	Long Beamline Building
LEBT	low-energy beam transport line
LED	light-emitting diode
linac	linear accelerator
LL	live load
LLRF	low-level radio frequency
LO	local oscillator
MAWP	maximum allowable working pressure
MC	Monte Carlo
MCS	moderator cryogenic system
MEBT	medium energy beam transport line
MO	master oscillator
MOTS	mercury off-gas treatment system
MP	medium pressure
MPS	Machine Protection System
MTBF	mean time between failures
MW	megawatt
NCL	normal conducting linac
NEPA	National Environmental Policy Act of 1969
NFPA	National Fire Protection Association
NScD	Neutron Sciences Directorate
OD	outer diameter
OFT	overflow tank
OHSAS	Occupational Health and Safety Assessment Series
OLCF	Oak Ridge Leadership Computing Facility
ORNL	Oak Ridge National Laboratory
ORP	outer reflector plug
PBW	proton beam window
PC	performance category
PCB	printed circuit board
PDRC	PSC Design Review Committee
PFN	pulse forming network
PI	proportional-integral
PIV	particle image velocimetry
PLC	programmable logic controller
PMB	Performance Measurement Baseline
PPS	Personnel Protection System or pulses per second
PPU	Proton Power Upgrade
PPUP	Proton Power Upgrade Project
PSID	pounds per square inch differential
PSIG	pounds per square inch gauge
PUP	Power Upgrade Project
PW	pattern width

QA	quality assurance
QAP	Quality Assurance Plan
QF	quality factor
Q_{ex}	external quality factor
R&D	research and development
RF	radio frequency
RFQ	radio frequency quadrupole
RFTF	Radio Frequency Test Facility
RRR	residual resistivity ratio
RSB	Ring Service Building
RTBT	ring-to-target beam transport line
RTDL	real time data link
RTST	ring to second target transport line
SBMS	Standards Based Management System
SC	superconducting
SCL	superconducting linac
SCR	silicon-controlled rectifiers
SLPM	standard liters per minute
SME	subject matter expert
SNS	Spallation Neutron Source
SRF	superconducting radio frequency
STS	Second Target Station
TBD	to be determined
TC	technical component
TESLA	Tera-Electron-Volt Energy Superconducting Linear Accelerator
THL	Thermal Hydraulics Laboratory
TRCC	transmitter cooling cart
TRIP	Target Reliability Improvement Program
TTF	Target Test Facility
UBC	Uniform Building Code
UL	Underwriters Laboratories
UPS	uninterruptible power supply
USI	unreviewed safety issue
VESDA	very early smoke detection apparatus
VSWR	voltage standing wave ratio
WBS	Work Breakdown Structure
ZCS	zero current switching
ZVS	zero voltage switching

1. INTRODUCTION

Oak Ridge National Laboratory (ORNL) operates and develops world-leading neutron scattering user facilities as centers of scientific excellence, attracting the best researchers from universities, industry, and national laboratories to advance scientific discovery and solve challenging technology problems that are best addressed using neutrons. As the first megawatt-class pulsed neutron source, the ORNL Spallation Neutron Source (SNS) generates the world's most intense, highest-peak-brightness neutron beams, providing US researchers with capabilities that are unique in the world. The use of SNS beam lines now generates about twice as many high-impact publications per neutron scattering instrument as the next-highest peer neutron facility. The Proton Power Upgrade (PPU) project is critical to keep SNS at the international forefront and ensure continued leadership by maximizing the neutron flux available at the First Target Station (FTS) and providing the capability to drive a Second Target Station (STS). [1] The PPU will upgrade the SNS accelerator complex to double its current proton beam power capability—from 1.4 to 2.8 MW. The 2 MW delivered to the FTS will improve performance across the entire existing and future instrument suite, and the future STS [2] would provide a wholly new capability in the form of a transformative new source optimized to produce the world's highest peak brightness of cold neutrons.

Experiments at FTS are flux-limited, and demands for beam time far exceed the availability. The PPU will immediately impact FTS by increasing the number of experiments that can be conducted on current and future FTS instruments. This increase will accelerate the pace of science discovery that relies on neutrons to provide unique information on the structure and dynamics of new materials. The increase in neutron peak brightness provided by PPU will add new scientific capabilities, especially for experiments that benefit from ongoing simultaneous advances in neutron scattering methods and technologies and in data analysis, theory and computation. Current developments in sample environments, spin manipulation, and instrument technologies, combined with the higher neutron flux and peak brightness enabled by the PPU, will extend the reach and scientific impact of neutron scattering methods. Examples of how gains in flux translate directly into better experimental parameters include smaller samples sizes, smaller gauge volumes, more extremes of sample conditions, better time resolution, better energy resolution, faster scanning speeds, and access to slower dynamics regimes.

For example, in soft matter research, PPU will make possible new time-resolved in operando measurements of the formation of complicated molecular architectures that have great promise for technological applications requiring highly tunable morphologies. It will extend the reach of studies of the dynamics of polymers and liquids by reducing sample size requirements. It will also make possible completely new types of measurements of in-plane surface structures in thin films and adhesives by enabling the routine use of grazing incidence methods.

In functional materials research, the PPU will broaden the application of neutron scattering to the study of fundamental parameters that drive performance improvement in alloys and bulk metallic glass by making possible higher temporal, temperature, and/or spatial resolution. It will provide the rapid turnaround needed for characterizing 3D printing of polymer, metal, or ceramic parts. It will make possible routine in situ characterization of critical engineering structures, such as structural components of suspension bridges, that at present is too time consuming. The increase in flux will allow researchers to quantitatively study the structural and dynamic evolution of electrode and electrolyte materials in real systems. With more access to beam time, the cycle time between material synthesis, characterization, and improvement will be reduced.

PPU will make currently marginal experiments in quantum materials feasible. Examples include measurements under high pressures and high magnetic fields, and inelastic neutron scattering using polarization analysis. Combining the higher neutron flux provided by the PPU with new diamond anvil cells developed at ORNL and pulsed high-field magnet technologies will enable the exploration of

hitherto unattainable phase space for neutron diffraction and spectroscopy, making possible new scientific discoveries. Combining polarization analysis with PPU-enhanced inelastic neutron scattering will provide valuable insight into the exotic properties of numerous quantum materials, including multiferroics, superconductors, and topological states.

In biology, the increase in neutron flux provided by the PPU will reduce sample size requirements, making possible crystallographic experiments that are not feasible at present. When this advance is combined with the in situ control of the neutron cross section of hydrogen provided by dynamic nuclear polarization, the possibilities are game-changing in terms of increasing throughput and enhancing the ability to directly visualize hydrogen during drug binding and enzyme catalysis. The nondestructive nature of neutron scattering, and the capability to use deuteration to highlight specific components or molecules, position neutrons to play a key role in addressing challenges in understanding specific components of complexes or pathways within living systems. This "in-cell neutron scattering" approach opens new lines of research. However, these techniques are signal-to-noise limited, and the PPU will provide the flux increases required for further development.

PPU will also provide a necessary platform for STS, which will be the world's highest–peak-brightness cold neutron source and will enable new scientific capabilities complementary to those of the ORNL High Flux Isotope Reactor (HFIR) and the FTS, especially in the areas of soft matter and chemistry. In combination, the FTS, STS, and HFIR will provide the United States with unrivaled capabilities, and unrivaled flexibility, for the foreseeable future. The US research community urgently needs the improved instrument performance and new science capabilities enabled by a PPU-powered FTS.

Provisions for an accelerator power increase were made in the original SNS project, and these are being leveraged to provide a cost-effective means of doubling the beam power. Additionally, accelerator developments and operational experience over the last 10 years of operation provide a strong technical basis for much of the design. The plan for doubling the proton beam intensity capability per pulse is to increase the beam energy from 0.97 to 1.3 GeV and increase the average linear accelerator (linac) beam current from 26 to 38 mA.

Three sets of beam parameters are shown in Table 1.1. The first column shows present operational parameters corresponding to 1.4 MW operation. The "full accelerator upgrade capability" set of parameters corresponds to the ultimate power capability if all pulses were run at the maximum intensity possible. The beam pulses sent to the STS will be at full intensity. However, the accelerator will also supply the FTS with beam, and the FTS target systems are designed for 2.0 MW. Therefore, the pulses sent to the FTS will be reduced in intensity. The reduction in beam intensity per pulse is accomplished by increasing the beam macro-pulse chopping fraction on the front end (i.e., reducing the average beam current, as discussed in Section 2). For eventual operation with both FTS and STS, the linac chopping fraction will be modulated pulse-to-pulse, depending on the target destination of each pulse.

Since the PPU is designed for the extreme case of powering all pulses at the full STS peak intensity, it can accommodate a change in the ratio of pulses delivered to the FTS or the STS. The beam parameters for 60 Hz operation at 2.0 MW to the FTS are also shown in Table 1.1. The equipment needed to modulate the beam intensity pulse-to-pulse will be included in the STS project, with the exception of some low-level radio frequency scope described in Section 4.

Table 1.1. High-level operational parameters for the PPU and current 1.4 MW operation.

	Current SNS 1.4 MW	Full accelerator upgrade capability	FTS 60 Hz operation
Proton beam power capability (MW)	1.4	2.8	2.0
Beam energy (GeV)	1.0	1.3	1.3
Proton pulse length on target (μs)	0.75	0.75	0.75
RFQ* output peak beam current (mA)	33	46	46
Average linac chopping fraction (%)	22	18	41
Average macropulse beam current (mA)	25	38	27
Pulse repetition rate (Hz)	60	60	60
Macropulse length (ms)	1	1	1
Ring extraction beam gap (ns)	250	200	450
High-beta cryomodules	12	19	19
Proton per pulse capability	1.55×10^{14}	2.24×10^{14}	1.60×10^{14}
Energy per pulse (kJ)	23	47	33

* RFQ = radio frequency quadrupole

The range of operational frequency considered for the STS is 10–20 Hz. Between 6 and 12 pulses per second from the 60 Hz stream produced by the accelerator will be redirected to the STS, depending on the final STS frequency choice. The remaining 40–50 pulses per second from the accelerator will be directed to the FTS. If the STS operates at 20 Hz, the pulses going to the FTS will also be at full intensity and correspond to 1.87 MW. If the STS operates at 10 Hz, the remaining pulses directed toward the FTS will be reduced in intensity to correspond to 2 MW, as indicated in Table 1. The PPU will deliver an accelerator capable of accommodating whatever operational frequency the STS adopts.

More effective use of H^- beam chopping reduces the required peak ion source current from earlier plans, obviating the need to develop a dual ion source front-end system, as envisioned in earlier accelerator upgrade plans [3]. This approach, the accelerator physics basis for the upgrade, and the radio frequency (RF) system requirements are described in Section 2.

The beam energy increase is accommodated by the addition of seven new superconducting RF (SRF) cryomodules in existing space at the end of the linac tunnel. The new cryomodules will be copies of the spare cryomodule built at SNS and installed in 2012. The PPU will use the same gradients that this operational spare cryomodule has demonstrated. Some existing SRF cavity performance will be improved using the ongoing in situ plasma processing campaign. The SRF scope is described in Section 3. The new SRF cryomodules will be powered by new RF sources installed in the end of the klystron gallery, which has sufficient space for this equipment. This RF equipment includes 28 new klystrons, 3 new high-voltage convertor modulators, and associated support equipment. Additionally, some existing RF source equipment will need to be upgraded to accommodate the increased beam loading. The RF scope is described in Section 4. Together, the SRF and RF systems make up the majority of the PPU scope.

More than 95% of the installed ring and transport systems are presently capable of 1.3 GeV operation. Also, operational developments over the last10 years in the injection area and ring damper area provide a solid base for increased intensity in the ring. Upgrades are limited to the ring injection and extraction areas, described in Section 5. The ring injection upgrade will require new chicane magnets, which will be modifications of the present design. The extraction area upgrade involves upgrading the power supply equipment.

In addition to upgrading accelerator components, the PPU includes some conventional facilities (CF) and target system scope. The target system effort (Section 6) covers upgrading the mercury target vessel to handle a 2 MW beam, adding a high-volume helium injection system to mitigate cavitation damage issues, and evaluating other target system components (e.g., shielding, cooling) to validate 2 MW operation at 1.3 GeV. The CF scope (Section 7) includes outfitting the klystron gallery effort for installation of the energy upgrade technical equipment, adding a water pump room, and providing a tunnel stub in the transport line from the ring to the target to facilitate the subsequent connection to a future transport line to the STS target.

The technology deployed for the PPU is largely a direct extension of existing operational equipment and thus does not require significant research and development (R&D). The primary area in which development is supported is a large-volume fraction gas injection system for the mercury target damage mitigation effort. This work is described in Section 8.

Section 9 addressed environmental, safety, health, and quality issues. Finally, the initial cost estimate is presented in Section 10.

REFERENCES

1. Subcommittee on Basic Energy Sciences Facilities Prioritization, *Report of the Basic Energy Sciences Advisory Committee Subcommittee on BES Facilities Prioritization*, February 26–27, 2013, US Department of Energy, Washington, DC, February 2013. Available at https://science.osti.gov/-/media/bes/besac/pdf/Reports/BESAC_Facilities_Prioritization_Report_2013.pdf. Accessed May 2020.

2. J. Galambos, D. E. Anderson, D. Bechtol, et al., *Technical Design Report, Second Target Station*, ORNL/TM-2015/24, January 2015. Available at https://info.ornl.gov/sites/publications/files/Pub54035.pdf. Accessed May 2020.

3. S. Henderson, et al., "Status of the SNS Beam Power Upgrade Project," pp. 345–347 in *Proceedings of EPAC 2006*, Edinburgh, Scotland, June 26–30, 2006. Available at https://acclconf.web.cern.ch/accelconf/e06/PAPERS/MOPCH129.PDF. Accessed May 2020..

2. ACCELERATOR SYSTEMS

The PPU project will double the beam power by doubling the energy delivered per pulse. The SNS accelerator was designed with a power upgrade in mind. Additional empty space was provided in the linac tunnel and in the radio frequency (RF) support building to accommodate the energy increase portion of the power upgrade.

A key aspect of the proposed accelerator upgrade is leveraging lessons learned during the initial 10 years of operation. For example, fewer superconducting RF (SRF) cryomodules are needed for the energy increase than originally planned, based largely on the experience with the successful spare cryomodule presently in operation. Also, incorporating intelligent H^- beam chopping patterns has reduced ion source requirements, obviating the need for a dual source development.

Much of the proposed additional accelerator equipment is of the same type as is presently in use throughout the accelerator. Thus, much of the accelerator scope does not involve development effort. One development area concerns the high-voltage convertor modulators (HVCMs), which supply modulated high-voltage waveforms for the RF generating sources. The increased beam loading associated with the higher beam intensity per pulse creates higher loads for this equipment, and some development is needed. Also, in the storage ring, the increased intensity raises some issues regarding the charge exchange injection process and space charge, which are discussed later in this section.

2.1 SYSTEM REQUIREMENTS

The accelerator systems will be upgraded from the baseline capability of 1.4 to 2.8 MW. This will be accomplished by a combination of increased beam energy and increased beam current. The beam energy, presently 1.0 GeV, will be increased to 1.3 GeV by plasma processing of some existing superconducting linac (SCL) cavities and the addition of seven cryomodules. The average macropulse beam current (including the chopping effect) will be increased from 25 to 38 mA by improvements to the chopping scheme, replacement of the RF-quadrupole (RFQ) to improve transmission, and modest ion source improvements. Some minor modifications to the ring are also required to accommodate the higher beam energy. The FTS will be upgraded to accept 2.0 MW of beam power. The SNS initial baseline and PPU design parameters are summarized in Table 2.1.

Table 2.1. Present operational and upgraded parameters.

Parameter	1.4 MW operation	Upgraded FTS	PPU capability
Beam power on target (MW)	1.4	2.0	2.8
Beam energy (GeV)	0.97	1.3	1.3
Average linac current (mA)[a]	1.6	1.6	2.3
Average linac macropulse current (mA)[a]	25	27	38
402.5 MHz, 2.5 MW klystrons	7	5	5
RFQ peak output linac current (mA)	45	46	46
Ion source output current (mA)	50	54	54
Ring chopping fraction	0.25	0.41	0.18
402.5 MHz, 3 MW klystrons	0	3	3
805 MHz, 5 MW klystrons	4	4	4
805 MHz, 550 kW klystrons	81	81	81

Table 2.1. Present operational and upgraded parameters (continued).

Parameter	1.4 MW operation	Upgraded FTS	PPU capability
805 MHz 700 kW klystrons	0	28	28
SRF transmitter racks	14	19	19
SRF high-voltage converter modulators	7	10	10
High-beta cryomodules	12	19	19

[a]Assumes 5% of linac beam power is sent to injection dump owing to stripping inefficiency.
SRF = superconducting radio frequency

2.1.1 Chopping Requirements

The RFQ output peak current requirement (46 mA) is substantially lower than the peak current requirement for the original power upgrade planning [1] (59 mA). Some ion source parameters for the present design are compared with those for the original power upgrade proposal in Table 2.2. The reduction in required peak current is driven primarily by a decrease in the fraction of beam chopped to provide a gap for fast extraction in the ring. In the original design, 30% of the beam was chopped, whereas in the present design, only 18% of the beam is chopped. We have demonstrated during high-power operation (1.4 MW) that it is possible to chop only ~21% of the beam and still maintain low extraction beam loss. Simulations show that it is possible to further reduce the chopping fraction by varying the minipulse width (also referred to as pattern width [PW]) throughout the injection cycle. Figure 2.1 shows one example of a PW variation that increases the beam charge per pulse by 5% beyond the constant PW=51 case presently used in operation, yet achieves good extraction efficiency. [2] Further gains in beam charge should be possible by also varying the RF buncher voltage during the ring injection time. Pursuing these measures greatly decreases the required peak ion source current, especially because the RFQ transmission decreases sharply above 60–70 mA input. With the present requirements, the existing RFQ design is a feasible approach, and the required ion source output has been demonstrated. An upgraded chopper system in the existing low-energy beam transport line (LEBT) chopper system is being designed and installed outside the PPU project to allow variations in the minipulse width beyond the initial ramp as discussed above.

Table 2.2. Comparison of required front end parameters for the present PPU design and the earlier accelerator upgrade plan.

Parameter	Original upgrade design	Present PPU design
Ion source output (mA)	74	54
RFQ output current[a] (mA)	59	46
Chopping fraction	0.30	0.18
Average linac macro-pulse current (mA)	41	38

[a] Calculated for transmission of a 0.25 pi-mm-mrad emittance input beam with the design field profile along the RFQ.

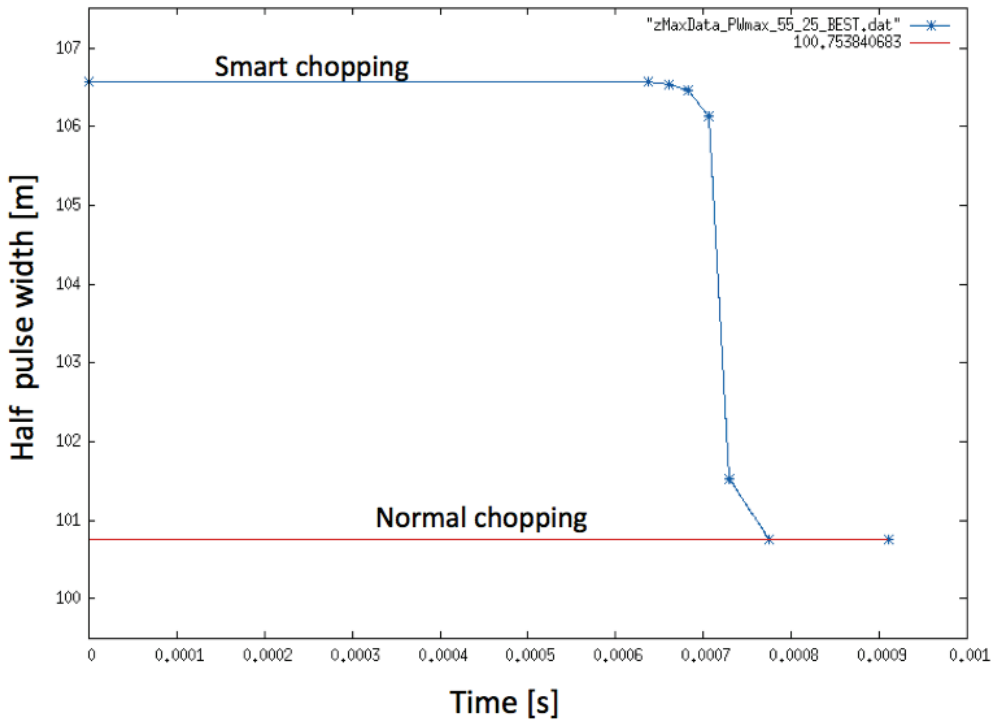

Figure 2.1. Example pattern width variation over the ring injection cycle leading to a clean extraction gap with 5% higher charge per pulse. Blue line: pattern width variation that results in higher beam charge. Red line: example of constant pattern width in use today.

2.1.1.1 Linac RF Power Requirements

The linac RF cavities will require more RF power to maintain the same accelerating gradient at the higher PPU beam currents. In the warm linac, it is not possible to mitigate the power increase by lowering the gradient. This is so because the geometry of the cavities dictates the beam energy for each cavity and because many cells within the cavities are powered by a single klystron, which fixes the RF phase at each cell. Therefore, the only option is to increase the RF power delivered to each cavity. The existing RF power margin is not sufficient for some systems, so these RF systems will be upgraded to support an acceleration of the 38 mA average linac macropulse beam current. The linac RF power requirements are summarized in Table 2.3 and discussed further in Chapter 4.

Table 2.3. Linac RF high power requirements.

System	RF power requirement
Warm linac 402.5 MHz	Upgrade to support 38 mA avg. macropulse beam current
Warm linac 805 MHz	Presently sufficient to support PPU
SCL 805 MHz—existing cryomodules	Presently sufficient to support PPU
SCL 805 MHz—new cryomodules	New RF systems to support 38 mA avg. macropulse beam current at 16 MV/m gradient

In the SCL, there is more flexibility because there are only six cells per cavity (and one cavity per klystron). To support the acceleration of a 38 mA beam current (averaged over the macropulse), some SCL operational gradients will be decreased because the RF power systems are already close to their

maximum output powers. Other SCL cavities that are not RF power-limited will have increased gradients. Plasma processing will allow these gradient increases (see Section 3). The seven new cryomodules will take advantage of klystron and coupler improvements that raise the maximum output power from 550 to 700 kW. Figure 2.2 shows the SCL RF cavity gradients after the PPU. The resultant energy gain profile is shown in Figure 2.3. The latter shows an output beam energy of 1,343 MeV; but in practice, the capability above 1,300 MeV will be used as reserve capacity. The last HVCM will feed ten klystrons, resulting in a 10% reduction in available RF power. This is reflected in the reduced operating gradient and RF power for the last ten cavities in Figures 2.2 and 2.4. The corresponding SCL klystron output power requirements are shown in Figure 2.4, including the beam loading and a control margin of 25%.

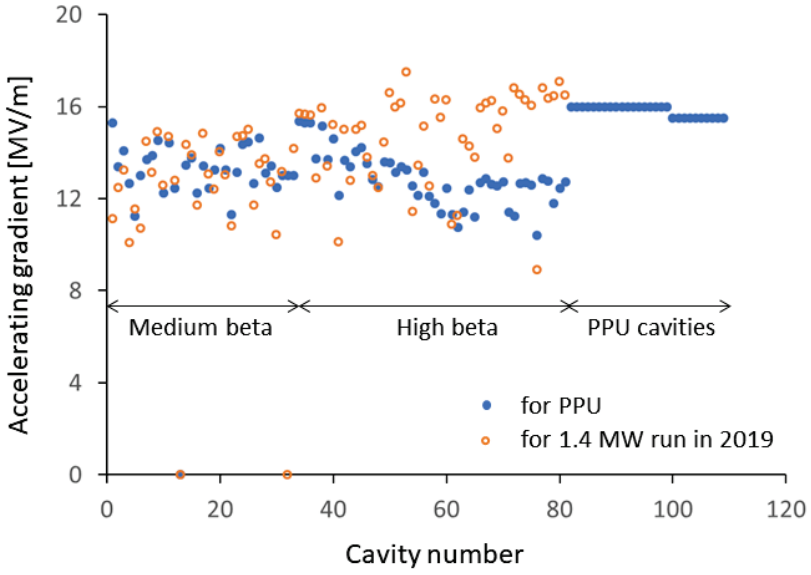

Figure 2.2. SCL cavity gradients after the proton power upgrade.

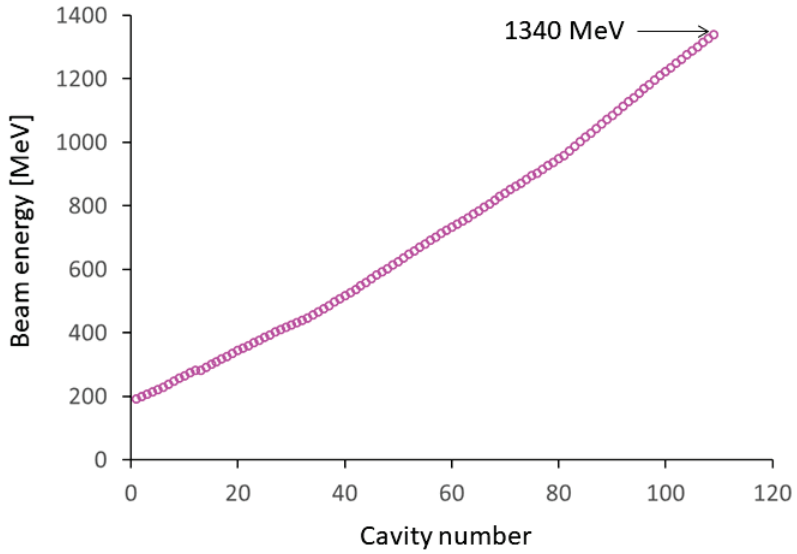

Figure 2.3. The energy gain profile of the SCL. The output energy of 1,340 MeV includes the reserve energy gain from the last three cavities.

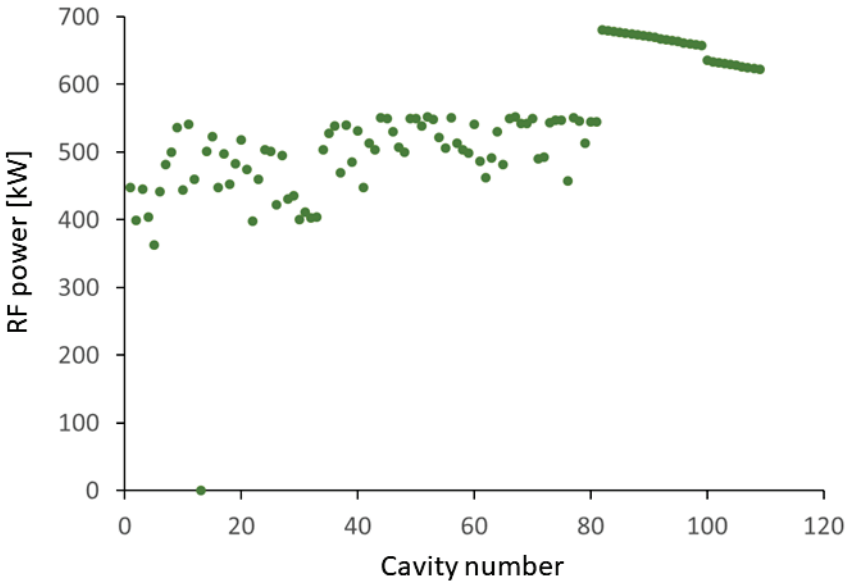

Figure 2.4. Required SCL klystron output power requirement vs. SCL cavity number.

2.2 BEAM SIMULATIONS AND COLLECTIVE EFFECTS CONSIDERATIONS

2.2.1 Linac Simulations

Particle tracking simulations [3] have been performed for the PPU linac to verify the new linac design (personal communication from Z. Wang, Institute of Modern Physics, Lanzhou, China, to M. Plum, ORNL, May 2014). One million particles were tracked from the exit of the RFQ to the exit of the SCL. The initial particle distribution was assumed to be a 3-sigma Gaussian with Twiss parameters, taken from the standard SNS baseline case and reproduced in Table 2.4. The beam current was assumed to be 50 mA and the beam energy 2.5 MeV (design output energy of the RFQ).

Table 2.4. Initial Twiss parameters for the linac simulation.

	Alpha	Beta (m)	Emittance (pi-mm-mrad)
X	–1.9619	0.18314	0.21
Y	1.7681	0.16203	0.21
Z	0.0196	0.58	0.24153

The resultant transverse and longitudinal beam envelopes are shown in Figure 2.5, and the rms emittance growth is shown in Figure 2.6. The simulation results are close to expectations and do not present any problems.

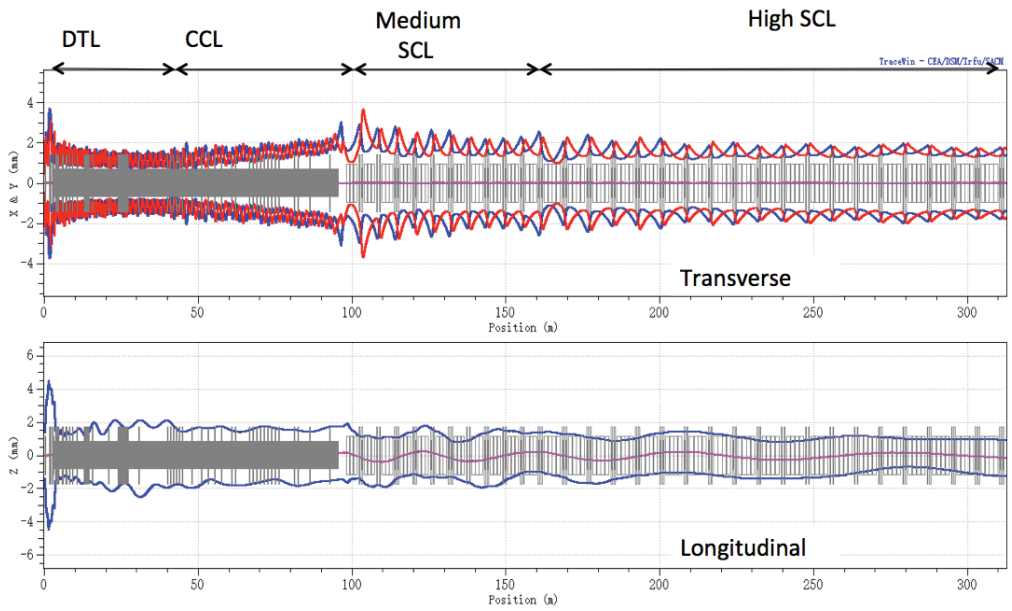

Figure 2.5. Transverse and longitudinal beam envelopes for the STS linac.

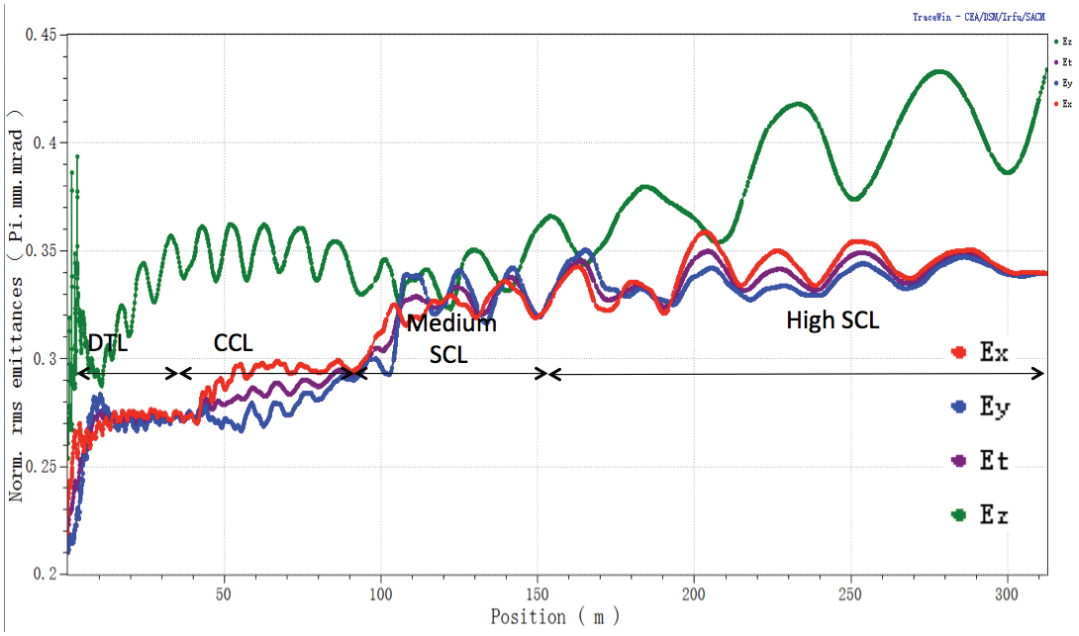

Figure 2.6. Simulated rms emittance growth in the STS linac.

2.2.2 High-Energy Beam Transport Line Simulations

The beam distribution from the linac simulation was used as a starting point for a separate particle-tracking simulation, using the ORBIT particle tracking code [4], of the high-energy beam transport line (HEBT) ending at the primary stripper foil in the ring injection. The results are in good agreement with expectations and are similar to the SNS baseline case. Figure 2.7 shows one of the resulting plots. The beam distribution at the foil is suitable for charge-exchange injection into the accumulator ring at the stripper foil.

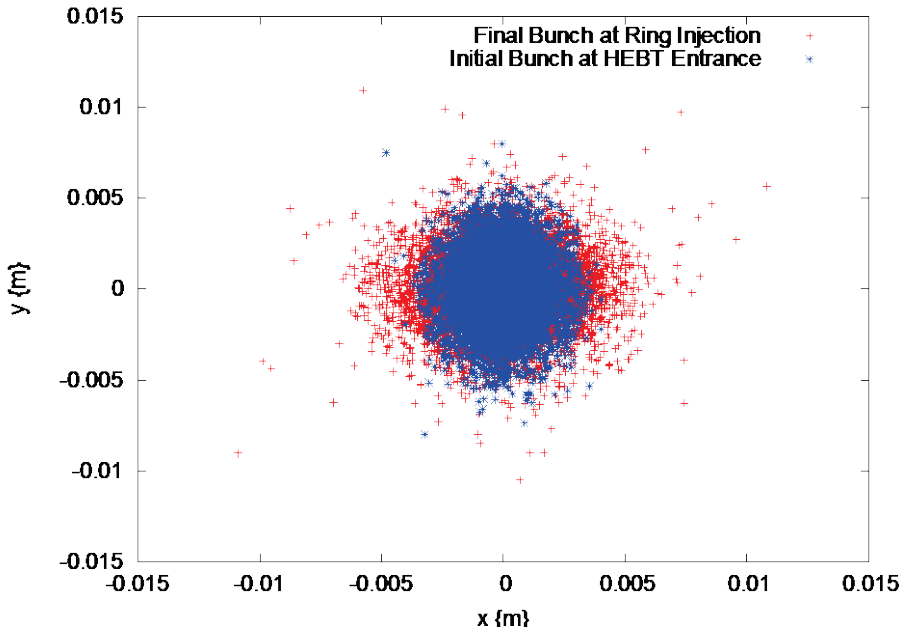

Figure 2.7. Beam distribution at the HEBT entrance (blue) and at the primary stripper foil in the ring injection area (red).

2.2.3 Ring and Ring-to-Target Beam Transport Simulations

The ring simulation assumes the original SNS design input beam distribution at the stripper foil. This is acceptable because the STS HEBT simulation mentioned in Section 2.2.1 produces essentially the same distribution, and because the input distribution represents a small paintbrush stroke into the much larger ring aperture that is filled by the injection painting process. The simulation shows that beam delivery to the FTS will be essentially the same before and after the PPU. Figures 2.8 and 2.9 show the resultant beam distributions at the proton beam window upstream of the first target and at the face of the first target, respectively. No beam loss of concern is seen in these simulations, and the qualitative features are similar to the existing beam profiles on the target. Of course, the peak density is higher owing to the increased number of protons striking the target. For example, the 2.0 MW, 50 Hz case shown in Figure 2.9 has a peak density of 220 mA/m^2, which is 22% higher than the 180 mA/m^2 design case for 1.4 MW, 60 Hz. The 2.0 MW, 50 Hz case has 28% more protons per pulse. The scaling is not exact because of small differences in the beam profiles.

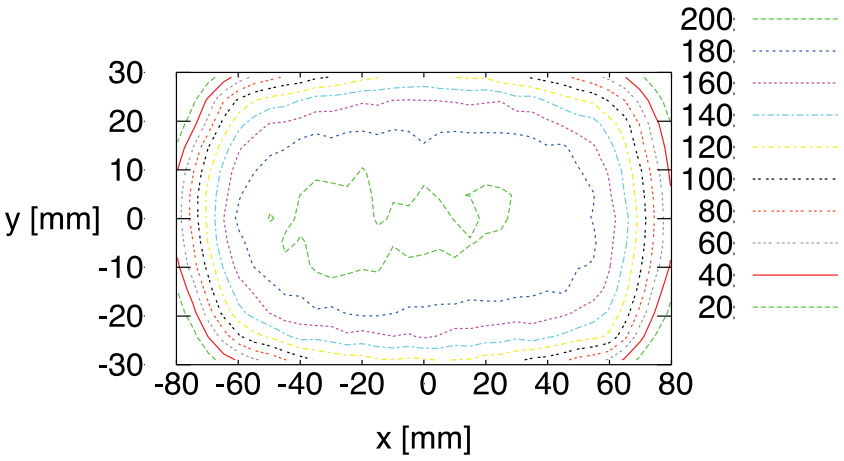

Figure 2.8. Beam distribution at the proton beam window upstream of the first target. The plot contours show the mA/m^2 value assuming a beam power of 2.0 MW at 50 Hz. The beam distribution for the 2.0 MW, 60 Hz case is practically identical.

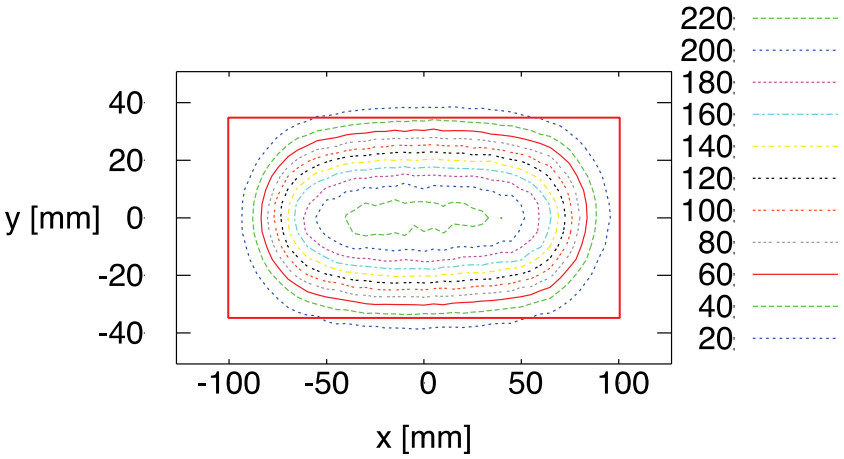

Figure 2.9. Beam distribution at the first target. The plot contours show the mA/m^2 value assuming a beam power of 2.0 MW at 50 Hz. The beam distribution for the 2.0 MW, 60 Hz case is practically identical.

2.2.3.1 Space Charge Effects

The purpose of this section is to assess the impact of collective effects on beam accumulation and transport at the proposed higher intensities for the PPU. Because the allowable losses in SNS are extremely small, the accumulator ring was constructed with a large aperture; and the beam pipe was coated with titanium nitride to reduce electron multipacting. The primary collective phenomena that could contribute to losses in the SNS ring are space charge, and extraction kicker impedances or electron cloud–driven instabilities. In present operation, none of these phenomena contributes significantly to beam loss. Losses in the SNS ring at this time are dominated by beam scattering from the primary stripper foil [5]. However, it is necessary to assess the impact of collective effects as operation at still higher intensities is considered.

In the longitudinal direction, it is operationally possible to maintain a clean gap for beam extraction to the target with significantly less RF power than is called for in the original SNS design. From this fact, we

can infer that longitudinal space charge and impedance effects will be mild. This is consistent with simulations performed during the SNS design that showed a wide margin of stability in the longitudinal plane [6]. In the transverse plane, space charge effects were observed to smooth the beam profiles and to introduce some coupling between the horizontal and vertical directions; but these had no effect on losses or on the ability to provide the required beam footprint at the target. In one controlled experiment, it was necessary to go to great lengths to induce instability because of the impedance of the extraction kickers. Simulations matched the observed growth rate of this instability under the conditions of the experiment [7], and similar simulations showed a wide margin of stability under normal operating conditions. The most likely cause of instabilities at high intensity may be electron cloud phenomena. In anticipation of this occurrence, the beam pipe in the ring was coated with titanium nitride to reduce electron multipacting. Even so, there are indications in the broadband transverse spectrum that the SNS ring beam may be at the onset of the electron cloud instability under present operating conditions. However, at present, no losses can be attributed to electron cloud activity.

It is possible to estimate analytically the effects of increased beam energy and intensity on the forces due to space charge and to known impedances. Table 2.5 presents such an estimate for four sets of parameters: present SNS production, the original design, the beam to the FTS with upgraded energy and intensity, and the beam to the STS with upgraded energy and intensity. The latter two cases use the parameters given in Plum et al. [8]. In all cases, the beam distribution sizes and shapes are considered to be the same, and the changes in impedance due to the altered ring and betatron frequencies are neglected. The scaling of the space charge and impedance forces is calculated as functions of beam energy and intensity only. However, an additional factor of 8/7 is included in the impedance-induced forces for the upgrade scenarios, because the number of extraction kickers was previously anticipated to be increased by 2, from 14 to 16, for the upgrade. The quantities used to compare the effects of the forces under the four scenarios are the induced energy changes for the longitudinal forces and the angular kicks for the transverse forces. The strengths of the forces for all cases are normalized to those for the present production parameters. Under the stated assumptions, the strengths of all forces increase linearly with increasing beam intensity, as measured by number of injected protons. Except for the longitudinal impedance, this increase with intensity is offset by decreasing strength with increasing energy, as a result of relativistic effects and increasing beam stiffness.

Table 2.5 shows that, because of these offsetting effects, neither longitudinal nor transverse space charge forces should pose a problem under upgraded operational scenarios. The longitudinal space charge force barely increases with the PPU parameters, and the transverse space charge force actually decreases. The forces associated with the extraction kicker impedance do increase, especially for the PPU parameters. Previous simulations [7, 9] showed there is a wide margin of stability—a factor of at least five in the longitudinal direction and more than two in the transverse direction—with respect to the extraction kicker impedance. Given these results and the values in Table 2.5, we anticipate that operation at the upgrade parameters should be stable with respect to the space charge and impedance forces. To further support those expectations, we have performed simulations of the first and second target upgrade scenarios with the ORBIT code, which indicate stable operation with upgraded beam parameters.

Table 2.5. Comparison of collective forces in SNS for four operating scenarios: present production, the original design, first target with an intensity upgrade, and second target with intensity upgrade.

Case	Production	Design	FTS at 2 MW, 60 Hz	Full intensity 2.8 MW, 60 Hz
Kinetic energy (GeV)	0.94	1.0	1.3	1.3
Relativistic γ	2.002	2.066	2.386	2.386
Relativistic β	0.866	0.875	0.908	0.908
N protons ($\times 10^{14}$)	1.55	1.5	1.61	2.241
Longitudinal space charge ($\Delta E \sim N \times \gamma^{-2}$)	1.0	0.909	0.728	1.026
Longitudinal impedance ($\Delta E \sim N \times \beta$)	1.0	0.977	[a]1.24	[a]1.745
Transverse space charge ($\Delta\theta \sim N \times \gamma^{-3} \times \beta^{-2}$)	1.0	0.863	0.556	0.784
Transverse impedance ($\Delta\theta \sim N \times \gamma^{-1} \times \beta^{-1}$)	1.0	0.928	[a]0.945	[a]1.333

[a]Impedance forces for upgrade scenarios multiplied by 8/7 to account for two additional extraction kickers.

Simple analytic estimation is not possible for the effect of electron clouds on the accumulating proton beam. The specifics of the generation mechanisms, locations, and quantities of ambient electrons in the accelerator are not precisely known. It is generally accepted that ambient electrons are generated by beam collisions with the beam pipe (beam loss), by ionization of the imperfect vacuum by the beam, and by multipacting from existing electrons striking the beam pipe [10]. A possible additional mechanism in SNS is incomplete collection of stripped electrons at the injection point. The behavior of ambient electrons generated in the beam pipe will depend on their location. Electrons in a drift space, dipole field, or quadrupole field have different orbits and will respond to the beam in different ways. Little is known of the locations of electrons in the SNS ring, but it may be assumed that they are located in the vicinity of the highest beam losses, downstream of the injection point and in the collimation section.

At the SNS, steps have been taken that mitigate the electron generation mechanisms, although the primary motivation for some of these steps is to minimize activation from beam loss. Fractional beam losses are maintained at a very low level ($\sim 10^{-4}$), and low beam loss corresponds to the generation of fewer electrons. The large beam pipe aperture (8 in. diameter) helps in loss minimization, and it places the location of electron multipacting further from the beam. A high vacuum of 10^{-8} torr is maintained in the ring, so electron generation by gas ionization is small. The geometry of the magnetic field in the vicinity of the stripper foil has been carefully designed and studied [11] to guide the stripped electrons to a collector. The walls of the SNS ring have been coated with titanium nitride for the specific purpose of reducing the secondary electron yield from multipacting. Additionally, a broadband feedback system has been developed to counter the effect of any observed electron cloud–induced instability [12].

Some simulations of the electron cloud dynamics in SNS have been performed [13,14]. According to Shishlo et al. [14], a linearized stability model and more detailed simulations are consistent with one another in predicting that, with 2×10^{14} protons, SNS should be stable for first harmonic RF voltages exceeding 15 kV. The available first harmonic RF voltage in SNS is 40 kV. Overall, we anticipate that SNS can be operated stably with respect to electron clouds at the upgraded parameters. If electron cloud instabilities should arise, additional measures, such as broadband feedback stabilization and longitudinal profile tailoring, are presently available and can be applied.

2.3 BEAM LOSS AND RESIDUAL ACTIVATION

With the increase in beam power, there will be an associated increase in beam loss and residual activation [15].

2.3.1 Residual Activation vs. Beam Energy

The residual activation (dose rate) depends on the beam power lost and the beam energy, as shown in Figure 2.10. The functional dependence, assuming copper (other materials are similar), is

$$\text{dose rate} = 0.33 \cdot (E^{-9})^{1.8}/E\,, \tag{2.1}$$

where E is the beam energy in MeV, and the dose rate is in mrem/h at 30 cm after a 4 hour cooldown. The plot ends at 1.2 GeV, and we assume that is still approximately correct at 1.3 GeV.

For a given number of protons lost per second, and keeping everything the same except for the beam energy, the activation is then proportional to

$$dose\ rate \propto (E-9)^{1.8}\,. \tag{2.2}$$

For a given number of protons lost per second at 1.3 GeV, the dose rate will be 1.61 times higher than at 1.0 GeV.

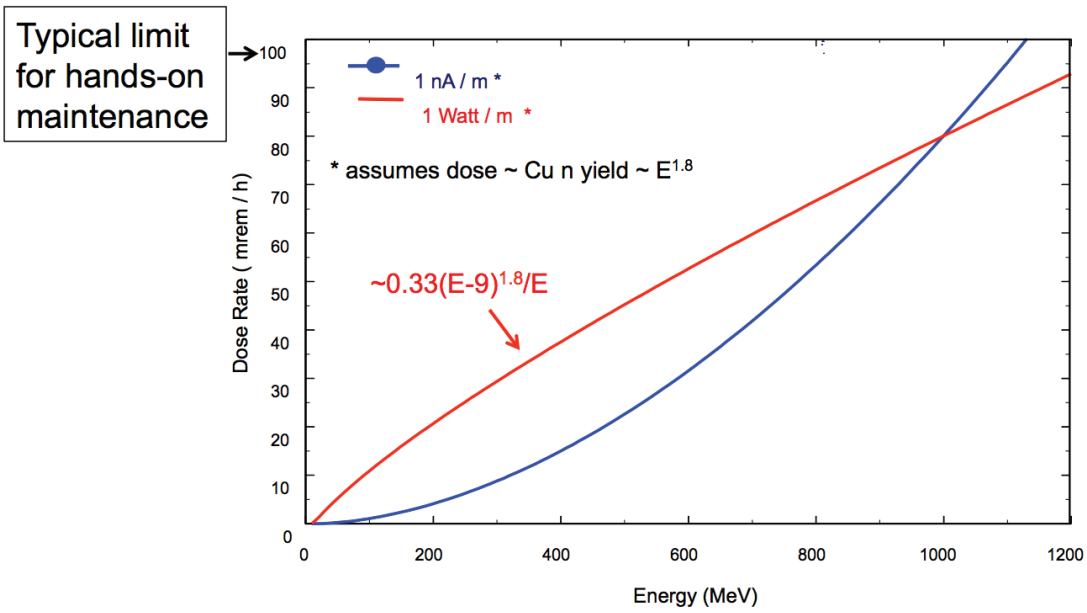

Figure 2.10. Activation as a function of beam energy [16].

2.3.2 Beam Loss in the Warm Linac

Beam loss in the warm linac is dominated by residual gas stripping and halo scraping (personal communication from A. Shishlo, ORNL, to M. Plum, ORNL, August 4, 2016). Intra-beam stripping is present but at levels much lower than the other mechanisms. To first order, we expect the beam loss to be proportional to the average beam current. The 2.8 MW case has an average current that is 1.44 times higher than the 1.4 MW case, so we expect the warm linac beam loss to also be 1.44 times higher.

2.3.3 Beam Loss in the Superconducting Linac

Beam loss in the SCL is dominated by intrabeam stripping [17]. The beam loss caused by this mechanism is proportional to the square of the beam density. Compared with the 1.4 MW case, the 2.8 MW case will

have a 25 us longer macropulse and 1.44 times higher average current, so the beam density will be 1.404 times higher. The beam loss is therefore expected to be 1.97 times higher.

In the downstream portion of the SCL, where the dummy section is now located, the activation levels could be more than 1.97 times higher, simply because of the beam energy exceeding 1.0 GeV in this area. Therefore, at the end of the SCL, the dose rate could increase by a factor of 1.97·1.61 = 3.17 (see Section 2.3.1 for the 1.61 factor discussion). However, note that, in practice, the SCL activation levels do not seem to depend significantly on the beam energy (perhaps because of adiabatic damping?), so historical evidence provides a counter-argument for the extra factor of 1.61.

2.3.4 Beam Loss in the Ring Injection Area

The ring injection area has by far the most radioactivation in the accelerator, and the dominant cause is large-angle Coulomb and nuclear scattering in the stripper foil. At the Los Alamos National Laboratory Proton Storage Ring, nuclear and large-angle Coulomb scattering contribute nearly equal amounts to the beam loss (~35% due to large-angle Coulomb vs. ~30% due to nuclear) [18]. The following discussion assumes equal contributions. At SNS the excited-state H0 losses are expected to be very small as a result of placing the stripper foil inside the chicane magnet.

2.3.4.1 Coulomb Scattering

The probability of a large-angle Coulomb scattering event causing beam loss is [18]

$$P = 5.674 \cdot 10^{-8}\{\mathrm{cm}^2\}\left(\frac{Z}{\gamma\beta^2}\right)^2\left(\frac{\rho t}{A}\right)\left[\frac{1}{\theta_{xl}\theta_{yl}} + \frac{1}{\theta_{xl}^2}\tan^{-1}\left(\frac{\theta_{yl}}{\theta_{xl}}\right) + \frac{1}{\theta_{yl}^2}\tan^{-1}\left(\frac{\theta_{xl}}{\theta_{yl}}\right)\right], \qquad (2.3)$$

where ρt is the effective foil thickness, Z and A are the atomic number and atomic mass of the foil material (carbon), β and γ are the relativistic factors, and θ_{xl} and θ_{yl} are the limiting angles, obtained from the limiting apertures. The foil thickness at 1.3 GeV will be 8% thicker than at 1.0 GeV.

Based on Eq. (2.3), the scattering probability is directly proportional to the foil thickness ρ. From this equation, we see that the scattering probability scales inversely with $\gamma^2\,\beta^4$. Per injected proton, the number of beam particles lost will therefore be lower at 1.3 GeV than at 1.0 GeV because the factor of 1.91 decrease in scattering probability more than compensates for the 8% increase in foil thickness.

For a given number of injected protons, keeping everything the same except for the beam energy and the foil thickness, the activation is then proportional to

$$\text{dose rate} \propto \left(\frac{1}{\gamma\beta^2}\right)^2 (\rho t)(E-9)^{1.8}\,. \qquad (2.4)$$

For a given number of injected protons, the dose rate at 1.3 GeV is 12% higher than at 1.0 GeV.

To compare 1.0 GeV, 1.4 MW, with 1.3 GeV, 2.8 MW, note that there are 2.24/1.55 = 1.44 times more injected protons (stored proton intensity ratio) for the 2.8 MW case. So the dose rate for the 2.8 MW case is 1.63 times the dose rate for the 1.4 MW case.

2.3.4.2 Nuclear Scattering

Until detailed simulations can be performed, we estimate the nuclear scattering effect by assuming the proton-carbon cross section is proportional to the sum of the pp and pn cross sections. Based on data from the Lawrence Berkeley Laboratory Particle Data Group, the sums of the pp and pn total cross sections are nearly the same at 1.696 and 2.386 GeV/c (corresponding to 1.0 and 1.3 GeV beam energies). We conclude that the probability of beam loss due to nuclear scattering is approximately equal for the 1.0 and 1.3 GeV cases (for a given foil thickness). Following the arguments in Section 2.3.4.1,

$$\text{dose rate} \propto (\rho t)(E-9)^{1.8} \, . \tag{2.5}$$

Including the greater number of injected protons, the dose rate due to nuclear scattering at 2.8 MW is expected to be 2.51 times greater than at 1.4 MW.

2.3.4.3 Both Large-Angle Coulomb and Nuclear Scattering

We assume that large-angle Coulomb and nuclear scattering contribute equally to the total beam loss because of stripper foil interactions. The dose rate then scales as

$$\text{dose rate} \propto \left[1+\left(\frac{1}{\gamma\beta^2}\right)^2\right](\rho t)(E-9)^{1.8} \, . \tag{2.6}$$

For a given number of injected protons, keeping everything the same except for the beam energy and the foil thickness, the dose rate at 1.3 GeV is expected to be 1.56 times higher than at 1.0 GeV. Adding in the factor of 1.44 times more protons for the 2.8 MW case compared with the 1.4 MW case gives an estimated dose rate 2.26 times higher.

2.3.4.4 Beam Loss in the Ring Collimation Section

In addition to large-angle Coulomb and nuclear scattering in the stripper foil, there is small-angle scattering. This type of scattering causes a slow growth in the beam tails that primarily causes beam loss in the collimation section.

Based on the work of Hinterberger, Mayer-Kuckuk, and Prashun [19], the rms scattering angle of a proton beam passing through a very thin film is

$$\theta_{rms} = \frac{14.1 \text{ MeV}}{p\beta c}\sqrt{\left(x/x_{rad}\right)} \, , \tag{2.7}$$

where p is the proton beam momentum, βc is the proton velocity, x is the stripper foil thickness, and x_{rad} for carbon is 42.7 g/cm^2. (This is similar to Eq. [2.6], but without the logarithmic term). For our case, at 1.0 GeV and for a 0.385 mg/cm^2 thick foil, $\theta_{rms} = 2.2\times10^{-5}$ rad; and at 1.3 GeV and a 0.416 mg/cm^2 thick foil (8% thicker), $\theta_{rms} = 2.0\times10^{-5}$ rad. The rms scattering angle is 9% lower at 1.3 GeV, but the beam energy is higher.

It is not exactly correct to say that the beam loss scales with the rms scattering angle, but we can use it as a rough estimate. We assume that

$$\text{dose rate} \propto \theta_{\text{rms}}(E-9)^{1.8} \tag{2.8}$$

and find that for a given number of injected protons, keeping everything the same except for the beam energy and the foil thickness, the dose rate at 1.3 GeV is expected to be 1.46 times higher than at 1.0 GeV. Adding in the factor of 1.44 times more protons for the 2.8 MW case compared with the 1.4 MW case gives an estimated dose rate 2.11 times higher.

2.3.5 Beam Loss in the HEBT and Ring-to-Target Beam Transport

The fractional beam loss in the HEBT and ring-to-target beam transport (RTBT) should be about the same at 1.0 and 1.3 GeV. The space charge effects are small at these energies. We therefore expect the number of particles lost will scale with the total number of particles. The dose rate will be higher because of the higher beam energy.

For a given number of protons, keeping everything the same except for the beam energy, the dose rate at 1.3 GeV is expected to be 1.61 times higher than at 1.0 GeV. Including the factor of 1.44 times more protons for the 2.8 MW case compared with the 1.4 MW case gives an estimated dose rate 2.33 times higher.

2.3.6 Activation

Figure 2.11 shows recent dose rate data taken after 1.3 MW operation. The expected increase in dose rate at 1.0 GeV, 1.4 MW, is a factor of 1.4/1.3 = 8% times greater. The expected dose rate increase from 1.4 to 2.8 MW is summarized in Table 2.6.

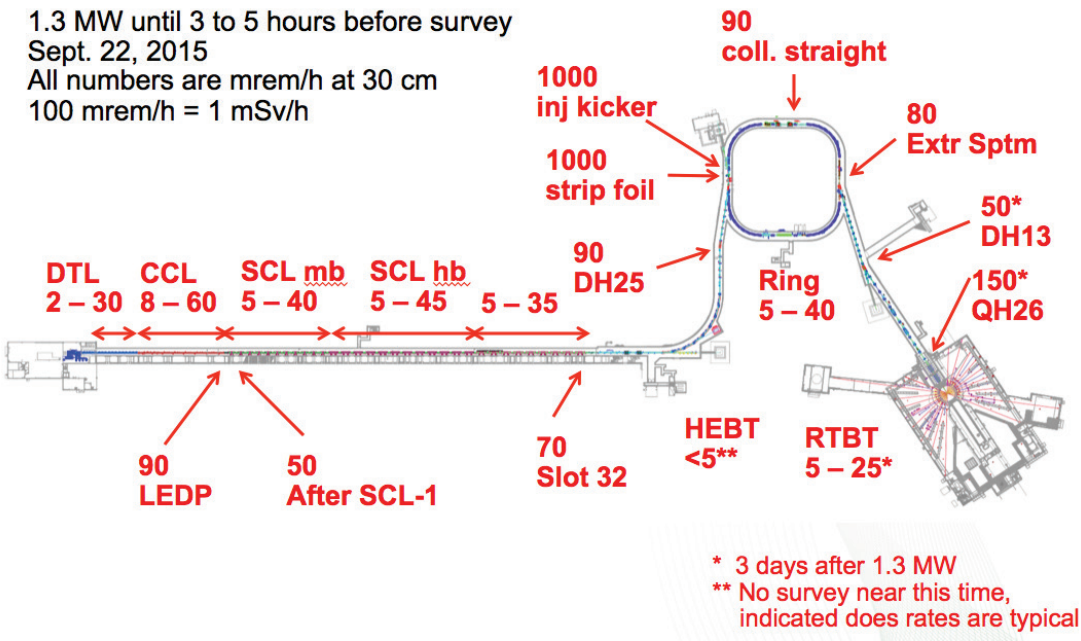

Figure 2.11. Recent dose rate data measured on September 22, 2015, after 1.3 MW operation.

Table 2.6. Expected increase in dose rates from 1.4 to 2.8 MW operation

Location in accelerator	Dose rate increase factor
Warm linac	1.44
SCL (up to 1.0 GeV section)	1.97
SCL (1.3 GeV section)	1.97 – 3.17
HEBT	2.33
Ring injection	2.26
Ring collimation	2.11
RTBT	2.33

2.4 HEBT ARC BEAM LOSS VS. BEAM ENERGY

The HEBT was designed to transport H^- beam at energies up to 1.3 GeV. The discussion in this section details the consequences of increasing the beam energy beyond 1.3 GeV.

Magnetic stripping [20] as a function of beam energy is

$$\frac{df}{ds} = \frac{B(s)}{A1} e^{-A2/\beta\gamma cB(s)}, \tag{2.9}$$

where $A1$ = 2.47E–6 V sec/m, $A2$ = 4.49E9 V/m, $B(s)$ = magnetic field, and β, γ, c are the usual relativistic factors.

The HEBT arc has eight dipoles that bend the beam by 90°. The magnetic length of each dipole is 5.432 m, and the total magnetic length is 43.456 m. To bend the beam through an angle θ requires a B-field,

$$B = \frac{\theta(B\rho)}{L}, \tag{2.10}$$

where $(B\rho)$ is the beam rigidity, $B\rho = 3.1297\beta\gamma$ for proton beams, and L is the magnetic length. Then df/ds can be expressed in terms of just β and γ, and the fractional loss per meter in the HEBT arc can be expressed in terms of just the beam energy. A plot of the result is shown in Figure 2.12.

At a beam energy of 1.3 GeV, the fractional loss per meter is 5.5E–8. For a beam power of 2.8 MW, this corresponds to 0.154 W/m. The rule-of-thumb upper limit is 1 W/m for the total beam loss, so beam operation at 1.3 GeV, 2.8 MW, leaves only a small margin for the other beam loss mechanisms. If the beam energy were 1.36 GeV, the magnetic stripping losses would be 1 W/m and the total losses would certainly exceed 1 W/m. The 1.3 GeV design energy of the HEBT therefore represents a fairly hard upper limit.

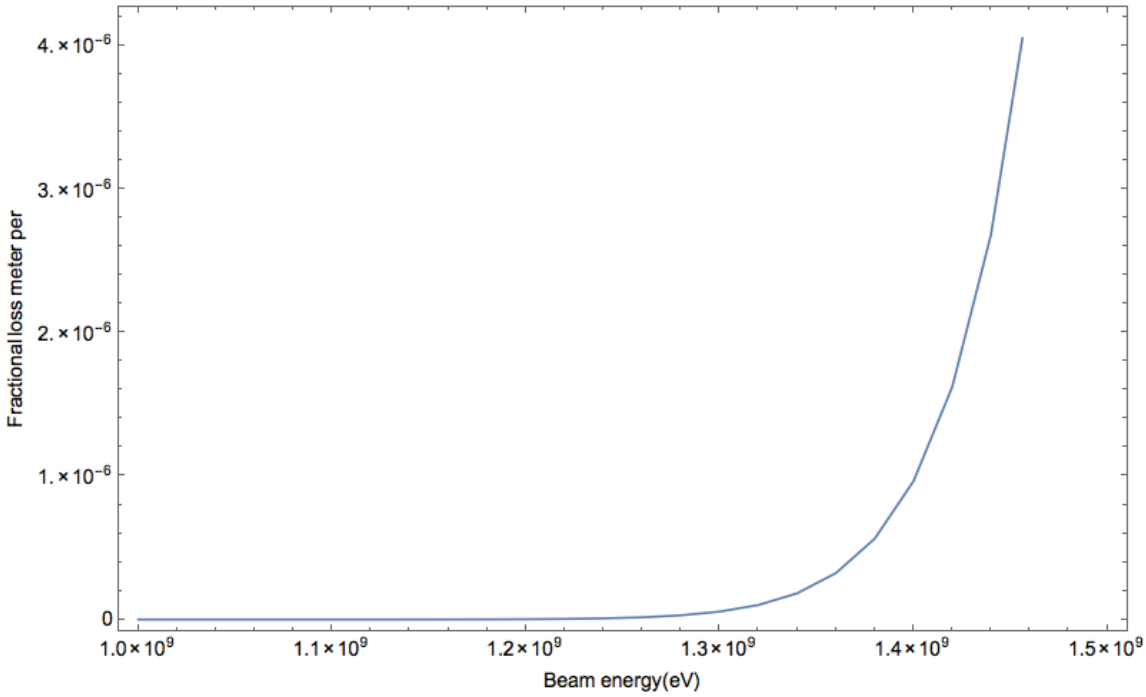

Figure 2.12. Plot of the fractional loss per meter in the HEBT arc vs. beam energy.

2.5 MAJOR ASSUMPTIONS

This section describes major assumptions for the PPU design. Detailed assumptions for the various subsystems are described in the sections describing these systems, and the scope to be covered by SNS operations is covered in the *PPU Project Assumptions Document* [21]. Primary technical assumptions described here relate to the front-end system (ion source) and the choice of which beam parameters to increase to accomplish the power upgrade.

2.5.1 Front End Systems

The PPU power increase will require a peak current of 46 mA out of the RFQ. This implies a peak current of about 54 mA delivered by the source, which corresponds to an 87% RFQ beam transmission rate. No increase above the present beam duty factor is planned for STS operation; it will remain at 60 Hz × 1 ms, or 6%. The baseline plan to reach a 54 mA source output is incremental improvement of the present ion source design using the existing ion source test stand. The recently procured new RFQ has demonstrated the required beam transmission at >46 mA peak current. Also, a modified chopping pattern waveform procedure will be implemented to produce the required 82% unchopped beam fraction, as discussed in Section 2.1.1.

Ion source beam production currents over recent years are shown in Figure 2.13 (personal communication from Baoxi Han, ORNL, to J. Galambos, ORNL, March 2020). These data are measured at the entrance to the RFQ on the front end of the SNS linear accelerator. Three primary sources are used in operations. They have averaged about ~50 mA in recent years with some demonstrating up to ~60 mA (note that for much of the period shown, there was not a demand for higher beam current, as the beam power was target limited). There has been a steady increase in source performance of ~20% over the past 3 years. The PPU requirement of 54 mA has been achieved.

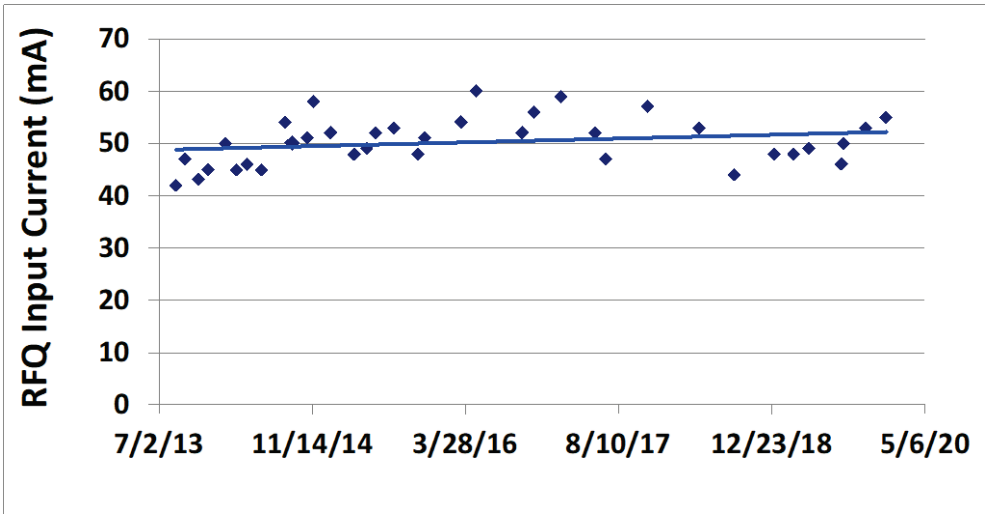

Figure 2.13. Recent ion source current, measured at the RFQ entrance on the SNS front end. Note, from 8/18 – 8/19 the ion source current was not pushed, as a new RFQ was installed, and the required 1.4 MW accelerator power was easily attained with reduced current.

Increasing the reliable source output to 54 mA (~10% additional performance increase) will be accomplished by

- increasing the RF power capability
- reducing the ion source output emittance
- optimizing the source collar aperture and dumping the magnetic field profile

These planned development areas are a continuation of the ongoing efforts, which have resulted in the increased ion source performance shown in Figure 2.14. The additional ~10% source performance improvement will provide operational margin for reliable high-power capability. The present ion source has also demonstrated high reliability over this period (~99.5%) and is not a significant driver of overall accelerator availability. The path proposed here of incremental improvement of proven technology is deemed lower in risk than the development of a new source technology. For example, earlier SNS power upgrade plans [1] employed a dual ion source solution [22], one operated as a hot spare with a bend magnet in a new downstream magnetic LEBT to switch between sources. The earlier upgrade design aimed for an ion source output current of 67 mA, which would have required a more serious source improvement. Improved chopping scenarios deployed at SNS over the past few years and incorporated into PPU significantly reduce the ion source output current requirement. As a result of the lower source requirement and improved production source capability, the development of a dual source and magnetic LEBT (with fast chopping) technology is not included in the PPU scope. This change significantly reduces accelerator development requirements.

2.5.2 Radio Frequency Quadrupole

The expected RFQ beam transmission is shown in Figure 2.14 for several input beam emittance levels [23]. For the nominal input emittance of 0.25 pi-mm-mrad, the transmission is ~87% for an input current of ~54 mA. Above ~70 mA, the transmission efficiency begins to drop quickly, but this current level is well above the PPU requirement.

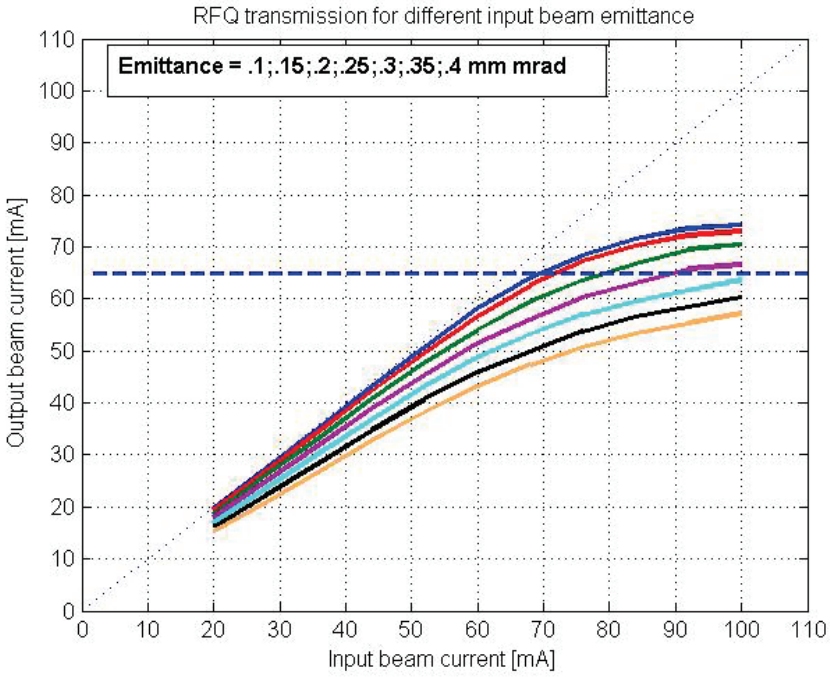

Figure 2.14 RFQ beam transmission from simulations for the design value field profile along the RFQ.

Nonetheless, 87% transmission is significantly higher than the measured transmission of 60–80% in the original RFQ installed at SNS. There was a known field profile issue with the original RFQ, which is the original equipment item delivered from Lawrence Berkeley National Laboratory. The original RFQ, however, had several detuning incidents; and the field profile at the RFQ entrance is not known. (After the last detuning incident, the field profile was corrected along most of the RFQ; but measurements were not possible at the RFQ entrance because of access limitations.) To address this problem, a new RFQ was manufactured using the same physics design but incorporating a more robust structure. The new RFQ was installed and operational in the SNS and has demonstrated the required 90% beam transmission with >46 mA exit beam current. RF gasket issues were identified on this new RFQ, so another RFQ has been ordered with design improvements to eliminate the RF gasket problem. It is planned to test and install this RFQ before PPU completion.

2.6 POWER LEVEL

The PPU project scope is to double the proton beam power capability from 1.4 to 2.8 MW. The original accelerator construction provided accommodations for a doubling of the proton power. The path for delivering 2.8 MW uses these accommodations and is described in the STS *Technical Design Report* [23]. The high-level beam parameters are shown in Table 2.7. Power for a pulsed beam is the product of the beam energy, the macro-pulse beam current, and the duty factor. The PPU choices for the energy and current increase to reach the 2.8 MW power capability have several advantages:

- Ion source beam current is demonstrated.
- It can reach 1.3 GeV with only seven new cryomodules using existing klystrons and coupler designs.
- Only three new modulators are required.
- Most of the warm linac klystrons are capable of accelerating the additional beam current.

- There are modest HVCM improvements from the existing technology (4–5% increase in capacitor bank voltage).

These choices heavily leverage the accelerator development work done to reach 1.4 MW, with minimal further development needed. Although it is possible to design for a higher power than 2.8 MW, the project cost and, more critically, project risk increase beyond this level. The factors leading to the choices in Table 2.7 are described in the beam power report [24] and summarized here.

Increasing the beam energy is the most straightforward path to higher beam power. There are advantages to pursuing this path to the extent possible. A higher energy per proton means fewer accelerated protons are required and reduces the probability of beam loss, both from individual particle loss mechanisms and from collective loss mechanisms. At higher beam energy, the collective effects are reduced, so beam loss and instability issues in the storage ring are reduced. However, for beam energies above 1.3 GeV, magnetic stripping of the accelerated H^- beam in the transport line to the ring begins to exponentially increase to intolerable levels, so the 1.3 GeV beam energy is a rather hard upper limit.

It is possible to increase the beam current beyond the baseline value for 2.8 MW; an example is shown in Table 2.7. However, doing so would require development of the ion source capability and the design of a new RFQ to transmit higher beam current. These are primary reasons for limiting the average linac beam current to 38 mA. Also, there would be additional burdens on RF equipment (klystrons, modulators, and couplers) due to the additional beam loading, which add to the project cost and technical risks. A major complication of this approach is the need to rework many of the presently installed cryomodules with higher-power couplers. There also would be increased risks in the foil charge exchange area and beam stability associated with the higher stored beam intensity in the accumulator ring.

Table 2.7. Beam parameters for Proton Power Upgrade options

	2.8 MW PPU baseline	3.5 MW higher duty factor	3.5 MW higher current
Beam energy	1.3	1.3	1.3
Average linac current (mA)	38	38	47.5
Peak ion source current (mA)	54	54	75
Macro-pulse length (ms)	1	1.25	1
Beam repetition rate (Hz)	60	60	60
Stored protons in ring (10^{14})	2.26	2.83	2.83
Stored energy per pulse (kJ)	47	59	59
Normalized ring transverse space charge	0.78	0.98	0.98
Additional high-beta cryomodules	7	7	8-9
Additional high-voltage convertor modulators	3	3	4

It is also possible to increase the linac beam pulse length (duty factor), as indicated in Table 2.7. This approach would significantly increase the technical risk for the ion source reliability and performance capability (it becomes increasingly difficult to produce high currents at increasing duty factors). Also, there would be increased risks for the other pulsed RF equipment, such as klystrons and modulators, at higher operational duty factors. The equipment has never been tested beyond the design value corresponding to a 6% beam duty factor. Also the warm copper RF structures (drift-tube linac and

coupled-cavity linac) cooling systems were designed for a 6% duty factor. These systems would have to be reworked to accommodate an increase in the duty factor. Finally, the electrical cost for operation of the RF equipment (a major driver in accelerator electricity usage) is proportional to the duty factor, so a 25% increase in the duty factor would result in about a 15–20% increase in utility costs.

Finally, any discussion of increased accelerator power capability should also include a mention of target limitations. As is discussed in Section 6, the FTS target is being designed for a 2.0 MW capability at 60 Hz. Increasing the accelerator power beyond the 2.8 MW level would potentially benefit the pulses directed toward the STS, but the remaining pulses (45 pulses per second from the 60 Hz stream) directed toward the FTS would be limited in intensity to 33 kJ/pulse. Thus, a large fraction of the increased beam potential would be underutilized for the pulses directed to the FTS. While it may be possible to develop higher-power FTS targets, and upgrade the FTS support systems to handle higher power, doing so is a high-risk option.

2.7 REFERENCES

1. S. Henderson et al., "Status of the SNS Beam Power Upgrade Project," pp. 345–347 in *Proceedings of EPAC 2006*, Edinburgh, Scotland (2006). http://accelconf.web.cern.ch/AccelConf/e06/PAPERS/MOPCH129.PDF. Accessed May 2020.

2. J. Lyon and S. Cousineau, "Study of simulations of variable chopper pattern widths," summer intern presentation, 2015.

3. TraceWin, The Service of Accelerators, Cryogenics, and Magnetism, available at http://irfu.cea.fr/Sacm/logiciels/index3.php. Accessed May 2020.

4. J. A. Holmes, S. Cousineau, V. V. Danilov, et al., "ORBIT: Beam dynamics calculations for high-intensity rings," *ICFA Beam Dynamics Newsletter* 30, pp. 100–107, International Committee for Future Accelerators (April 2003).

5. J. A. Holmes and M. A. Plum, "Beam loss due to foil scattering in the SNS accumulator ring," pp. 254–258 in *Proceedings of the ICFA High Brightness Workshop HB2012*, Beijing, September 17–21, 2012.

6. K. Woody, J. A. Holmes, V. Danilov, et al., "Longitudinal impedance simulations in ORBIT: Benchmarking and application to the SNS extraction kicker," pp. 2057–2059 in *Proceedings of the 2001 Particle Accelerator Conference* (PAC 2001), Chicago, June 18–22, 2001.

7. J. A. Holmes, S. Cousineau, V. Danilov, et al., "Comparison between measurements, simulations, and theoretical predictions of the extraction kicker transverse dipole instability in SNS," *Phys. Rev. Special Topics—Accelerators and Beams* **14**, 074401 (2011).

8. M. A. Plum, J. Galambos, and S.-H. Kim, "Accelerator systems modifications for a Second Target Station at the Oak Ridge Spallation Neutron Source," in *Proceedings of the International Particle Accelerator Conference (IPAC14)*, Dresden, Germany, June 15–20, 2014.

9. J. A. Holmes, V. Danilov, and L. Jain," Transverse stability studies of the SNS Ring," in *Proceedings of the Particle Accelerator Conference (PAC05)*, Knoxville, Tennessee, May 16–20, 2005.

10. M. A. Furman and M. Pivi, "Probabilistic model for the simulation of secondary electron emission," *Phys. Rev. Special Topics—Accelerators and Beams* **5**, 124404 (2002).

11. S. Cousineau, J. A. Holmes, M. A. Plum, et al., "Dynamics of uncaught foil-stripped electrons in the Oak Ridge Spallation Neutron Source accumulator ring," *Phys. Rev. Special Topics—Accelerators and Beams* **14**, 064001, 2011.

12. C. Deibele, S. Assadi, M. Schulte, et al., "Status and implementation of a wideband feedback system for E-P instabilities in the SNS," p. 462 in *Proceedings of the High Brightness (HB2008) Conference,* Nashville, Tennessee, August 25–29, 2008.

13. M. Blaskiewicz, M. A. Furman, M. Pivi, et al., "Electron cloud instabilities in the Proton Storage Ring and Spallation Neutron Source," *Phys. Rev. Special Topics—Accelerators and Beams* **6**, 2003, 014203.

14. A. Shishlo, S. Cousineau, V. Danilov, et al., "Electron cloud self-consistent simulations for the SNS ring," pp. 2832–2834 in *Proceedings of the European Particle Accelerator Conference (EPAC06)*, Edinburgh, Scotland, June 26–30, 2006.

15. M. Plum, *Beam Loss and Activation for PPU-STS*, ORNL/LTR-2016/375, Oak Ridge National Laboratory, August 8, 2016 .

16. J. Galambos, "SNS Beam Loss, Activation, and Collimation," Snowmass 2001, Snowmass Village, June 30—July 21, 2001, July 7, 2001.

17. A. Shishlo et al., "First observation of intrabeam stripping of negative hydrogen in a superconducting linear accelerator," *Phys. Rev. Lett.* **108**, 114801, 2012.

18. R. Macek, "PSR beam losses at injection," in *High Intensity and High Brightness Hadron Beams: 33rd ICFA Advanced Beam Dynamics Workshop*, ICFA-HB2004, eds. I. Hoffmann, J.-M. Lagniel, and R. W. Hasse, Bensheim, Germany, October 18–22, 2004, AIP Conference Proceedings, June 8, 2005.

19. F. Hinterberger, T. Mayer-Kuckuk, and D. Prashun, "Monte Carlo simulations of thin internal targets in intermediate energy proton storage rings," *Nucl. Inst. Meth*. **A275**, 239–245, 1989.

20. A. Jason, D. W. Hudgings, and O. B. VanDyck, "Neutralization of H^- beams by magnetic stripping," *IEEE Trans. Nucl. Sci.* **NS-28**(3) 2704, June 1981.

21. [21] *PPU Project Assumptions Document*, PPU-P01-MO0001-R01, Oak Ridge National Laboratory, March 2019.

22. [22] B. Han and M. Stockli, "The new LEBT for the SS Power Upgrade Project," pp. 1823–1825 in *Proceedings of EPAC 2006*, Edinburgh, Scotland, June 26–30, 2006. http://accelconf.web.cern.ch/AccelConf/p07/PAPERS/TUPAS075.PDF. Accessed May 2020.

23. [23] J. Galambos, D. E. Anderson, D. Bechtol, et al., *Technical Design Report, Second Target Station*, ORNL/TM-2015/24, Oak Ridge National Laboratory, January 2015. Available at http://www.osti.gov/scitech/biblio/1185891. Accessed May 2020.

24. [24] *PPU Beam Power Level*, PPU-P01-TR0001, internal project technical report, Oak Ridge National Laboratory, November 2016.

3. SUPERCONDUCTING LINAC

3.1 SUPERCONDUCTING LINAC OVERVIEW

Requirements for superconducting linac (SCL) scope. Seven cryomodules will be installed in the reserved space at the end of the linac tunnel to produce a linac output energy of 1.3 GeV with an energy margin specified in Section 2.1. In support of the PPU key performance parameters, the SCL requirements are listed in Table 3.1.

Table 3.1. Superconducting linac requirements.

Category	Requirement	Description	FDR section
Beam energy	1.3 GeV	Objective key performance parameter	3
Energy margin	>15 MeV	Provide adequate energy margin for operation at 1.3 GeV and 38 mA	3.2.1
Beam current	38 mA	Support 38 mA PPU beam loading	3.3.1
Radio frequency (RF) integration— existing cavities	550 kW (peak)	Exiting cavities/couplers operate with existing RF systems (48 kW average power)	3.2.1
RF integration—PPU cavities	700 kW (peak)	PPU cavities/couplers will be powered by new RF systems (65 kW average power)	3.2.3
Cryomodule (CM) slot length	7.891 m	PPU cryomodules shall fit in existing linac slots	3.3
Central helium liquefier (CHL) primary helium circuit	>105 g/s	Existing CHL hardware shall provide cryogenic cooling for cavities at 2 K with adequate margin	3.3.1 and 3.4
CHL secondary helium circuit	>15 g/s	Existing CHL hardware shall provide cryogenic cooling for couplers at 4 K with adequate margin	3.3.1 and 3.4
CHL shield helium circuit	>8300 W	Existing CHL hardware shall provide cryogenic cooling for shields at 35 K with adequate margin	3.3.1 and 3.4
Beamline vacuum	$<5 \times 10^{-10}$	Cold measurement of beamline vacuum	3.5
Insulating vacuum	$<5 \times 10^{-5}$	Cold measurement of insulating vacuum	3.5
Cooling water integration	>1 gpm (per CM)	Existing quadrupole magnet cooling system shall provide coupler inner conductor cooling at air side with adequate margin	3.5

The optimum geometric beta of the cavities for the PPU is higher than that of the original high-beta cavities; but the module length and, accordingly, the cavity geometric beta will be kept the same for economic reasons. All helium transfer lines were previously installed during the SNS project with bayonets for the high-beta cryomodules. Waveguide penetrations from the klystron gallery to the linac tunnel were also previously installed.

Some changes that do not require modification of the overall layout will be made based on the lessons learned from experience over the past 12 years and on the pressure-vessel compliance issue. Table 3.2 summarizes the design changes between the original SNS high-beta cryomodule and the high-beta cryomodule for the PPU. Some details for the changes are described in the following subsections.

Table 3.2. Design parameter changes.

Parameters	Original SNS high-beta cryomodule	PPU high-beta cryomodule
E_{acc} (=E_oT_g, T_g: Transit time factor at β=0.81) (MV/m)	15.8	16.0
Fundamental power coupler (FPC) rating, peak and average (kW)	550, 50	700, 65
External Q of FPC, Q_{ex}	7×10^5 (±20%), fixed type	8×10^5 (±20%), fixed type
Material of cavity	High RRR niobium (RRR>250) for cells, reactor-grade niobium for end groups	High RRR niobium (RRR>300) for both cells and end groups
Higher-order mode couplers per cavity	Two (one at each end group)	None
Tuner	One mechanical tune, one fast piezo tuner	1 mechanical tuner (no fast piezo tuner)
Pressure vessel	Good engineering practice	Code stamp required

RRR = residual resistivity ratio

3.2 SUPERCONDUCTING RADIO FREQUENCY CAVITY

The cavity radio frequency (RF) parameters for the PPU are the same as for the original ones. Table 3.3 shows the common parameters between the original and PPU cavities.

Table 3.3. Major parameters of the SNS high-beta cavity.

Frequency (MHz)	805
Type	Elliptical
Operating mode	pi
Geometric beta	0.81
Equivalent cavity length (mm)	906
Bore radius (mm)	48.8
Inter-cell coupling (%)	1.6
r/Q at geometric beta at β=0.81 (ohm)	483
E_{peak}/E_{acc}	2.2
B_{peak}/E_{acc} (mT/MV/m)	4.75
Wall thickness (mm)	4 (~3.8 after chemical processing)
Operating temperature	2 K
Q_o	$>5 \times 10^9$ at 2 K
Number of cells per cavity	6
Stiffener	Yes (at r = 80 mm)
Fundamental power coupler per cavity	1

3.2.1 Accelerating Gradient

The accelerating gradients of the PPU cavities, shown in Section 2.1, are based on the results from the spare high-beta cryomodule and the R&D for performance improvements.

New cavities for the PPU. A high-beta spare cryomodule was developed in-house and has been installed in the tunnel for operation since summer 2012. All four cavities in the spare cryomodule were commissioned at 17 MV/m or higher at the full duty factor. Only one cavity shows minor x-rays starting from 15.5 MV/m, and all four cavities have been running at 16 MV/m for the production run [1,2]. The available RF power limits the operating gradients to 16 MV/m for these cavities. Originally, the performance of the SNS cavities in the linac was mainly limited by field emission and multipacting, resulting in lower operating gradients at 13.0 MV/m on average. After the deployment of plasma processing to 7 high-beta cryomodules out of 12 cryomodules, the average operating gradient of all high-beta cavities is now 14.8 MV/m. Improvement of the cavity performance for the spare cryomodule came from changing the cavity chemical processing recipe from buffered chemical processing (BCP) to electropolishing (EP). EP produces a smoother surface finish and has typically shown higher operational gradients and higher field emission onset. Another identified limitation of all original SNS cavities is that the end group surfaces are very rough as a result of high-aspect-ratio deep drawing and the additional heat treatments. These end groups were fabricated from reactor-grade niobium, rather than high-purity or high–residual resistivity ratio (RRR) material, in an attempt to reduce the material costs of the cavities. The reactor-grade material was then heat-treated in a vacuum furnace to improve its thermal conductivity, but the treatment increased the niobium grain size in the process. The increased grain size, coupled with BCP, resulted in preferential etching of the grain edges, creating a very rough surface finish on all original SNS cavities. This rough surface on the end groups is difficult to clean and has many sharp edges at the grain boundaries. It could also produce trapped volumes for particulates and gases, consequently increasing the secondary emission yield and field emission. The EP process that was applied to the spare cryomodule cavities improved the surfaces of both the cells and the end groups and allowed for better cleaning of all surfaces following the chemical processing. The cavity performance observed in the high-beta spare cryomodule offers high confidence that the PPU cryomodules will meet the gradient specification by using EP instead of BCP for the final chemistry and by improving the cavity end groups.

Original SNS cavities in the tunnel. The original cavities show electron loading from field emission and multipacting below the design accelerating gradients, which are the main limiting factor. In addition, as the repetition rate was increased, more severe collective effects between cavities were observed—i.e., operation of one cavity affecting the performance of neighboring cavities. The severity of the collective effects is determined not only by the amplitude of the accelerating gradients in the cavities of a cryomodule, but also by their relative RF phases. This is so because both affect the trajectories of the electrons, the electron energies, and the locations at which the electrons impact on the cavity surfaces. As a result of the collective effects, cavities became thermally unstable at lower gradients than they did during lower-repetition-rate operation, thus limiting the final linac output energy. When electrons hit any intermediate-temperature region in the cavity string, bursts of adsorbed hydrogen gas can sometimes occur and trigger vacuum interlocks. These can lead to redistribution of the adsorbed gas in the cavity string and to lower operating gradients. Therefore, operation into high electron loading must be prevented for the sake of stability, which limits the final linac output beam energy. Each cavity is set at a stable gradient based on the collective limiting gradients achieved through a series of superconducting RF (SRF) cavity/cryomodule performance tests at SNS, whereas the design calls for setting uniform gradients [3].

At SNS, in situ processing in the tunnel has been identified as an important area of research for improving the SRF cavity performance while minimizing the machine operational impact and reducing the cost of the improvements. Research and development for in situ processing using plasma was successfully performed at SNS [4]. The plasma processing technique was deployed to seven high-beta cryomodules during the machine maintenance periods between 2016 and 2018. The results show that the accelerating gradient of the plasma-processed cavities was increased by 2.5 MV/m (or 20%) on average. Consequently, the beam energy has been increased from 940 MeV to 1010 MeV. The accelerating gradients of the original cavities for the PPU baseline assume some gradients for medium-beta cavities have been increased by plasma processing.

The high-power RF systems for the original cavities will be kept the same for economic reasons. Since the output power of the original high-power RF systems at saturation is 550 kW, the accelerating gradients of high-performing original high-beta cavities will need to be lowered for the PPU beam loading, as shown in Figure 2.2.

In addition, a spare medium-beta cryomodule is available for conducting repairs on the inoperable medium-beta cavities, 1a, 5a and 11b. It is assumed that at least one of these cavities will be repaired for operation in advance of the PPU. The medium beta spare cryomodule was installed in the linac tunnel in March, 2020 and cryomodule 1 was removed to repair a leak in a ceramic window on the inner conductor of a fundamental power coupler.

If performance improvements after the repairs or plasma processing do not meet expectations, the linac output energy will still be 1.3 GeV, but with a reduced energy margin.

Dynamic detuning compensation. The observed dynamic detuning of the original SNS high-beta cavities due to the Lorentz force is in the range of 1–2 Hz/(MV/m)^2 during the whole pulse. The dynamic detuning during the beam is less than 0.5 Hz/(MV/m)^2. Since the cavity bandwidth is relatively large (half bandwidth is ~570 Hz) or the external Q is relatively low ($<10^6$) because of the high beam loading, the additional RF power needed to compensate for the dynamic detuning is minor. This amount of detuning is well managed by the adaptive feed-forward (AFF) implemented in the SNS low-level RF system. Fast piezo tuners were installed to mitigate any unexpected mechanical resonance conditions. To date, there has been no strong need to use them, so they have never been operated. Moreover, the present SNS piezo tuner design has proved to be mechanically unreliable and will not be part of the tuners for the PPU.

3.2.2 End Group

End group thermal stability. The RRR of niobium for the end group of the original cavities is about 70 after heat treatment. The end group is cooled by indirect conduction to the helium circuit. The thermal processes of the end group are relatively slow, since the surface magnetic fields are relatively small and the cooling relies on conduction. In terms of thermal stability, the end group can allow fairly large material defects because the field is low and the total thermal load is small. But the end group is sensitive to heating from a broad range of thermal loads—such as thermal radiation from the inner conductor of the fundamental power coupler (FPC), field emission, and multipacting—because of the long conduction path to the thermal sink. As mentioned earlier, most of the original cavities show large field emission, which is the major operational limiting condition, leading to end group heating, gas bursts, and cavity quench [5].

The primary helium is supplied to a cryomodule through a Joule-Thomson (JT) valve. During normal operation, these valve positions are very stable, indicating that the thermal load of each cryomodule is constant. Several cryomodules have shown sudden increases in the JT valve position during normal operation, which indicates the heat load has increased by as much as 40 to 50 W. This kind of heat load can only be sustained in the end group without producing a full quench of the cavity. Operating the cavity with a metastable condition sustaining a normal conducting section in the end group is referred to as a "partial quench." The initial seed point heat load is estimated to be <1 W. This spot interacts with stray RF fields, and the interaction creates the partial quench condition. By upgrading the cavity design to include a high-RRR niobium end group, the thermal conductivity of this section of the cavity is greatly improved. With the increase in thermal conductivity, the normal conducting section of the end group is unable to expand, and the partial quench condition is eliminated. Horizontal test apparatus testing of a medium-beta cavity with high-RRR end groups was performed. In this test, a point heat load was applied to the end group while the cavity was at operating gradient. The thermal stability of the cavity was greatly improved, by a factor of 10, from the simulation model of the original SNS cavities.

The other thermally weak location in the original cryomodules is the cavity end group at the field probe side at the warm-to-cold transitions (Figure 3.1). At normal operating conditions, the temperature at this location is about 7–8 K. When there is electron loading, other external thermal loads such as beam halo, or a combination of these around this warm-to-cold transition, the local temperature easily goes to the hydrogen evaporation temperature. This can result in a large vacuum burst, in which the electrons interact with the RF field. Sometimes, a vacuum burst changes the cavity condition drastically, and cavities then require serious conditioning or reduction of the gradient. In the high-beta spare cryomodule, a thermal cooling block cooled by 5 K supercritical helium was installed at each side.

With these two changes—a higher RRR for the cavity end groups and the cooling blocks for the warm-to-cold transition—the whole system will have a much larger thermal margin against thermal radiation from the FPC; thermal loads from electron loading, such as field emission and multipacting; and any other additional external thermal loads. These are all included in the PPU design.

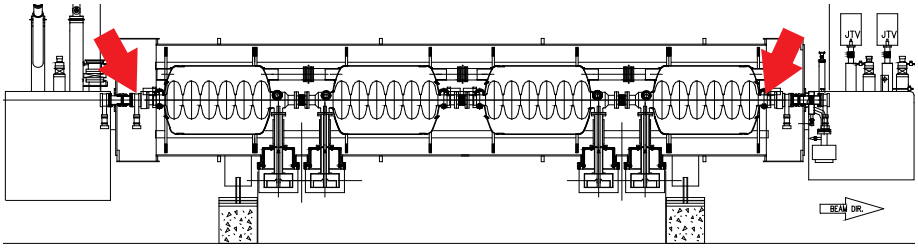

Figure 3.1. Thermal block locations for the 5 K boundary.

Higher-order mode (HOM) coupler. When an HOM is near the beam spectral lines, the induced voltage could be harmful to the beam and/or generate large HOM-induced power on the RF surface. To address these two main concerns, systematic studies were carried out. In the case of SNS, bunch tracking simulations for both the transverse and longitudinal directions show that beam instabilities are not a main concern if the external quality factor Q_{ex} for each HOM is less than 10^8, the loaded cavity Q for each non-pi mode fundamental mode has the expected value, and the expected cavity-to-cavity frequency variation is present. With respect to the HOM-induced power issue, general analytic expressions of beam-induced voltages and the corresponding HOM power from the multiple beam time-structures were analyzed and were fully understood by exploring the parameter space of the HOM properties. The damping requirement of each mode is set up in terms of Q_{ex} by taking into account the actual HOM frequency behavior of elliptical superconducting cavities. The probability that a cavity HOM frequency will coincide with a beam driving spectral line was estimated to be very small during the linac design phase. However, many factors can cause HOM frequencies to move around over time; and to permanently satisfy the damping requirement, an HOM coupler was installed on each end group of the SNS cavity as a simple precautionary measure [6,7,8].

Unfortunately, operational experience showed that the accelerating mode can sometimes be coupled out and lead to failure of the HOM RF feedthroughs. About 15% of installed cavities in the SNS SCL are showing abnormal signals through their HOM feedthroughs. All attenuators for the HOM signals were damaged in 1 year of operation during the early days of commissioning and operation. Observations and physical conditions near the HOM couplers imply that HOM coupler failures or degradation are a result of electron activity originating from multipacting, field emission, and even gas discharge at the fundamental mode. A few cavities were inoperable as a result of large coupling with the fundamental accelerating mode. In 2007, the SNS reevaluated the HOM characteristics, including dangerous HOM measurements for all installed cavities. It was concluded that HOM couplers are not needed for the SNS, and it was decided to remove HOM couplers whenever cryomodules are taken out of the tunnel for

repairs. Five cryomodules have been taken out of the tunnel so far, and leaks were detected in half of their HOM feedthroughs. Therefore, the PPU cavities will not have HOM couplers.

Refurbishment of the spare cavities and new cavities. Consideration was given to using the existing 20 high-beta spare cavities, produced during the SNS project, in the PPU. However, given the end group design of the original cavities, meeting the gradient specification (16 MV/m) for the PPU project is a large risk. Two cavities were refurbished at a cavity vendor's facility. The reactor grade end groups were removed from the cavities and replaced with high-RRR end groups. The refurbishment proved to be difficult and resulted in poor operating performance of the refurbished cavities. This outcome supported the plan to move forward with all new cavities for the PPU. New cavities give the best chance of success in meeting the gradient requirement and, ultimately, producing the required beam energy. Figure 3.2 shows a model of the original cavity versus the modified cavity for the PPU. Figure 3.3 depicts the completed end group replacement.

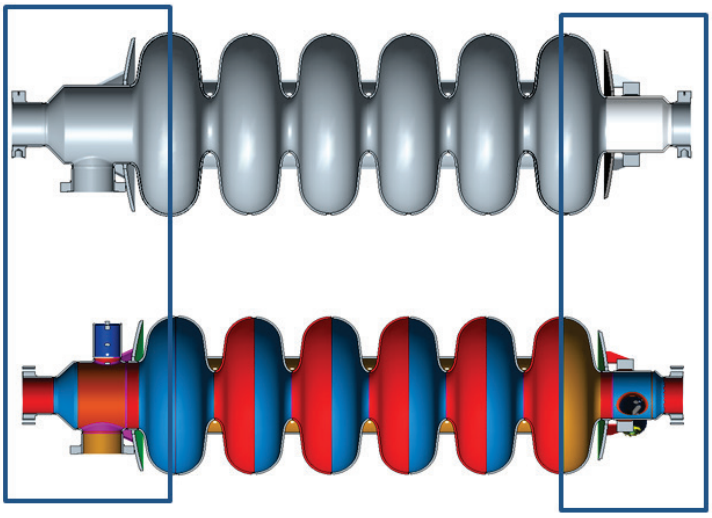

Figure 3.2. End group modification. (Top: cavity with modified end group for the PPU. Bottom: Original SNS high-beta cavity).

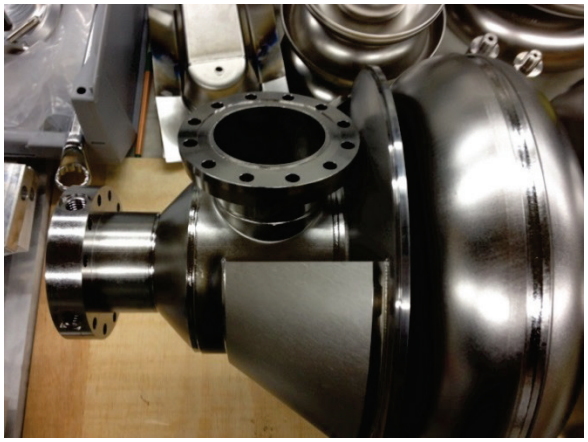

Figure 3.3. Completed end group replacement.

Helium vessel. The helium vessel is constructed of titanium and a niobium/titanium alloy. In the original design, the stiffeners in the head of the vessel were welded to a ring that allowed flexibility in adjusting the final position of the vessel body to the heads of the vessel. Because of the position of this ring, a full-

penetration weld was not possible. The new design eliminated this ring and redesigned the stiffener to fit completely with the heads of the vessel. Therefore, the main body of the helium vessel was lengthened to account for the added length of the slip fit rings. The main body of the vessel will be attached to the heads of the vessel via full-penetration welds. This arrangement more closely meets the intent of the ASME Boiler and Pressure Vessel (B&PV) Code. Figure 3.4 shows the original helium vessel design versus the new design. This modification was successfully incorporated in the spare high-beta cryomodule.

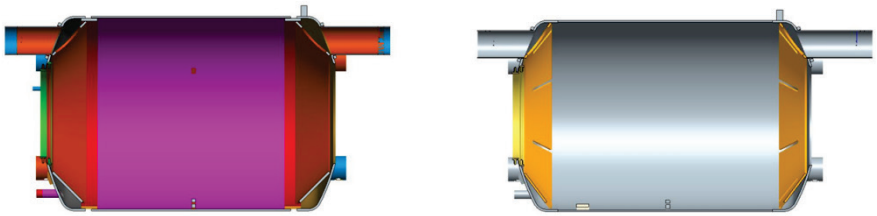

Figure 3.4. Original (left) versus new (right) helium vessel designs.

3.2.3 Fundamental Power Coupler

The original SNS FPC is designed and scaled from the one KEK developed for 508.8 MHz. A simple window geometry was chosen to facilitate manufacturing and assembly. The design of the SNS FPC relies on a simple coaxial line at 50 Ω. The planar alumina window includes impedance-matching elements, as well as a TiN anti-multipacting coating. The chokes at both sides of the ceramic window have the important role of improving the window matching. The depths of the chokes were optimized in the simulations to allow sufficiently low return loss and insertion loss [9]. The transition between the WR975 waveguide from the klystron and the coaxial line of the FPC is provided by a doorknob configuration. Even a small mechanical change inside the structure can result in a significant change in the RF performance; such disturbances include grooves, slits, rounded corners, and others. The FPC includes the possibility of biasing the inner conductor, via a capacitor gap between the doorknob and the inner conductor itself, at variable voltages between –2.5 and +2.5 kV. The gap is filled with Kapton foil, which is capable of withstanding the biasing voltage. The requirement for the maximum allowable thermal radiation from the FPC to the end group is 2 W. The outer conductor of the FPC has a direct conduction path to room temperature. To minimize heat transfer to the end group, the FPC outer conductor is designed to be cooled by supercritical helium at 3 atm and 5 K with a 0.04 g/s mass flow rate, which removes about 30 W of static and dynamic heat load. The inner surface of the outer conductor is designed to be copper-plated with 15 μm (RRR=10) of copper on stainless steel to reduce wall dissipation. The inner conductor of the FPC is made of copper and does not have active cooling. Figure 3.5 shows an FPC schematic, the inner conductor assembly, and the outer conductor assembly.

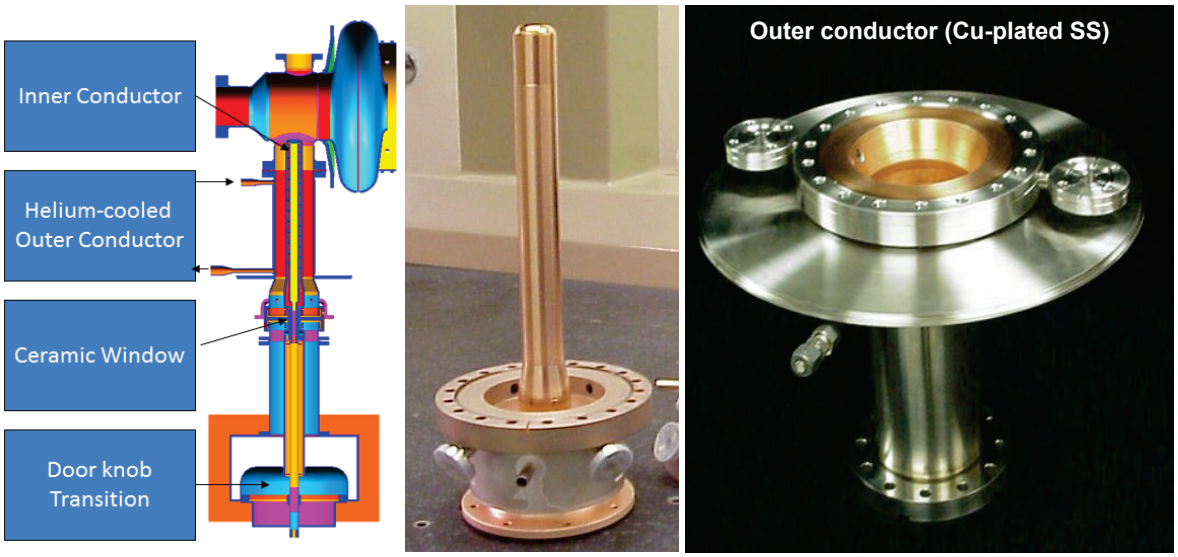

Figure 3.5. SNS fundamental power coupler (left: schematics, middle: inner conductor assembly, right: outer conductor assembly).

The original FPCs were tested at up to a 2 MW peak, a 0.6-ms long RF pulse width, and 60 pulses per second (pps) for the full traveling wave condition and in excess of 600 kW at a 1 ms long RF pulse width and 60 pps for full standing wave mode in the test stand. The FPCs have been reliably performing at over 550 kW peak power in real cavity operation at various standing wave ratios limited by the operational envelope in the linac. The FPC for the PPU cavities must be able to transfer up to 700 kW peak power over a 1.3 ms pulse width at a repetition rate of 60 pps. Based on the testing and operational experience, the RF performance of the original FPC can satisfy the PPU requirements; however, a design modification is needed to maintain the inner conductor temperature at a sufficiently low level. Since the thermal radiation from the inner conductor will be higher as a result of the increased average RF power, a thicker inner conductor will be used for the PPU, which is sufficient and provides the simplest solution. Active cooling for the inner conductor was also taken into account, if the passive enhancement of cooling with the thicker inner conductor is not adequate. Active cooling will require a more complex design configuration and may result in operational difficulties at an upset condition. The temperatures are calculated for various inner conductor thicknesses at both full traveling and standing wave conditions. During pulsed operation, the actual condition in the FPC is between full standing and full traveling wave conditions, closer to the full traveling wave condition. Figure 3.6 shows comparisons of inner conductor tip temperatures. With a 7.5 mm thick inner conductor, the inner conductor tip temperature at the PPU condition can be kept below that of the FPCs presently operating at SNS, which have an inner conductor thickness of 3 mm. The prototype FPC for the PPU with the increased wall thickness was manufactured by the vendor that provided the original FPCs, installed in a horizontal test apparatus, and successfully tested. Except for the wall thickness of the inner conductor, all other designs are exactly the same. The Q_{ex} value chosen for the PPU in Table 3.1 is optimized to reduce the RF power requirement.

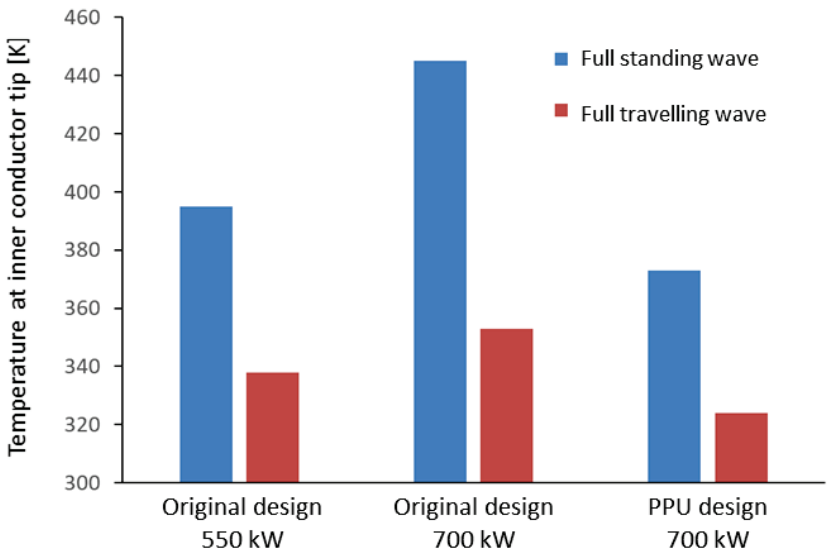

Figure 3.6. Comparisons of calculated inner conductor tip temperatures.

3.3 CRYOMODULES

The SNS SCL consists of 23 cryomodules, 11 of which are medium-beta and 12 high-beta. The medium-beta cryomodules each contain three six-cell elliptical cavities, whereas the high-beta cryomodules contain four six-cell elliptical cavities. The cavities are described in Sect. 3.1. The design was based on the Continuous Electron Beam Accelerator Facility cryomodule, with improvements inspired by the Large Hadron Collider, TESLA (Tera-electron-volt Energy Superconducting Linear Accelerator), and the Jefferson Laboratory 12 GeV upgrade design efforts [10]. Figure 3.7 shows the elevation view of the original high-beta cryomodule design by Jefferson Laboratory.

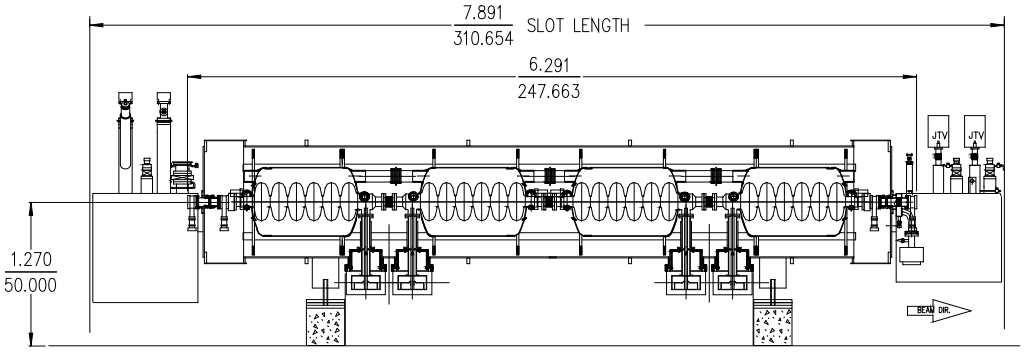

Figure 3.7. The original high-beta cryomodule.

The cryomodule consists of a cavity string, a space frame, a thermal shield, two layers of magnetic shielding, a vacuum vessel, and two end cans. The general arrangement of these components is depicted in Figure 3.8.

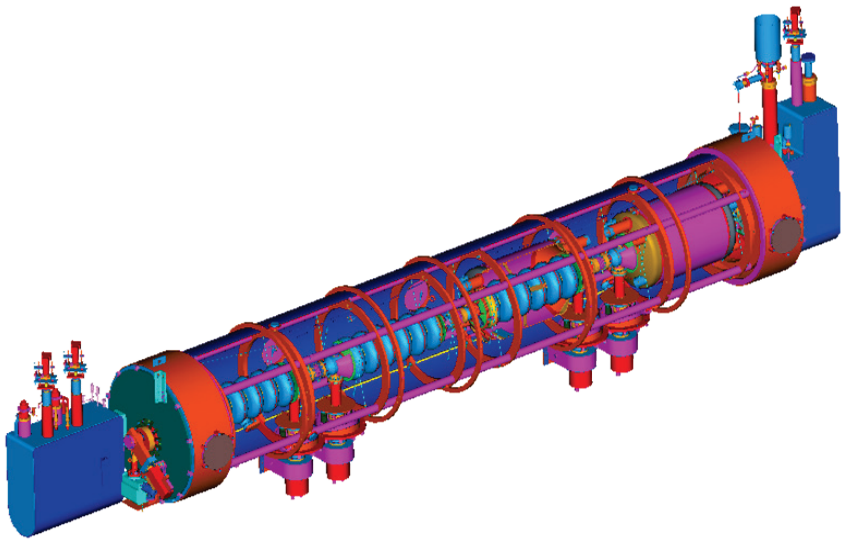

Figure 3.8. Cut view of the original high-beta cryomodule.

During the PPU project, seven cryomodules similar to the original high-beta cryomodules will be installed in the linac tunnel. The relevant parameters for the mechanical design of the original high-beta cryomodules, which remain as design constraints for the new cryomodules, are listed in Table 3.4.

Table 3.4. Design constraints for the PPU cryomodules.

Parameter	Value
Slot length	7.891 m
Cryomodule length (bore tube)	6.291 m
Number of bayonets	4
Number of control valves	5

In 2012, SNS completed fabrication and testing of a spare high-beta cryomodule. The approach to the engineering design for this cryomodule was to maintain critical features of the original design, such as bayonet positions, coupler positions, cold mass assembly, and overall footprint. The components that were fixed in location and those that were considered movable are shown in Figure 3.9. This new cryomodule design was required to meet the pressure requirements put forth in 10 CFR 851, "Worker Safety and Health Program." The most significant engineering change was applying Section VIII of the ASME B&PV Code to the vacuum vessel of this cryomodule, instead of using the traditional designs in which the helium circuit is the pressure boundary. Applying the B&PV Code to the helium circuit within the cryomodule was also considered. However, it was determined to be schedule-prohibitive because it required a code case for the niobium materials, which are not currently covered by the code. Good engineering practice, however, was applied to the internal components to verify the quality and integrity of the entire cryomodule [1]. Details of the changes to the vacuum vessel and end cans to apply the code to these components are detailed in Sections 3.2.3 and 3.2.4, respectively.

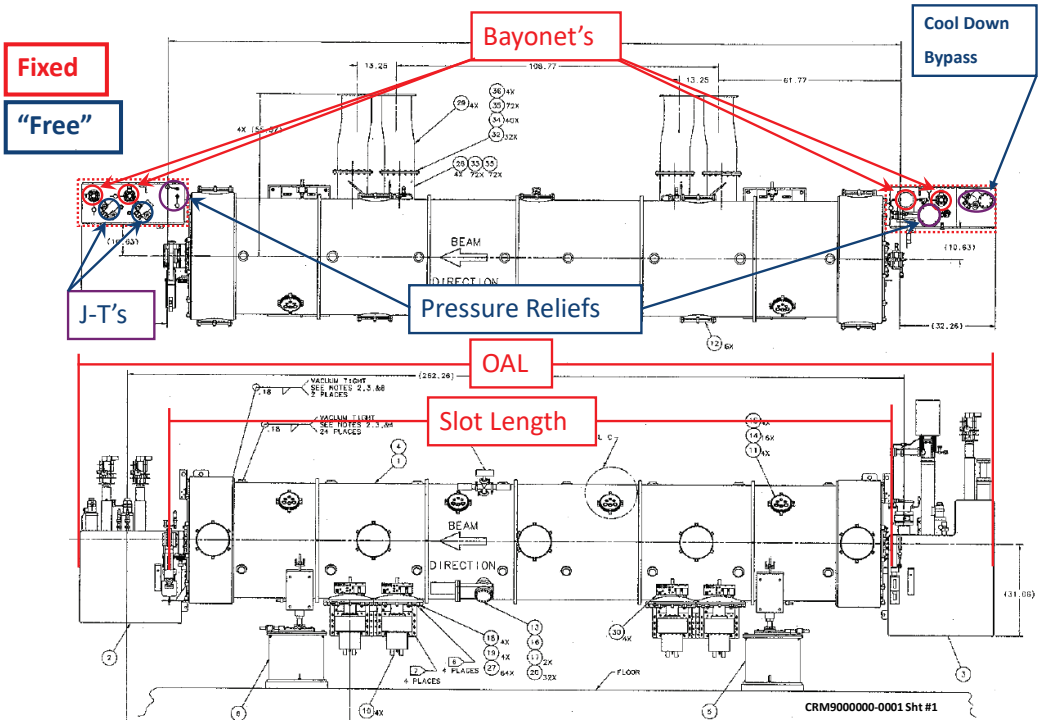

Figure 3.9. Cryomodule reference interface locations.

Several other improvements were made to the spare high-beta cryomodule beyond the changes implemented as a result of applying the B&PV Code. The HOM feedthroughs on the end groups of the cavities were blanked. The helium vessels were upgraded to meet the intent of the code. Cooling blocks were added to the outside end groups of the cavity string to thermally stabilize these regions. Cold instrument feedthroughs were minimized in the design to prevent possible leaks. All of these improvements are discussed in detail in this report. The completed high-beta spare cryomodule is shown in Figure 3.10.

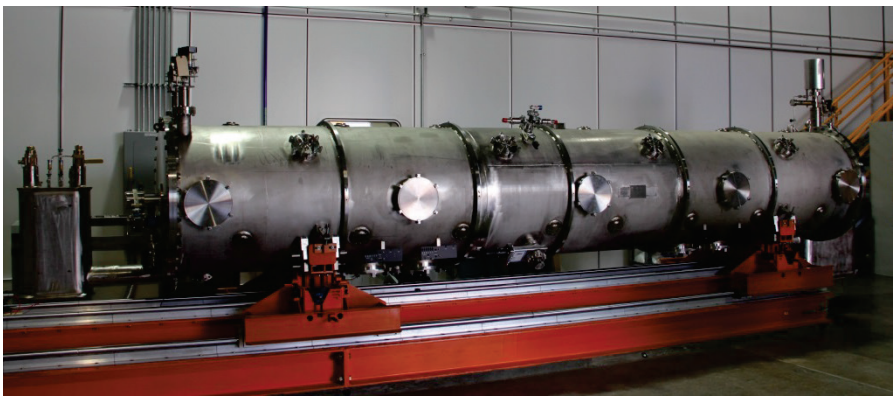

Figure 3.10. SNS spare high-beta cryomodule.

The spare high-beta cryomodule serves as the baseline design for the PPU cryomodules. A couple of modifications to this design will be necessary for the cryomodule to function according to the requirements of the PPU. The cavities will be upgraded as detailed in Sect. 3.1 and an upgraded FPC will be used as discussed in Sect. 3.1.3. Other than these two changes, the PPU cryomodule is very similar to

the spare high-beta cryomodule. Methodologies for fabrication and assembly were developed and staff expertise was gained during the assembly of the high-beta spare.

3.3.1 Heat Loads and Helium Circuits

There are three cooling circuits within the cryomodule. Primary cooling provides the liquid helium that cools the cavities within the helium vessels. Secondary cooling provides supercritical helium cooling to the couplers. Because the FPC requires 5 K supercritical helium to cool the outer conductor, as mentioned in Section 3.1.3, the Large Hardon Collider concept of producing 2 K helium in the cryomodule rather than in the refrigerator is used [10]. This drives the design of placing individual heat exchangers in each of the cryomodules rather than locating one large heat exchanger in the refrigerator. In addition, efficiencies are improved with this heat exchanger placement. Shield cooling provides cooling to the thermal shield located in the cryomodule and transfer lines. Figure 3.11 is the updated flow diagram for the spare high-beta SNS cryomodule. The PPU cryomodules will have the same helium circuits as the spare high-beta cryomodule.

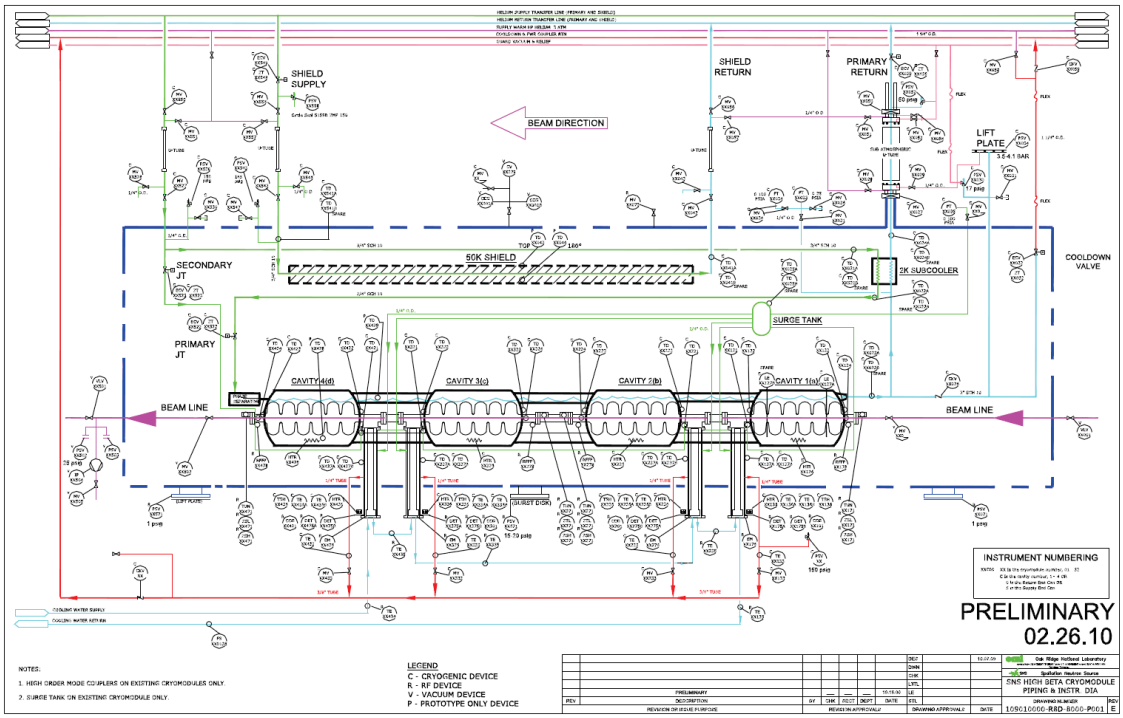

Figure 3.11. Helium flow schematic and instruments for the spare high-beta cryomodule.

The primary helium flow to the cryomodule will be split into two circuits, the primary and the secondary. The primary helium flow will enter the cryomodule in the supply end can and flow through the heat exchanger in the return end can, through the primary JT valve located on the supply side of the cryomodule, and into the helium vessels. Helium will exit the helium vessels and flow either out the cooldown circuit or through the heat exchanger back into the return transfer line. The cooldown path will be used to imbalance the heat exchanger during the cooldown of the cryomodule so that a desired cooldown rate of 100–150 K/h can be achieved.

The secondary circuit will flow through a secondary JT valve, a cooling block on the end group of the supply side cavity, each of the FPC flanges, a cooling block on the end group on the return side cavity, into a surge tank, and out to four parallel paths to the FPC outer conductors. The return from the couplers

will flow though metering valves for each of the couplers. The four flows will be combined and discharged into the cooldown header and act as a liquefaction load on the refrigerator.

The shield flow will be supplied from the turbine 1 outlet in the main cold box at approximately 38 K. It will flow from the turbine outlet, through the transfer line, and into the cryomodules through the shield supply valves. Helium will then flow through the cryomodule and back into the return transfer line, where it will return to the medium-pressure header in the main cold box. The design criteria for the original high-beta cryomodule [11] are listed in Table 3.5, along with those for the PPU based on the operating experience of the spare high-beta cryomodule.

The original SNS cryogenic system was designed with a 100% capacity margin from the primary and secondary circuits and a 35% margin for the shield passage. This was done to account for the uncertainty of the design, to mitigate risk to the project, and to ensure capacity for upgrade. With these margins in place, it is anticipated that the addition of seven cryomodules to the linac tunnel will be well within the capability of the SNS cryogenic system. See Section 3.4 for more detailed cryogenic system information.

Table 3.5. Cryogenic load design values for the high-beta cryomodule.

Parameter	Original cryomodule	PPU cryomodule
2 K heat load (static/dynamic)	28/20 W	25/40 W
Coupler flow	0.075 g/s	0.067 g/s
Shield load including transfer line	200 W	200 W

3.3.2 Cold Mass

The cold mass of the cryomodule consists of the cavity string, space frame, 50 K thermal shield, magnetic shield, and insulation. Figure 3.12 shows the cold mass of the spare high-beta cryomodule just before the second layer of magnetic shielding was installed.

Figure 3.12. Cryomodule cold mass assembly.

The original SNS tuner design shown in Figure 3.13 has been adapted from a Saclay design for the TESLA Test Facility cavities [12]. It is attached to the helium vessel at three points—two standard standoffs and one piezo tuner. The tuner is adjusted by a motor and harmonic drive unit. This provides a tuning range of approximately 400 kHz [13].

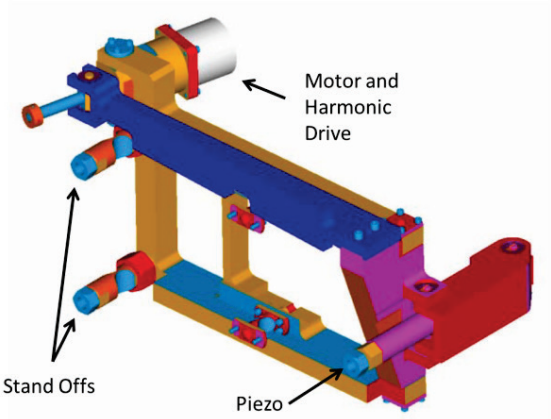

Figure 3.13. Schematic of the original SNS tuner assembly.

One key change to the original cavity string assembly is the removal of the piezo tuner from the tuner assembly. The original design included the piezo tuner to mitigate any unexpected mechanical resonance conditions driven by the Lorentz force. Since the SNS cavity RF circuit has a large bandwidth, and the SNS cavities do not have adverse mechanical resonance conditions, the cavity phase and RF amplitude are well managed within the requirements by the AFF implemented in the SNS low-level RF system [14]. The piezo tuners have never been actuated in operation at SNS. Moreover, several failures with piezo stacks have occurred because of pressure changes in the cryomodules either during the 2 to 4 K transition or during upset conditions. The piezo tuners were replaced with the standard standoffs used on the other two legs of the tuner. Because of this history, it was decided to eliminate them from future cryomodules built for SNS.

Thermal and magnetic shielding is incorporated in the design of the cold mass. The cavity string is surrounded by a thermal shield that operates at approximately 50 K. This shield is wrapped in multilayer insulation and provides a thermal radiation barrier between the cavities and the ambient environment. The thermal shield used for the PPU cryomodules is very similar to the original shields used for the original cryomodules. Two layers of magnetic shielding are incorporated into the cold mass assembly. One layer is installed on the outside of the helium vessels within the cavity string, and the other on the outside of the space frame. These layers reduce the Earth's magnetic fields by a factor of 20 or higher to minimize the effect on cavity operation. The only change to the shields is to adjust their geometry to properly fit within the new B&PV Code–compliant vacuum vessel.

Another component of the cold mass is the space frame, which was developed at Jefferson Laboratory to facilitate the installation of long cavity strings into cryomodules at a relatively low cost. Because the original cryomodules were assembled at Jefferson Laboratory and shipped to SNS, the space frame was strengthened to handle the transportation load while maintaining the alignment of the cavities. This same design will be used in the PPU cryomodules. The space frame provides support to the cavity string through nitronic rods. The space frame is supported from the vacuum vessel. The use of this system to support the cavity string limits the conduction of heat to the cavities. Nitronic rods were selected to support the transportation loads because of their high strength.

3.3.3 Vacuum Vessel and Support Stands

To meet the new B&PV Code, the decision was made to define the vacuum vessel and end can envelope as the pressure boundary because of the difficulty in applying the pressure code to materials in the helium circuit. The niobium, titanium, and niobium–titanium alloys are not code-listed at the operating

temperature that is routinely maintained within the cryomodules. The approach of using the vacuum vessel as the pressure boundary made use of an interpretation of VIII-1-89-82 in which it was deemed acceptable to stamp the exterior vessel of a heat exchanger if the tube side exceeds the rated operating pressure, provided the shell and associated relief devices are designed to withstand the highest design pressure associated with the tube side. Moving the pressure boundary from the cavity helium circuit to the vacuum vessel has additional safety benefits: (1) The vacuum shell material is 304 stainless steel, which is one of the best materials for fracture toughness and ease of fabrication. (2) The vacuum shell will never reach the helium operating temperature even with a catastrophic failure of the helium lines because of the thermal mass of the vessel material, which is at room temperature. Therefore, the material properties at LN2 temperature can be used. (3) The vacuum vessel envelope could be easily pressure-tested without the SRF cavity string installed [15].

Enacting the code allowed the removal of the bridging ring from the original design concept. That required that the main part of the vacuum vessel in the spare cryomodule be longer than the original cryomodules. Removal of the bridging ring complicated assembly in the warm-to-cold transition region, necessitating design changes to this region of the cryomodule. The changes affected the flexibility of the alignment of the string to the warm beamline flange. Therefore, modeling of the string within the vacuum vessel had to be very precise because the movement of the warm-to-cold transition in the old design was eliminated. The alignment during the spare high-beta cryomodule assembly was performed with a laser tracker, and the modeling was successful, so that the string aligned with the warm valve within the specification limit of 1 mm [1]. Figures 3.14 and 3.15 depict changes in the design of the vacuum vessel.

To simplify the supply end can as much as possible, the primary and secondary JT valves were moved from the end can to the vacuum vessel. This required a change in the vacuum vessel design, and more piping was added to the main body of the cryomodule. Figure 3.16 depicts this change.

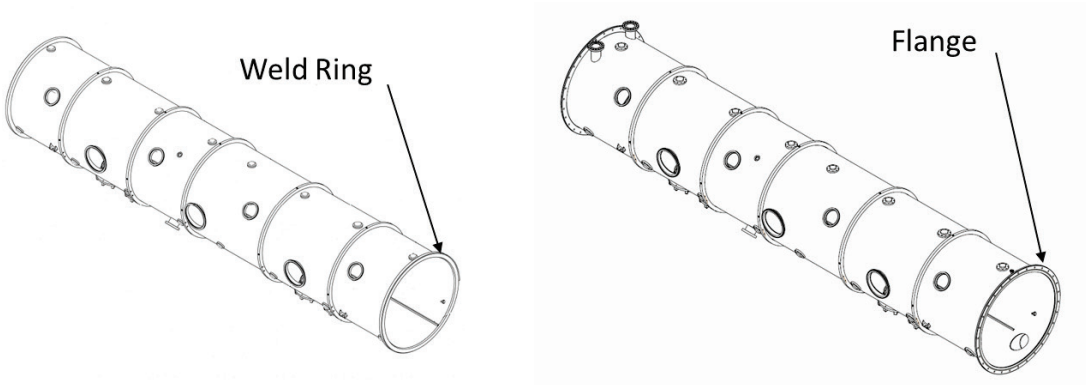

Figure 3.14. Original (left) versus new (right) vacuum vessel.

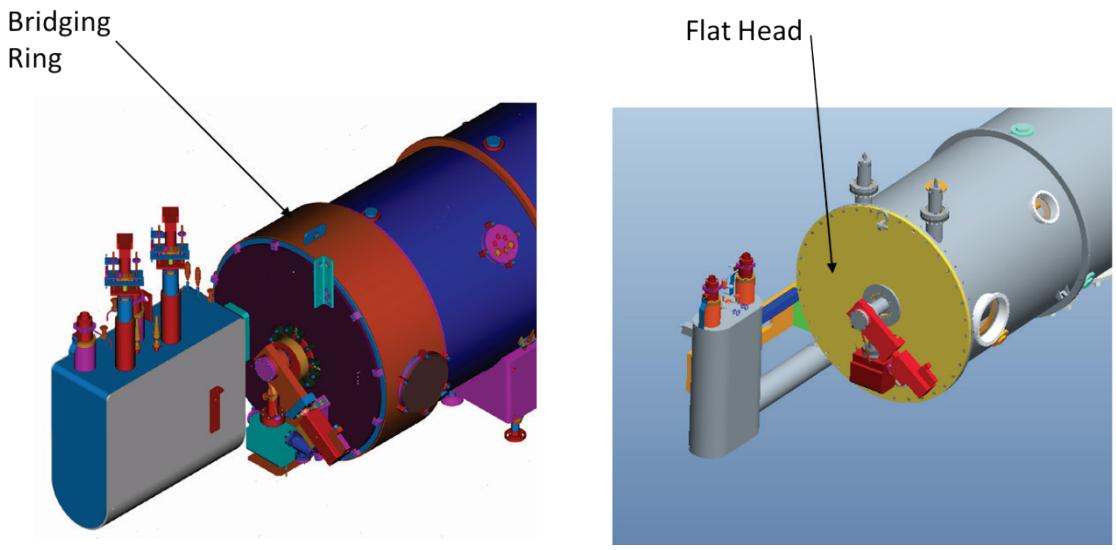

Figure 3.15. Original (left) versus new (right) vacuum jacket design.

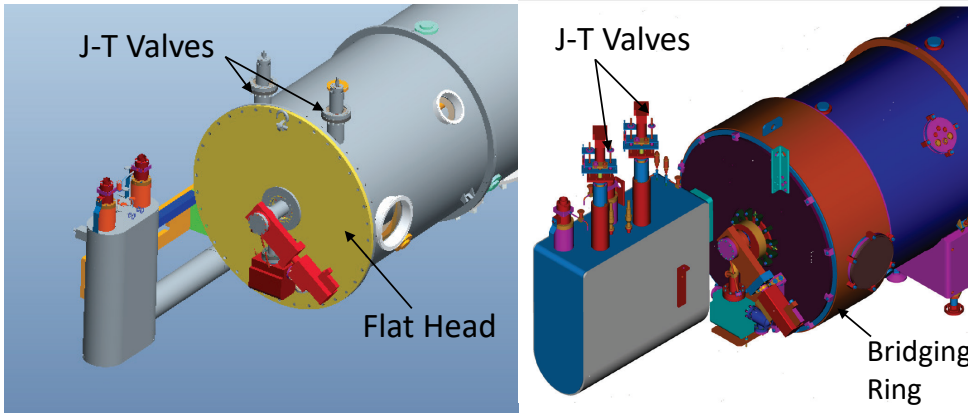

Figure 3.16. JT valve positions for the PPU cryomodule (left) and the original (right) cryomodule.

3.3.4 End Cans

In designing the high-beta spare cryomodule, multiple changes were made to the end cans. Previously, the end cans had not been designed or fabricated in such a way that the vacuum boundary could withstand pressure. Therefore, the shape and the thickness of the end cans were modified. Because of the design approach of having three separate pressure stamps, the end cans had to be capable of being pressure-tested individually; the same was true for the vacuum vessel. The end cans attach to the side of the vacuum vessel by a flanged connection, an arrangement that allows easy pressure testing of all three vessels.

The piping within the supply end can was significantly reduced. The new supply end can design is compared with the original design in Figure 3.17. A similar analysis was conducted to simplify the return end can by moving the heat exchanger into the vacuum vessel. To do so, it would have been necessary to change the heat exchanger. However, the decision was made to keep all the original equipment in the return end can, since that was a proven and reliable design. The piping in the return end can was simplified as much as possible for ease of fabrication as shown in Figure 3.18. Because the new pressure-rated end cans were connected differently to the vacuum vessel, they required new mechanical support brackets, as shown in Figure 3.19.

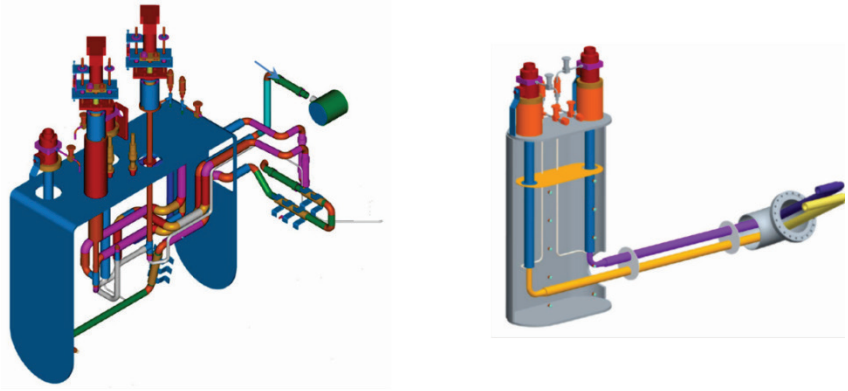

Figure 3.17. Original (left) versus new (right) supply end can.

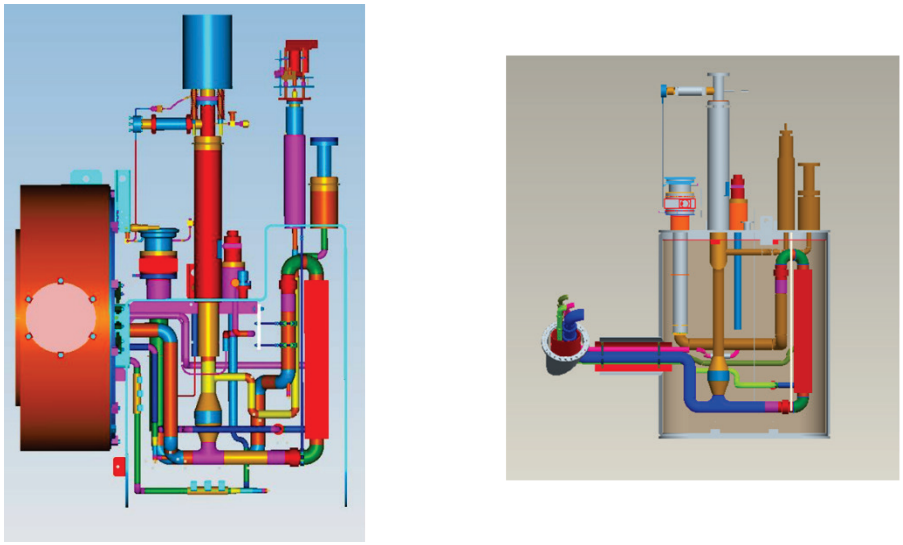

Figure 3.18. Original (left) versus new (right) return end can.

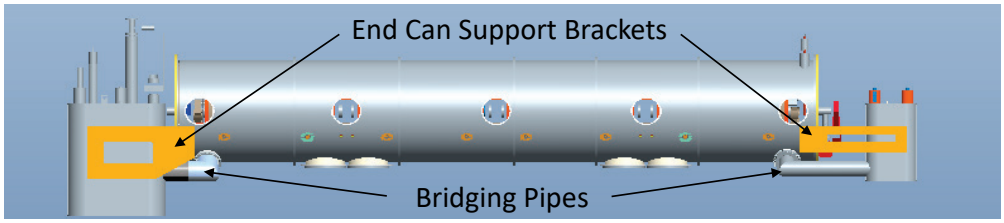

Figure 3.19. Interfaces between end cans and vacuum vessel for the PPU cryomodule.

For the spare high-beta cryomodule, the end cans were custom fitted and attached to the vacuum vessel at ORNL. Since ORNL has a U-stamp and an R-stamp, code welds could be made while ensuring the bayonets were properly located and aligned. For the production PPU cryomodules, code welds cannot be made by the partner laboratory. A design effort was conducted to provide adjustment capability to locate and align the bayonets. A bellows was added to the bridging insulating vacuum pipe to both the supply and return end cans. The bellows incorporated into the end can design is shown in Figure 3.20. The bellows design was incorporated into the medium-beta return end can, which gives good confidence to the successful application to the PPU cryomodules.

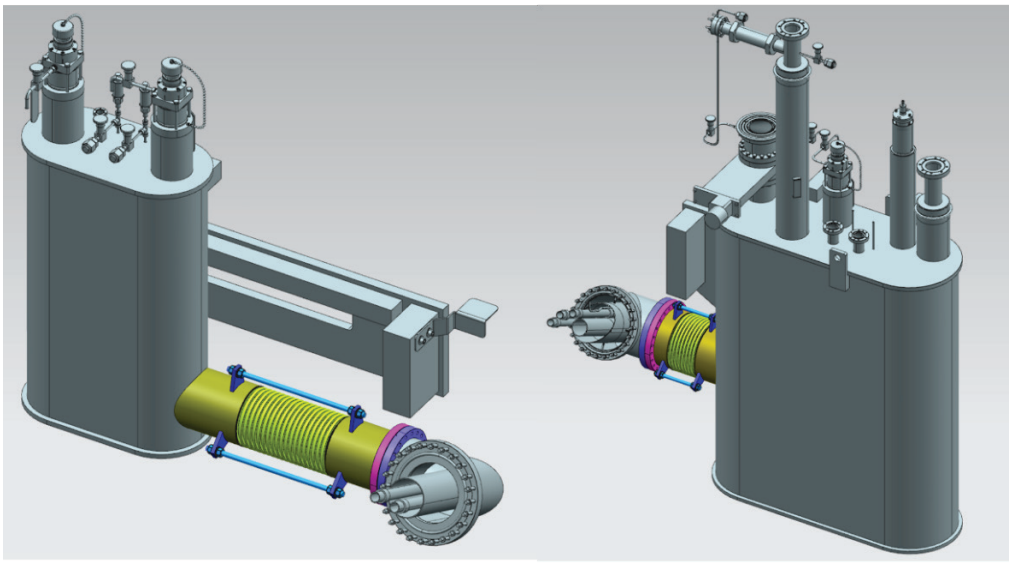

Figure 3.20. PPU cryomodule end cans with bellows for bayonet position adjustment.

Although the helium circuit is not code-stamped under this design philosophy, good engineering practice was applied to this portion of the cryomodule for the spare high-beta cryomodule. The helium vessels were modified so that the stiffening in the heads of the vessels was increased. In addition, the design of the cylindrical portion of the helium vessel was modified so that all welds could be full-penetration welds. The fabrication techniques used were consistent with ASME code practices and procedures. The inspection requirements were also consistent with those called out in the ASME B&PV Code. All welds that would eventually be subjected to cryogenic temperatures were made using low-ferrite filler material. Ferrite is known to reduce toughness in cryogenic applications; therefore, the filler material had a ferrite number below 5 [16].

3.3.5 Instrumentation Hardware

The original cryomodules were equipped with many in-process diodes for accurate temperature measurement of helium streams. The in-process diodes required a cold instrument feedthrough to bring the wires out of the process space into the insulating vacuum space. During welding for the original cryomodule fabrication, the ceramic portions of some of the feedthroughs were overheated. Many leaks in the cryomodules were observed before the operation of the SNS linac. Multiple repairs were performed by cutting through the insulating vacuum boundary and thermal shield to access the diodes. In the new design for the spare high-beta cryomodule, the cold feedthroughs were removed and replaced by surface-mounted diodes. These surface-mounted diodes have given reliable temperature feedback, and operation using these readings has been successful. The diodes located on the cavity surfaces at the top and bottom of each cavity were also relocated to the outside of the helium vessel for the spare high-beta cryomodule. Using these diodes to determine the cooldown rate has proven to be very similar to using the cryomodule with diodes directly mounted to the cavities. The only operational issue with the surface mount diodes is that their operational lifetime is adversely affected by the high radiation levels in the linac tunnel. On the PPU cryomodules, these diodes will be replaced with Cernox sensors.

Because of the high radiation levels within the tunnel, the pressure transmitters used on the original SNS cryomodules failed in a short time. They were replaced by Honeywell strain gauges with no internal electronics, making them much more reliable in a high-radiation environment.

3.3.6 Shipping

The completed cryomodules will be shipped from the partner laboratory to SNS using the SNS shipping fixture that was used to ship the original cryomodules from Jefferson Laboratory to SNS. The shipping fixture will require modification to accommodate design changes in the PPU cryomodule to meet the pressure vessel code. It is expected that the shipping integrity of the PPU cryomodule will be very similar to that of the original SNS cryomodules. Twenty-four cryomodules were shipped during the original project, providing confidence that the shipping will be successful. A shipping test using a "dummy" cryomodule is included in the baseline plan and will provide valuable data ahead of the PPU cryomodule shipping iterations.

Perhaps the most concerning design change that might affect the cryomodule integrity during the shipment is doubling the FPC inner conductor wall thickness. Extensive modeling was conducted for this component. It was determined that adding a stiffening plate on the outside of the coupler during shipment would produce very similar harmonic oscillations to those in the original cryomodules. Figure 3.21 shows the location of the support.

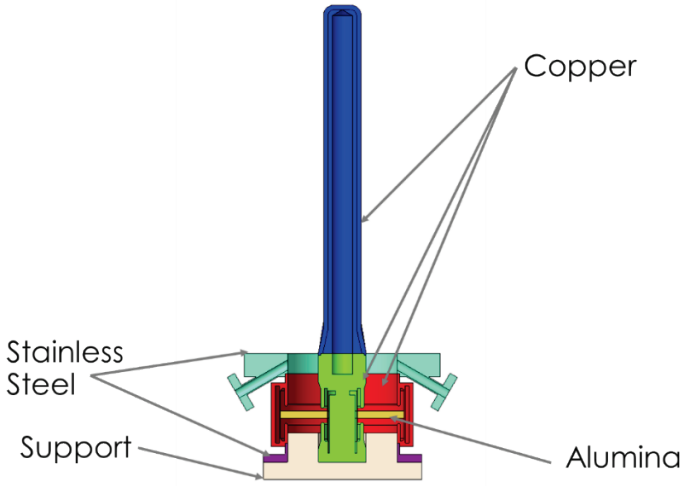

Figure 3.21. FPC inner conductor with support.

Table 3.6 displays the simulation results for the original SNS inner conductor versus the PPU inner conductor. The results show that the frequencies of the original coupler are very similar to those of the supported PPU coupler.

Table 3.6. Comparison of original and PPU coupler frequencies.

Mode	Original coupler frequency (Hz)	PPU coupler frequency (Hz)	PPU coupler with SS support frequency (Hz)	PPU coupler with polyethylene support frequency (Hz)
1	86	70	83	79
2	88	71	84	80
3	700	609	662	647
4	702	636	664	649
5	708	639	922	686
6	1116	1023	932	1057

Additionally, coupler shipping tests are being conducted to assess the shipping integrity of the inner conductor. The results from these tests will provide valuable data for verifying the shipping modeling efforts.

3.4 CRYOGENICS

The SNS cryogenic system design closely resembles that of the Thomas Jefferson National Accelerator Facility cryogenic system, with some modifications [17]. The SNS cryogenic system was designed to provide refrigeration capacities of 125 g/s at 2.1 K, 8300 W of shield cooling, and 15 g/s of liquefaction flow. This cryogenic capacity is enough to accommodate the PPU project, and no additional equipment is required for the central helium liquefier. A flow diagram of the system is shown in Figure 3.22.

The current design load for the cryomodule shield circuit is 5300 W. Adding seven cryomodules, at an additional 200 W each, would produce a total shield load of 6700 W. SNS currently owns a new nozzle for the current 4KCB that would increase the total shield circuit capacity to about 10 kW.

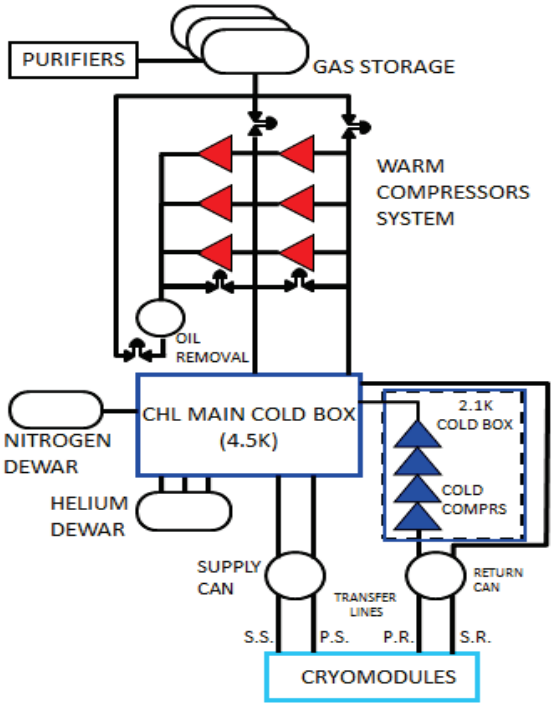

Figure 3.22. Cryogenic system overview.

The control system is an integral part of the SNS cryogenic system. Within the Experimental Physics and Industrial Control System (EPICS), multiple control sequences run to control the operation. These sequences include the 2 K pump-down, the heater control, the 2 K trip response, and the JT off sequence. Each time a cryomodule is added to the tunnel, these sequences must be amended to include the new cryomodules. Testing of the sequences will be an essential part of ensuring the success of SCL operation during the PPU project. Perhaps the most critical of these sequences to test is the 2 K pump-down sequence. This is an empirically derived sequence that adjusts the gear ratios of the cold compressors as pressure decreases in the return transfer line header. If cryomodules are added to the tunnel, the flow dynamics and temperature profiles within the system could change, requiring development and modification of the 2 K pump-down sequence.

Because the initial design of the cryogenic system had a large margin of capacity, turn-down studies of the cryogenic system were conducted at SNS to enable the system to run more efficiently. The results of these studies showed that the SNS cold compressors could operate successfully while reducing flow by approximately 25% from the design flow [18]. Results of the turn-down studies are presented in Table 3.7. Typically, the system is operated with the flow turned town 12.5% from the design flow. This allows more efficient operation of the system by reducing power consumption and decreasing nitrogen usage while maintaining the robustness of the original design. Even with the system turned down, it is necessary to input approximately 1 kW of heat into the helium baths of the cryomodules with electric heaters to maintain the minimum flow for the 2 K cold box. When seven additional cryomodules are added, the turned-down system will be more efficient. The heat load of the additional cryomodules will be less than the heat that is currently added to the system. Therefore, the heater sequence will be adjusted to reduce the external heat presently added, as additional new cryomodules are installed.

Table 3.7. Results of turn-down study.

	Design basis	**Maximum capacity**	**Nominal capacity**	**Minimum capacity**
First stage compressors (kW)	608			
C1 (kW)		300	250	244
C3 (kW)		300	300	203
Second stage compressors (kW)	2074			
C4 (kW)		1456	1355	762
C5 (kW)		1456	1355	1154
LN2 usage (g/s)	120	200	180	150
Total electric input power to compressors (kW)	2682	3512	3260	2363
LN2 equivalent power (@35% Carnot) (kW)	216	360	324	270
Total input power equivalent (kW)	2898	3872	3584	2633
HP to cold box (Atm)	16.8	17	16.5	12.9
MP cold box out (Atm)	4	2.8	2.8	2.5
Cold box HP flow (g/s)	1150	1077	1030	829
CC flow (g/s)	**125**	**140**	**125**	**90**
Liquefaction load (g/s)	15	4	4	4
Shield load (kW)	5300	8300	5300	5300
Carnot work based on 2.1 K operations				
Primary load (kW)	400	448	400	288
Liquefaction load (kW)	102	27	27	27
Shield load (kW)	61	39	39	39
Total load Carnot work	**563**	**514**	**466**	**354**
Carnot efficiency based on 2.1 K operation	**0.194**	**0.133**	**0.130**	**0.134**

Table 3.7. Results of turn-down study (continued).

Carnot work based on 4.5 K operation				
Primary load (kW)	542	607	542	390
Liquefaction load (kW)	102	27	27	27
Shield load (kW)	61	39	39	39
Total load Carnot work(kW)	**705**	**673**	**608**	**456**
Carnot efficiency based on 4.5 K operation	**0.243**	**0.174**	**0.170**	**0.173**

HP = high pressure; MP = medium pressure.

3.5 SUPPORTING SYSTEMS

The support systems for the SCL portion of the PPU project include cooling water, beamline vacuum, and insulating vacuum.

The cooling water system will provide cooling to the air-side portion of the FPC inner conductor and is anticipated to be a direct copy of the existing system. As in the operation of the original high-beta cryomodules, a water circuit will provide water cooling for four FPCs in series with a resistance temperature detector at the outlet of each FPC and a flow switch at the return header. The water cooling system is designed to remove a maximum of 200 W per FPC with a 1 gpm minimum flow. The existing quadrupole magnet cooling system was already verified to meet PPU requirements without modification.

The beamline vacuum system of the PPU cryomodules will be a direct copy of the original SNS cryomodules [19]. Each cryomodule will be equipped with an ion pump that maintains high vacuum. Warm isolation valves will be located at each end of each cryomodule to isolate that section of beamline in the event of a leak. Additionally, these valves will be used to facilitate maintenance on the cryomodules.

Originally, SNS cryomodules were not equipped with an insulating vacuum system [19]. However, leaks were observed on about a third of the cryomodules. Some of these leaks were from the helium circuit to the insulating vacuum, and some were from the air to the insulating vacuum. Individual pump carts were placed on the cryomodules that had leaks. Because of the elevated radiation levels in the tunnel, the controllers for these pumps did not have long lifetimes. A two-turbo molecular pumping system was manifolded to four cryomodules, and the controllers were relocated to the klystron gallery. This system has proved effective. However, it is expensive and has a limited pumping capacity. Recently, a cryomodule positioned in the tunnel beyond the manifolded pumping systems was found to leak. A turbo pump was directly connected to the cryomodule with a backing scroll pump. The controller is in the klystron gallery away from the radiation environment.

An insulating vacuum system with improved performance over the existing systems is required for the PPU. The design criteria for this new system are presented in Table 3.8. The required vacuum levels for the insulating and beamline vacuum are 5×10^{-5} and 5×10^{-10} at cold, respectively. The design bases for both the insulating and beamline vacuums systems are specified, while the cryomodule is warm. Operational experience in the SNS linac has shown that achieving these warm vacuum levels will result in achieving the required cold operating vacuum levels because the cold helium surfaces will be cryo-pumping both vacuum spaces. The largest gas loading for the insulating vacuum of 1×10-3 torr·L/s is

based on the largest leak in an SNS cryomodule currently being pumped in the linac. The largest gas loading for the beamline vacuum of 1×10^{-7} torr·L/s is based on measured values from an operating cryomodule in the SNS linac. Once the crymodule is cold, the only load on the ion pump is the hydrogen outgassing and hydrogen generated from beam operation.

The new system will be modeled after the recent upgrade to the warm linac pumping system, consisting of turbo-molecular pumps and their corresponding valves and instrumentation directly mounted to each cryomodule, and a centralized roughing pump system backing all the turbo pumps [20]. Both the turbo-molecular pumps and the roughing system will be controlled through EPICS. Placing the roughing system outside the tunnel allows minimizing personnel access to the tunnel and reducing the amount of ancillary equipment located in the tunnel. This system will also include all the interconnecting piping between the turbo-molecular pump discharge and the roughing pump system.

Table 3.8. SCL insulating and beamline design basis.

	Units	Design	Operating
Insulating vacuum			
Dry screw pumping speed	L/s	91.6	~ 10
Fore line pressure drop (P_i/P_o)	–	5	< 2
Fore line pressure	torr	5×10^{-2}	1×10^{-3}
Turbo pump gas load (at 700 L/s)	(torr·L) / s	1×10^{-3}	$< 1 \times 10^{-5}$
Insulating vacuum pressure	torr	5×10^{-3} (warm)	$< 5 \times 10^{-5}$ (cold)
Beamline vacuum			
Ion pump gas load (at 45 L/s)	(torr·L) / s	1×10^{-7}	$< 1 \times 10^{-8}$
Beamline pressure	torr	5×10^{-7} (warm)	$< 5 \times 10^{-10}$ (cold)

3.6 INSTALLATION AND INTEGRATION (INCLUDE ICD SUMMARY)

Seven cryomodules will be installed in the east end of the existing linac tunnel. There are nine available slots for cryomodules with the cryogenic transfer line, utilities, and warm sections in place. To prepare for the installation of these cryomodules, all the cable pulls will be completed before the PPU cryomodules enter the tunnel. Additionally, the stands that will support the cryomodules will be installed and grouted in place before cryomodules are moved to the tunnel.

A coordinated effort will be required to install, test, and commission the cryomodules within the scheduled outages. Existing procedures have been developed for removing and installing cryomodules in the SNS tunnel. After over 10 years of operation, these iterations have become routine. However, for the PPU cryomodules, there is some added complexity. Since these cryomodules are being installed in slots not previously used, the instrumentation and controls checks of these cryomodules will be more involved. All the control sequences for RF, heaters, JT valves, and 2 K pump-down will have to be updated and tested.

The coordination effort for the installation is aided by the Interface Control Documents (ICDs), which detail where the interfaces are and who is responsible for the scope of work on each side of the interface. An example of the block flow diagram in an ICD is shown in Figure 3.23.

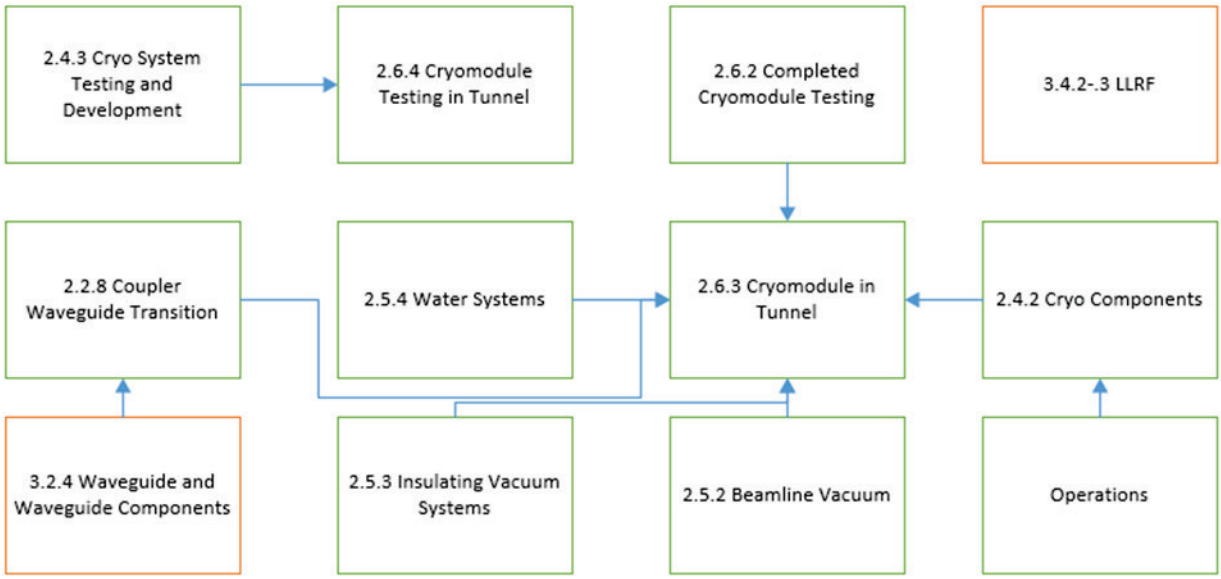

Figure 3.23. Cryomodule interface block diagram.

The mechanical installation of the cryomodules requires a diverse set of resources. including craft riggers and operators, SCL system technicians, survey and alignment personnel, vacuum team members, water team support, RF technicians, and the Instrument and Controls group. Careful scheduling and planning will be conducted to optimize the work environment and ensure safe, efficient installation of the cryomodules. Multiple shifts may be used during these installation activities to expedite this effort.

3.7 ASSUMPTION LIST

To prepare the final design approach for the SCL portion of the PPU, the following assumptions were made:

- The performance of the medium-beta cavities gradient is improved by an average of 10%.
- A spare medium-beta cryomodule will be available to conduct repairs on underperforming medium-beta cavities that are not candidates for plasma processing.
- Cavity 1a will be repaired in advance of the installation of PPU cryomodules.
- Cavity 11b will be repaired before the end of PPU.
- Cavity 5a will not be repaired in advance of the PPU.
- Available RF power to the original cavities is 550 kW (current configuration).

3.8 ACCEPTANCE DOCUMENTATION

The following documents have been developed to impose quality assurance through the SCL project scope:

- Cavity Incoming Inspection (PPUP-200-TA0001)

- Coupler Inner Conductor Incoming Inspection (PPUP-202-TA0001)
- Cavity VTA Testing (PPUP-202-TA0002)
- Coupler Inspection Post-Conditioning (PPUP-202-TA0003)
- Coupler Assembly Inspection (PPUP-202-TA0004)
- Coupler Baking Inspection PPUP-202-TA0005)
- Coupler Outer Conductor Incoming Inspection (PPUP-202-TA0006)
- PPU High Beta Cryomodule Performance Requirements and Minimum Acceptance Criteria (104210200-M8U-8200-A001-MAC-R0)
- Cryogenic Equipment Receipt (PPUP-204-QA0001)
- SNS Receipt of Cryomodules (PPUP-206-TA0001)
- SNS Testing in RFTF Test Cave (PPUP-206-TA0002)

3.9 REFERENCES

1. M. Howell, et al., "The First ASME Code stamped cryomodule at SNS," pp. 2465–2467 in *Proceedings, 3rd International Particle Accelerator Conference (IPAC2012)*, New Orleans, May 20–25, 2012.
2. S. Kim, et al., "The status of the Superconducting Linac and SRF activities at the SNS," pp. 83–88 in *Proceedings, 16th International Conference on RF Superconductivity (SRF2013)*, Paris, France, September 23–27, 2013.
3. S. Kim, "SNS Superconducting Linac operational experience and upgrade path," pp. 11–15 in *Proceedings of 24th International LINAC conference (LINAC08)*, Victoria, Canada, September 29–October 3, 2008.
4. M. Doleans, P.V. Tyagi, R. Afanador, C.J. McMahan, et al., "In-situ plasma processing to increase the accelerating gradients of superconducting radio-frequency cavities," *Nuclear Instruments and Methods in Physics Research A*, 812, 2016.
5. S. Kim, "Simulation of quench dynamics in SRF cavities under pulsed operation," pp. 1365–1367 in *Proceedings of the Particle Accelerator Conference 2003 (PAC2003)*, Portland, Oregon, May 12–16, 2003.
6. R. Sundelin, et al., "SNS HOM damping requirements via bunch tracking," pp. 1984–1986 in *Proceedings of the 2001 Particle Accelerator Conference (PAC2001)*, Chicago, June 18–22, 2001.
7. S. Kim, et al., "Higher-order-mode (HOM) power in elliptical superconducting cavities for intense pulsed proton accelerators," *Nuclear Instruments and Methods in Physics Research A*, **492**(1–2), 1–10, October 2002.
8. S. Kim, I. E. Campisi, D. Jeon, et al., "Study on fault scenarios of coaxial type HOM couplers in SRF cavities," pp. 770–772 in *Proceedings, 23rd Annual Conference, Linear Accelerator Conference 2006*, Knoxville, Tennessee, August 21–25, 2006.

9. Y. Kang, et al., “Electromagnetic simulations and properties of the fundamental power couplers for the SNS superconducting cavities,” pp.1122–1124 in *Proceedings of the 2001 Particle Accelerator Conference (PAC2001)*, Chicago, June 18–22, 2001.
10. W. J. Schneider, et al., “Design of the Spallation Neutron Source (SNS) cryomodule,” pp. 1160–1162 in *Proceedings of the 2001 Particle Accelerator Conference (PAC2001)*, Chicago, June 18–22, 2001.
11. C. Rode, “The SNS Superconducting Linac system, pp. 619–623 in *Proceedings of the 2001 Particle Accelerator Conference (PAC2001)*, Chicago, June 18–22, 2001.
12. D.A. Edwards, *TESLA Test Facility Linac Design Report*, DESY Print TESLA Rep. 95-01, 1995.
13. J. Preble, I. E. Campisi, E. Daly, et al., “SNS cryomodule performance,” pp. 457–461 in *Proceedings of the 2003 Particle Accelerator Conference (PAC2003)*, Portland, Oregon, May 12–16, 2003.
14. H. Ma, et al., “Low-level RF control of Spallation Neutron Source: System and characterization,” *Phys. Rev. Special Topics—Accelerators and Beams* **9**, 032001, March 2006.
15. J. Mammosser, “Spallation Neutron Source status and upgrade plans,” pp. 62–65 in *Proceedings of the 14th International Conference on RF Superconductivity (SRF2009)*, Berlin, Germany, September 20–25, 2009.
16. *ASME Boiler and Pressure Vessel Code*, Section VIII, Division 1–2010 UHA 51(a)(4)(a)(1), American Society of Mechanical Engineers.
17. F. Casagrande, I. Campisi, P. Gurd, et al., “Status of the cryogenic systems commissioning at SNS,” pp. 970–972 in *Proceedings of the 2005 Particle Accelerator Conference*, Knoxville, Tennessee, May 16–20, 2005.
18. F. Casagrande, P. Gurd, D. Hatfield, et al., “SNS 2.1 K cold box turn-down studies,” pp. 514–516 in *Proceedings, 10th European Particle Accelerator Conference (EPAC2006)*, Edinburgh, Scotland, June 26–30, 2006.
19. P. Ladd, et al., “Overview of the Spallation Neutron Source Vacuum Systems,” *J. Vac. Sci. Technol. A* **23**, 1270, 2005.
20. C. Stone, et al., “Improving vacuum performance in the warm linac of the Spallation Neutron Source,” to be submitted to *J. Vac. Sci. Technol. A* **37**, 061601, 2019.

4. RADIO FREQUENCY SYSTEMS

The PPU project will ultimately double the proton beam power at the SNS from 1.4 to 2.8 MW. This will be accomplished by increasing the beam energy to 1.3 GeV through the installation of additional cryomodules and by increasing the beam current to 38 mA. The increase in beam energy for the PPU will require the installation of an additional 28 radio frequency (RF) systems in the superconducting linac (SCL) and the upgrading of three RF systems in the normal conducting linac (NCL). Table 4.1 displays a high-level overview of the operational parameters needed for the PPU RF systems.

Table 4.1. High-level operational parameters for the PPU.

Category	Requirement	Description
Beam energy	1.3 GeV	Objective key performance parameter
Beam current	38 mA	Support 38 mA PPU beam loading
RFQ–DTL2 and DTL6/CCL1-4 klystron peak power	2.5/5MW	No change for PPU
DTL3- DTL5 klystron peak power	3 MW	Upgrade of three DTL RF stations for 38 mA proton beam
Existing SCL RF station peak power	550 kW	Provide RF power to the existing superconducting accelerating cavities
New SCL RF station peak power	700 kW	Provide RF power to the 28 new superconducting accelerating cavities
New LLRF system	28 new systems	Control and protect the new SCL RF stations and cavities
Existing HVCM (DTL/CCL/SCL)	128/135/75 kV	Support the upgrade of the three DTL stations; otherwise no change
New HVCM (SCL)	82 kV	Support new klystron output of 700 kW peak
Utilities	–	Provide electrical and mechanical utilities for the technical equipment
RF controls	–	Provide LLRF development support, user interfaces, and accelerator network connections for RF equipment
Global controls	–	Extend existing machine protection, personnel protection, timing, and accelerator network systems

DTL=drift-tube linac; CCL=coupled-cavity linac; SCL=superconducting linac; LLRF=low-level radio frequency; HVCM=high-voltage converter modulator.

4.1 HIGH-POWER RADIO FREQUENCY SYSTEMS FOR THE PPU (FINAL/PRELIMINARY)

The existing SNS linac high-power RF (HPRF) systems are well described by Lynch et al., Champion, and Hardek et al. [1,2,3]. The high-level beam parameters for the PPU that drive the linac RF system design considerations are described in Section 2.1. There are two primary impacts to the RF systems:

1. The PPU will require additional SCL HPRF systems to support the additional accelerating structures required to reach a beam energy of 1.3 GeV.

2. Modifications will be required to some existing NCL HPRF systems to support the additional beam loading associated with the increase in the average linac beam current.

Table 4.2 summarizes the requirements for the PPU RF system design.

Table 4.2. Design requirements.

Linac structure	Klystron peak power available (KW)	HVCM voltage required (kV)	High voltage pulse width (mS)	Pulse repetition rate (Hz)
RFQ–DTL2, DTL6	2500	130	1.5	60
DTL3–DTL5	3000	130	1.5	60
CCL	5000	135	1.5	60
SCL (existing)	550	78	1.5	60
SCL (new)	700	82	1.5	60

RFQ = radio frequency quadrupole.

The SCL high-power systems are described in Section 4.1.1. These are divided into (1) systems powering already installed cryomodules and (2) systems supporting newly installed cryomodules. The upgrades to the high-power systems supporting the already installed lower-energy normal conducting structures are described in Section 4.2.2.

4.1.1 SCL High-Power Radio Frequency Systems (Final)

4.1.1.1 SCL Transmitters

Existing SCL HPRF transmitters

Each of the existing 81 superconducting cavities is driven with RF power from a single 805 MHz klystron. Currently, all 81 klystrons in use are manufactured by Communications and Power Industries (CPI). Seventy of them are model VKP-8291A, and 11 are model VKP-8291B. The VKP-8291A model is specified to produce a peak RF power of 550 kW and an average power of 49.5 kW. The VKP-8291B is specified to produce a peak RF power of 700 kW and an average power of 87 kW. RF power is transmitted via rectangular waveguides from the output of each klystron, located in the Klystron Gallery, to the cryomodules located in the accelerator tunnel. The klystrons are protected from reflected power by a waveguide circulator and a high-power water load. Each klystron is provided power, utilities, controls, and monitoring by a transmitter. Each transmitter supports a group of 6 klystrons and includes 6 filament power supplies, 12 magnet power supplies, an ion-pump vacuum controller, a high-voltage power supply, 6 solid state RF amplifiers, coolant monitoring, 2 high-voltage klystron tanks, klystron cathode current monitoring, personnel and equipment safety interlocks, and a programmable logic controller (PLC) that provides system control. A single high-voltage converter modulator (HVCM) provides a 75 to 80 kV DC pulse to a grouping of 10 or 11 parallel klystrons spread across multiple transmitters. The new design for the PPU will follow the same convention, but with slight modifications.

SCL HPRF transmitters for PPU

The increase in beam energy for the PPU will require installing an additional 28 RF systems to provide power to 28 superconducting accelerating cavities in 7 new cryomodules. An RF system consists of a single klystron and the associated transmitter components necessary for it to operate. To support 28 klystrons, the PPU will install 5 additional HPRF transmitters to replicate the 6 klystron per transmitter configuration currently in use at SNS.

Each PPU transmitter will consist of the major components shown in Table 4.3.

Table 4.3. Major PPU transmitter components.

Item no.	Description	Quantity
1	Dual filament power supply, 1000 VA AC output	3
2	Magnet power supply for the klystron gun, 1.2 kW DC output	6
3	Magnet power supply for the klystron body, 3.0 kW DC output	6
4	Ion pump controller and supply for klystron vacuum, six parallel outputs, 5 kV output	1
5	Prime AC distribution chassis	1
6	Secondary AC distribution chassis	3
7	Dual RF amplifier, 805 MHz, 17 W output	3
8	Temperature control units for the waveguide circulators	6
9	Programmable logic controller	1
10	Operator interface	1

In addition to the ten major items, various circuit boards, flow transmitters, temperature transmitters, AC current transformers, DC current transducers, and other diagnostic components will be included in the complete transmitter system.

To maintain continuity of spare parts across SNS, the new transmitters are specified to use the same chassis as the existing ones and, where possible, the same components, such as circuit boards (see Figure 4.1). For replacing obsolete items, the specification requires that the updated parts be backward-compatible with the existing installation. Any exceptions must be reviewed and explicitly approved by SNS. The details are captured in two documents, SNS-RAD-RF-SW-0004, *Statement of Work for the SNS Superconducting Radiofrequency Transmitters* and SNS-RAD-RF-EQ-0004, *SNS Superconducting Radiofrequency Transmitter Technical Specification.*

Figure 4.1. The physical layout of PPU RF transmitter racks will be similar to the layout of these existing racks.

4.1.1.2 SCL Klystrons

The increase in average linac beam current will require additional RF generator power because of the increase in beam loading. The estimated required RF generator power profile, resulting power margin, and baseline minimum control power margin are shown in Figure 4.2.

The PPU project will use 28 CPI VKP-8291B klystrons. The VKP-8291B klystron operates at 805 MHz and is specified by the manufacturer to produce a peak RF power of 700 kW. Data are available from CPI demonstrating that the klystron can produce up to 1 MW of peak power. The VKP-8291B is physically identical to the VKP-8291A klystron, except for minor modifications to cavity tuning and output cavity coupling, and slightly increased cooling requirements to allow operation at the higher output power level. In addition, the VKP-8291B electron gun operates at a nominal 82 kV, which is a higher cathode voltage than the VKP-8291A.

The VKP-8219B klystron can be used as a direct replacement in the existing SCL HPRF klystron sockets. The existing operational transmitters currently include 11 VKP-8291B klystrons, although they are operated at the 550 kW baseline power level.

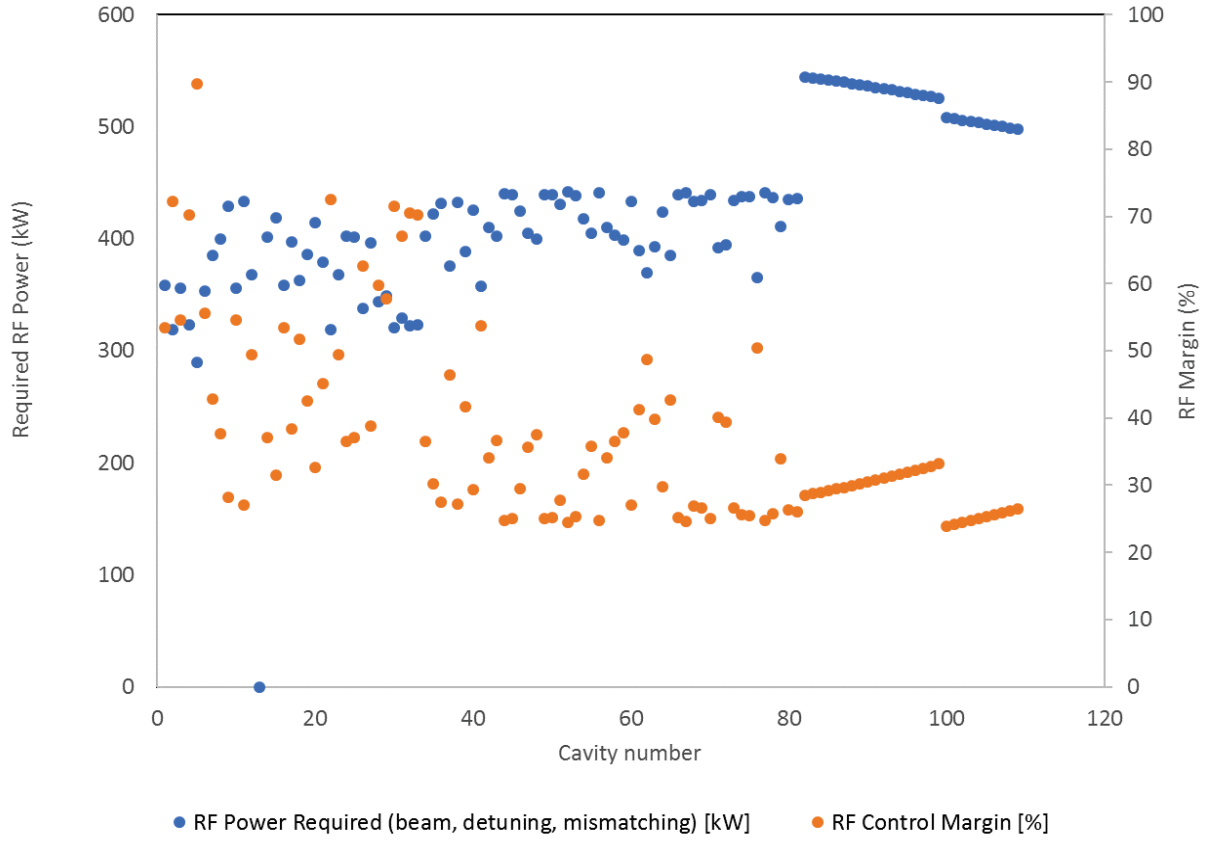

Figure 4.2. Estimated required RF generator power for the SCL.

4.1.1.3 SCL Waveguide and Waveguide Components

The scope of the waveguide runs includes all sections and components from the output elbow of the klystron to the flange on the flexible connection to the cavity coupler. As in the existing RF transmitters, the waveguide is rectangular aluminum WR1150, transitioning to WR-975 just prior to the chase *inserts*. The waveguide will have flat flanges, and it will not be pressurized (Figure 4.3). The waveguide installation for PPU will be very typical of the existing SCL waveguides at SNS. Components designed

into the transmitter waveguide include transitions, straight sections, E-plane sweeps, H-plane sweeps, E-plane miter bends, H-plane miter bends, flexible sections, and dual-directional power couplers.

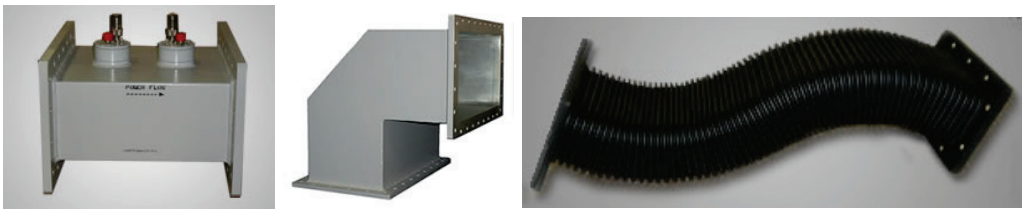

Figure 4.3. Typical waveguide components in use at SNS. *Source:* **MEGA Industries 2016 [4].**

The waveguide was drawn into the 3-dimensional engineering model of the Klystron Gallery buildout using the standard sizes, bend radii, and lengths available from major manufacturers. A bill of material was developed from the model so that all of the waveguide can be procured at one time. In addition, the waveguide will be palletized by cavity so that the material needed for each run is kept together and installed more efficiently. Another advantage of modeling the waveguide is early identification and correction of interferences with other infrastructure before construction begins. See Section 7 of this document, "Conventional Facilities," for more details of the three-dimensional model.

4.1.1.4 SCL Waveguide Circulators

In addition to the waveguide components, the PPU design includes high-power waveguide circulators. The circulators provide a matched load for the output of the klystron by transmitting any reflected power from the RF cavity in the tunnel to a waveguide water load. Port one of the circulators is terminated to the klystron output, port two is terminated to the waveguide connected to the accelerator cavity, and port three is terminated to the load. The SCL circulators are specified to operate in any orientation, including upright or inverted.

DC power supplies provide power and control to the circulator biasing solenoids. The control units are installed in the transmitter and adjust the DC current to the solenoids based on the input and output temperatures of the circulator cooling water, as well as the ambient temperature of the air. The return loss of the circulator is a minimum of 32 dB and a minimum of 23 dB or greater across a 24 MHz bandwidth centered on 805 MHz. The circulators are specified for a peak forward power rating of 700 kW. The technical details are captured in SNS-RAD-RF-SW-006, *Statement of Work for the Superconducting Linac High Power Radiofrequency Waveguide Circulator*, and SNS-RAD-RF-TS-0009, *Specification for the Superconducting Linac High Power Radiofrequency Waveguide Circulator.* An example of the circulator can be seen in Figure 4.4.

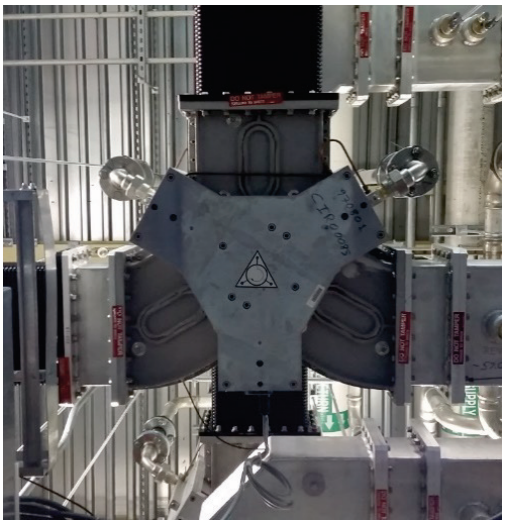

Figure 4.4. High-power waveguide circulator installed in an SCL system at SNS.

4.1.1.5 SCL Waveguide Water Loads

Any reflected power from the RF accelerating cavity will dissipate in a waveguide load. The load is specified for a peak forward power rating of 700 kW and will be terminated to port three of the waveguide circulator to absorb reflected power. The bandwidth of the load is 24 MHz, centered on 805 MHz, and the voltage standing wave ratio (VSWR) will be 1.05:1 or better at 805 MHz. The VSWR will not exceed 1.15:1 across the 24 MHz bandwidth. An example of the water load can be seen in Figure 4.5. The technical details are captured in SNS-RAD-RF-TS-0010, *Specification for the Superconducting Linac High Power Radiofrequency Waveguide Load.*

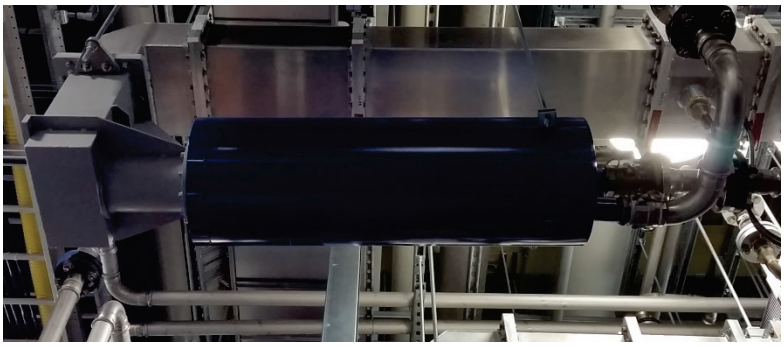

Figure 4.5. Water load installed in an SCL system at SNS.

4.1.1.6 SCL HPRF Transmitter Cooling Carts

The current SCL transmitter cooling cart (TRCC) will be identical to the existing cooling carts in the SCL, except that resistance temperature detectors (RTDs) have been added to the RF equipment supply and return circuits to enable temperature and power monitoring. In general, each cooling cart will consist of 4 in. diameter stainless steel supply and return piping, which will form the manifold for all of the water-cooled components in each transmitter. The manifold will consist of thirteen 1.5–2 in. stainless steel pipes that provide the supply and return for each component.

As in the existing transmitters, each klystron body will have separate supply and return piping for 6 of the 13 cooling circuits, and the remaining components will be connected in series. Two waveguide circulators will be connected in series with a single supply and return for 3 of 13 circuits. Three collectors will be

connected in series for 2 of the 13 circuits, and 3 of the circulator loads will be connected in series on the remaining 2 cooling cart circuits. Figure 4.6 shows the SCL TRCC cart and components.

The nominal flow requirements for each circuit will be as follows:

- Klystron body—5 gpm
- Klystron collector—45 gpm
- Circulator—8 gpm
- Circulator load—35 gpm

The existing cooling carts monitor flow only with vortex style in-line meters, but the upgraded cart is specified to monitor temperatures using in-line RTDs. The new flow meters are vortex-style and are backward-compatible with the existing TRCCs.

The TRCCs are located near the north wall of the Klystron Gallery. The piping is designed so that it routes up the north wall and over the waveguide and terminates at the associated equipment. The piping is designed so that it does not obstruct access to RF transmitter components.

Layouts of the redesigned cooling cart are shown in Figure 4.6, and the details are captured in PPUP-307-EQ0001, *Equipment Specification SCL Transmitter Cooling Carts (PPU Project).*

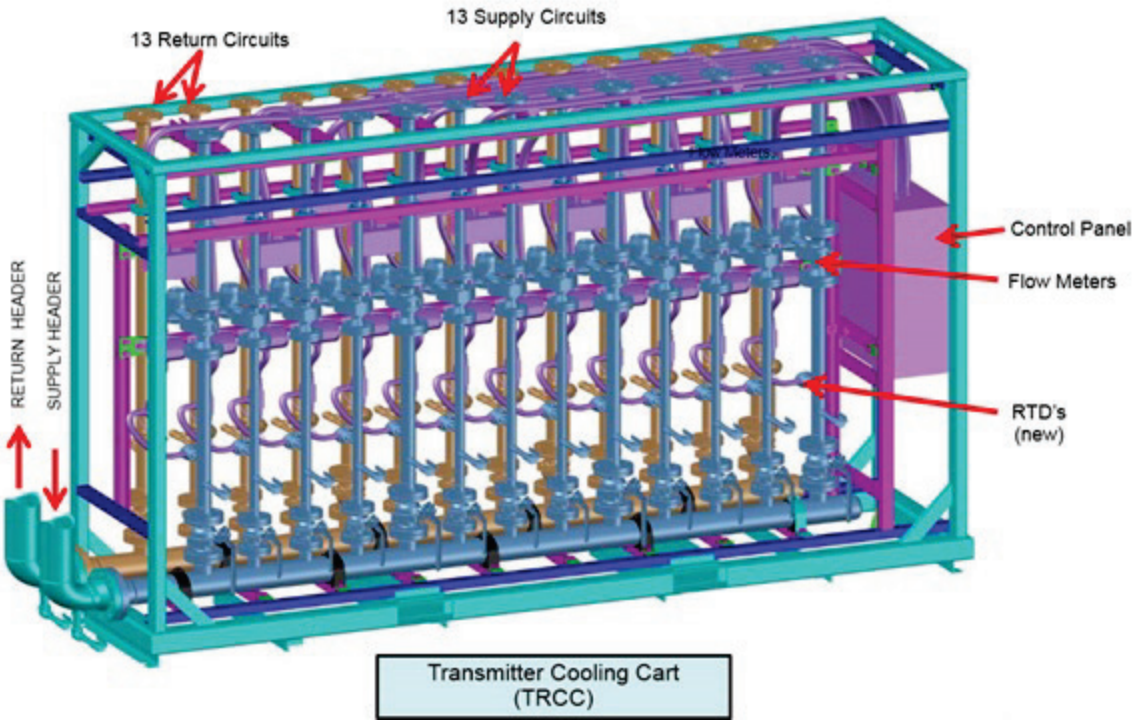

Figure 4.6. Three-dimensional model of the redesigned TRCC.

4.1.2 Normal Conducting Linac High-Power Radio Frequency Systems (Final)

4.1.2.1 Required RF Generator Power for the Normal Conducting Linac

The baseline system requirements for the existing NCL are detailed in a 2000 ORNL report [5] and the original SNS design criteria. The design criteria used to size the existing HPRF systems were based on the estimated required RF generator power for an average linac beam current of 35 mA, calculated using

accelerating structure parameters provided by 2-dimensional cavity simulations. The average linac beam current for the PPU will be increased to 38 mA, requiring upgrades to multiple NCL RF systems to provide adequate RF power margin.

The power margin for the existing HPRF power sources provides RF power over and above the estimated required RF generator power for 35 mA operation. It accommodates losses between the klystron and cavity; variations in klystron and HVCM performance; and the LLRF phase, amplitude, and resonance control required to maintain steady-state operation in response to beam-induced and environmentally induced disturbances.

PPU will follow the same convention for the increased beam current. For PPU, the minimum power margin required in the NCL is 25%. The 25% margin matches the original SNS design criteria and was maintained to support high operational availability. The SNS RF systems operating parameters are often adjusted for increased machine reliability. Table 4.4 details the power margin budget in terms of RF system adjustments.

Table 4.4. NCL RF trip faults and downtime percentages.

Fault description	Downtime percentage
Prevent nonlinear (fully saturated) operation	10
HVCM voltage adjustment	5
Variation in klystron output	5
Operation of detuned cavities	3
Increased power required for adaptive feed forward learning	2
Total	**25**

Power margin measurements

To inform the NCL HPRF design, SNS formed a power margin task force whose duties included determining the RF power margin of the existing NCL HPRF systems. Power margin is defined as a percentage of available RF power and is calculated as

$$Power\ Margin\ (\%) = \left(\frac{Psat-Prf}{Prf}\right) * 100\%\ , \tag{1}$$

where

P_{sat} is the rated saturated output power of the RF station as determined by in situ testing
P_{rf} is the power required to accelerate a 38 mA proton beam as determined by the high current studies

The power margin measurements began in the spring of 2017 with a series of experiments designed to record the RF power, as measured by the RF control system, needed to transport a 38 mA proton beam from the ion source through the coupled-cavity linac (CCL). Using the initial results from the beam test data, the maximum available output power was measured from a select group of RF stations, including drift tube linac (DTL) 2-6 and CCL3. In addition, cathode currents were characterized using a precision shunt to ensure that the klystrons were not overdriven to achieve the desired power margin.

Table 4.5 summarizes the results, which indicated the need to install 3.0 MW_{pk} klystrons in the DTL3-5 stations. Using the saturated power data, the measured power margin is 1% for DTL4, 4% for DTL5, and 13% for DTL3. The power margin values for DTL6 and CCL3 exceed 25% and are considered

acceptable. The power margin for DTL2 is 19% and is also considered acceptable based on the existing radio frequency quadrupole (RFQ) HVCM configuration. The DTL2 measurements did indicate the potential need for upgrades to the RFQ HVCM to maximize the power output of a 2.5 MW klystron, which is covered in a subsequent section.

Table 4.5. Peak power and power margin.

Structure	Prf (kW)	Psat (kW)	Power margin (%)
DTL2	1847	2194	19
DTL3	2038	2300	13
DTL4	2336	2370	1
DTL5	2215	2310	4
DTL6	1770	2513	42
CCL3	3324	4699	41

4.1.2.2 NCL Klystrons (Final)

The new klystrons were specified in SNS-RAD-SW-002, *Statement of Work for SNS 402.5MHz, 3MW Peak Power Pulsed Klystrons* and SNS-RAD-RF-TS-0003, *SNS 402.5MHz, 3MW Peak Power Pulsed Klystron Technical Specification*, to meet the mechanical and electrical constraints of the existing systems. The klystrons are designed to operate at 402.5 MHz with an average peak power of 3.0 MW. The output circuit of each tube is constructed to be operated without pressurization. Table 4.6 shows additional specifications for each klystron.

Table 4.6. 3.0 MW klystron specification.

Parameter	Requirement
RF duty factor	9% minimum
Pulse repetition rate	60 Hz maximum
Beam voltage	<128 kV at maximum power
Beam current	42 A maximum
RF power gain	45 dB minimum

4.1.2.3 NCL HPRF Transmitters (Final)

The 3 MW klystron specification requires that the new tubes be able to operate within the existing electrical and mechanical constraints of the NCL HPRF transmitters. There are no changes to the chassis that support klystron operation (Table 4.7).

Table 4.7. NCL HPRF transmitter chassis output.

Filament P.S.	1800 VA	1225 VA
Magnet P.S. 1	6400 W	3500 W
Magnet P.S. 2	6400 W	500 W
Solid state amp	150 W	84 W

4.1.2.4 NCL Waveguide Circulators (Preliminary)

Engineering analysis indicates that the existing NCL circulators are adequate for PPU operating levels. There is existing engineered protection against reflected power in excess of 600 kW. Based on that protection, and the beam studies described in Section 4.2.2.1, HPRF engineers developed an electromagnetic model that calculated the peak voltage gradients in the circulator across all phases. The maximum calculated electric field with a forward power of 2.5 MW (maximum forward power needed for a 38 mA proton beam) and a reflected power of 600 kW (current operational protective setting) was 871 kV per meter. A full description of the simulations and results is documented in PPUP-300-TR0002, *Warm Linac Circulator RF Power Specification Considerations.*

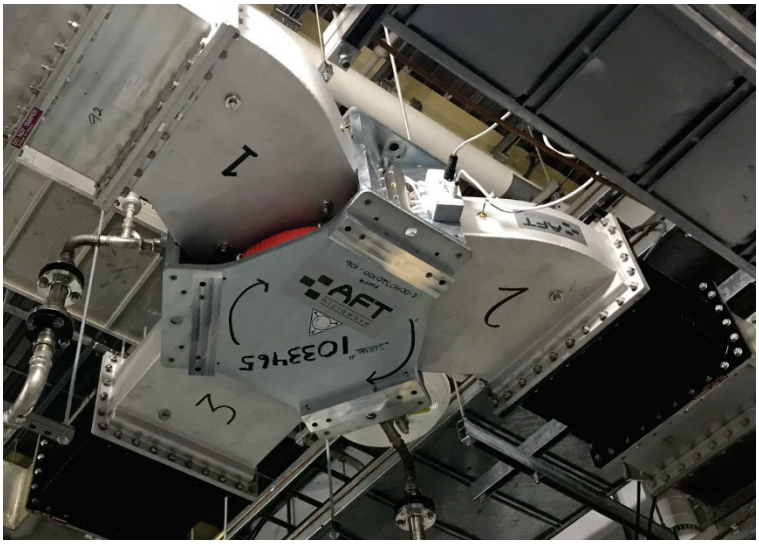

Figure 4.7. DTL waveguide circulator installed in an NCL system at SNS.

4.1.2.5 NCL Waveguide Glycol Loads (Preliminary)

Engineering analysis has shown that the existing NCL waveguide glycol-water loads are adequate, and upgrades are not necessary. Flow rates can be increased for the existing loads to compensate for the rise in temperature. Figure 4.8 shows the temperature change in glycol versus the flow rate at 300 kW_{ave} into the load. Data points for the figure were obtained using a simple heat exchanger equation relating flow rate to temperature change. The calculation assumes that 100% of the energy is being dissipated into the glycol-water mixture. The same engineered protection described in Section 4.2.2.4 will also limit the power seen by the glycol load to 600 kW peak, or approximately 60 kW on average.

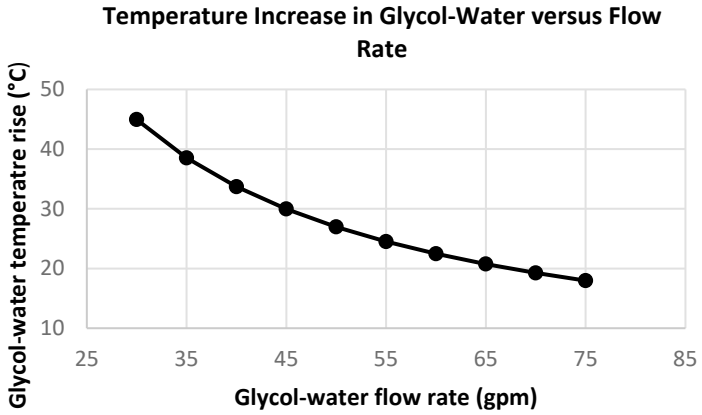

Figure 4.8. Glycol-water temperature rise vs. flow rate. *Source:* Ferrite Microwave 2016 [6].

Using the same operational parameters, a 230 kW_{ave} glycol-water load with a 45 GPM flow rate should see a temperature increase of about 22.97ºC. To maintain the same temperature rise at 300 kW_{ave}, the flow rate would need to be increased to about 60 GPM. Therefore, the 230 kW_{ave} loads supporting the 2.5 MW_{pk} klystrons can support PPU operations for the 3 MW_{pk} (240 kW_{ave}) klystrons if the glycol-water flow rate is increased to 60 GPM.

4.1.2.6 Normal Conducting Linac HPRF Summary

The increase in the average linac beam current to 38 mA requires modifying the DTL3 – DTL5 HPRF systems to accommodate a 3 MW_{pk} (240 kW_{ave}) klystron. The HVCMs supporting these systems will be upgraded accordingly; the details are provided in subsequent sections.

The new klystrons were specified in SNS-RAD-SW-002, *Statement of Work for SNS 402.5MHz, 3MW Peak Power Pulsed Klystrons* and SNS-RAD-RF-TS-0003, *SNS 402.5MHz, 3MW Peak Power Pulsed Klystron Technical Specification*, to meet the mechanical and electrical constraints of the existing systems. Integrating a 3 MW_{pk} klystron is anticipated to be straightforward. In addition, the increase in RF power requires additional cooling to remove an estimated maximum incremental increase of ~80 kW_{ave} per klystron in collector power (no RF, 7.4% duty factor), which is covered in a subsequent section.

No changes are required to the CCL RF stations for the PPU.

Table 4.8 summarizes the baseline warm linac RF equipment and the additional required RF equipment to support the PPU.

Table 4.8. Normal conducting linac high-power RF systems for the PPU.

Major equipment	Baseline	PPU upgrade	Final configuration
DTL klystron	6 (2.5 MW)	Upgrade three sockets to 3 MW	3(2.5 MW), 3(3 MW)
DTL transmitter	6	Modify to support 3 MW tube	3(2.5 MW), 3(3 MW)
DTL circulator	6	Upgrade to support 3 MW tube	3(2.5 MW), 3(3 MW)
DTL circulator load	6	–	6(2.5MW)
CCL klystron	4 (5 MW)	–	4(5 MW)
CCL transmitter	4	–	4

4.2 LOW-LEVEL RADIO FREQUENCY SYSTEMS (PRELIMINARY)

4.2.1 System Overview

The LLRF systems provide low-power RF drive to the linac HPRF systems and, most importantly, control the phase and amplitude of each cavity. The initial baseline stability requirements for the control are ±1.0° in phase and ±1.0% in amplitude. The LLRF control systems on the 96 existing systems exceed this specification, with ±0.5 degrees in phase and ±0.5% in amplitude routinely observed. A block diagram of the PPU LLRF system is shown in Figure 4.9. The PPU system is like the existing LLRF system with the VXI-based field control module (FCM) and high-power protection module (HPM) being replaced by µTCA-based modules.

The existing LLRF system is a digital control system that fundamentally realizes a proportional-integral (PI) feedback controller along with adaptive feed forward (AFF) to support cavity filling and beam loading conditions. The heart of the system, the FCM, digitizes four analog input channels (cavity field, reference, forward, and reflected signals), digitally processes the data stream, and produces an output signal at either 402.5 or 805 MHz, depending on the location in the linac. External communication is achieved via the slot-zero input-output controller (IOC) running the VxWorks operating system. The LLRF finite state machine is implemented as an EPICS sequencer running on the IOC. The LLRF control system also provides RF high-power protection and interlocks via the HPM, which provides for fast shutdown of the RF drive in case of overpower; cavity quench; arcs in the distribution system; poor vacuum; or "soft" interlocks such as cryo, coupler cooling, and HPRF permit. Down-conversion of reference and cavity signals is performed in a temperature-regulated chassis. The master oscillator provides low-noise, phase-coherent reference signals that are distributed throughout the Klystron Gallery and tunnel [7].

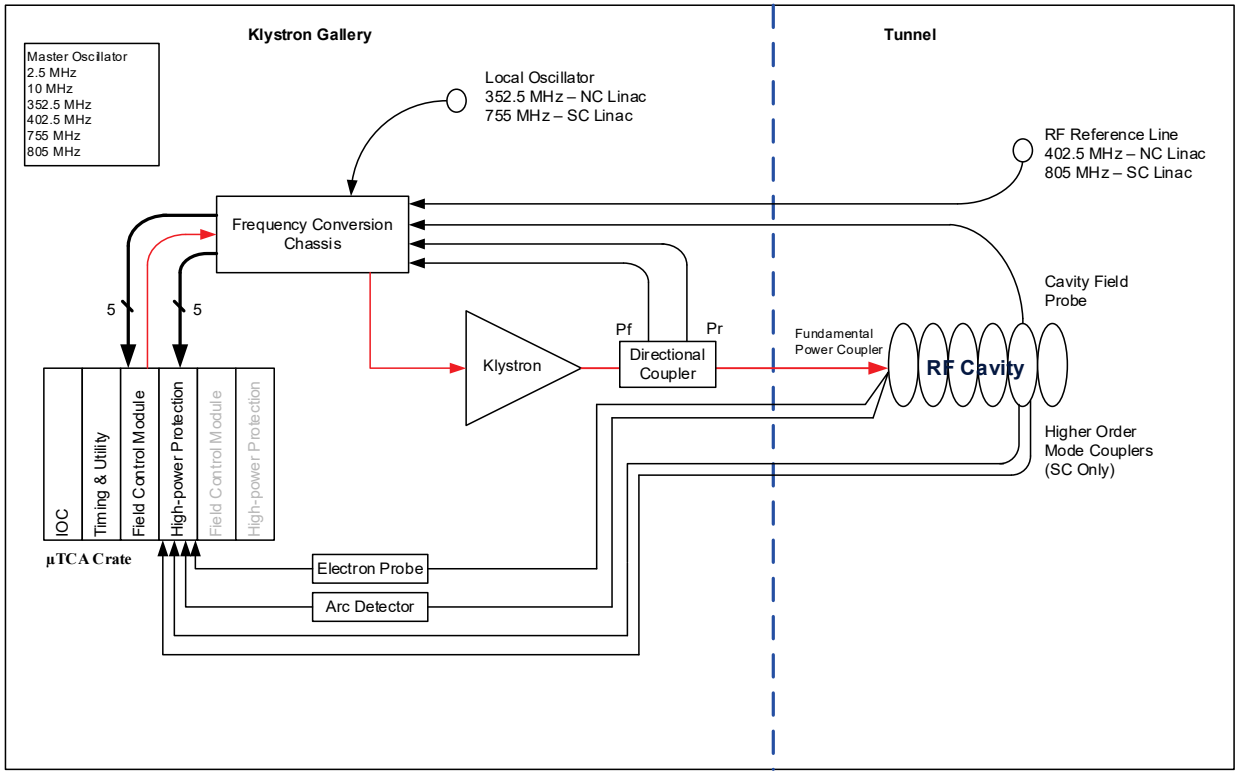

Figure 4.9. Block diagram of the SNS low-level control system.

Although the existing LLRF system meets the requirements for the PPU project, for several reasons, the system is not the ideal solution for the PPU project. The following are the known limitations of the system:

- Several key components (including the field-programmable gate arrays [FPGAs]) are obsolete and cannot be acquired, so additional modules cannot be fabricated.

- The current system's VXI backplane bus bandwidth limits the update rate from the IOC to the LLRF hardware to 20 Hz, which will not allow for pulse-to-pulse AFF correction and the desired improvement in the learning times of the system.

- For the STS, a second beam loading feed-forward buffer will be required to meet specifications, and the current hardware is inadequate to support this feature.

For these reasons, it is necessary to implement a redesigned LLRF system for both the PPU and STS projects. For PPU, only the 28 new systems will receive the replacement LLRF system. The 96 existing systems will be upgraded as part of the STS project.

4.2.2 SCL LLRF Systems for PPU

The increase in beam energy for the PPU will require installing an additional 28 LLRF systems to provide RF power to 28 superconducting accelerating cavities in 7 high-beta cryomodules in the SCL. The replacement LLRF systems for the PPU will be installed with two systems per crate in a single LLRF rack, grouped in a three-rack layout to support six cavities. This layout will maintain the pattern used for the initial SNS installation. Figure 4.10 shows the physical layout of the LLRF racks.

Figure 4.10. The physical layout of the PPU LLRF racks will be similar to that of the existing racks, shown here.

The plan for the PPU is to develop a µTCA.4-based LLRF system with hardware capable of supporting the full STS requirements. For PPU, only one beam loading flavor is required, but placeholders will be provided for additional flavors for STS. This technology supports PCIe-based backplane communication that provides adequate bandwidth to easily support 60 Hz AFF operation, as well as potential future upgrades that may be desired. It will be similar to the current LLRF system in that it is crate-based with

two LLRF control systems installed per crate. The IOC and the timing module are also installed in the crate. To limit the development time, commercial components will be used where possible. The major hardware components that will be purchased are shown in Table 4.9. The quantities listed will support two LLRF systems.

Table 4.9. Commercially available components.

Item no.	Description	Quantity
1	µTCA.4 chassis with 12 AMC slots and 1000 W power module	1
2	µTCA MCH module and shelf manager	1
3	AMC523 Dual DAC with Kintex-7 FPGA carrier card	4
4	AMC 726-core I-7 processor	1
5	AMC502 FPGA carrier with timing FMC card	1

Several major pieces of the LLRF system cannot be purchased and require design and development effort. For the replacement FCM, a commercial AMC FPGA carrier card (AMC523) will be used for the digital signal processor implementation and PCIe (peripheral component interconnect express) interface for communication with the processor. The AMC523 carrier card chosen provides a large Xilinx Kintex-7 FPGA (XC7K410T), along with a digital phase lock loop clocking scheme, which allow the system to be synchronized to the reference system. A dedicated FCM rear transition module that mates with the carrier was developed in collaboration with VadaTech; it is shown in Figure 4.11. This module provides eight 16-bit analog-to-digital converters (ADCs), two 16-bit digital-to-analog converters (DACs), and input/output (I/O) functions. Of the eight analog-to-digital converters, four are used to process the usual cavity, forward, reflected, and reference signals. Two channels are used for monitoring of the local oscillator and RF output of the system, and two additional channels are available for future improvements.

Figure 4.11. Field control module-II rear transition module.

To replace the protection features, a new HPM was also designed (see Figure 4.12). It is similar in form factor to the FCM rear transition module, but its width was increased to accommodate the additional I/O requirements. To simplify spares requirements, the same commercial AMC carrier used for the FCM was chosen for the implementation of the protection and communication functions of the HPM. The replacement HPM covers all functions of the original module but improves on the resolution of the

digitized signals and provides history buffers for all ADC channels, unlike the original system that only provided two history buffers. Two 16-bit DACs were added to the HPM-II to support expanded I/O requirements in the future. The replacement system will keep the current 50 MHz intermediate frequency so that the installed reference line and local oscillator distribution can be maintained.

Figure 4.12. High-power protection module-II rear transition module.

The present dual down-converter chassis was redesigned to include all frequency conversion functions; this simplified the design of the FCM and allows for improved temperature stability of the overall system by temperature-compensating all high-frequency components. This chassis architecture is based on the design that was developed for the 50 MHz FCM temperature dependence studies in 2010, [8] but it was decided to make the frequency conversion chassis support only a single cavity versus the dual-cavity design of the existing systems. This approach will allow a single chassis style to be installed anywhere in the linac when the STS upgrade is accomplished. Additional features added to the frequency conversion chassis are diagnostics to monitor power supply currents and temperature regulation. A status bit is provided to the control systems to assist with troubleshooting.

Because of the new hardware, the current firmware will need to be updated to support the added features. The firmware used in the original FCM is based on under-sampling using a five-over-four routine that allows for I\Q signals to be obtained. Plans are for the new firmware to use non I\Q techniques that will improve measurement precision by avoiding spectral aliasing. Plans also include increasing the buffer sizes to support decreased granularity of the feed-forward system to achieve tighter overall regulation. Finally, improved AFF learning techniques will need to be implemented to support faster correction times and a second buffer set to allow for dual beam types. The second buffer is not required for the PPU, and the development effort for this feature will be deferred until the STS project is approved.

MicroTCA was chosen for the LLRF development after comparisons with other available platforms. It is currently used for the ring LLRF system and several Controls Group projects. It is an embedded, scalable, architecture that offers flexibility. It supports both PCIe and gigabit Ethernet communication protocols and has enough bandwidth for the PPU LLRF application. Because MicroTCA is used for other applications at the SNS, the development effort is reduced for the underlying software drivers for the system, allowing allow the effort to be placed at the application level. The plan is to maintain the current

look and feel of the operational LLRF EPICS screens to minimize the learning curve for the operation staff. It will require modifying the existing EPICS screens to support the additional hardware features and properly map to the new database.

4.2.3 Arc Detectors

The ARC4 arc detector system, a commercial product provided by Advanced Ferrite Technology, is used throughout the SNS installation. The system will be used for the PPU and can support up to 16 arc detector channels per chassis. It routes light from five test points located in the RF distribution system (vacuum and air sides of the RF cavity windows or couplers, RF circulators, RF circulator loads, and klystron windows) via fiber optic cables. Radiation-hardened plastic fibers are used in high-radiation areas to prevent darkening of the fibers. An arc test system is used to verify the integrity of critical fiber paths daily to ensure the functionality of the system. The continued use of this system will minimize the number of spares required to support operations. Figure 4.13 is an image of the Advanced Ferrite Technology chassis and one of the arc detector cards. The nominal SCL system contains two banks of five arc detector cards and a shared dual output interface card that serves two cavities.

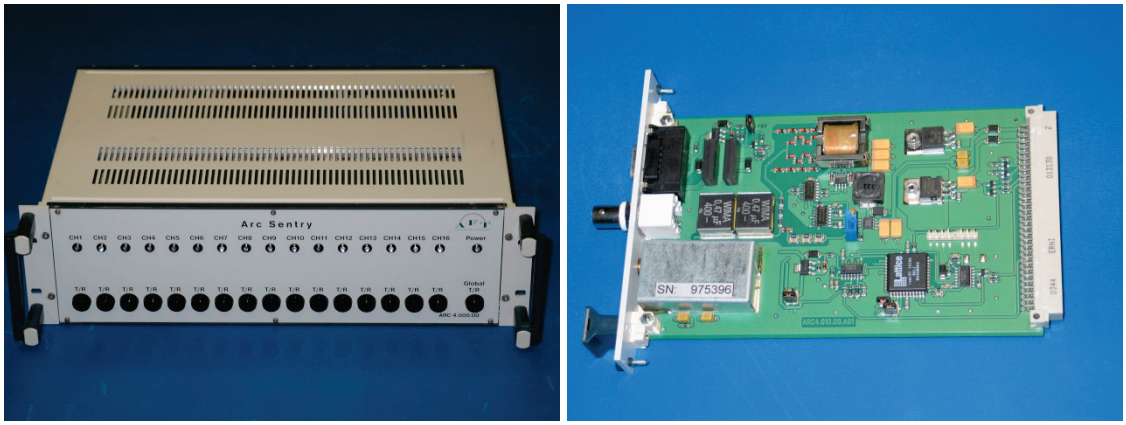

Figure 4.13. Advanced Ferrite Technology arc detector system.

4.2.4 Reference Line

The SNS RF reference system includes the master oscillator, the local oscillator (LO) distribution system, and the reference RF distribution system (see Figure 4.14). The master oscillator generates six continuous wave coherent low-noise output signals by using an ultra-low noise 10 MHz oscillator for the primary crystal. Direct analog frequency synthesis is used to generate 2.5, 352.5, 402.5, 755, and 805 MHz, but only the final four signals are used by the LLRF system. These RF signals provide the capability to control the phase relationships between the fields in the front-end and linac RF cavity structures [9].

The 805 MHz RF reference distribution system is installed through the end of the linac tunnel, but four additional temperature compensation chassis will need to be fabricated and installed to support the PPU project. The 755 MHz LO distribution will require one additional directional coupler in the existing primary 755 MHz Heliax distribution line, one additional LO distribution amplifier, and Heliax distribution cables going to the PPU LLRF rack groups.

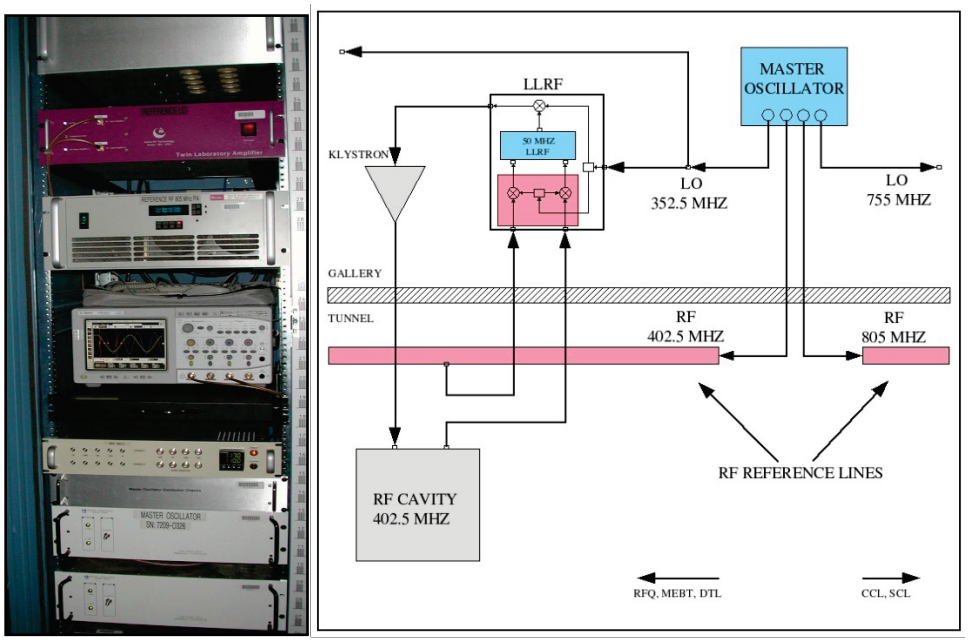

Figure 4.14. Master oscillator rack and block diagram.

4.3 MODULATOR SYSTEMS

4.3.1 System Overview

The HVCM uses AC power from the 13.8 kV utility feeds and coverts it into high-voltage pulses used to drive high-power klystrons [10]. The SNS uses three different types of klystrons, operating at different frequencies and power levels, with the modulators configured differently in the DTL, CCL, and SCL sections of the linac. Using different ratios of klystrons to modulators allows all modulators to operate at essentially the same power level, but the different voltage requirements mandate slightly different component selections for the HVCM systems. This results in a minimum number of spare parts and system interchangeability, and minimizes the training required to support and maintain the modulator systems.

A basic modulator system-level block diagram is shown in Figure 4.15, along with photographs of the major subsystems in Figure 4.16. The 13.8 kV 3-phase AC is transformed down to 2100 V after passing through 5th and 7th harmonic filters. The AC is rectified, using silicon-controlled rectifiers (SCRs), to produce DC voltages of up to ±1300 V. Two large capacitor banks store up to 200 kJ of energy. The DC bus feeds three insulated gate bipolar transistor (IGBT) H-bridge “switch plates” that chop the DC up at nominally 20 kHz. The bridges supply power to the primaries of nanocrystalline core step-up transformers submerged in an oil-filled tank. The outputs of the transformers are then rectified to produce DC, and the three phases are combined to generate the high-voltage pulses. After passing through a π filter to remove some of the high-frequency content, the pulses are transmitted down a triaxial cable to the klystron load(s).

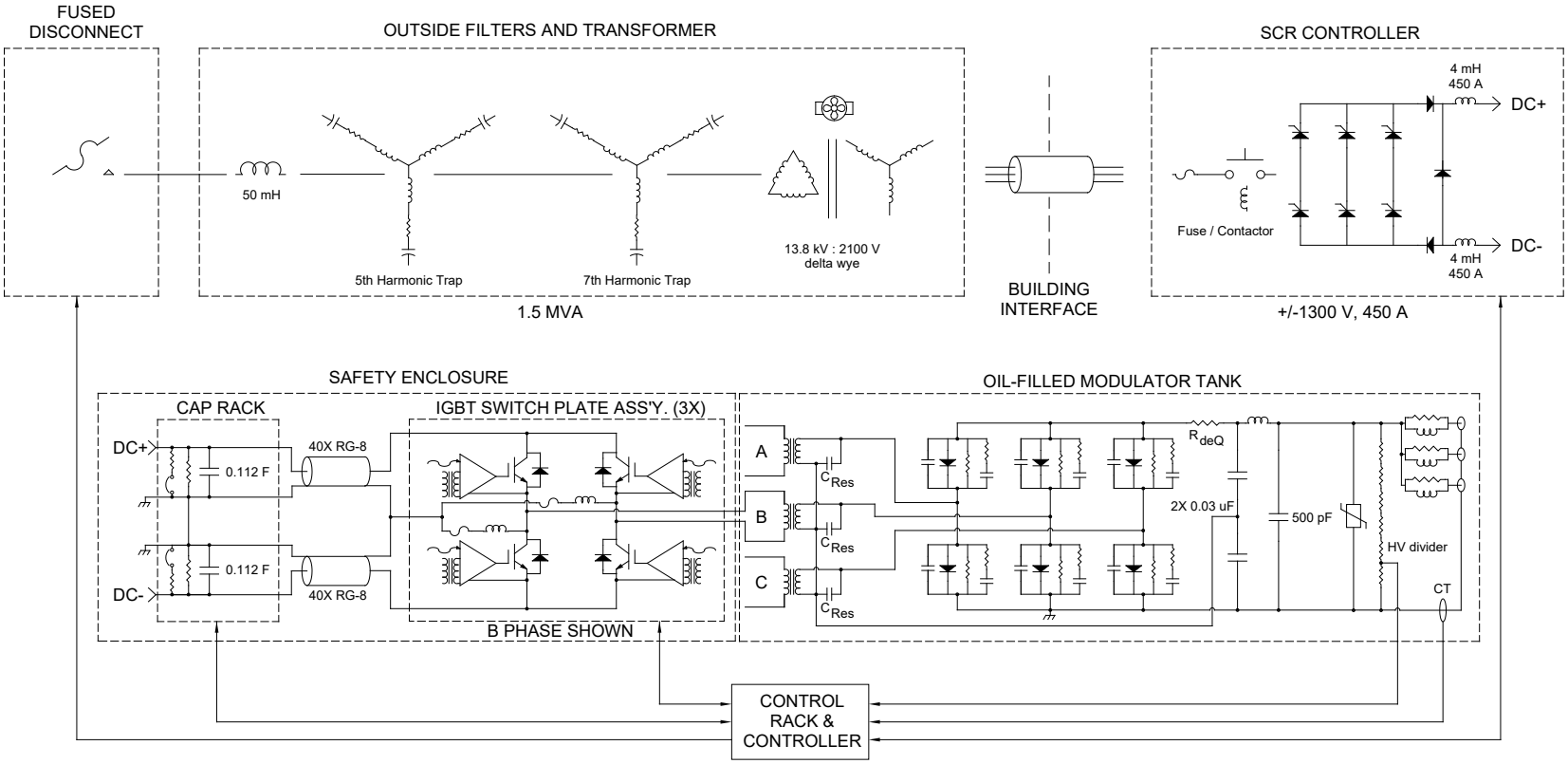

Figure 4.15. Block diagram of the HVCM system.

Outside 13.8 kV:2100 V 1.5 MVA transformer

Safety enclosure and oil-filled modulator tank

SCR controller

Control rack

Figure 4.16. Major components in the HVCM system.

4.3.2 System Requirements and Interfaces

The modulator design for the PPU involves several trade-offs necessary to ensure that system reliability is at least equivalent to the current HVCM operational performance. The system requirements are dictated by the cavity power requirements and the klystron performance characteristics, which are defined in Section TBD. The increased and/or new cavity power requirements demand the following from the modulator systems:

- Increased operating voltage levels to drive the 700 kW klystrons supplying the 28 new cavities

- Increased operating voltage levels in the warm section of the linac to support the higher beam current loading and supply adequate power to the three new 3.0 MW, 402.5 MHz DTL klystrons (DTL-3, DTL-4 and DTL-5) [11]

- Increased operating voltage levels in the RFQ-Mod1 to provide 25% control margin to the DTL-2 klystron and permit future operation with 3.0 MW, 402.5 MHz klystrons

Each of these situations will be considered separately in the following subsections. Wherever possible, the modulators will be similar to the existing HVCMs to minimize spare parts inventories, optimize operational efficiency, and minimize the amount of training necessary to support modulator operation. If minor topological changes result in increased efficiency and component stress reduction, they will be implemented. Table 4.10 summarizes the major parameters for the new and upgraded modulator systems required to support the PPU.

Table 4.10. Present and projected operating parameters for existing and new HVCM systems.

HVCM system	Present output voltage (kV)	Present output current (A)	PPU output voltage (kV)	PPU output current (A)	PPU modulator average power (kW)
Upgraded RFQ HVCM	N/A	N/A	−123	110.5[a]	1030
Upgraded DTL HVCMs	N/A	N/A	−128	83.7[b]	810
Existing CCL HVCMs	−133	67.7	−136	72.0	710
Existing SCL HVCMs	−74	116	−77	121	775
New SCL HVCMs	N/A	N/A	−81.7	123.2	836

[a] 3.0 MW klystron in RFQ and DTL-1 positions, 2.5 MW klystron in DTL-2 position.
[b] 3.0 MW klystron in both positions.

Since components used on the HVCM systems operate outside manufacturer's published operating parameters, operational limits are established empirically. The SNS HVCM IGBTs operate reliably at 70% of their voltage rating without snubbers and at >75% of their rating with snubbers. Experience has shown that turning off an IGBT while it is conducting 1 kA or greater is detrimental to its long-term durability. Likewise, maintaining switching losses below approximately 5 kW is desirable to maintain system reliability. It is also desirable to maintain these operating limits to permit the use of existing SCR controllers and 13.8 kV:2100 V dry cast distribution transformers. Some additional HVCM requirements are listed in Table 4.11.

Table 4.11. HVCM requirements for new and existing systems.

Parameter	Value
Input voltage, AC RMS	13.8 kV ±3%, 3 phase
Input AC apparent power	1.5 MVA
161 kV: 13.8 kV transformer rating	25/33/41.6 (OA/FA/FA) MVA
Source impedance of 161 kV: 13.8 kV transformer	8–10%
Permissible harmonic generation	IEEE Std 519
Maximum power factor	0.95
Maximum pulse repetition frequency	60 Hz
Pulse width	0.3–1.5 ms
Maximum output voltage	105% of Table 4.10, negative polarity
Maximum output current	105% of Table 4.10

Table 4.12. HVCM requirements for new and existing systems (continued).

Parameter	Value
Maximum rise time, 0–90%	125 μs
Maximum fall time, 90–10%	250 μs
Maximum droop	1%
Maximum ripple	1%
Maximum fault (short-circuit) energy	20 J
Maximum response time to detected high-speed fault	2 μs
High-speed data acquisition / fault channels, >25 MSa/s	≥32
Interlocks	Consistent with current HVCM systems, available upon request
Local human machine interface	Keyboard/mouse and/or touchscreen
Remote human machine interface	EPICS via Ethernet
Controller power	208 V rms, 3 phase, uninterruptible power supply
Reliability MTBF	24,000 hours
Mean time to repair, 90% of failures	≤2 hours
Minimum component voltage rating	150% of maximum operating level
Operating temperature	50–90°F
Cooling water	Deionized (1–5 MΩ·cm), ≤60 gpm, ≤90°F supply temperature (20 gpm for SCR controller)
Maximum size transformer	170 in. × 110 in. × 110 in. tall
Maximum weight transformer	15,000 lb
Maximum size SCR controller	50 in. × 50 in. × 120 in. tall
Maximum size modulator	170 × 100 × 90 in.
Maximum weight modulator tank, no oil	4,500 lb
Modulator dielectric fluid	Envirotemp FR3

4.3.3 Existing Normal Conducting Linac Cavities

The additional beam current required for the PPU project does impact the warm section modulators. Most of the warm linac structures should be capable of operation at higher beam current with adequate RF control margin now that the new controllers have been installed and pulse flattening to <1% has been achieved [12].

A task force was established in 2017 to study the impact of operating the SNS warm linac at 38 mA, which is required for PPU [11]. Through a series of studies of the linac, it was demonstrated that 38 mA could be transmitted through the linac with the existing RF equipment and modulators. However, the study also identified unacceptable power margins—the ratio between the difference of the saturated and required RF power levels and the required RF power level—in several DTL klystrons, as shown in Table 4.12. Only CCL-3 was measured; other CCL stations require lower power levels. As seen in the table, most of the DTL stations do not possess the required 25% power margin for reliable operation.

To achieve 25% margins on the DTL-3 – DTL-5 klystrons, it is necessary to upgrade the existing 2.5 MW klystrons to 3.0 MW. The current DTL modulators do not support operation of the higher-perveance 3.0 MW klystrons and must also be upgraded. The DTL-2 power margin of 19% is lower than the desired 25% but is deemed acceptable. However, to reduce stress on and permit eventual operation with 3.0 MW

klystrons, the RFQ-Mod1 modulator, which powers the RFQ, DTL-1, and DTL-2 klystrons, must also be upgraded.

Table 4.13. RF power level, saturated power and resulting power margin for select warm linac klystrons.

Station	P_{RF} (kW)	P_{sat} (kW)	Power margin (%)
DTL-2	1847	2194	19
DTL-3	2038	2300	13
DTL-4	2336	2370	1
DTL-5	2215	2310	4
DTL-6	1770	2513	42
CCL-3	3324	4699	41

4.3.3.1 RFQ and DTL Modulator Systems

The RFQ and DTL sections of the SNS are powered by three HVCM systems. RFQ-Mod1 powers the RFQ, DTL-1, and DTL-2 klystrons; DTL-Mod3 powers the DTL-3 and DTL-4 klystrons; and DTL-Mod5 powers the DTL4 and DTL5 klystrons. All three of these modulators need to be upgraded for PPU to achieve the desired RF power margin, as discussed earlier.

Initial efforts focused on different upgrade solutions for the RFQ-Mod1 and the two DTL modulators. Early designs considered used modest changes in component values for the DTL HVCMs, while a variety of options for the RFQ-Mod1 were explored. Options considered for the RFQ modulator included optimizing component selection in the existing modulators or adding a new single-phase modulator dedicated to powering a single RFQ klystron only, while configuring the original RFQ modulator to be identical to the other DTL modulators. The final option—changing the modulator circuit topology to one where the secondaries of the pulse transformers are connected in series, as is done with the alternate topology (AT) HVCMs (Figure 4.17)—was the path ultimately selected. The option to add a dedicated HVCM for the RFQ was rejected because of space limitations in the Klystron Gallery.

Selecting the series-connected secondary design offers the desired operational flexibility to permit either a 2.5 MW or 3.0 MW klystron to be installed in any socket. A preliminary design review of the series-connected secondary topology for RFQ-Mod1 was held in July 2019, and the review committee recommended seeking a common solution for upgrading both RFQ-Mod1 and the DTL modulators. This minimizes the required number of spares and simplifies operations.

Circuit simulations were used to find optimal component values for both the parallel- and series-connected circuit topologies. Either topology could produce a common modulator design, but the series-connected topology results in lower sensitivity of component values, reduces component stresses, and achieves the desired operational flexibility mentioned previously. A comprehensive sensitivity analysis of component values was performed to determine which values produced the required output for the worst-case loading configuration for the RFQ and DTL modulators while still maintaining component operating levels within empirically defined limits.

Figure 4.18 shows one example of the SPICE circuit simulation sensitivity analysis when the value of the resonant capacitor and transformer turns ratio are varied for both the RFQ and DTL modulators while other parameters are held constant. In this case, the effect on the output voltage is plotted, but similar plots were made for IGBT peak and commutating currents. The effect of varying the leakage inductance was also part of the sensitivity analysis.

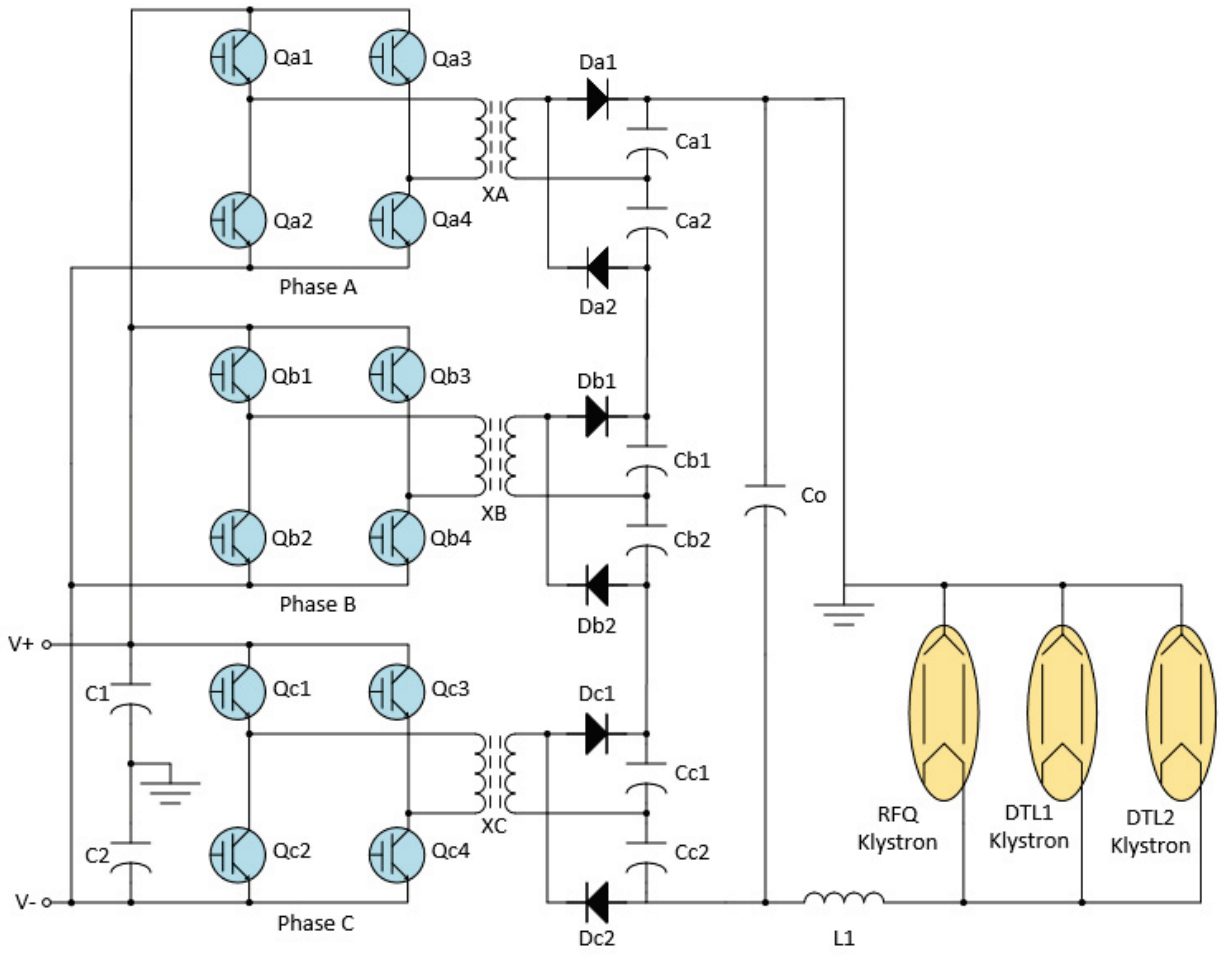

Figure 4.17. Series-connected 3-phase modulator topology for RFQ-Mod1.

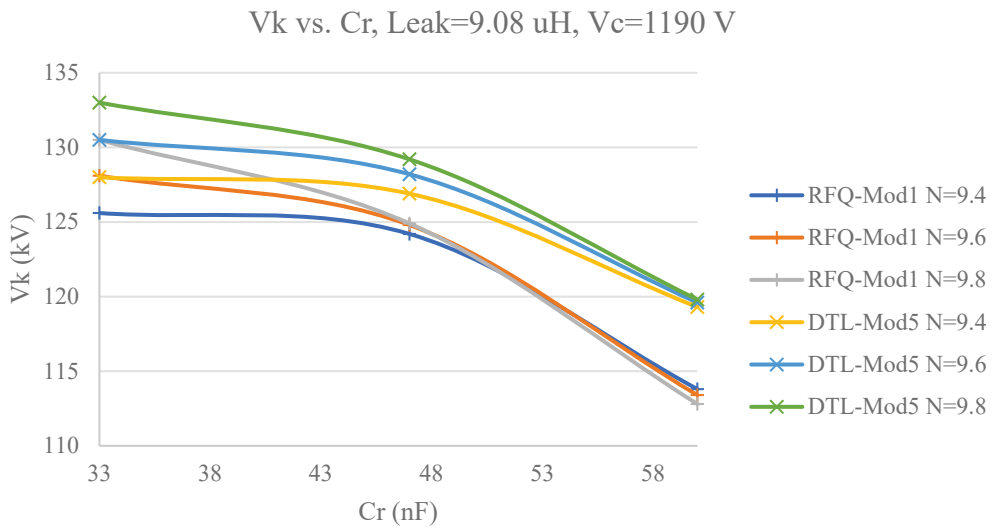

Figure 4.18. Cathode voltage vs. resonant capacitance for both RFQ-Mod1 and a DTL modulator.

The DC bus voltage was held at a constant ±1180 V for all the simulations. Reliable operation at higher DC bus voltages has been demonstrated with test stand operation of the IGBTs at up to ±1250 V for

several hundreds of hours. This approach will be further tested in FY 2021 on the high-energy beam transport (HEBT) and RF Test Facility (RFTF) HVCM test stands to verify reliable operation is achievable at these increased voltage levels. The result of the sensitivity analysis, and the optimized component values, are shown in Table 4.13.

Table 4.14. Design values for a common RFQ/DTL modulator.

Parameter	Value	Units
Output voltage	−123 (RFQ_Mod1)	kV
	−128 (DTL_Mod5)	kV
Output current	103.1 (RFQ_Mod1)	A
	82 (DTL_Mod5)	A
Maximum charge voltage	±1180	V
Storage capacitance	2X.0.128	F
IGBT peak current	4000	A
Maximum commutating current	1000	A
Transformer turns ratio	9.6:1	–
Transformer leakage inductance	9.08	µH
Resonant capacitance	47	nF
Output filter capacitor	15	nF
Output filter choke	25	mH

Figure 4.19 shows the output voltage and the IGBT switch current for RFQ-Mod1 providing a 25% power margin and using the worst-case configuration of klystrons (3.0 MW klystrons in all but the DTL-2 location). The simulation uses parameters shown in Table 4.13, and similar results can be produced for the less-demanding DTL system with the same parameters. The simulation is not configured to have adjustable start pulses for start-up ringing minimization, or to provide variable switching frequency for capacitor droop compensation. In both cases, the required output levels are achieved with modest bus voltages operating within empirical component limits.

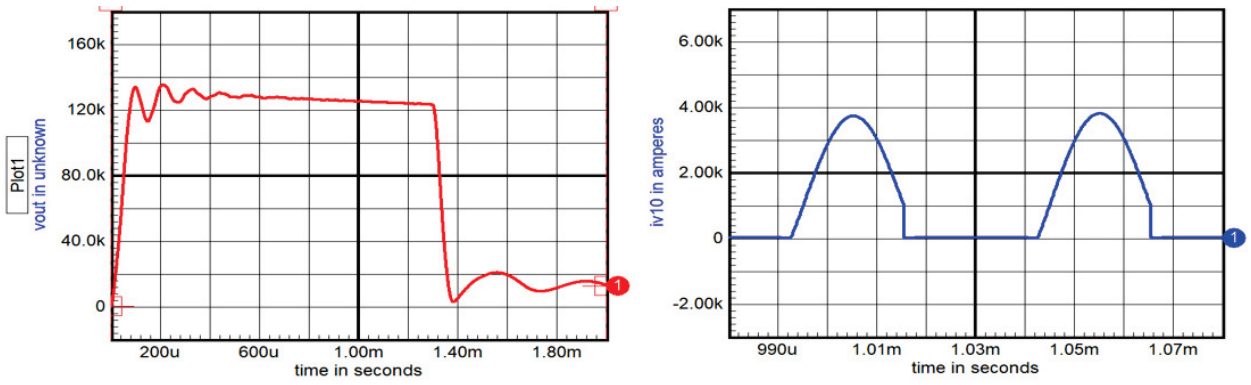

Figure 4.19. RFQ-Mod1 output current and IGBT currents during worst-case operation.

The majority of changes, compared with the current operational modulators, occur inside the high-voltage oil-filled tank. Figure 4.20 shows those components with the tank hidden. Boost transformers are identical in design to the current units but use different turns on the primary and secondary to achieve the lower step-up ratio. Each phase produces approximately 1/3 of the output voltage, or 43 kV, but the last transformer secondary is “floating” at the full output voltage. The resonant capacitors consist of an array

of 20 in-series, 2 in-parallel, FPG86Y047J, 4000 V peak capacitors. During normal operation, individual capacitors operate at 2.75 kV, or 68% of their rating. Series-connected FPG capacitors were evaluated in a more demanding application for over 7500 hours and exhibited an average change in capacitance of less than 0.1% after 3700 hours of operation. An array of DSEI2X101-12A fast recovery epitaxial diodes makes up the rectifier assembly, with 84 in series for each half-bridge, resulting in diode operation at 40% of their rating. Forced cooling of components is achieved with the upgraded cooling system, employing a magnetically coupled centrifugal pump with eductors and nozzles directing flow to the highest-power dissipating components.

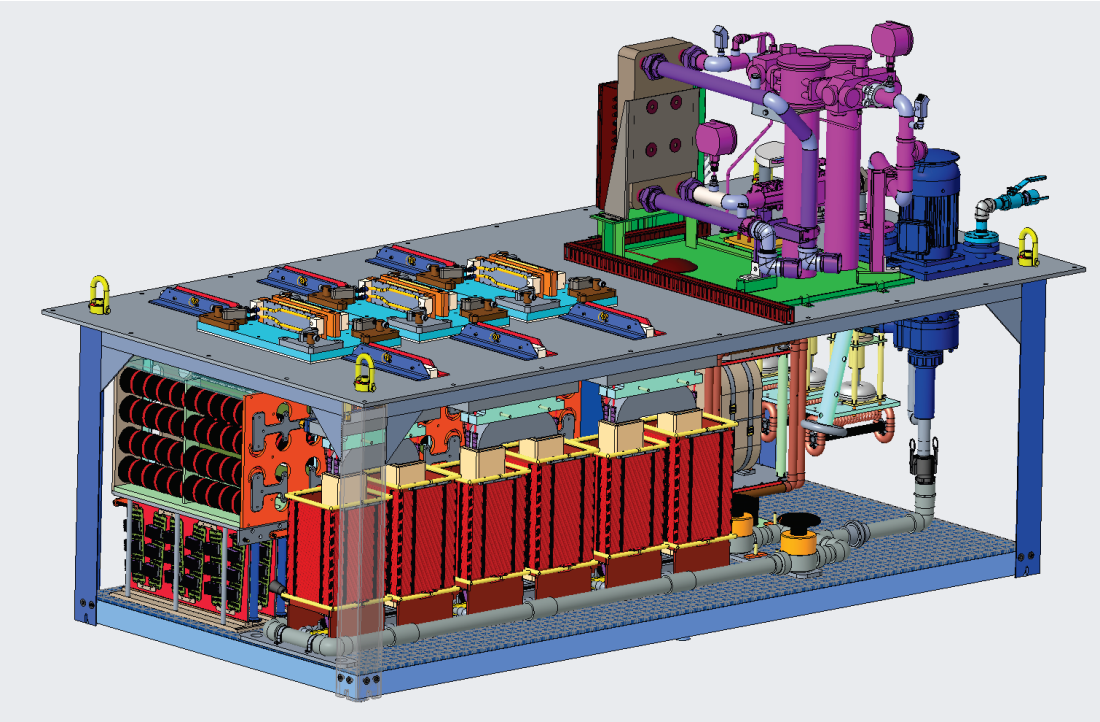

Figure 4.20. View of components inside the oil-filled high voltage tank.

The IGBT H-bridge switch plates and laminated bus interconnections are identical to those developed for the AT-HVCM. One of the switch plates, along with the laminated bus overhead developed for ORNL by Mersen, is shown in Figure 4.21. Use of the laminated bus minimizes parasitic inductance between the energy storage capacitor bank and the H-bridge, thereby reducing the need for significant numbers of bypass capacitors. It also simplifies maintenance, reduces mean time to repair, and increases the reliability of the high-current connections at the H-bridge to primary contact points. Using this design reduces spare component and subassembly counts because they are shared with the AT-HVCM system being installed for the three new high-beta modulators for the PPU project. Not shown in the figure is that one additional capacitor per capacitor bank is required in the RFQ-Mod1 to reduce droop, but there is adequate space in the current safety enclosure to accommodate this addition.

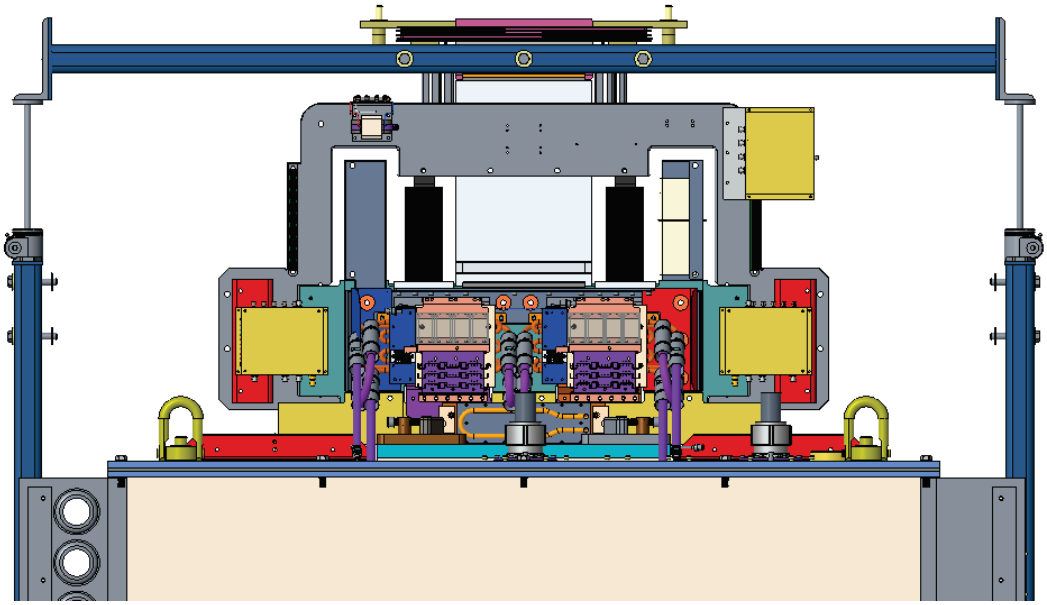

Figure 4.21. IGBT H-bridge switch plate, laminated bus, laminated bus support structure, and high-voltage oil-filled tank.

4.3.3.2 CCL Modulator Systems

During a series of tests in 2017 to demonstrate the ability to transmit 38 mA through the SNS linac, the forward power in the CCL klystrons was measured and compared with levels at 26 mA [11]. Table 4.14 summarizes those results. Adding the required 25% control margin to the operating power level at 38 mA for the highest-power klystron indicates that a saturated power of 4.68 MW (3.78 kW × 1.25) is required for PPU operation.

Table 4.15. Measured CCL klystron operating levels for present and PPU operation.

Station	P_{RF}, 26 mA (kW) measured Feb. 2017	P_{RF}, 38 mA (kW) measured Apr. 2017
CCL-1	2945	3179
CCL-2	3306	3514
CCL-3	3421	3781
CCL-4	3395	3679

In 2018, measurements were performed on the Thales TH2168009 klystron on the RFTF test stand, revealing that 5.1 and 4.8 MW of saturated power can be achieved at cathode current levels of 72.4 and 70.0 A, respectively. A cathode current of 72 A corresponds to 136 kV of modulator output voltage, a level that has been demonstrated in the RFTF test stand repeatedly, operating at a modest DC bus voltage of ±1180 V. With the inclusion of snubbers across the IGBTs, the maximum collector-emitter voltage was measured to be 2800 V at the 136 kV operating point. Thus, no upgrade to the CCL modulator systems is required to support the PPU operating levels in the linac.

4.3.3.3 Technology Readiness

The RFQ/DTL modulator draws heavily on the design of the AT-HVCM system. The upgraded modulator topology modifications, and associated components and subassemblies, have been under nearly

continuous testing in the HEBT modulator test stand for over 2 years. The components and subassemblies outside the high-voltage oil-filled tank are identical to the AT-HVCM system and therefore have been thoroughly tested under similar operating conditions.

Several of the in-tank components and subassemblies are identical to those used in the operational modulators currently installed at the SNS. New components are variations on the design of the AT-HVCM system. In those cases, component de-ratings and power dissipations have been calculated and determined through simulation and are quite conservative for the selected components. Where new designs are subject to high voltages, finite element analysis has been used to ensure the field stresses are low.

It is still necessary to assess the impact on system performance and reliability of powering multiple 3.0 MW klystrons. Since no 3.0 MW klystrons currently exist at ORNL, another solution must be found. A resistive load was procured through Ohmite to mimic any combination of klystron loading for the modulator and is shown in Figure 4.22. This load will permit operation to up to 6 Hz, or 10% of the nominal average power, and perhaps higher depending on component temperatures. Full peak power testing is planned for late 2020 on the HEBT test stand. For longer-term, higher-average-power testing, the prototype system will be installed in the RFTF or RFAX (RF Annex) modulator test stands where existing klystrons are available as loads. This test is scheduled to run for at least 4 months.

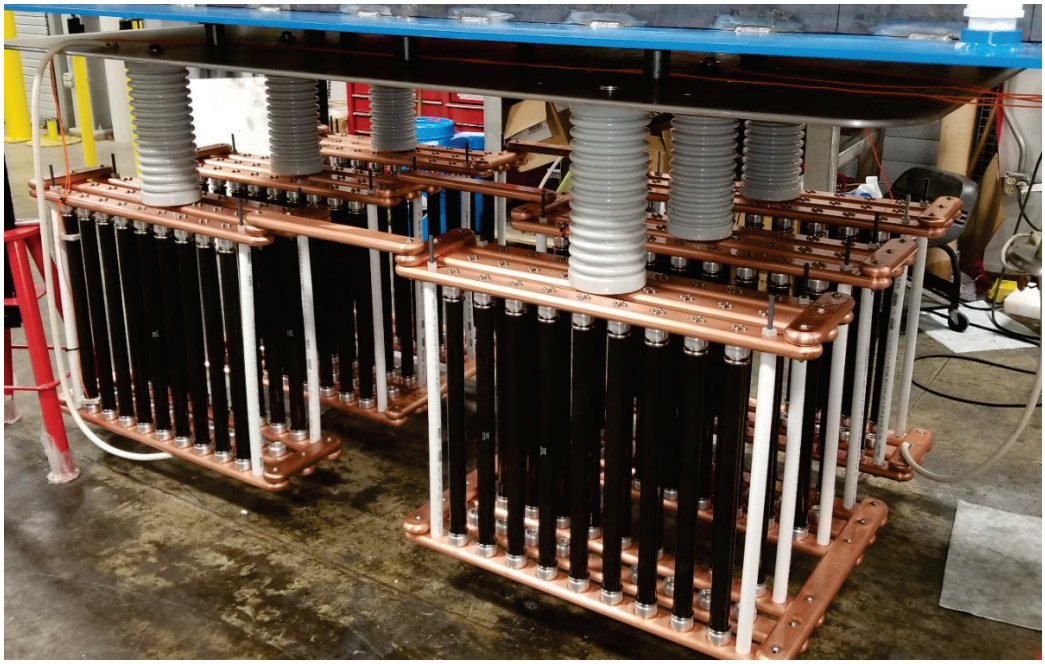

Figure 4.22. Dummy high-voltage resistive load for modulator testing, shown removed from the oil tank. Changing individual resistive elements permits customizing the load resistance to mimic a variety of klystron load impedances.

4.3.3.4 Acquisition and Installation Strategy

Where possible, all required component upgrades and/or replacements will be purchased as custom assemblies based on an ORNL-generated specification. When the components vary from those currently employed in the HVCM systems now in operation, sufficient spares will also be purchased at the time of procurement to reduce the overall project cost. Quality will be ensured by requiring the manufacturers to test components to at least 150% of the operating voltage or the components' voltage ratings, whichever is greater. Additionally, the manufacturers shall be required to test components to relevant ASTM and/or IEEE standards, such as IEEE Std. 390-1987, *IEEE Standard for Pulse Transformers*.

As extensive experience exists at ORNL, and to further train operational support staff on the new system modifications, the subassemblies will be assembled in-house using manufactured and fabricated components based on ORNL-generated drawings. Since installation activities are long in duration, installation into the existing RFQ and DTL modulators will be performed during the extended outage period. Additional resources are available as needed to support these activities.

4.3.4 New and Existing SCL Cavities

To provide 805 MHz RF power to the additional 28 cavities required for the STS, twenty-eight 700 kW peak power klystrons will be installed in the existing Klystron Gallery. The ratio of klystrons to modulators is based on optimization of the modulator performance parameters. Because of the increased beam current, additional forward power will need to be supplied to the existing 81 superconducting cavities. This will require additional voltage and current from the modulators. Figure 4.23 shows the RF power, including a 25% control margin, and modulator voltage, based on SPICE circuit simulations, required to drive the klystrons to produce those power levels for each location in the Klystron Gallery. RF power is shown in red and modulator rated operating voltage in blue.

The required forward power for each of the additional 28 cavities decreases linearly from 680 to 622 kW, including a 25% control margin, as the beam travels down the linac. This decrease will be used advantageously in the modulators. The first two modulators, each of which powers nine klystrons, can generate up to 82 kV. The additional operating margin, greater than the required 25% control margin, is used to account for system losses not captured in the circuit simulations, although testing of the prototype on the HEBT test stand revealed that 82 kV operation is achievable [13]. The last modulator is then able to power 10 klystrons, rounding out the 28 klystrons, since it can do so by supplying a lower voltage of approximately 80 kV. Power and other performance parameters will be virtually identical for the three new modulator systems, with an approximate 15% power increase in the new modulators compared with the existing ones. Existing SCR controllers and utility transformers have adequate margin to support the increase in power levels and therefore will be identical to the existing units.

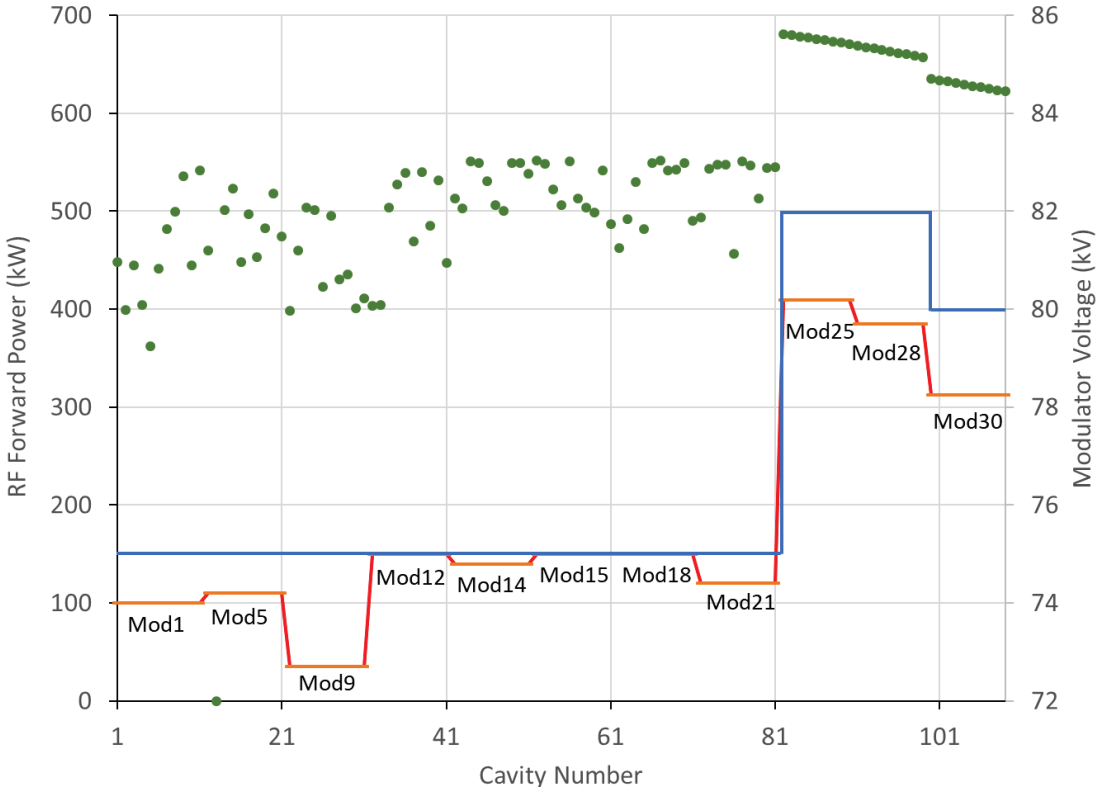

Figure 4.23. Required RF power and modulator operating voltages for existing and new SCL systems. Green dots represent the required forward RF power for each cavity on the left vertical axis, the red/orange line represents the minimum modulator operating voltage for each station to realize a 25% control margin, and the blue line represents the modulator rated operating voltage.

4.3.4.1 Existing SCL Modulator Systems

The baseline option is to use the existing HVCM topology and increase the voltage to accommodate the higher required output voltage. While all modulators support full 75 kV operation, it is desirable to operate the modulators at lower voltage levels provided they can generate enough power to support the required klystron forward RF power to improve reliability. Operation with a 15% control margin may be feasible in the SCL cavities. For 15% control margin, all modulators could operate at 73 kV or lower. For 25% control margin, 75 kV operation is required.

Figure 4.24 summarizes the issues associated with employing the current HVCM design to power the existing SCL cavities for the PPU based on PSpice simulations. Blue and red bars represent the required DC bus voltage for operation with a 15% and 25% control margin, respectively. Recent testing on an existing SCL modulator system in the HEBT demonstrated over 100 hours of operation at DC bus voltage levels of ±1200 V and ±1250 V with no issues. In no case does the required DC bus voltage exceed ±1200 V. The green bars show the IGBT commutation currents associated with 25% control margin operation for each modulator. Empirically, a limit of 1000 A has been established for reliable modulator operation. This level is not exceeded for PPU operation. Thus, no upgrades are required for existing SCL modulator systems.

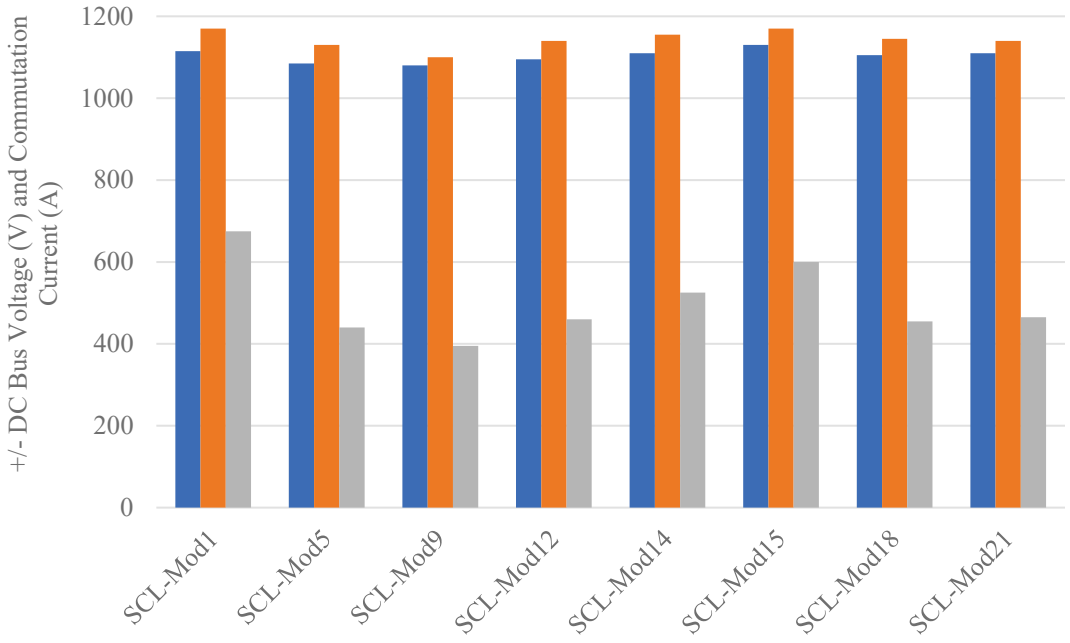

Figure 4.24. Operating levels for existing SCL modulators to support PPU increased beam loading operation. Minimum required DC bus voltages for 15% control margin (blue bar) and 25% control margin (red bar) are shown. The green bar shows the IGBT commutation current in each modulator associated with 25% control margin operation.

4.3.4.2 New SCL Modulator Systems

Unlike in the present HVCM, the three phases in the AT-HVCM are series-connected (see Figure 4.25), and each generates 1/3 of the output voltage (~30 kV per phase). A low transformer turns ratio of 7:1 is sufficient to step up the 2200 Vdc primary bus, provided by the SCR controller, to 15 kV. The voltage is doubled by the transformer's secondary rectifier circuit, and series-connected outputs of the rectifiers produce the required 82 kV.

To switch the IGBT modules used in the H-bridge converters efficiently at high frequency, a resonant circuit is created between the transformer's leakage inductance and circuit capacitance. In this topology, the resonant capacitor across the secondary winding is eliminated, and the output filter capacitors become the resonant components. If the resonant frequency is designed to match the 20 kHz switching frequency, each IGBT will turn on and off under zero current and zero voltage conditions. A SPICE circuit simulation shows the resultant IGBT current and voltage waveforms in Figure 4.26.

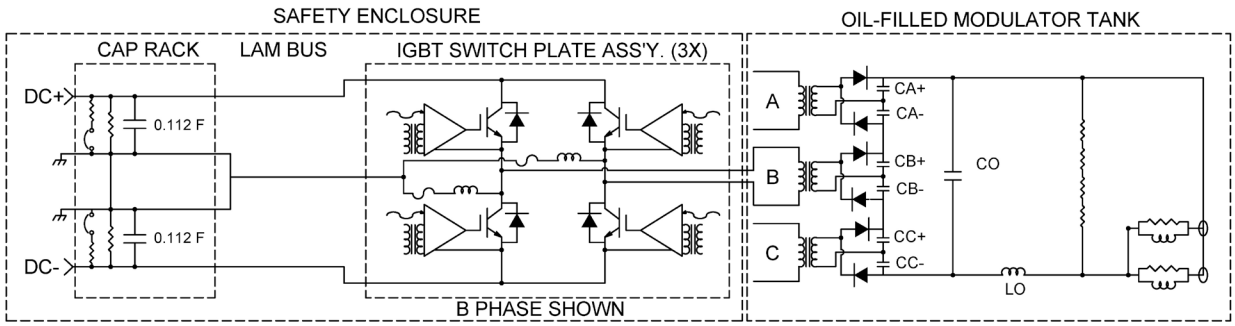

Figure 4.25. Block diagram of AT-HVCM topology (showing only a single phase).

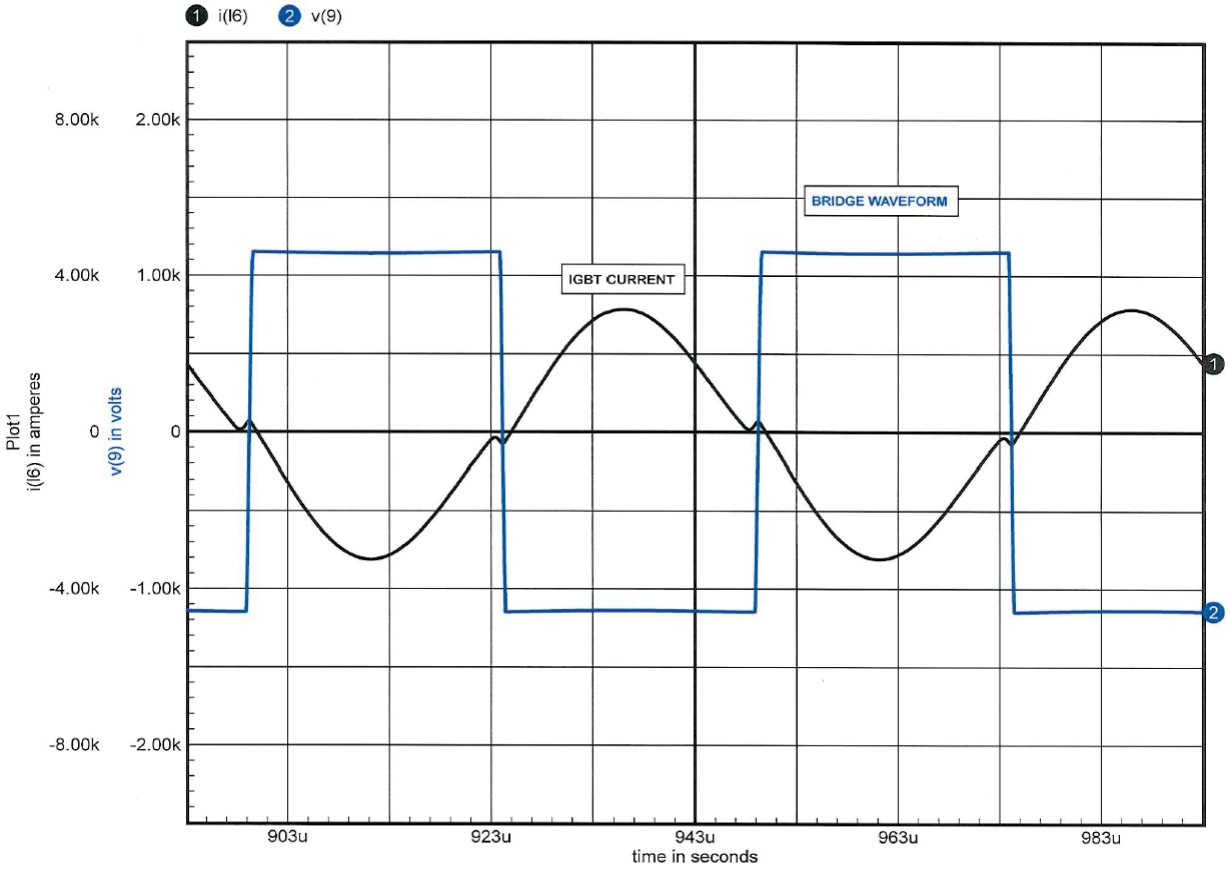

Figure 4.26. SPICE simulation of the ATM IGBT operating waveforms. The black trace is IGBT current. The blue trace is primary voltage across the boost transformer.

This topology change offers several advantages over the current topology:

- The current HVCM resonant capacitor accounts for a significant amount of modulator downtime. Relocating the resonant capacitor after the rectifier reduces the voltage across the capacitor and eliminates capacitor voltage reversal at every 20 kHz switching cycle. This results in improved lifetime compared with the present film/foil capacitors installed in HVCM systems. The lifetime of the film/foil capacitors is dramatically affected by voltage reversal, and it scales as the ratio of operating voltage to design voltage to the –8th power. Implementing the proposed topology permits a longer mean-time-between-failure (MTBF) design that can be installed in the available space.

- Zero voltage switching and zero current switching reduce the IGBT switching losses significantly. This in turn reduces the transient thermal heating of the junction. Since IGBT losses are dominated by switching losses, and every ~10°C of operating temperature reduction results in a doubling of the lifetime, this should significantly increase the MTBF of the IGBTs.

- The lower DC bus operating point for the design improves the voltage safety margin for the IGBTs, resulting in additional MTBF gains for the IGBTs.

- Since the transformer turns ratio is reduced from 13:1 to 7:1, it is much easier to achieve the required low leakage inductance values while still maintaining adequate insulation voltage margin.

- The topology supports a wide dynamic load range, driving from 2 to 10 klystrons with no performance degradation.

Table 4.15 compares operating parameters of the current SCL HVCM system operating at new linac modulator levels to those of the proposed AT-HVCM design. Performance parameters that generally affect the overall lifetime of the modulator are emphasized.

Table 4.16. Comparison between the current HVCM systems (scaled to deliver power to the new PPU klystrons) and the AT-HVCM delivering the same output.

	Current HVCM	AT-HVCM
V_{out}	82.6 kV	82.8 kV
I_{out}	128 A	129 A
Bus V_{dc}	2.8 kV	2.2 kV
Bus I_{dc}	310 A	390 A
$I(IGBT)_{pk}$	2.1 kA	3.1 kA
$I(IGBT)_{rms}$	420 A	430 A
$I(Diode)_{rms}$	22 A	63 A
$I(C_{boost})_{rms}$	13 A	51 A
$V(C_{boost})$pk-pk	91 kV	30 kV
Transformer step-up ratio	13:1	7:1

Note that the DC bus (or cap bank) voltage for the current HVCM is 2800 V, or ±1400 V, a level that is clearly too high to achieve reliable operation of the IGBTs. Also note that the boost capacitor for the proposed AT-HVCM is three times lower in voltage and yet occupies the same volume as the current HVCM. This results in a significantly more robust boost capacitor.

The trade-off for all these voltage reductions for the AT-HVCM configuration is that the currents are higher in the IGBTs, diodes, and boost capacitors. This is because each phase of the AT-HVCM delivers full output current to the klystron; whereas in the current HVCM, because the secondaries are connected in parallel, only 1/3 of the output current is delivered by each phase. However, since most of the past and present failure modes are voltage-related, higher overall system reliability is predicted.

SCL modulator system technology readiness

Following the March 2018 Conceptual Design Review, testing continued to include arc output energy system characterization and data collection from numerous current, voltage, and thermal diagnostics located around the modulator, culminating in a 60 Hz, 30 day run at the maximum specified 82 kV, 120 A

PPU load requirement [13]. The modulator was operated between 20 and 26 kHz, at constant output load, to determine the modulator voltage gain characteristic, as shown in Figure 4.27. The characteristic shows a peak around 23 kHz and falls off below and above resonance. The gain curve derivative is greater (2×) when the modulator is operating below resonance.

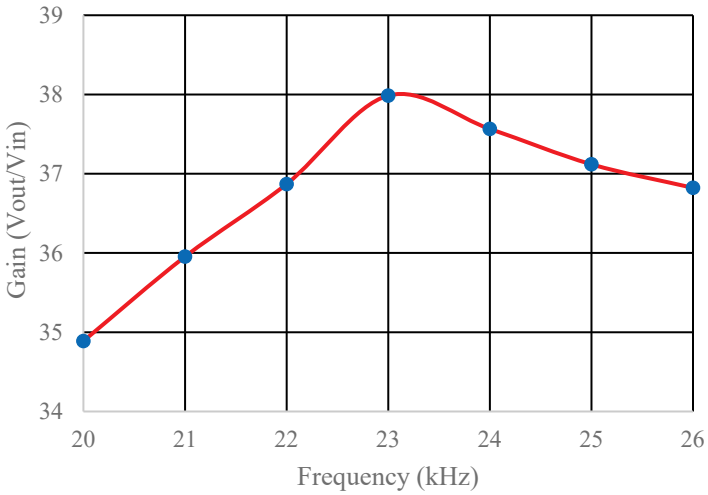

Figure 4.27. Modulator gain, measured at a fixed 80 kV output, by varying the DC bus voltage.

An example waveform data set, measuring IGBT collector-emitter voltage and collector current at 23 kHz, is shown in Figure 4.28; it includes measured IGBT switching losses. Analyzing the data collected at 1 kHz increments permits determination of the IGBT turn on/off losses as a function of frequency, as shown in Figure 4.29.

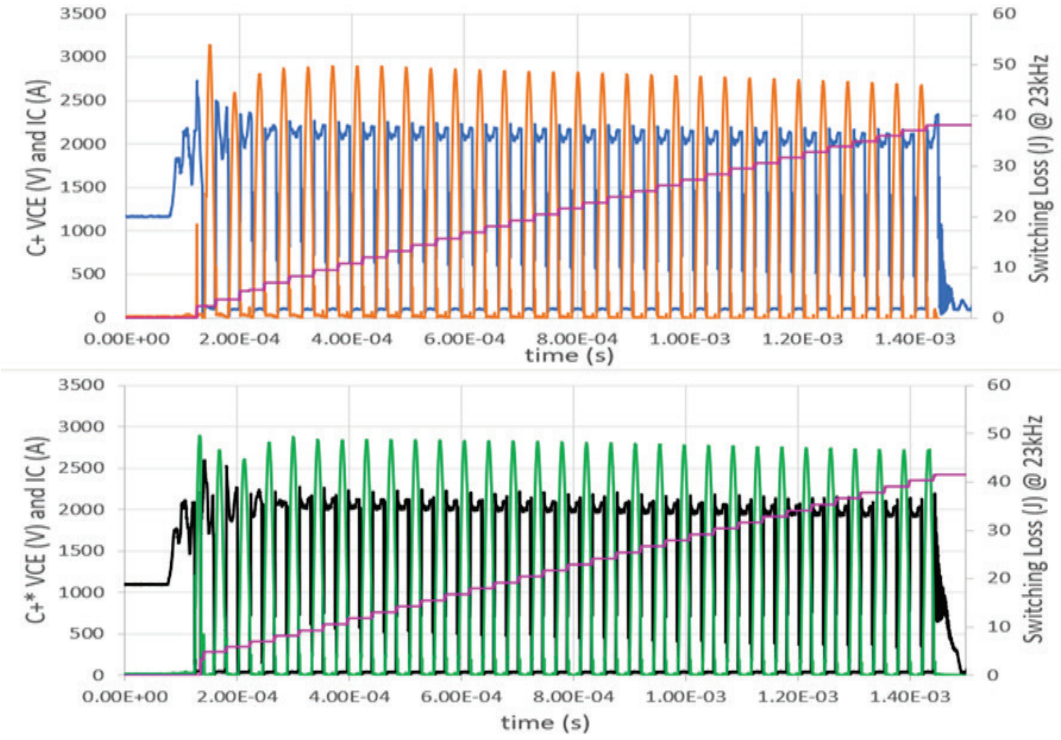

Figure 4.28. IGBT voltage V_{CE}, current I_C, Eon/Eoff waveforms at 23 kHz switching frequency.

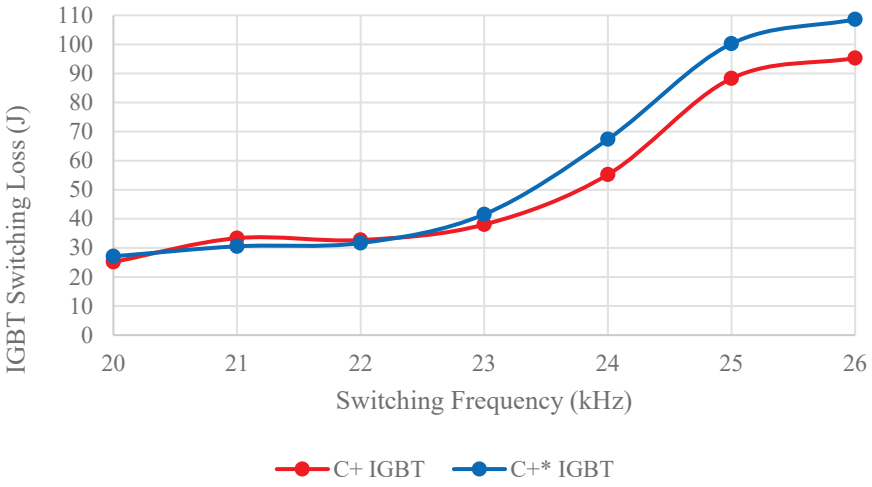

Figure 4.29. Eon/Eoff losses as a function of switching frequency for H-bridge IGBTs on the AT-HVCM modulator.

Combining the IGBT loss data in Figure 4.29 with the modulator's gain characteristic in Figure 4.27, it becomes evident that operating below resonance achieves pulse flattening over a smaller frequency range and with lower IGBT losses. Typical AT-HVCM IGBT losses are 30 J/pulse (1.8 kW) compared with 40 J/pulse (2.4 kW) for the present HVCM [14]. Figure 4.30 shows the modulator output pulse with a 21.4 kHz to 23.0 kHz frequency sweep.

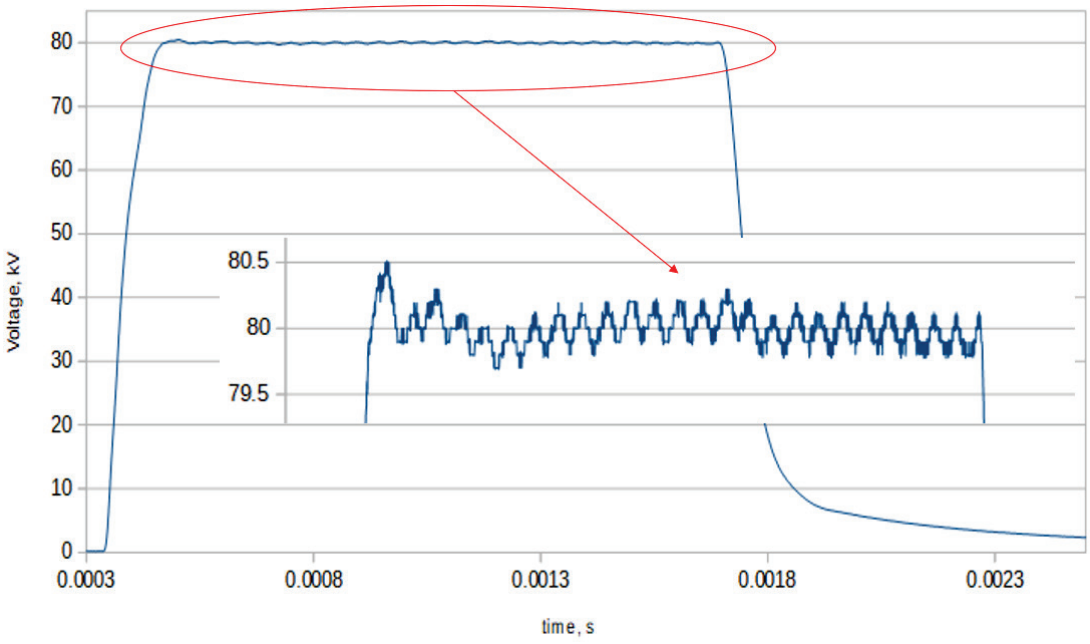

Figure 4.30. ModV pulse performance for 21.4 kHz to 23.0 kHz frequency sweep.

To meet PPU ripple and transient specifications, additional electrical components were incorporated in the design. Freewheel diodes, across each of the six resonant capacitor banks, were added to provide an initial charging condition (of zero volts) on each capacitive element. A filter capacitor, in parallel with the series-connected resonant capacitors, was added to attenuate voltage transients propagating during the macropulse. The AT-HVCM output ripple was determined to be ~300 Vp-p (0.4%); combined with the flatness shown in Figure 4.30, it meets the 1% ripple and flatness specification for the complete 1.35 ms

pulse duration. No large voltage deviations, which can cause issues with klystron and LLRF performance, are evident at turn on.

Pulse reproducablility was determined from data collected over a 3 day period, sampled at a single point during each pulse. The mean of 26,000 modulator voltage measurements, shown in Figure 4.31, was 81.17 kV with a standard deviation σ of 32V (0.039%). A 30 day thermal run at full PPU loading was undertaken using the original 1.5 hp pump, with overall oil flow being limited to 30 gpm. Thermal data, from infrared thermocouples connected to the major components (transformer assembly, rectifer, resonant capacitors, freewheel diode) within the tank basket, were collected during the run period and are displayed in Figure 4.32.

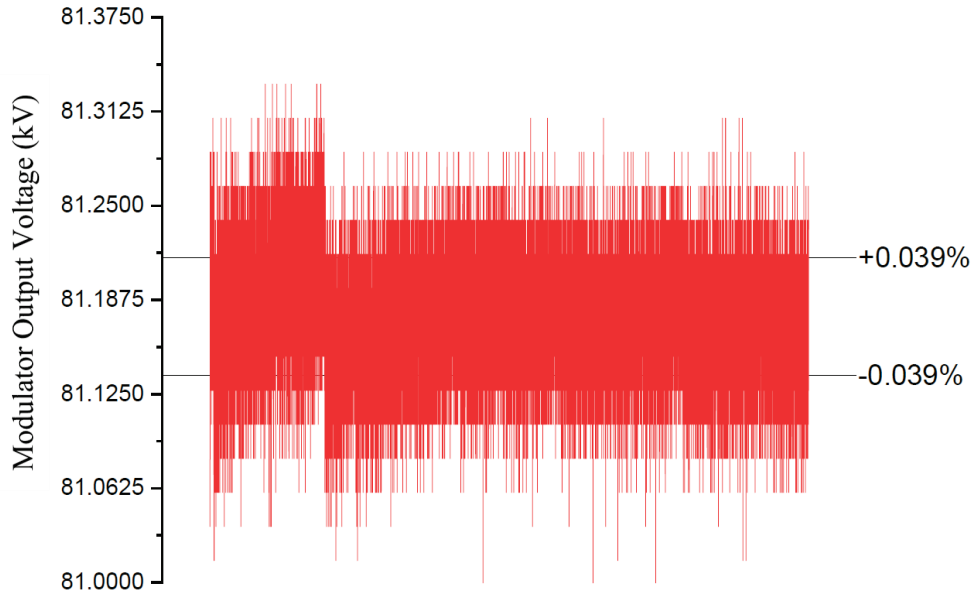

Figure 4.31. Measured modulator output voltage taken from a single point in the output pulse over 26,000 shots. A standard deviation of 32 V is shown, and measurement bit error can be seen from the 14-bit ADC accuracy.

Spark gap testing of the final AT-HVCM output configuration was conducted with 2 inch lengths of various AWG wires series connected to a spark gap. Calculations based on vaporization of a 36 AWG test wire at 70.6 kV concluded the energy delivered to the test wire was 3.1 J, well below the 20 J klystron manufacturer's limit.

All of the AT-HVCM drawings have been combined with the SNS-LINAC Production RF Power Systems HVCM drawing tree. Where feasible, original Los Alamos National Laboratory (LANL) drawings are used. Drawings that were updated from the original LANL package at Oak Ridge are also used. Design features that are unique to the AT-HVCM were produced for fabrication and possess the drawing number suffix "CXXX"; "XXX" is a number representing the major subassembly with which the drawing is associated.

A laminate bus, produced to ORNL specifications by Mersen, is a low-impedance ring bus where the modulator currents from three switch plates are superimposed, in an interleaved return, positive, negative, positive, negative six-conductor structure. Vertical bus stubs connect the laminate bus to each of the three IGBT H-bridge switch plates, as shown in Figure 4.33. Tests conducted on HVCM and AT-HVCM systems indicate the laminate bus assembly provides an order-of-magnitude improvement in bus ripple compared with the existing cable header system, as shown in Figure 4.34.

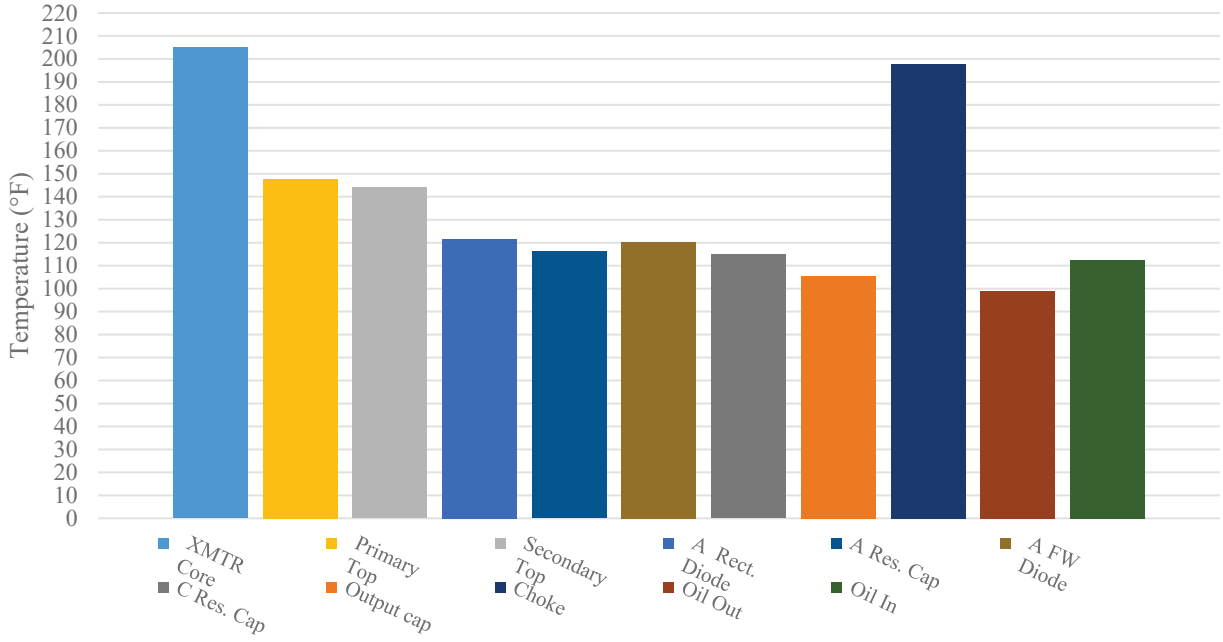

Figure 4.32. Thermal data taken from major components in the oil-filled high voltage tank at thermal equilibrium.

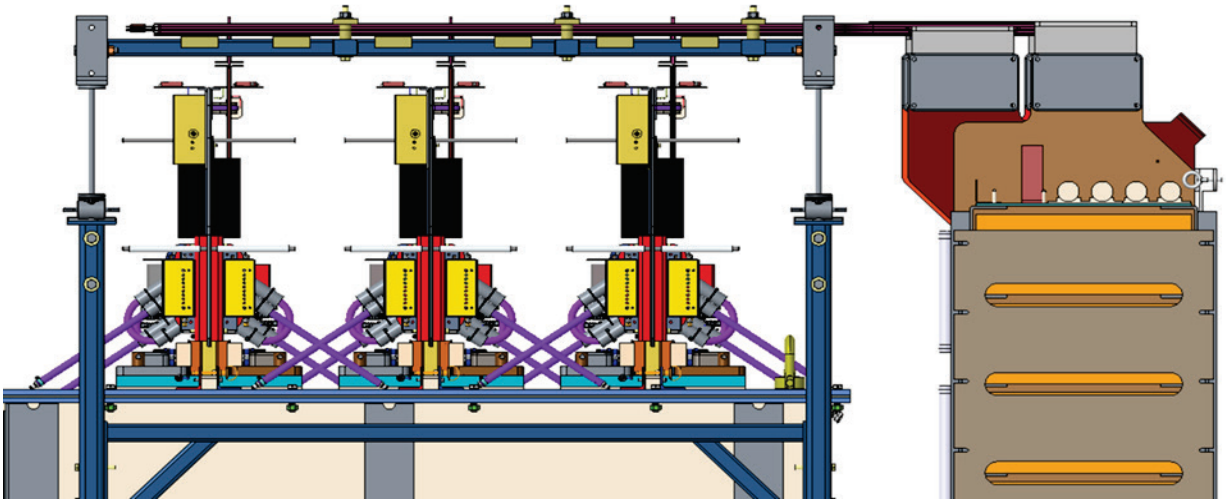

Figure 4.33. CAD model showing section through the safety enclosure.

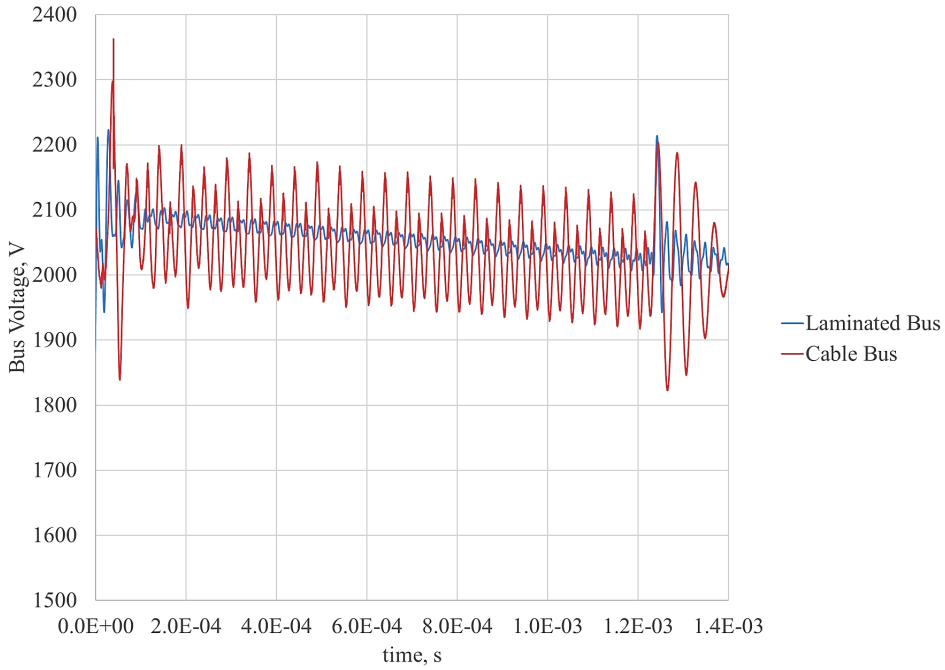

Figure 4.34. Comparison of DC bus ripple on the AT-HVCM laminated bus vs. the traditional cable bus used on orignal HVCM systems.

A tank aligment system, shown in Figure 4.35, was developed to ensure all elements of the energy delivery system, the modulator tank, switch plates, laminate bus and capacitor banks, are properly aligned. This ensures that during maintenance activities, tanks can be interchangibly installed in multiple locations without interference. It also aids in ensuring IGBT H-bridge switch plates align properly with the laminated bus and tank features, thereby reducing mean time to repair.

The secondary AT-HVCM HV components mounted in the oil-filled high-voltage tank are illustrated in Figure 4.36, along with the rectifier and resonant capacitor assemblies that are unique to the AT-HVCM design. The resonant capacitor bank assembly was redesigned to incorporate a freewheel diode across each bank and to facilitate assembly and simplify wiring connections to the transformer and diode rectifier assembly. The rectifier assembly was redesigned to accommodate connectorized rectifier cards that are guided into mating connectors with custom-designed buswork. In addition to alleviating maintenance and serviceability concerns, the connectorized system ensures rectifier cards can be installed only in the correct electrical configuration.

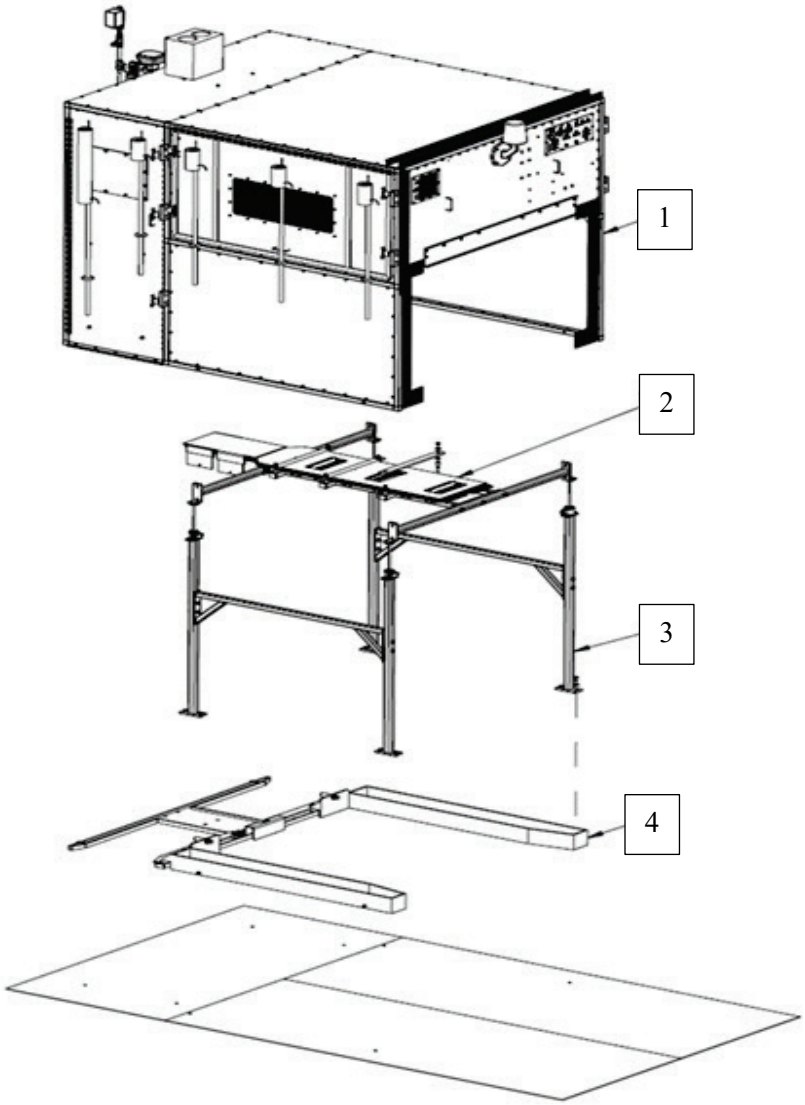

Figure 4.35. The tank alignment assembly showing (1) the safety enclosure assembly, (2) laminated bus, (3) support structure, and (4) alignment fixture.

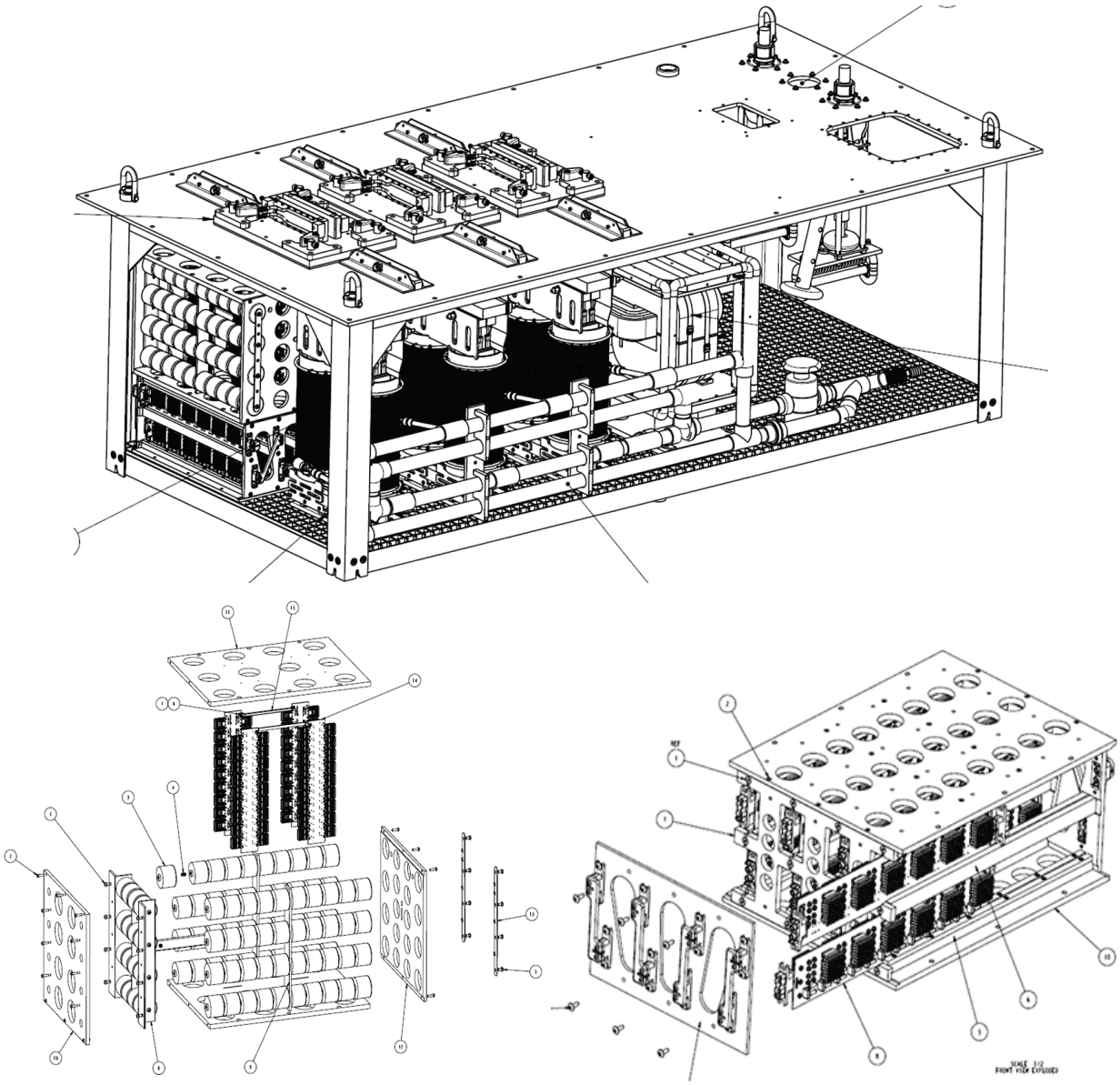

Figure 4.36. Components mounted in the oil-filled high voltage tank shown in the upper view. Exploded views of the resonant capacitor assembly and rectfier assemblies are shown on the left and right, respectively, in the lower view.

New SCL modulator controls

Although the proposed control system is virtually identical to the upgraded units used on the currently installed operational modulators, the original manufacturer of most of the custom hardware has gone out of business; and some of the National Instruments PXI FlexRIO modules are nearing obsolescence. To address these issues, ORNL staff reviewed the original custom hardware vendor drawings and created a complete new set of ORNL-issued drawings. During this process, component obsolescence issues were addressed, new printed circuit board (PCB) Gerber files were obtained from the original vendor and enhancements were incorporated into the design. Working with a local vendor, the custom hardware was ordered to support installation of a new modulator system to support testing of RF equipment for the PPU project. This acquisition was successful, and the intent is to use the same vendor to purchase three sets of additional custom hardware for installation of the three new modulator systems.

As a result of product maturity and the market demanding more capability from modern FlexRIO modules, there was no direct swappable replacement available for the FPGA module used in the original controller design. Two modules, NI 5751, now replace the original unit, as shown in Figure 4.37. The PXI crate has sufficient space for a second module, the backplane is compatible with the module, and the second module overcomes capacity limitations present in the original module. The remaining National Instruments hardware is identical to the original or uses an upgraded version that is backward-compatible with the original system.

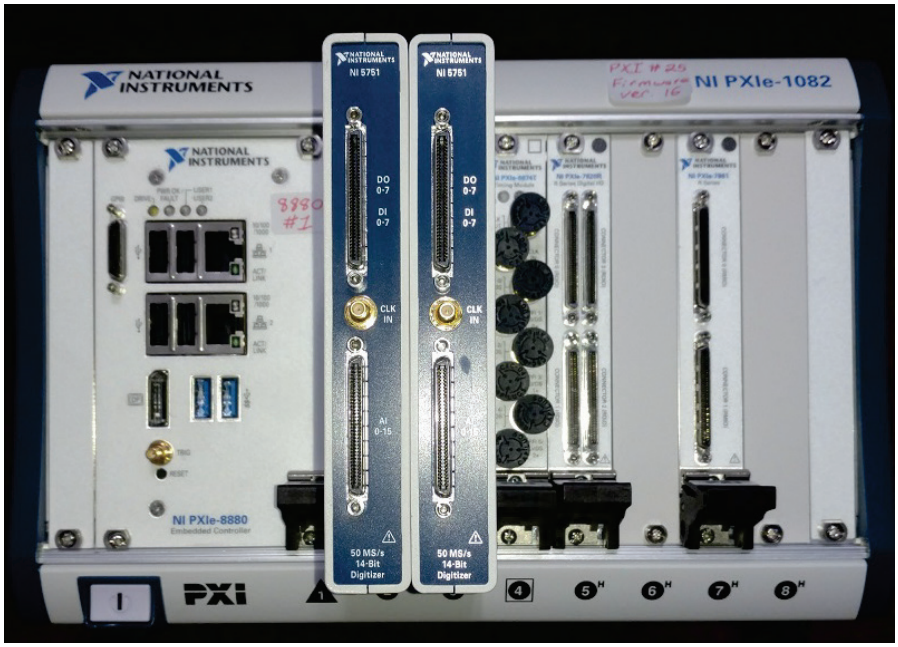

Figure 4.37. The new National Instruments NI 5751 FPGA modules replace the obsolete module and offer additional I/O and enhanced functionality.

The use of dual FPGA modules to replace the original unit forced a redesign of the auxiliary I/O module and the digital interface module. The digital interface module was an evolution from the original ORNL design. The auxiliary I/O module for the updated system had changed enough that a new design was required. Both designs have been prototyped and passed initial tests as of April 2020; the auxiliary I/O prototype PCB is shown in Figure 4.38. The LabView software is also being modified to be compatible with the new hardware. Additionally, as a result of more I/O channels being available on the dual FPGA modules, it is possible to accommodate future upgrades.

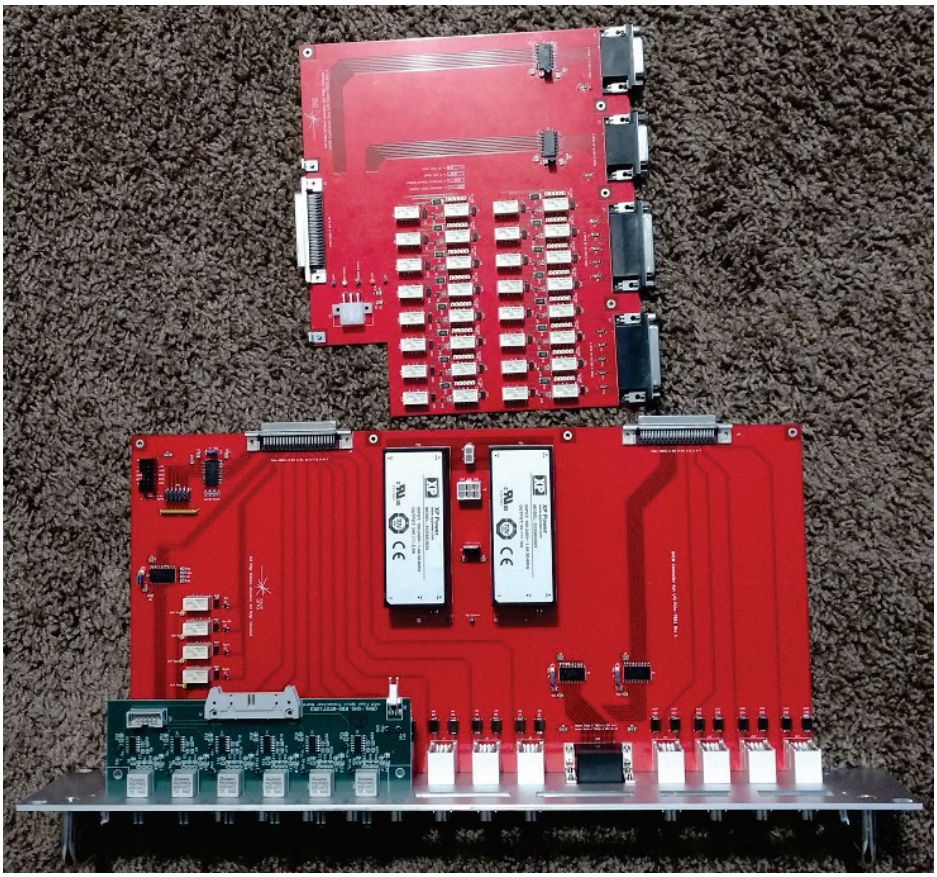

Figure 4.38. Fully assembled prototype auxiliary input/output PCBs ready for integrated testing.

4.3.4.3 SCL Modulator Systems Risks and Contingencies

The risks for the current SCL systems are minimal, as the only real requirement is to increase the operating voltage. Should extended reliability tests uncover issues, a similar approach to what is proposed for the new SCL modulators can be employed.

The prototype development activities undertaken to date on the AT-HVCM, the current baseline design for the three new modulators for PPU, suggest that the risks are low, with several thousand operational hours demonstrated in the HEBT test stand with a CPI beam stick load. Two continuous 30 day runs were conducted before the final design review held in May 2019, and the system has been in virtually continuous operation since that time to further characterize system reliability. As of April 2020, no failures have occurred during operation of the AT-HVCM system.

4.3.4.4 SCL Modulator Systems Spares

Spares are not an issue for the current SCL HVCMs. Sufficient spares are already on hand and are restocked when inventory runs low. Most of the AT-HVCM systems use identical components to those currently installed in existing HVCM systems. The components that are unique to the AT-HVCM—mainly the IGBT H-bridge switch plates, transformers, transformer bus headers, laminated bus, rectifier assemblies, and resonant capacitor assemblies—will be stocked at sufficient levels to support continuous operation of the three new SCL modulators. Furthermore, a complete tested tank assembly will be procured and serve as a “hot” spare should an in-tank component failure occur during operation.

4.3.4.5 Acquisition Strategy for the new AT-HVCM SCL Modulators

The proposed acquisition strategy is similar to that employed during initial construction of the SNS. Four major procurement packages will be generated for the four major subsystems associated with the modulator: the outside 13.8 kV: 2100 V transformer, the SCR controller, the AT-HVCM, and the controls electronics. Since the outside transformer and the SCR controller requirements are identical to those currently in use in the other 17 modulators, they will be procured via a sole source procurement from the original vendor. This will minimize the spare parts needed and minimize the amount of additional training of operations staff to operate and maintain these systems. Procurement documentation has been modified to incorporate some of the upgrades made to these systems over the decade of SNS operation, and one transformer and SCR power supply were pending delivery to the SNS as of April 2020.

The AT-HVCM systems will be purchased as a build-to-print subcontract. Since the SNS has a complete set of drawings for the design and associated 3-dimensional Creo and .stp files, the build-to-print contract should be straightforward. Vendors have been selected which possess experience building similar systems to permit incorporating changes, based on their experience, as appropriate. To achieve economies of scale and ensure the success of the vendor fabrication, options for spare parts—including a full modulator system—and full-power system testing will be solicited during the procurement cycle.

Controls electronics will be procured and assembled in-house, except for the control rack, power distribution chassis, and personal protection interface chassis. SNS employees developed the control system and have significant experience in procuring, assembling, testing and installing the system. Since most parts are off-the-shelf or simple custom assemblies, the risk of doing this work in-house is very low.

4.3.4.6 Quality Assurance Plan for the New AT-HVCM SCL Modulators

A full fabrication and assembly documentation package has been modified and improved to ensure a successful product is delivered. In addition to creating as-built drawings of the system, industry standards, assembly procedures, component specifications, subassembly and assembly test procedures, acceptance criteria, and other quality documentation will be created and incorporated into the Statement of Work. ISO 9001–certified companies will be used whenever possible; or, if quality vendors are selected who are not certified, a thorough review by the SNS quality assurance representative shall be conducted before awarding the contract.

As experience with the original construction of SNS has revealed, to obtain a quality product, it is imperative to work closely with the vendor manufacturing the system, especially in the case of a build-to-print subcontract. It is anticipated that an engineer will need to spend approximately 30% of their time at the vendor's facility while assembly and testing are occurring. More time will likely be required during factory acceptance testing.

Before the award of a subcontract, each company will be evaluated based on an inspection and visit before being considered for the preferred vendors list. Each company's manufacturing capabilities, staff competency, internal quality assurance plans, and infrastructure will be assessed.

A rigorous subcontract evaluation criteria document will be generated before the release of the request for quotation, and a committee will be selected to evaluate all bids. Weighting of criteria will focus more on technical aspects of the work and less on price to ensure a high-quality product and best value procurement.

4.4 KLYSTRON GALLERY UTILITIES

4.4.1 New SCL RF Cooling System

A new Klystron Gallery cooling system (KL-06) shall be provided for the cooling of the RF and modulator equipment that will be added to the open east end of the Klystron Gallery. The new RF system components that require water cooling include 5 separate TRCCs that measure and distribute water to 28 circulators, 28 water loads, and 28 klystrons. The three new HVCMs and three new SCR cabinets will also require water cooling. The new cooling pumps, heat exchanger, and all major pump room equipment will be the identical manufacturer, model, and size as the existing SCL cooling systems KL-02 and KL-03.

Figure 4.39 shows the layout for the KL-06 cooling system in Building 8300, Sector G4. Conventional facilities (CF; WBS P.6.2.1) will provide the new building addition and area utilities. The new cooling system and all associated piping are included within this task.

The KL-06 system will provide 1500 gpm of 92 F DI water at 105 psig to remove 2700 kW of heat from the new technical equipment during peak operation. This will require 800 GPM of site cooling water at 80°F. The design basis for the new KL-06 cooling system is presented in Table 4.16. System flows were determined based on a hydraulic model of the new KL-06 piping system; Reference Document *PPUP-307-DA001 KL-06 Hydraulic Modeling.* System heat loads are based on maximum heat rejection scenarios that occur when the klystrons are operating in diode mode;*, Reference Document PPUP-307-DA002 Klystron Gallery DI Water Heat Loads for PPU.*

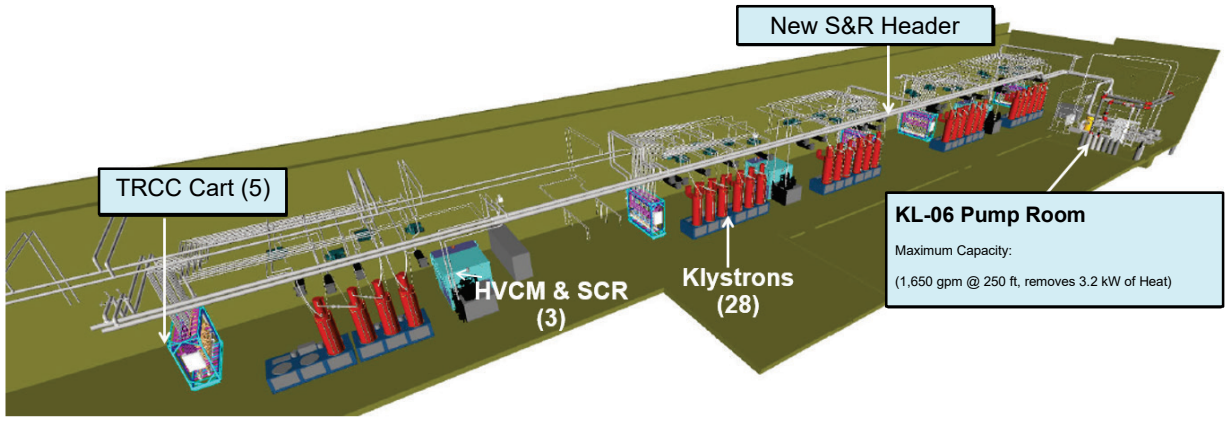

Figure 4.39. KL-06 SCL RF cooling system layout.

Table 4.17. Design basis for new KL-06 cooling system.

Technical component (TC)	HVCM			Klystrons		RF equipment		KL-06 totals
	IGBT	Oil heat exchanger	SCR	Coll.	Bodies	Circ.	Loads	
Required heat removal, kW/TC	32.0	32.0	23.0	77.8	5.5	0.5	0	
Required heat removal, kW/circuit	32.0	32.3	23.0	233.5	5.5	1.0	0	
TC water flow rate, GPM	34.0	34.0	12.0	64.0	7.0	10.0	33	
Number of TC	3.0	3.0	3.0	28.0	28.0	28.0	28	
Number of TC/circuits	3.0	3.0	3.0	10.0	28.0	14.0	10	
Total heat load, kW	96.0	96.9	69.0	2335.0	154.0	14.0	0	**2,764**
Total flow, GPM	102.0	102.0	36.0	640.0	196.0	140.0	330	**1,546**
Water inlet temp, °F	92.0	92.0	92.0	92.0	92.0	92.0	92	92
Temperature rise,°F	6.4	6.5	13.1	24.9	5.4	0.7	0	12.2
TC press drop, psid/unit				11.0	15.5	38.0	30	
TC water volume, FT3	0.37	1.0	0.061	0.1	0.03	0.007	2.85	
Connection size, inches	1.5	1.5	1.0	2.0	1.0	1.0	2	
Operating pressure, PSIG	105.0	105.0	105.0	105.0	105.0	105.0	105	
Maximum design pressure (MAWP), psig	150.0	150.0	150.0	150.0	150.0	150.0	150	

TC = technical component.
PSID = pounds per square inch, differential.
PSIG = pounds per square inch, gauge.
MAWP = maximum allowable working pressure.

4.4.2 Existing SCL RF Cooling Systems

The existing SCL RF cooling systems (KL-02 and KL-03) have adequate cooling capacity for the additional PPU heat loads. No changes are required, according to *PPUP-307-DA002 Klystron Gallery DI Water Heat Loads for PPU.*

4.4.3 Existing DTL RF Cooling System

The existing DTL DI water cooling system (KL-04) pumps must be upsized primarily to accommodate increased flow rate requirements for the three new 3.0 MW klystrons being added in the DTL. Although the current heat exchanger has adequate thermal capacity for PPU power levels, the pumps are too small to deliver the flow required. The KL-04 deionized (DI) water system provides cooling water for the RFQ and DTL TRCC skids, which cool the klystron collectors, bodies, circulators, HVCMs, and SCRs, as well as the Front-End Building equipment.

The DI water pumps are currently running over their rated capacities. The system is designed for single-pump operation with an installed spare, but currently both pumps are run in parallel to achieve the design flow rate without negatively affecting pump reliability. Larger pumps are needed, along with larger motors and associated electrical feeders to accommodate the additional PPU flow requirements.

The new pumps will require that the motor horsepower be increased from 100 to 150 hp. The associated motor control center breakers, wiring, and variable-frequency drives must be replaced with higher-capacity electrical components. The existing steel pump decks will be replaced with conventional

concrete foundations to accommodate the larger motor bases and minimize vibration. The new pumps will be Goulds 3196 size 4×6-17, identical to the other existing cooling pumps in the Klystron Gallery.

The upgraded pumps will deliver 1117 gpm of 92°F DI water at 105 psig to remove 2862 kW of heat from the DTL RF equipment and the front-end equipment. This will require 900 GPM of 80°F site cooling water during peak operation. System flows were determined based on a hydraulic model of the KL-04 piping system; *Reference Document PPUP-307-DA0005 KL-04 Cooling Loop Flow Scoping Calculations.* System heat loads are based on maximum heat rejection scenarios, which occur when the klystrons are operating in diode mode; *Reference Document PPUP-307-DA002 Klystron Gallery DI Water Heat Loads for PPU.*

4.4.4 Front End Building Cooling

A new Front End Building cooling system will not be required. The upsized KL-04 pumps in the DTL will have adequate capacity to continue to cool the Front-End Building equipment, as well as all of the RF equipment in the DTL at PPU power levels.

4.4.5 Existing CCL RF Cooling System

The existing CCL klystron cooling system (KL-01) has adequate cooling capacity for the additional PPU heat loads. No changes are required, according to *PPUP-307-DA002 Klystron Gallery DI Water Heat Loads for PPU.*

4.4.6 Existing Electrical Utilities and Technical Equipment Cabling

The existing AC power distribution in the Klystron Gallery will be the model for the installation of the new equipment needed to support the PPU project. In general, AC power for the technical equipment is distributed from an existing exterior pad-mounted substation (KL-SS4) that provides approximately 2000 A at 480 Vac per unit. The 480 Vac is terminated into multiple distribution or “DP” panels located on the south wall of the Klystron Gallery. Multiple power panels designated “PP,” and lighting panels, designated “LP,” are distributed out of the distribution panels. The power panel distribution is routed through 45–75 kVA transformers that step the voltage down from 480 to 208/120 Vac. The technical loads are then fed from the power panel circuits. In addition, some generator and uninterruptible power supply (UPS) –backed power panels, designated “UP,” support critical accelerator loads. The UPS will be backed up by an existing ATS emergency generator system. More details are provided in Cannon Design drawings CF-E0502 and CF-E0602.

For the AC power distribution, the cable installation for the technical equipment controls and instrumentation will be modeled on the existing infrastructure. All of the cables necessary for the operation of the five transmitters and seven cryomodules are included in the scope of work and are described in more detail in the following sections.

4.4.6.1 New PPU Loads

As mentioned earlier, the new electrical loads for the PPU project include three new HVCMs, five new RF transmitters, seven cryomodules, and other support equipment such as cooling skids and cryomodule controls. Building loads such as heating, ventilation, and air-conditioning systems; utility outlets; and lighting will be installed by CF electrical personnel. Only technical loads are covered in this report. The design distributes all AC power from the existing KL-SS4 substation.

Power requirements for the technical equipment are listed in Table 4.17.

Table 4.18. Technical equipment power requirements.

Equipment	Power (kVA)	Voltage (V)	Comments
HVCM	2700	13,800	Power supply by others
HPRF transmitters	270	208	
Cryo-controls	48	120	
LLRF	115	120	
HVCM controls	7	208	
Integrated Control System controls	10	120	
Vacuum	5	120	
SCL cooling upgrade	250	480	

4.4.6.2 Electrical Equipment

The design includes the installation and use of the power panels listed in Table 4.18.

Table 4.19. Additional power panels for PPU.

Panel designation	KVA	Circuit use
KL-4PP10	3.5	Power for outdoor transformer and Sector 11 exhaust fan
KL-4PP11	78.6	Power for cryo-controls, modulator controls, RF controls, HPRF transmitter, reference line heater
KL-4PP12	5.1	Power for cryo-controls, modulator controls, RF controls, HPRF transmitter
KL-4PP18	15.8	Power for subpanels KL-4PP10, Kl-4PP12, KL4-PP14
KL-4DP7	500	Power for 208 V transformers, KL-06 pump room and air handler
KL-4PP13	66.0	Power for cryo-controls, LLRF, RF controls, HPRF transmitter, vacuum system
KL-4PP14	7.1	Power for LLRF, HPRF transmitter, reference line heater, vacuum system
KL-4PP15	68.2	Power for LLRF, HPRF transmitter, reference line heater, vacuum system
KL-4UEP6	59.4	Uninterruptible power for the vacuum system and cryo-controls

The PPU scope includes the installation of four 120 V, 20 A utility receptacles along the base of each new rack row. The Klystron Gallery CF scope includes the continuation of the main cable tray “ring” in the Klystron Gallery (Figure 4.40). The cable tray from the main ring to the racks, tunnel chases, and other technical equipment will be designed and installed as part of the technical utilities scope. In addition, the scope will include any miscellaneous conduit or other raceway necessary to support the PPU cables.

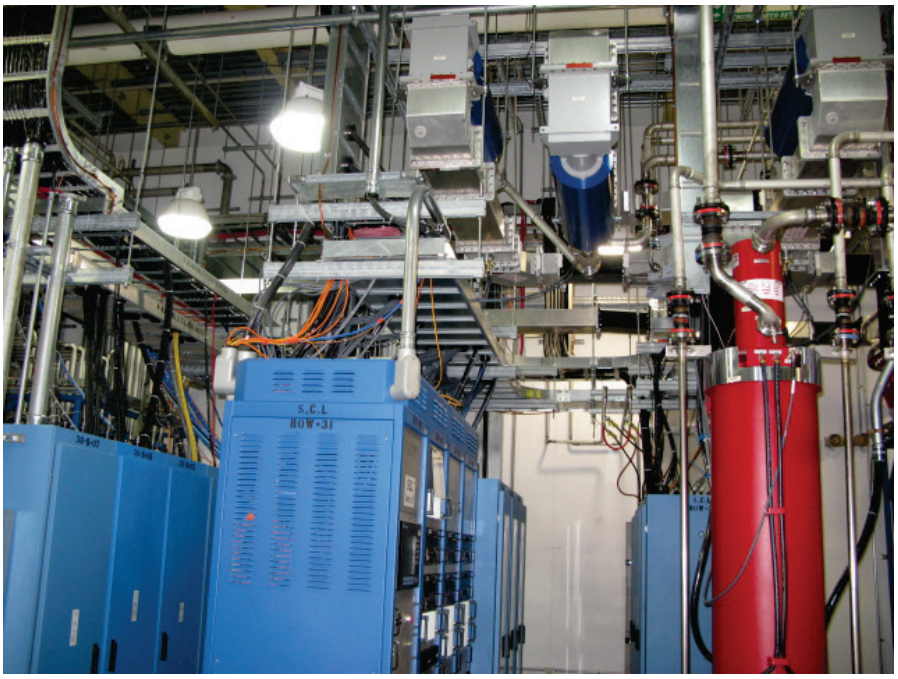

Figure 4.40. Existing cable tray in the Klystron Gallery.

4.4.6.3 Electrical Grounding and Cables

The PPU project will install the new low-impedance ground plane necessary for the five new RF transmitters and associated three new HVCMs. The design includes approximately 300 ft of 12 in. wide copper plane for the main trunk and 250 ft of 8 in. wide copper plane for the branches. The copper plane will be riveted flat to the concrete floor, as indicated in Figure 4.41.

Figure 4.41. Existing ground-plane installation in the Klystron Gallery.

The PPU project will install bare copper grounding conductors on all raceways, power panels, equipment racks, and other equipment enclosures. The scope of work for the SCL electrical utilities includes the

routing and termination of all technical equipment cables. These include cables that route from the gallery into the tunnel. A primary, but not exhaustive, list of the cables for each major subsystem is in Table 4.19.

Table 4.20. Description of cable requirements for PPU electrical systems.

System name	Cable type	Description
HVCM	Okoguard, 3-conductor, 500 kcmils	Armored power cable from outdoor switchgear to the SCR cabinet
	Single conductor 4/0	From the SCR cabinet to the modulator
	Multi-conductor #10, #12 and #14 AWG	From the modulator controls cabinet to the switchgear, HVCM, and SCR cabinet
	Paired cable, #18 AWG	From the HVCM to the CO_2 system
	#10, #12 and #14 power cables	From the HVCM to CO^2 system, SCR cabinet, and HVCM for control, ancillary and pump power
	Coaxial and triaxial cable	Diagnostic and signal cables from HVCM to controls cabinet
	Fiber optic	From HVCM to controls cabinet, from HPRF transmitters to HVCM, from timing master to HVCM
	Dielectric Sciences 2042TVJ	High voltage cable from HVCM to HPRF transmitters
	Ethernet cable	From HVCM controls cabinet to accelerator network
HPRF Transmitters	3/8 in. Heliax	From transmitter rack to RF coupler outputs and LLRF racks
	High-voltage (HV) coaxial	From transmitter rack to klystron ion pumps
	Multi-conductor #14 and #10 AWG	From transmitter rack to the klystron HV tank electromagnetic interference (EMI) enclosure
	Multi-conductor #2 AWG	From transmitter rack to the klystron magnet
	Vendor cable	From the transmitter rack to the waveguide circulator
	Fiber optic	From the LLRF racks to arc detector ports and HV tank EMI enclosure
	Fiber optic	From the LLRF racks to arc detector ports and HV tank EMI enclosure
LLRF	3/8 in. Heliax	From LLRF racks to the solid state amplifier input, RF coupler outputs, higher-order mode couplers, field control module field probes, high-power protection module, field probes reference line, and local oscillators
	Fiber optical	From LLRF racks to the window arc detectors
Integrated Control System controls	Twin-axial cable	For event utility links
	RS-232	For SCL controls to cryo-controls
	Belden 9512	For fast protection links
	Belden 9512	For fast-protection links
Personnel Protection System (PPS)	Multi-conductor #16 AWG	For SCR and HPRF PPS connections
Vacuum		
	HV coaxial	For vacuum gauge connections
	Belden 8219	For vacuum valves
	Belden 9318	For vacuum controls
	Belden 9512	For vacuum controls
	Belden 9344	For vacuum controls
Cryogenic Controls		
	1-pair #16 AWG	For the tuner cooling flow switches
	2-pair #20 AWG	For the liquid helium level probes
	4-pair #16 AWG	For the cavity and window heaters and signal trunk cables
	4-pair #22 AWG	For JT valve linear variable differential transformer connections

Table 4.19. Description of cable requirements for PPU electrical systems (continued).

System name	Cable type	Description
	16-pair #20 AWG	For the silicone diodes
	8-pair #20 AWG	For the silicone diodes and thermocouples
	4-pair #22 AWG	For signal trunk
	Coaxial cable	For ControlNet
Cooling Systems		
	Commscope 5070	For PLC (programmable logic controller) communication
	Belden 1032A	For instrumentation to PLC I/O
	Belden 9368	For instrumentation to PLC I/O
	Belden 27110A	For PLC AC power

4.4.7 RF Waveguide Chases

Twelve new chase assemblies have been installed to route all cabling and RF waveguides from the Klystron Galley to the linac tunnel. The chase assemblies were modified slightly from the original design for ease of installation; conduit designations remain the same as the original design. Figure 4.42 shows the 12 penetrations that received new chase assemblies (shown in gray). Cryomodules 24 and 26 are not being installed, so no chase assemblies are required in those penetrations (94, 95, 98, and 99), the chase 102s assembly is already in place, and the first article of chase number 105 has been installed (summer 2015).

The 12 new chase inserts have been pre-installed before the RF equipment is installed in the Klystron Gallery and will permit existing chase wiring to be re-pulled into the new chase conduits.

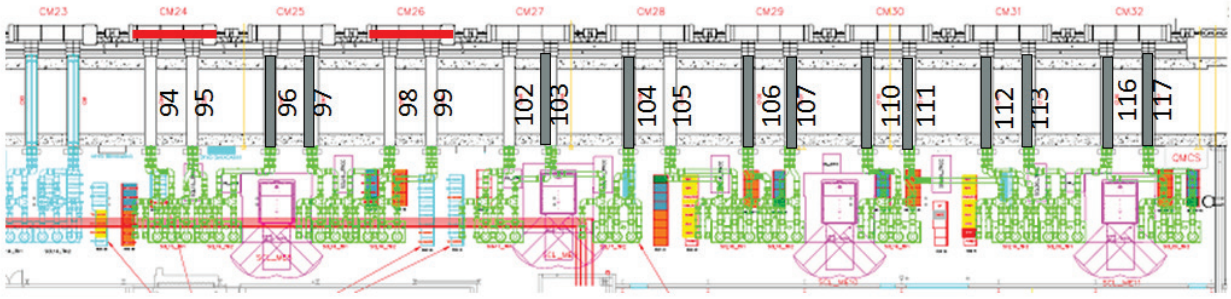

Figure 4.42. Chase assembly penetrations.

4.5 RF CONTROLS

Controls provided for the linac RF include the following:

- EPICS interface to the new HVCMs and supporting IOC hardware.
- Software interfaces to the new RF transmitters. Updates will be required to accommodate the new cryomodule cavity tuner, coupler bias, and coupler cooling control system design. This covers the IOC hardware, PLC, ladder logic, and EPICS software development.
- EPICS interface to the new LLRF systems.

- SCL cavity tuner motor controls will require a new design, as obsolescence prevents duplicating our current controller implementation. A PLC-based commercial-off-the-shelf hardware solution is under consideration.

- SCL coupler bias power supply controls.

- SCL coupler cooling water controls will also require a new design, as obsolescence prevents duplicating our current controller implementation. A PLC-based commercial-off-the-shelf hardware solution is under consideration.

4.6 GLOBAL CONTROLS

The SNS Integrated Control System (ICS) is a large distributed control system based on the EPICS toolkit. The ICS serves to integrate a diverse array of hardware to allow operators to control the accelerator using a common set of tools. The architecture is scalable, allowing new devices for the PPU to be integrated without changes to the underlying ICS architecture. For the PPU, global controls include four systems: Controls Infrastructure, Timing System, Machine Protection System (MPS), and Personnel Protection System (PPS). These systems will be extended to support the areas where PPU equipment will be installed.

Additionally, controls hardware and software will need to be developed for each new PPU system (e.g., cryomodule, RF, CF, target). In general, these subsystems will be controlled in a similar manner to the corresponding systems already operating at the SNS. These applications typically include commercial-off-the-shelf hardware and application software developed locally. Details for control of these devices are included in the chapter for the corresponding system.

4.6.1 Controls Infrastructure

The controls infrastructure includes the private network, which facilitates moving data among the various computers, servers, and workstations that store data and serve files to distributed processors and operator workstations. The ICS network will be extended to accommodate new equipment for the SCL extension. Network specifications for new equipment are the same as for equivalent existing operational equipment. The existing server infrastructure is sufficient to handle the expected additional computational load for the PPU.

Changes and additions to the network will include the following:

- “Edge switches” will be placed in the new rack rows housing PPU accelerator equipment at the east end of the Klystron Gallery.

- Some existing switches will require replacement to provide additional network ports to accommodate new equipment.

- An “aggregator switch” will be added to communication room 6 in the Klystron Gallery to accommodate the addition of the edge switches.

No changes to the SNS Central Control Room are anticipated for the PPU. The existing SNS suite of operator interface tools, based on EPICS and Control System Studio, will continue to be used for the PPU. These tools will be configured to include the new components added by the PPU.

4.6.2 Timing System

The PPU timing requirements will be handled by extending the existing SNS timing system infrastructure. Timing system equipment required for the PPU includes local timing receiver boards, timing link fan-outs, and distribution panels to extend the system to the newly populated SCL zones. The timing specifications are unchanged for the PPU, and there are no anticipated changes to the timing master, event link, or real time data link. EPICS interface software changes will be required to support the IOCs and timing hardware in the additional zones.

4.6.3 Machine Protection System

The MPS, which quickly turns off the beam if a beam loss event occurs, meets the functional requirements for the PPU. However, SNS staff can no longer manufacture the MPS custom hardware boards needed to support the expansion of RF equipment into the additional zones because of obsolescence. Redesign of the obsolete boards will be addressed by MPS AIP-39 starting in FY 2017, so SNS expects to be able to produce the needed board equivalents in time to meet PPU milestones. EPICS interface software changes will be required to support the additional MPS hardware installations.

4.6.4 Personnel Protection Systems

Safety systems include credited and defense-in-depth controls with the primary function of mitigating postulated accident scenarios that could otherwise result in harm to people or the environment. Hazards and accident scenarios will be addressed throughout the project, culminating in major revisions to the Proton and Neutron Facility Safety Assessment Documents (FSADs). The revised FSADs will describe the credited controls, including protection systems that form the basis for a new accelerator safety envelope. The FSADs are the primary drivers for safety system performance requirements.

The PPU project will include modifications to the accelerator PPS to accommodate the energy upgrade as well as to integrate new requirements to support the RTST tunnel stub. The new safety systems will be functional duplicates of the existing accelerator PPS.

The primary function of safety systems is mitigation of significant hazards addressed through DOE Order 420.2C, and the associated guidance 420.2A [15,16]. Critical devices are used to prevent beam transport to an area that is not in a safe configuration.

The safety system scope and deliverables include the following:

- System level operation, certification, and maintenance documentation
- Safety-system–specific, system-level networking and interconnection infrastructure
- Hardware/software required to interface the PPS systems to EPICS, e.g., “mail-box” PLC
- Safety-system–specific EPICS screens and archiver functions

4.6.4.1 Assumptions

- Accelerator Safety Order–related activities such as the FSAD and the Accelerator Safety Envelope development are outside the scope of the protection system work section.

- Ring to target beam transport line (RTBT) 2 will be accessible only when RTBT1 is in an access state.

- The FTS target will not be damaged by a minimum of two consecutive pulses or 2 seconds at 2.5 MW.

- Existing EPICS IOC(s) will be used for data collection and archiving.

- This work involves only the linac PPS and the new RF systems in the Klystron Gallery.

4.6.5 Linac Cryomodule Controls

Controls for the new PPU cryomodule will closely resemble the existing high-beta cryomodule controls. Changes will be required to accommodate silicon diode connections used in the updated cryomodule design. The major design change for the cryomodule controls is centered around the beamline interface and the wiring.

The PPU cryogenic control system includes equipment racks, PLC hardware, IOC hardware, level meters, pressure sensors, power supplies, and marshaling panels. It does not include valves, temperature sensors, heater elements, liquid helium level probe, connectors and wiring attached to the cryomodule, vacuum gauges, or RF instrumentation and wiring.

The cryogenic control systems will, by default, be powered from the UPS. An automatic transfer switch will be installed in each rack group and marshaling panel to provide a connection to “normal” power to ensure continued operation if the UPS circuit loses power. EPICS interface software changes will be required to support the new IOCs and cryomodule interface PLCs.

Because connectors will be installed before the conduit is pulled through, the connector size and number of conductors in a cable are important. Based on past experience, it was determined that the largest particle size for a connector that could be pulled through the conduit would allow the termination of an eight-shielded, twisted-pair cable. This determination changes the number and types of cables to be installed. It also forces the revision of most of the cryomodule control system drawings.

4.6.5.1 Known Issues

The tunnel access time required for cable installation and termination and cryomodule checkout must be greatly reduced from the time required for the original SNS construction. A new approach is proposed for the installation of cryomodule control system tunnel wiring to address this issue.

4.6.6 Linac Water System Controls

EPICS and PLC controls will be provided to control the new DI water system pump loop KL06. The new CF PLC and chassis will be installed in klystron building communication room 6. It will control new pump loop KL06 and new air handler AH-KL-06. Separate I/O panels local to KL06 and AH-KL-6 and the new I/O panels will be connected to the new PLC via Ethernet. EPICS interface software changes will be required to support the new IOC and PLC hardware.

4.6.7 Beamline Vacuum Control System

The beamline vacuum control subsystem provides vacuum controls for the new cryomodules, the warm sections, and the high-energy differential pumping section. These controls are used to monitor and control vacuum components and provide interlock signals to LLRF systems and the MPS. The existing SCL vacuum controls will be duplicated. Replication of the existing controls, PLC hardware, and ladder logic will be provided to monitor and control the new vacuum components along with the corresponding EPICS interface software.

4.6.8 Insulating Vacuum System Controls

The insulating vacuum system controls subsystem provides vacuum controls for pumping the insulating jackets of the cryomodules. The existing insulating vacuum controls for cryomodules 1–16 will be replicated. A typical single SNS insulating vacuum system handles pumping for eight cryomodules. These controls include PLC systems with ladder logic and EPICS interface software.

4.6.9 Ring Primary and Secondary Stripper Foil System Controls

EPICS and PLC controls will be provided to accommodate modifications to the primary and secondary stripper foil mechanism. The existing VME controls hardware is no longer available, so a new motor control design will be required. A PLC-based stepper motor controller is under consideration. The existing Ring Service Building racks will house the new equipment.

4.6.10 Ring Water System Controls

EPICS and PLC controls will be provided to accommodate modifications to the existing DI water system RN03 and implementation of the new DI water system RN04. The existing PLC system will be used to provide the processing capabilities with a new remote I/O panel installed in the Ring Service Building basement.

4.7 INSTALLATION AND INTEGRATION

For the SCL, 28 additional RF systems will be added to the existing systems to power the 28 superconducting accelerating cavities in 7 new cryomodules. For the NCL, three new klystrons rated at 3 MW_{pk} (240 kW_{ave}) necessary to produce the average beam current for the PPU will be installed in the Klystron Gallery at SNS. Additionally, three new circulators to support the new klystrons will replace the existing circulators currently in operation. Waveguide runs based on 3-dimensional model will also be installed in the Klystron Gallery to further aid PPU operations. Three new AT-HVCMs and 28 new LLRF systems are needed to power and control the new RF systems in the SCL. HVCM upgrades are needed in the RFQ, DTL-3, and DTL-5 modulators to support the new 3 MW klystrons.

Coordination of efforts will be required for the installation, testing, and commissioning of the RF systems. Interface Control Documents (ICD) detailing where the interfaces are and who is responsible for the scope of work on each side of the interface will be used to assist the coordination. Additional information can be found in PPUP-300-IC0003, R00, *Interface Control Document for P.3.2 SCL HPRF*; PPUP-303-IC0001, R00, *Interface Control Document for P.3.3 NCL HPRF;* PPUP-300-IC0002, *Interface Control Document for P.3.4 Low Level RF;* PPUP-306-IC0001, *Interface Control Document for P.3.6 New Linac Modulators*.

4.8 REFERENCES

1. M. Lynch, W. Reass, and P. Tallerico, “SNS Linac RF system overview,” *Proceedings of the 1999 Particle Accelerator Conference*, eds. A. Luccio and W. W. MacKay, New York, March 29–April 2, 1999.
2. M. Champion, “SNS RF system performance and operation,” *Proceedings of Particle Accelerator Conference (PAC07)*, ed. C. Petit-Jean-Genaz, Albuquerque, New Mexico, June 25–29, 2007.
3. T. Hardek, M. Crofford, Y. Kang, et al., “Status of the Oak Ridge Spallation Neutron Source (SNS) RF systems,” *Particle Accelerator Conference*, New York, March 28–April 1, 2011.
4. MEGA Industries, *MEGA Industries RF Solutions,* retrieved from Waveguide: http://www.megaind.com/waveguide/, August 3, 2016. Accessed September 2016.

5. *Design Criteria for Linac RF*, SNS-104010000-DC001, Oak Ridge National Laboratory, November 30, 2000.
6. Email correspondence between M. Fitzgerald of Ferrite Microwave and John Moss of Oak Ridge National Laboratory, subject line, DATE.
7. M. Champion et al., "Overview of the Spallation Neutron Source linac low-level RF control system," *Proceedings of the 2005 Particle Accelerator Conference (PAC05)*, Knoxville, Tennessee, May 16–20, 2005.
8. M. Crofford et al., "Spallation Neutron Source LLRF temperature dependence and solution," *LINAC10*, Tsukuba, Japan, September 2010.
9. M. Piller et al., "The Spallation Neutron Source RF reference system," *Proceedings of the 2005 Particle Accelerator Conference (PAC05)*, Knoxville, Tennessee, May 16–20, 2005.
10. W. Reass et al., "High-frequency multimegawatt polyphase resonant power conditioning," *IEEE Transactions on Plasma Science*, **33**(4), 1210–1219 (August 2005).
11. J. Moss, "Proton Power Upgrade (PPU) Project Warm Linac RF Power Margin," ORNL Report PPU-P03-TR0001 (March 2019).
12. G. Patel et al., "Experimental results from droop compensation for the high voltage converter modulators," *IEEE Transactions on Dielectrics and Electrical Insulation*, **20**(4), 1093–1100 (August 2013).
13. D. Solley, "AT-HVCM Final Design Report," ORNL Report PPUP-306-TR0002 (April 2020).
14. D. E. Anderson et al., "Recent developments in the improvement campaign for the high voltage converter modulator at the Spallation Neutron Source," pp. 672–675 in *Proceedings of IEEE International Power Modulator and High Voltage Conference*, Santa Fe, New Mexico, 2014.
15. US Department of Energy, *Safety of Accelerator Facilities*, DOE O 420.2C, Department of Energy, Washington, DC. 2011.
16. US Department of Energy, *Accelerator Facility Safety Implementation Guide for DOE O 420.2C, Safety of Accelerator Facilities*, DOE G 420.2-1A, Department of Energy, Washington, DC, 2014.

5. RING SYSTEMS

Most of the high-energy beam transport (HEBT), ring, and ring-to-target-beam transport (RTBT) were designed to support 1.3 GeV beams. The major exceptions are in the ring injection and extraction areas. Particle tracking simulations and estimates of space charge effects show no issues with beam dynamics for the 2.8 MW, 1.3 GeV case. The following sections describe the modifications to the ring hardware.

5.1 INJECTION REGION

The purpose of the ring injection system is to inject particles from the HEBT into the accumulator ring and transport the waste beams to the ring injection dump. The key components of the injection system are shown in Figure 5.1. Almost all the original beam optics parameters, such as the size of the injection bump, the injected beam spot position, and the injection painting, will be kept the same.

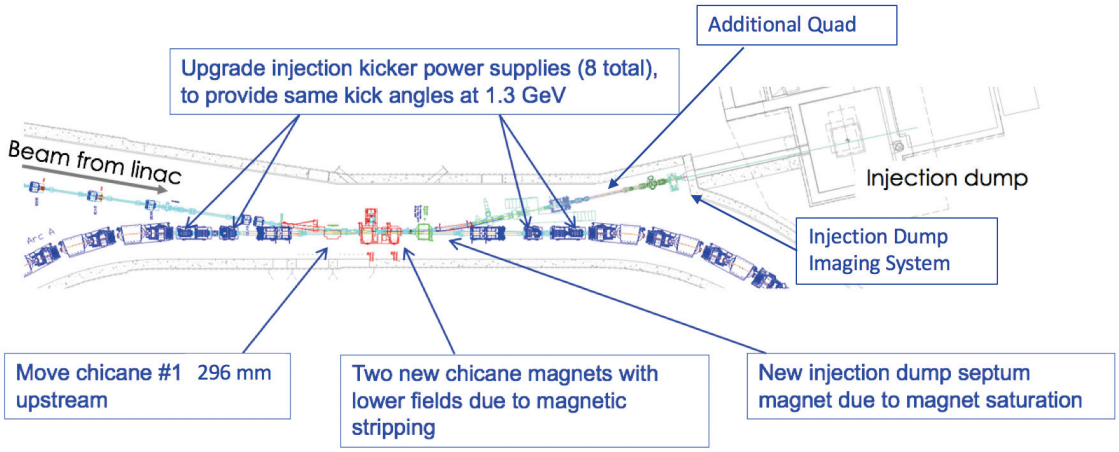

Figure 5.1. Layout of the existing ring injection section with changes indicated.

Chicane magnets. The currents in the middle two injection chicane magnets (DH_A11 and DH_A12) cannot simply be scaled up to accommodate the increased injection energy of 1.3 GeV because this would cause excessive H^- stripping. Therefore, these magnets must be replaced with longer, lower-field magnets. The first chicane magnet (DH_A10) will be moved upstream approximately 30 cm and 5 mm toward the inner wall to create the correct bump size with the new middle chicane magnets, and the fourth chicane magnet (DH_A13) will not be moved.

The two new magnets will have a new design with the coils wrapped around the back leg, reducing the dependence of the field quality on the precise placement of the coils. Physics specifications are shown in Table 5.1 and Table 5.2. A CAD model of the magnets, as last reviewed, is shown in Figure 5.2, pending final changes to the cooling hose and electrical bus. A long lower pole on the second chicane (DH_A11) is necessary to meet the longitudinal field requirement at the foil, which ensures stripped electrons are directed away from the foil. This vertical asymmetry also introduces harmonics that must be corrected. An interesting feature of this particular design is that the two magnet cores are identical, but DH_A12 is flipped vertically relative to the DH_A11 to cancel the harmonics induced by DH_A11. The electrical and cooling connections require some modification to accommodate the core orientation, but this is achieved with minimal hardware added to a base coil design. Because these magnets are in a hot region of the ring that is difficult to access, the PPU requires a full spare magnet, including coils and core. The common core geometry means only one full spare magnet is required. The new design creates larger stray fields than the existing chicane magnets, which are of particular concern for the waste beams downstream of the

chicane. A field clamp has been designed that will help reduce the effect of the stray fields on the waste beams. This C-shaped piece of material can be seen in Figure 5.3 just downstream of the new chicane magnets.

New vacuum vessels will be necessary to accommodate the new magnets and the stripper foil mechanism. The existing power supplies will be adequate for the two new magnets and the two existing chicane magnets when they are operated at their 1.3 GeV settings.

Table 5.1. Physics specifications for chicane magnet #2 (DH_A11) [1].

Proton beam energy	1.0 – 1.3 GeV
Magnet type	C magnet
Bend angle upstream of foil	42 mrad [Int(B*dl) = 0.2847 T-m for 1.3 GeV case]
Total bend angle	50.1 mrad* [Int(B*dl) = 0.3396 T-m for 1.3 GeV case]
Maximum magnetic field	0.25 T for magnetic stripping (1.3 GeV)
Magnetic field at foil	0.21 T < B < 0.22 T for H^0* states (1.3 GeV)
Good field region width	At least 188 mm
Good field region height	At least 53 mm above magnet center to at least 83 mm below magnet center
Multipole components	Less than 10 units at 10 cm for DH_A11 and DH_A12 together, centered on the magnetic field center
Gap between pole tips	24.8 cm (same as existing magnet)
Field tilt at foil	arctan(Bz/By) >0.100 rad
Coil package	Rad hard > 15e9 rad
H^0 and H^- waste beams	Good transport of these beams to the injection beam dump
Power supply current for 1.3 GeV beams	<4000 A

Table 5.2. Physics specifications for chicane magnet #3 (DH_A12) [1].

Proton beam energy	1.0 – 1.3 GeV
Magnet type	C magnet
Total bend angle	37.52 mrad* [Int(B*dl) = 0.2543 T-m for 1.3 GeV case]
Maximum magnetic field	0.20 T (1.3 GeV)
Good field region width	At least 233 mm
Good field region height	At least 52 mm above magnet center to at least 82 mm below magnet center
Multipole components	Less than 10 units at 10 cm for DH_A11 and DH_A12 together, centered on the magnet center
Gap between pole tips	24.8 cm (same as existing magnet)
Coil package	Rad hard > 15e9 rad
Power supply current for 1.3 GeV beams	<4000 A

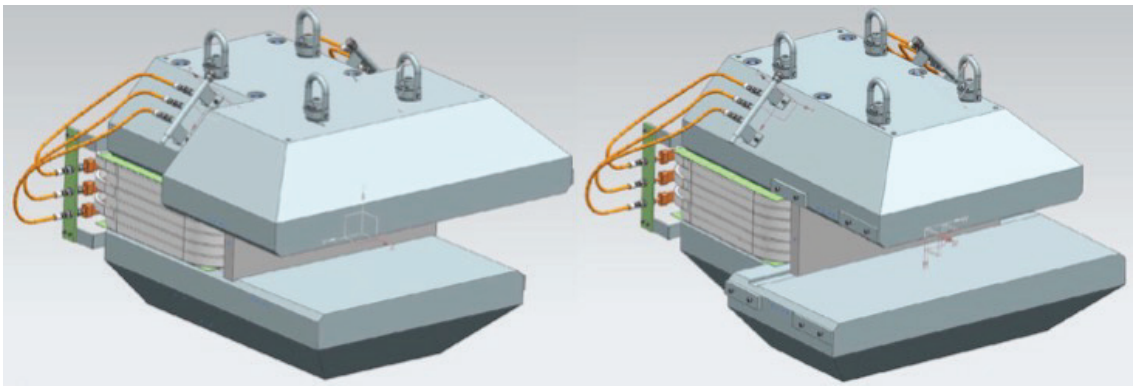

Figure 5.2. A CAD model of the two new chicane magnets. Cooling and power connections subject to change.

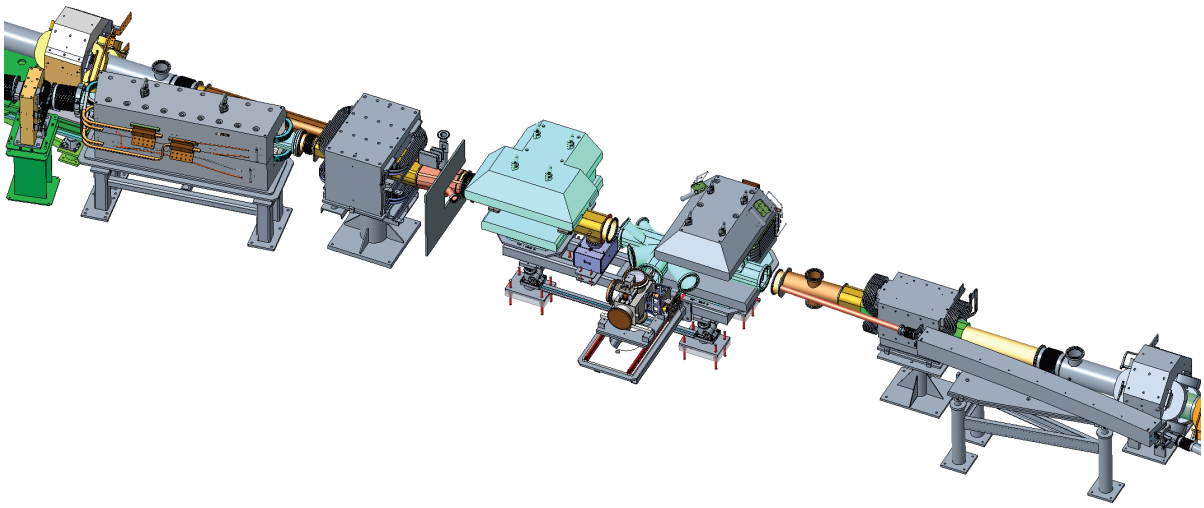

Figure 5.3. The injection region with new chicane magnets, field clamp, and dump septum installed.

Injection dump septum magnet. The injection dump septum magnet is a combined-function magnet that provides focusing and differential bending to the two waste beams. The magnet steel in the existing injection dump septum magnet would be driven into saturation to achieve the magnetic fields required for 1.3 GeV operation, exceeding the current available from the present power supply. Therefore, this magnet will be replaced with a new design that will occupy the same approximate installation footprint. Physics specifications are shown in Table 5.3. The new design is a C-magnet with an arc and a quadrupole component for focusing. To meet the focusing and bending requirements simultaneously, the pole faces had to be modified from a simple sector geometry. As of April 2020, this pole geometry is still being verified with 3-dimensional tracking. A preliminary CAD model is shown in Figure 5.4. The vertical aperture through the magnet will be at least as large as in the present design, and the horizontal aperture will accommodate the waste beams with appropriate clearance on each side. A new vacuum vessel for this magnet is also required. The existing power supply will be adequate for the new septum magnet. The new magnet design will that require existing magnetic shielding remain in place to prevent fringe fields from disrupting the circulating beam in the ring. Additional shielding may be added if room is available, although the effect of these stray fields has been included in the tracking simulations and has been shown to be negligible.

Table 5.3. Physics specifications for injection dump septum magnet [2].

Proton beam energy	1.0 to 1.3 GeV
Magnet type	Septum, sector bend, gradient
Horizontal good field region	Sufficient to include both beams in good field region. Beams are about 150 mm apart
Vertical gap	No smaller than present gap (~6.40 cm)
Bend angles	Steer "H^0" and "H^-" beams to injection dump "H^0" bend angle ~183 mrad "H^-" bend angle ~126 mrad Final values were determined by simulations
Quadrupole term	Sufficient to produce the required beam spot sizes in the beam line and at the injection dump. Final number to be determined by simulations. Approx. K1 = 0.187 m^{-2}
Multipole content	Less than 1 part in 1000
Field strength in region of circulating beam	Integrated field less than 1 G-m. It is acceptable to achieve this specification by placing thin magnetic shielding around the circulating beam pipe
Overall dimensions	Must fit in available space, approx. length 2 m
TiN coating on vacuum chamber	None
Rad hard coils	None
Power supply current for 1.3 GeV beams	<4700 A

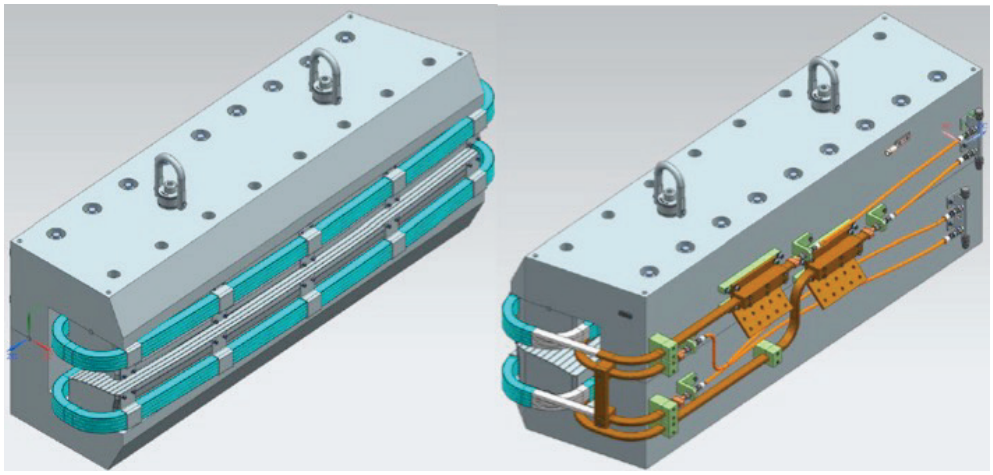

Figure 5.4. A preliminary CAD model of the new injection dump septum magnet showing the recirculating beam side (left) and aisle side (right).

Injection kicker system. The injection kicker magnets by themselves are capable of operating at the higher currents necessary to deflect the 1.3 GeV beam. Empirical field tests at high duty factors show the thermal performance of the magnets is adequate for the required PPU operational parameters. However, the power supplies for the kicker magnets will require upgrades for the magnets to deliver the same kick angles at the higher (1.3 GeV) beam energy. Upgrades of the power supplies were developed and verified to be simple changes. All eight injection kicker power supplies will be upgraded from 1400 to 1600 A. The average power delivered to the magnets will be roughly the same as in the original design because of

a reduction in the length of the pre-injection flattop of the waveform, a change that has already been implemented for normal operation. Specifications are shown in Table 5.4.

Table 5.4. Injection kicker power supply upgrade specifications.

Maximum current	1600 A

Ring stripper foils. To maintain stripping efficiency at 1.3 GeV, the stripper foil thickness must be increased. Operational experience at the present 1.0 GeV injection energy has shown a preference for ~0.38 mg/cm^2 thick nanocrystalline diamond foils. As illustrated in Figure 5.5, scaling this energy to 1.3 GeV requires a thickness of ~0.413 mg/cm^2. For 1.3 GeV, 2 MW operation, the beam current is nearly the same as for 1.0 GeV, 1.4 MW; and the heat load on the foil will also be nearly the same. Stripper foil survival is therefore not a concern for the 1.3 GeV, 2 MW case. However, for the 1.3 GeV, 2.8 MW case, the foil temperature will be higher by about 300 K (personal communication from Y. Takeda, J-PARC, to M. Plum, ORNL, April 2013). To ensure the foil will survive at the higher temperatures, a series of tests were conducted. Injected beam density on the foil has routinely been higher than design values to accommodate lower injection dump losses. This operating regime increases the foil heat load well above those expected with the design beam size at the foil at 2.8 MW operation. With the addition of the new injection dump dipole and quadrupole, we will be able to increase the beam size on the foil and still maintain low losses in the injection dump. Tests on the foil test stand, which comprises a 30 keV, 5 mA peak pulsed electron beam designed to produce PPU-level heat loads, have shown good agreement with the operational measurements. At design beam densities, we expect the foils would survive up to an SNS-like 1.3 GeV beam with current such that the time averaged power would be >5 MW.

A 2-dimensional pyrometer is being developed to actively measure the temperature distribution on the foil during operation. This device will provide temperature feedback to within ±100 K to operators when the beam size is tuned in the injection region.

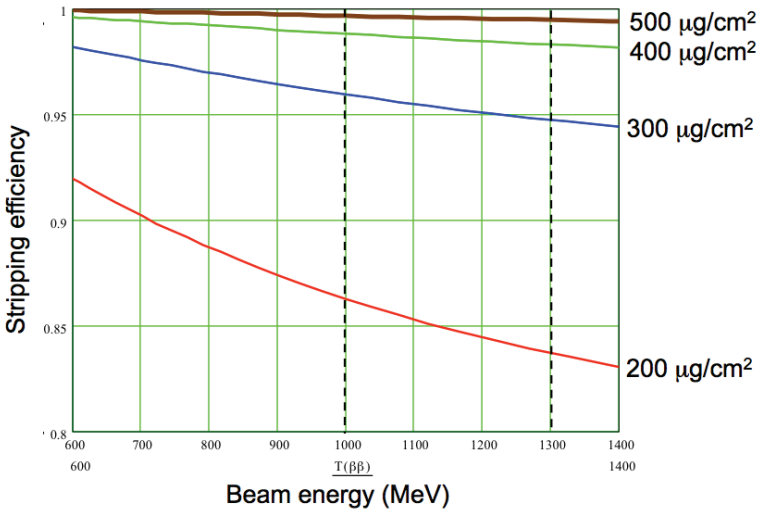

Figure 5.3. Stripping efficiency vs. foil thickness for a 1.3 GeV H- beam.

Primary stripper foil changers and electron catcher. The primary stripper foil changer will be evaluated and possibly redesigned if required by the new vacuum chamber configuration. The electron catcher is currently attached to a cooled plate brazed to the bottom of the chicane 2 vacuum chamber. The current design is not placed correctly relative to the injection point and has caused problems in the past because of its relatively limited acceptance. As part of the redesign of the vacuum chambers in this

region, the electron catcher will be redesigned so that is either movable or has large enough acceptance to mitigate the problems seen in the current design.

Secondary stripper foil changer. The existing secondary stripper foil changer is not adequate for the PPU project. It uses a two-part stripper foil bracket that unfolds as it is lowered into the vacuum changer, thus compromising its performance. Also, the view screen attached to the stripper foil mechanism is not wide enough to adequately characterize the waste beam positions. The new chicane magnet vacuum chambers will include a vacuum port with a diameter large enough to contain an unfolded secondary stripper foil and wider view screen.

Injection dump beamline quadrupole magnet. The beam dynamics in the existing injection dump beam line are severely constrained by the single quadrupole magnet in that beam line downstream of the foil. The combined-function injection dump dipole magnet provides focusing and bending, but the set point is determined by the bending requirements. The waste beam distributions on the beam dump are thus a compromise between optimizing ring injection, beam loss, and beam distribution on the dump face. This compromise leads to a beamlets that are too dense on the dump face to accommodate low losses at the injection point. The addition of a second quadrupole magnet will decouple the tuning of the injection spot and the injection dump and allow the beam distribution on the dump to be optimized for the dump with more control over bunch shape and size, thus improving the lifetime of the dump. The new magnet will be capable of maintaining a round beam at roughly ±30% the nominal beam size, without any additional aperture restriction. This quadrupole will be the same design as the existing 30Q58 magnet, minimizing additional cost. The power supply required to drive it will be a bipolar ±120 A with a stability requirement of 1% at 60 Hz. (the magnet current must be within 1% for each beam pulse). This is much lower than the 1 kA supply on the existing magnet; but because this magnet is only meant to supplement the existing optics for slightly different settings, it will still allow the roughly ±30% change in beam size while maintaining the optimal beam shape on the dump face.

Injection dump beamline diagnostics. The beam dynamics in the injection dump are complex, with two beamlets that originate from the partially stripped and fully stripped beam on the primary stripper foil. Currently, only a single wire scanner is available downstream of the injection dump quadrupole. To more completely characterize the waste beams, another wire scanner will be added between the two quadrupole magnets. (An additional imaging diagnostic to be installed at the dump window is covered in Section 5.3).

5.2 EXTRACTION REGION

The purpose of the extraction system is to redirect the trajectory of accumulated proton bunches from the ring toward the target via the RTBT in a single turn. The magnets making up the extraction system are shown in Figure 5.6. Fourteen extraction kicker magnets fire simultaneously to direct the beam downward into the extraction septum magnet aperture. The kicker magnets are contained withing two vacuum tanks, and each extraction kicker vacuum tank contains seven single-turn ferrite magnets. There are six slightly different magnet designs, primarily distinguished by vertical aperture size. The identification and installation arrangements for the existing kicker magnets are shown in Figure 5.7 and Figure 5.8.

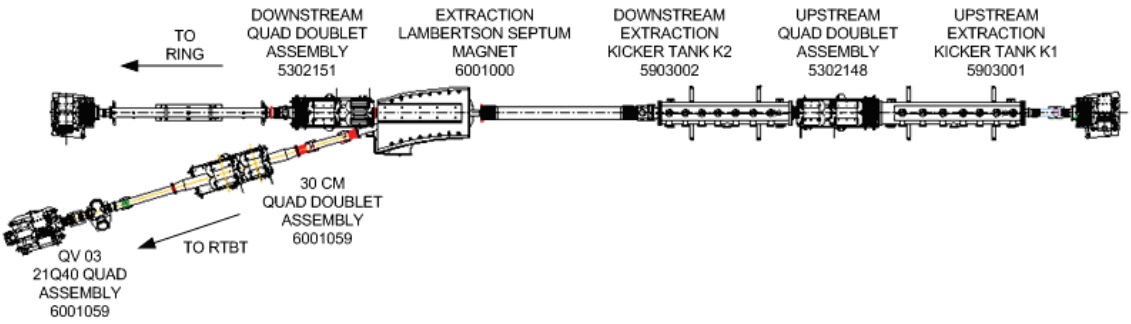

Figure 5.4. Extraction system magnets.

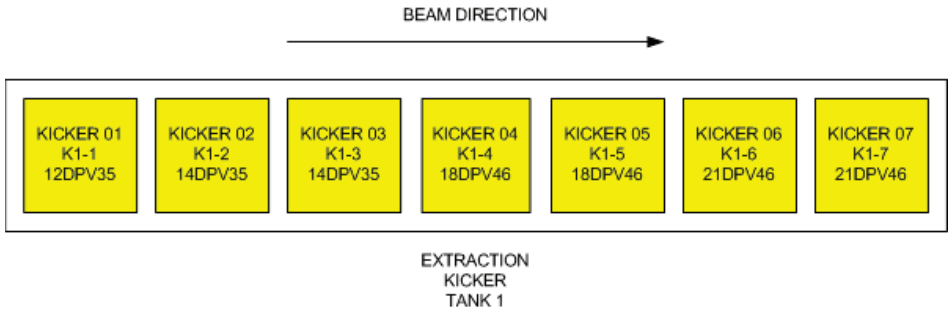

Figure 5.5. Schematic of the existing extraction kicker tank K1 with magnet types.

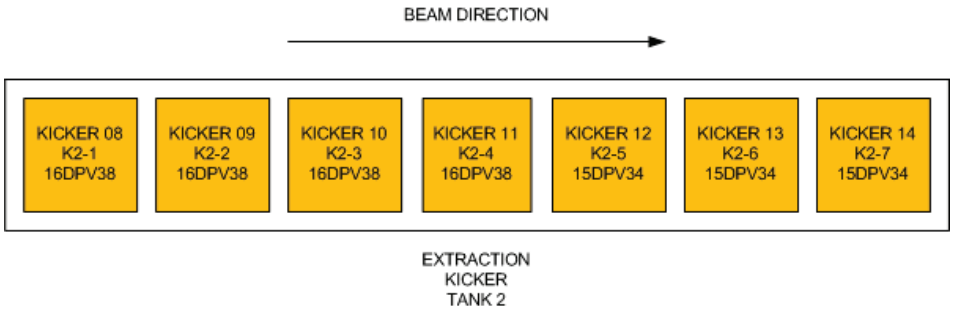

Figure 5.6. Schematic of the present extraction kicker tank K2 with magnet types.

The current kicker system is not capable of providing the angular deflection necessary to extract the beam because the charging system is not able to reach the necessary voltage in the 13 ms between the extraction of one pulse and the subsequent MPS verification of the kicker charge. The existing14 kicker power supplies will be upgraded with a resonant charger design. The resonant charger will allow the existing pulse forming networks (PFNs) to be charged to a higher voltage in a shorter time, thus providing higher magnetic fields strong enough to achieve the same kick angles for the 1.3 GeV case as for the 1.0 GeV case today. Specifications are shown in Table 5.5.

Table 5.5. Extraction kicker power supply upgrade specifications.

Maximum PFN charge voltage	45 kV
Maximum charge time	13 ms
Charging system type	Resonant charger

Extraction Lambertson septum magnet. This magnet, shown in Figure 5.9, contains pole tip shims optimized for a 1.0 GeV beam. These shims are necessary to cancel the skew quadrupole component of the magnetic field. When operated at the 1.3 GeV set point, the magnet will be slightly more saturated; and the shims may no longer adequately cancel the skew quadrupole component. A magnetic model of this device will be used to determine if new shims are required; and they are required, new shims will be designed and installed.

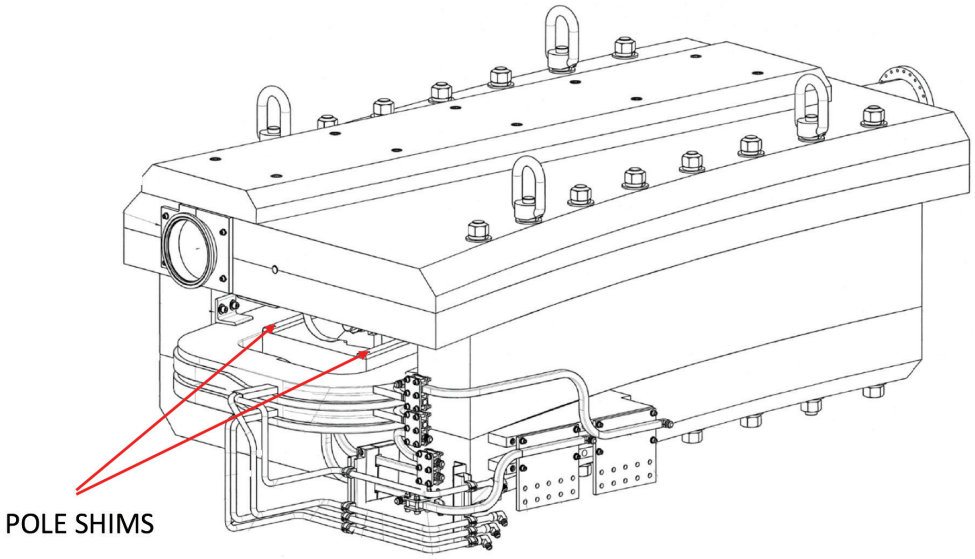

Figure 5.7. Extraction Lambertson septum magnet.

5.3 RING INJECTION DUMP

Power limit engineering study. The ring injection dump is presently rated for 1.3 GeV, 150 kW. This power rating is based on thermodynamic simulations of the water-cooled dump, the concrete that surrounds the dump, and the earth that cools the concrete [3] During normal operating conditions, about 3% of the linac beam power is delivered to the injection dump; so the dump power rating of 150 kW is well matched to 3 MW linac operation. A set of three thermocouple sensors, all mounted at the same place and embedded into the concrete near the entrance to the dump, have been periodically read out since initial operation of the SNS. These data were analyzed to determine if it is practical to increase the dump power rating [4].

The dump thermal model was benchmarked against the original design and compared with the measured temperatures from the thermocouple data, showing very good agreement (Figure 5.10).

Based on this modeling, it was determined that at 1.3 GeV, the dump would be very near the peak temperature limit. Engineers found concrete test data from the construction of the ring injection dump which shows that the concrete strength is sufficient to claim exception E.4.1 in *Code Requirements for Nuclear Safety-Related Concrete Structures (ACI 349-13) and Commentary* [5] to raise the peak temperature limit from 150°F (66°C) to 180°F (82°C), which should allow comfortable operation at 150 kW(Figure 5.11).

Injection dump imaging system. The lifetime of the injection dump, and the proton beam vacuum window in front of the dump, are maximized when beam is centered and has a distribution well matched to the dump. There are eight thermocouples mounted to the rim of the window to help center the beam. However, these thermocouples provide only a crude measure of the beam position and very little

information about the size and distribution of the beam. The PPU project will therefore design, fabricate, and install a beam imaging system that will allow measurement of the beam position, size, and distribution at the entrance to the dump. Specifications are shown in Table 5.6. It will be similar to the beam imaging system currently used on the FTS. This will reduce the risk of compromising the performance of the dump at the PPU and STS beam power levels.

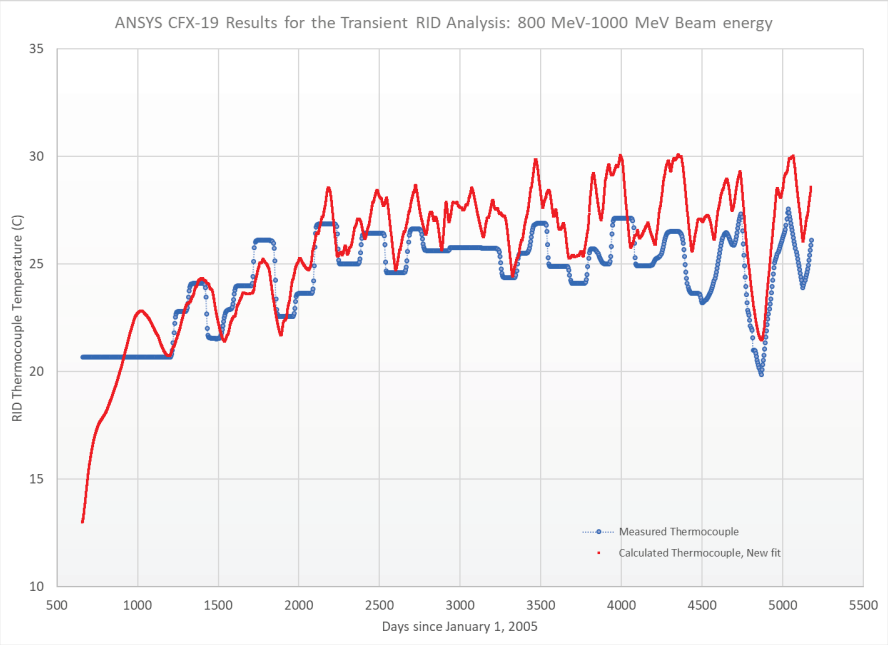

Figure 5.8. Ring injection dump temperature over the span of SNS operation as measured by thermocouples and predicted by the benchmarked thermal model.

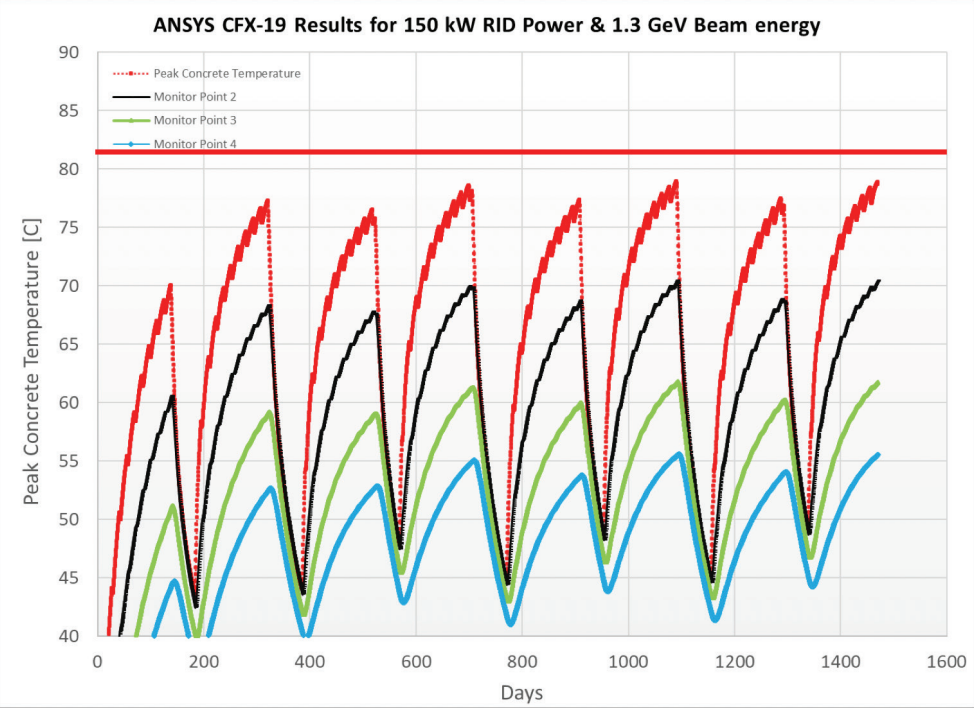

Figure 5.9. Peak concrete and installed thermocouple temperatures predicted by thermal model for 1.3 GeV operation at 150 kW.

Table 5.6. Injection dump imaging system design specifications.

"Pixel" size	<2 to 3 mm pixel size over 250 mm diameter
Absolute position accuracy	<10 mm
Position resolution	<4 mm
Active area	25 cm diameter circle, centered on the beam dump axis

We have selected a design that leverages our experience with the target imaging system, which has been in place for several years. As shown in Figure 5.12, the ring injection dump imaging system extends from the vacuum window to the ring tunnel. It will use a light-emitting coating on the upstream face of the vacuum window, likely the same type used for the target imaging system (chromium-doped Al_2O_3). The image will be viewed using a camera installed inside the ring tunnel, using a turning mirror located about 11 m upstream of the vacuum window. Bench testing has verified that the specifications can be met without any modification to the flight tube [6]. The camera and imaging optics will be installed just below the beamline in a shielded enclosure. The camera will be installed on a rail system that allows the camera to be extracted for replacement with minimal unstacking of shielding. The advantages of this design choice include relatively easy access to the optics system and no optics inside the harsh environment surrounding the beam dump.

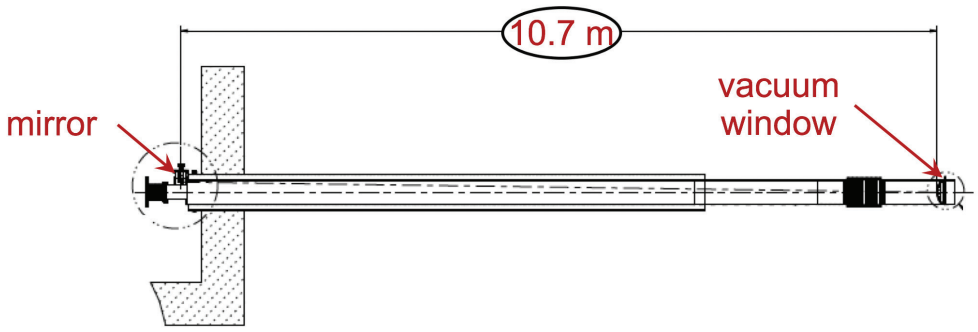

Figure 5.10. Cross section of the last part of the ring injection dump beamline, showing the main components of the imaging system.

5.4 RING UTILITIES

Ring injection magnet cooling water system (RN-01). Several of the ring injection magnets will be replaced with new magnets. The existing lines will be disconnected and then reconnected to the new magnets once the new magnets are installed. The flow and the flow requirements for the new magnets will be the same as or similar to those for the original magnets. The existing ring magnet cooling system already has adequate flow and heat capacity even after the addition of the new injection dump quadrupole magnet. The cooling water system will need to be rebalanced once the changes are made.

Ring magnet power supply cooling systems (RN-03). The increase in beam energy will add an average of 20% to the required magnet power supply currents. This will create additional heat load and flow to cool the existing and new power supplies. Power and thermal tests performed on the ring magnet system have shown that the existing Ring Service Building (RSB) power supply cooling system (RN-03) is not adequate to cool the supplies for the PPU power level requirements shown in Table 5.7 and Table 5.8. Therefore, the existing system will be upgraded. Two larger-capacity pumps will replace the existing three pumps, as shown in a preliminary CAD model in Figure 5.13.

Table 5.7. Ring magnet power supply cooling systems (RN-03) thermal requirements.

Need to remove heat rate	**kW**
Rejected heat at maximum load test	350
Calculated rejected heat for injection quad magnet power supply	10
Calculated rejected heat for new nine STS magnet power supply	140
Rejected heat rate for PPU and STS	**500**
Heat exchanger new plate pack cooling capacity	550
Margin for cooling capacity	10%

Table 5.8. Ring magnet power supply cooling systems (RN-03) hydraulic requirements.

Cooling water flow requirements	**GPM**
Cooling water flow from maximum load test	344
Required flow for new injection quad magnet power supply	3
Required flow for new nine STS magnet power supply	62
Total needed flow for PPU and STS	**410**
New pump flow capacity	475
Flow margin	16%

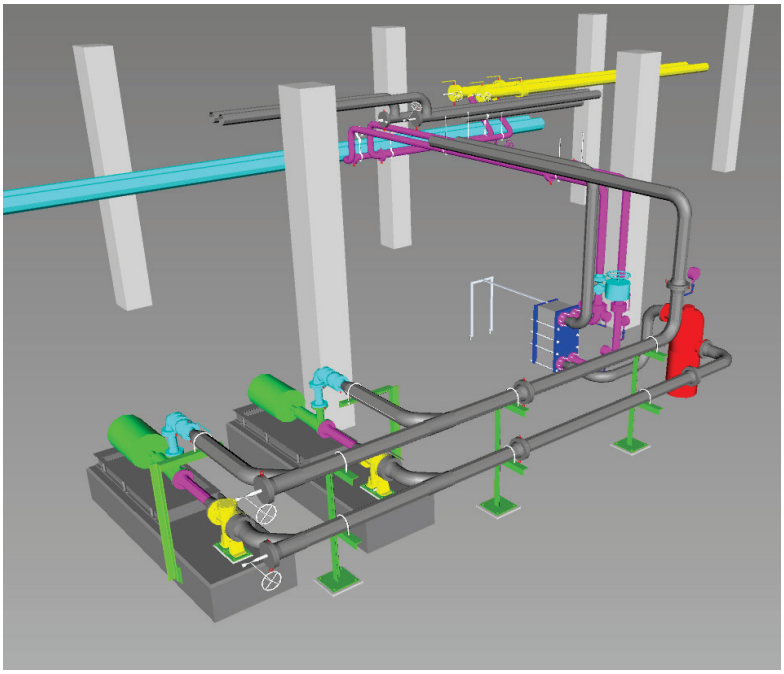

Figure 5.11. A CAD model of the two new RN-03 water pump skids.

Electrical utilities. Field tests of ring magnets operated at 1.3 GeV levels have shown that the main ring dipole magnet power supply will require that cooling fans be added to the main ring dipole substations, as shown in Figure 5.14. All the other power supplies have sufficient capacity, and no additional electrical power will be required for the RSB.

Figure 5.12. Photo of the main ring dipole power supply substation transformers with cooling fan images superimposed.

PFN room air conditioning. The PFNs are located in a dedicated room attached to the RSB. This room has no air conditioning, and temperatures can exceed 43°C during the hot summer months. The common wall between the PFN room and the RSB is not completely sealed, and the lack of PFN cooling affects the RSB temperature, humidity and pressurization. Also, although the equipment inside the PFN room itself can operate sufficiently well, it is an unpleasant place for people to work. Two Liebert fan coil units will be attached to the ceiling and will be locally controlled by manual thermostats. An expected side benefit is improved equipment reliability due to the lower room temperature and humidity during summer conditions.

PFN room cooling specifications:

- The project will install two chilled water fan coil units (FCU-RN-01 and FCU-RN-02).
- Each fan coil unit will have 8 tons of cooling capacity with 2850 cfm of cooling airflow. This results in 33% margin compared with the calculated peak building load.
- Supply air will be ducted within the room to enhance distribution. Return air will be unducted.
- The units will provide both cooling and heating. The existing local unit heaters will be removed.
- The chilled water and heating water supply and return piping will tie into the existing mains. Condensate piping will drop down an exterior wall and then exit the building. Exact routing will be determined during final design.
- Temperature control will mimic the existing controls: a local thermostat without any ties to the EPICS system.
- Existing wall louvers will be blanked off and insulated. Existing ceiling-mounted exhaust fan positions will be converted to outside air intake connections.

5.5 BEAM TRANSPORT LINES

5.5.1 High-Energy Beam Transport Line

The original design anticipated the 1.3 GeV upgrade, so no hardware modifications will be needed to the HEBT line that transports the beam from the linac to the accumulator ring.

5.5.2 Ring to Target Beam Transport Line

The RTBT beamline was designed for 1.3 GeV, so no magnet or beam dynamics changes are needed to accommodate the higher beam energy.

Beam power limiting system (BPLS). The FTS shielding Accelerator Safety Envelope [7] imposes a limit of 2.0 MW on the first target, integrated over several seconds to ensure the safety of personnel working in the Target Hall. After PPU, the accelerator complex will be capable of delivering 2.8 MW of beam. The STS will eventually accept 700 kW of beam, which will be deflected via kickers in the RTBT line. The BPLS is necessary to ensure that the beam power delivered to the first target does not exceed 2.0 MW, or a possible lower user-defined limit. The BPLS design will be based on beam current transformers positioned in the RTBT beamline upstream of the target but downstream of the ring-to-second-target transport line stub. To calculate the power delivered to the target, this system will independently verify the beam energy by reading back the current on the main RTBT dipole DH13 and continuously monitor the beam current delivered to the target by integrating the fast current transformer (FCT) signal. The system will trip the accelerator through the Personnel Protection System(PPS) if the power delivered to the target exceeds a limit to be specified in the Operations Envelope [8], which is below the limit determined in the Accelerator Safety Envelope. Machine protection will be provided by independent existing current measurement systems that do not interface with the PPS.

A high-level schematic of the BPLS system showing major components is presented in Figure 5.15.

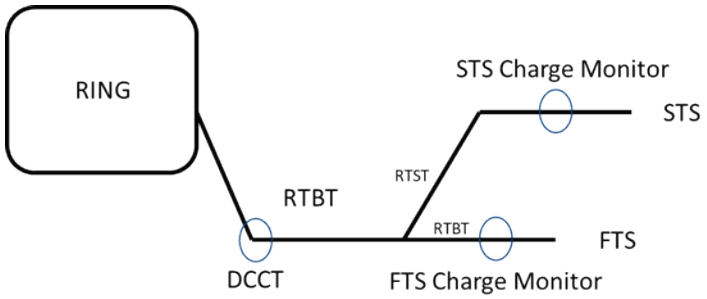

Figure 5.13. High-level schematic of the BPLS.

Figure 5.15 shows the location of the FCTs that measure the beam sent to the FTS, which is downstream of the ring-to-second-target (RTST) beamline. This figure also shows where the direct current transformer is used to measure the magnet current on DH13 to deflect the beam toward the SNS target systems. Measurements of both charge and energy are necessary to measure the beam power delivered to each target system.

The BPLS design follows a credited engineered controls design philosophy and interfaces to the PPS at the SNS. Since the design is credited engineering controls, a safety integrity level of 2 is assigned to the design, requiring a level of redundancy and of engineering analysis to qualify the design. The system is designed using commercial off-the-shelf components that have sufficient reliability documentation, thus streamlining safety documentation.

A schematic of the beamline is shown in Figure 5.16, and the magnet current for the magnet DH-13 is shown in Figure 5.17. Both Figure 5.16 and Figure 5.17 depict some of the system redundancy in the measurements that demonstrate that the system is designed to an safety integrity level 2 rating.

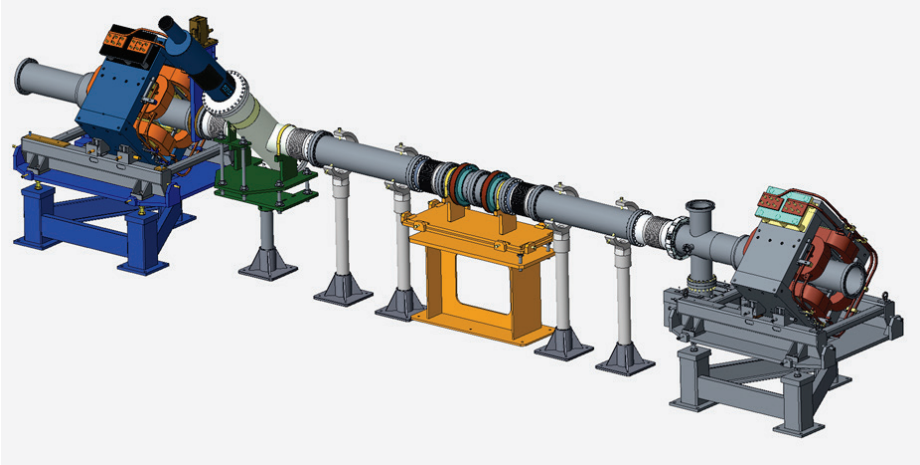

Figure 5.14. Schematic of the beamline showing the FCTs on the new stand shown in gold color.

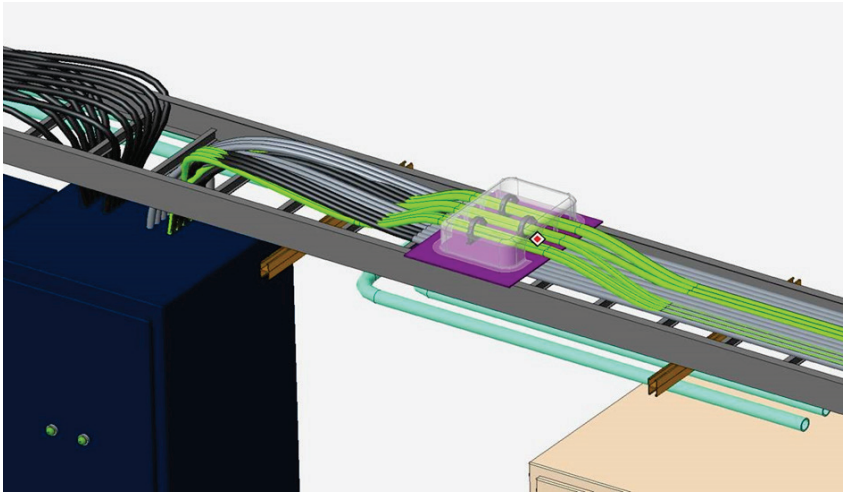

Figure 5.15. Direct current transformer measurement of the magnet current for DH-13.

An overall electronics schematic is shown in Figure 5.18. The system redundancy is shown, with the multiple measurements of beam current on the left-hand side, and the safety programmable logic controller (PLC) processor making multiple measurements from the magnet power supply. The digital processor shall use DO-254 [9] to govern the design of the digital architecture. The decision to use DO-254 [9] revolved largely around the engineering standards of aviation and the reliability required. A crosswalk between standards has been written that justifies the decision.

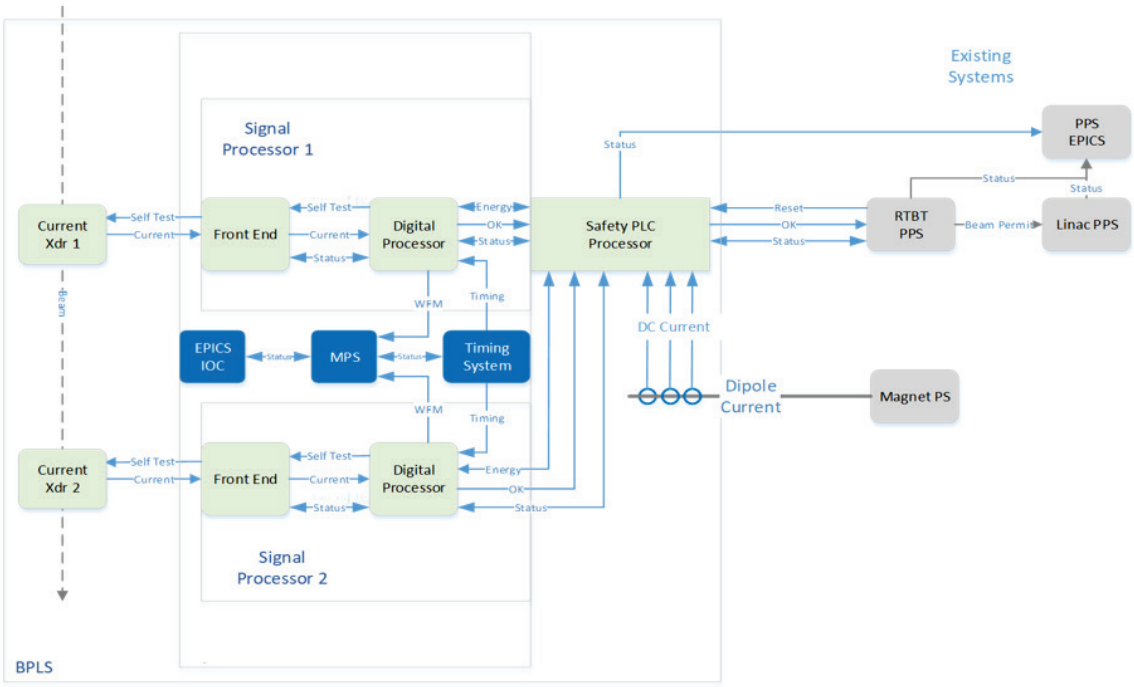

Figure 5.16. Electronics schematic of the BPLS system

Specifications for the electrical requirements for the FCT are shown in Table 5.9.

Table 5.9. Electrical requirements of the FCT.

Quantity	Range
Applicable frequency range	1 kHz – 22 MHz
Main winding magnitude flatness	±0.5 dB
Main winding phase flatness	±5 degrees
Maximum peak current	150 A
Transfer impedance to main output	0.25 V/A
Calibration winding to main winding turns ratio	1:1
Calibration winding frequency range	1 kHz –16 MHz
Calibration winding magnitude flatness	±0.5 dB
Beam current pulse width	0.7 – 1.5 μsec
Connectors	N-female, 50 Ω
Case to N outer conductor resistance	Galvanically isolated
Case to N center conductor resistance	Galvanically isolated
Cal and main winding impedance	50±1 Ω
Shielding of toroid assembly to outputs of current transformer	≥-80 dB to 100 MHz
Current transformer droop	≥1 ± 0.1 msec ≤(0.1± 0.01 %/μsec)

Table 5.9 shows that the FCT includes the design of a calibration winding. The calibration winding has multiple uses in the system. It is used to calibrate the FCT and during operation as part of a self-test mechanism. The self-test adds a level of observability and diagnostics that increases the system safety integrity level.

The design of the BPLS is unique compared with other existing protection systems in that it has an additional requirement to measure beam power. This means that the power calculation performed in the digital processor requires the beam energy communication from the safety PLC to the digital processor. The safety PLC does the voting for the measurement of the magnet current in addition to the voting between the two digital processors to determine if the beam power limit has been achieved.

A high-level fail-safe reliable PLC is a requirement to monitor the PPS charge monitoring system. The safety PLC shall be a TÜV-rated dual processor. A TÜV rating on a PLC indicates full compliance with IEC 61508 standards [10]. A safety PLC establishes communication with remote safety IOs using a cluster of unique safety network settings. These settings ensure a reliable fail-safe connection with safety input and output modules over the safety network. The safety PLC consists of the main safety processor and the safety partner processor. The two independent processors reside on the same back plane and ensure with a high a level of confidence that the inputs and outputs will respond and update according to the software settings. The Rockwell Automation processor 1756-L81ES, in conjunction with the safety partner 1756-L81SP, shall provide a fail-safe safety integrity level-3 [10] interlocking capability.

A high-availability isolated network switch Stratix 5400 will ensure that the connection between the safety PLC and the safety IO is reliable. Figure 5.19 shows the safety PLC architecture that will support the connections to the digital processing unit and to the existing PPS RTBT PLC over the safety network.

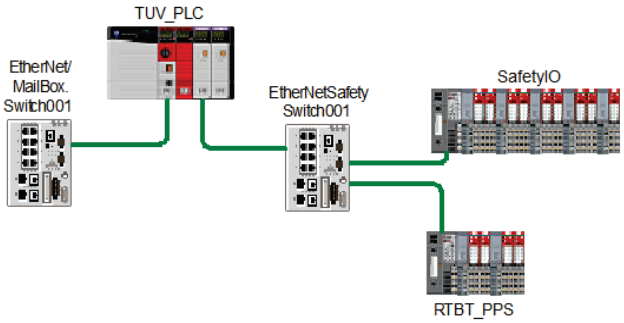

Figure 5.17. Safety programmable logic controller architecture.

5.5.3 RTBT-to-RTST Penetration

The new RTST beamline for the future STS project will start about halfway along the RTBT. A beam tunnel stub will be constructed as part of the PPU project to minimize future interference between RTST tunnel construction and the users of the FTS. Temporary shielding will be stacked in the stub, as shown in Figure 5.20. The future STS project will connect the new beamline tunnel to the stub and install the RTST beamline components. Details of the RTST stub can be found in Section 7 of this report, Conventional Facilities. No beamline components for the new RTST line are included in the PPU.

As part of the PPU ring systems scope, neutronics simulations were performed to specify the earth berm above the tunnel stub and the temporary shielding stack, and to verify the current earth berm above the RTBT is sufficient for 2.8 MW operation at 1.3 GeV upstream of the stub and 2.0 MW, 1.3 GeV operation downstream of the stub. Using 55.88 cm thick concrete tunnel walls, a 68.58 cm thick concrete ceiling, and a soil thickness above the tunnel of 495 cm, simulations [11] showed that level of shielding is sufficient to keep both the normal operating and accident cases below the applicable safety limits. Neutronics analysis of the radiation in the stub on the far side of the concrete shielding showed that 540 cm of concrete is required to meet the accident case limit of 10 Rem/h behind the stub [12].

The PPU ring systems scope also includes modifications to the PPS for the stub. These modifications will include a Chipmunk radiation detector to be located immediately downstream of the temporary shielding stack.

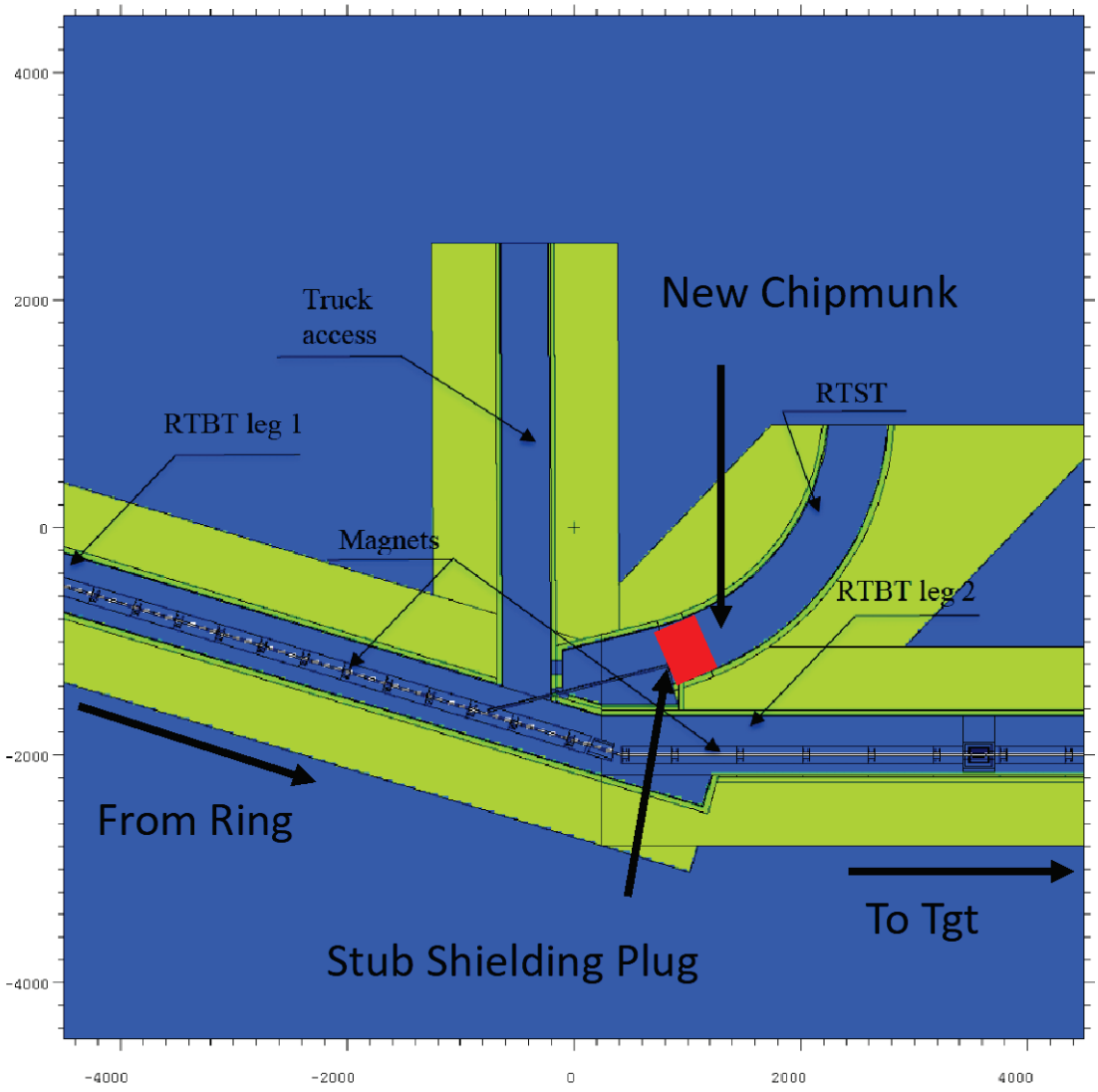

Figure 5.18. RTBT stub design showing temporary shielding stack and location of new radiation monitor.

5.6 ASSUMPTIONS

This section assumes that the PPU will have a replacement window for the injection dump ready for a replacement installation to be conducted by accelerator operations staff.

5.7 CRITICAL SPARES

Three new, one-of-a-kind magnets will be designed, fabricated, and installed in the ring injection section. Should any of these magnets fail, it would be impractical to replace just the coil packages. The magnets are located in a high-radiation area, and the radiation dose to workers replacing the coil packages would be higher than the dose for replacing the entire magnet. Therefore, the PPU project will acquire complete

spare magnet assemblies for the chicane and injection dump septum magnets. Because the chicane magnets are identical, only one spare chicane magnet will be built.

5.8 REFERENCES

1. M. Plum, *Physics Specifications for the New Chicane Magnets*, PPUP-402-TS0001-R00, Oak Ridge National Laboratory, January 30, 2019.
2. M. Plum, *Physics Specifications for the New Injection Dump Septum Magnet*, PPUP-402-TS0002-R00, Oak Ridge National Laboratory, January 31, 2019.
3. M. Wendel, *Thermal Analysis of the Ring Injection Dump*, 106090200-DA0001-R00, Oak Ridge National Laboratory, n.d.
4. *Ring Injection Dump Thermal Analysis Update and Calibration for Proton Power Upgrade*, 106090200-TR0001-R00, Oak Ridge National Laboratory, in preparation.
5. American Concrete Institute, *Code Requirements for Nuclear Safety-Related Concrete Structures (ACI 349-13) and Commentary*, Standard ACI-349-13,American Concrete Institute Committee 349, June 2014.
6. W. Blokland, *Ring Injection Dump Imaging System Optics Bench Testing*, 106090200-TR0002-R00, Oak Ridge National Laboratory, in preparation.
7. G. Dodson, *SNS Accelerator Safety Envelope (ASE) for Full Power Operations of the Front End, Linac, Ring, Transport Lines, Beam Dumps and Target*, SNS 102030103 ES0016 R05, Oak Ridge National Laboratory, June 1, 2007.
8. *SNS Operations Envelope*, SNS OPM 2.B 1, Oak Ridge National Laboratory, June 2019.
9. *Design Assurance Guidance for Airborne Electronic Hardware*, RTCA/DO-254/ED-80, RTCA SC-180 and EUROCAE WG-46
10. *Functional Safety of Electrical/Electronic/Programmable Electronic Safety-Related Systems*, IEC 61508-1:2010, International Electrotechnical Commission, 2010.
11. I. Popova, *Soil Thickness Above RTBT/RTST for Proton Power Upgrade*, SNS-106100200-DA0110-R00, Oak Ridge National Laboratory, Oct, 2019
12. I. Popova, *Shielding Plug for RTBT Stub*, SNS-106100200-DA0113-R0, Oak Ridge National Laboratory, February 2020.

6. PPU FIRST TARGET STATION SYSTEMS

6.1 INTRODUCTION

The PPU FTS systems will reliably operate the FTS at 2 MW with 1.3 GeV protons delivered at a 60 Hz pulse repetition rate. While the FTS has been operated up to 1.4 MW, the design basis for most systems was 2.0 MW with 1.0 GeV proton pulses delivered at a 60 Hz. Higher proton energy and pulse intensity requires reevaluation of the thermal, structural, and shielding margins of FTS systems, as well as changes in radiation damage rates. Affected target systems include the mercury target module, mercury process systems, off-gas systems, reflectors, moderators and their cryogenic systems, reflector vessels, shielding, utilities, and instrument line core vessel inserts (CVIs).

The mercury target module was an exception to the original FTS design basis, as it was initially rated for 1.0 MW and later increased to 1.4 MW and 1.0 GeV at 60 Hz. Operational experience has influenced the design of the mercury target vessel. Design changes have been incrementally incorporated and fabrication oversight has increased. Gas injection for reducing mercury vessel beam pulse-driven cavitation damage and fatigue stress started with target T18 in late 2017 and has since been used in six targets. Significant reductions in pulse stress and cavitation damage have been demonstrated with limited gas flows under 1.4 MW operation.

The jump to 2.0 MW requires more target gas flow capability and further design improvements. The PPU FTS systems scope includes the development and deployment of high-flow helium gas injection into the mercury target to provide maximum mitigation of beam pulse–induced cavitation erosion and mercury vessel fatigue stress. These two phenomena are the primary drivers of target damage. Up to 20 standard liters per minute of helium gas injection will be accommodated with PPU upgrades. A substantially new target vessel design builds on lessons from operational experience and post-irradiation examination of targets. Mercury vessel design optimization has prioritized maximizing pulse fatigue life before crediting gas injection benefits.

The original FTS design basis employed several simplified bounding assumptions for heating, in many systems, that were expected to provide some margin compared with evaluations performed with contemporary and more accurate methods for the 1.3 GeV beam. Evaluations conducted as part of PPU have confirmed these assumptions with a few exceptions. More accurate present-day analysis methods have revealed higher peak heating at a few locations and more irregular temperature distributions leading to regions of high thermal stress. No major changes to cooling systems are necessary. Design basis cooling utility heat loads have been updated as a result of PPU evaluation work.

The expected lifetime of the FTS has been extended to a total of 60 years with the completion of the PPU—20 more than originally considered. FTS neutron source components with the highest radiation damage rates are replaceable by design (e.g., the target module, proton beam window (PBW), and inner reflector plug [IRP]). For these components, higher damage rates can be addressed with increased operational replacement frequency or relaxation of the material administrative dose limits. Increased replacement frequency is not an option for permanent components. Evaluations of accumulated lifetime dose have been completed for the permanent components. The outer reflector plug (ORP) sees locally higher dose rates at 1.3 GeV, and evaluations have determined that the maximum end-of-life radiation damage in the FTS will be in the ORP, exceeding 17 displacements per atom (dpa) in a small region near the target on the proton beam port. A case has been made that justifies increasing the ORP lifetime administrative dose limit to 20 dpa (from 10 dpa). No other FTS permanent components will exceed their original design administrative dose limits.

Upgrades to achieve PPU FTS systems goals have been defined and preliminary and final designs developed and reviewed. These include the PPU target module, target high-rate gas injection supply systems, gas management in the mercury process system, mercury off-gas treatment systems MOTS, and ortho-to-parahydrogen convertors and phase diagnostics for the cryogenic moderator system (CMS). Other upgrades determined necessary to ensure reliable 2.0 MW operation of FTS systems will be implemented by SNS operations. The 2 MW target module will be at final design status at the time of the planned Independent Project Review scheduled for July 2020.

Parameter	**1.4 MW value**	**PPU value**	**Unit**
Beam power capability	1.4	2.0	MW
Beam pulse frequency at max power	60	60	Hz
Proton energy	1.0	1.3	GeV
Intensity per pulse	1.46E+14	1.60E+14	p/pulse
Target peak energy density per pulse	9.2	13.0	J/cm^3
Target gas injection rate	< 2	≤ 20	SLPM
Helium gas injection type	Once-through	Recycled	
Target bubble injector type	Orifice	Swirl	
Target gas at beam window	No	Yes	
Target lifetime goal at max. power	~ 1,600	1,250	hour
Time to reach target radiation damage limit at full power (12 dpa in shroud)	5,285	4,225	hour
Mercury pump speed	350	400	rpm
Mercury volume flow rate	283	252	gpm
Moderator ortho-/parahydrogen state	Est. 30/70	> 99% para	–

6.2 REQUIREMENTS FOR FTS SYSTEMS

High-level requirements for PPU FTS systems include the following:

- Reliable and safe operation of the FTS at 2 MW with 1.3 GeV protons delivered at 60 Hz pulse repetition rate.
- A 2 MW target module and supporting systems that will require no more than four target exchanges per year for reliable operation, with fewer exchanges desired.
- Confirmation that permanent components of the FTS have adequate radiation damage tolerance considering the PPU beam and facility life extension from 40 to 60 years.
- Confirmation that monolith and instrument shielding is adequate for PPU operation.
- Updating of the radionuclide inventory for PPU operation and facility life extension so that facility safety basis evaluations can be satisfied.
- Ensuring that cryogenic moderator neutronics performance is consistent and at expected levels by maintaining near 100% parahydrogen, regardless of beam power or hydrogen age.

The broad scope within FTS systems leads to more detailed requirements to satisfy this summary. Those are described in the subsystem sections.

6.3 KEY ASSUMPTIONS

The following are the key assumptions guiding the design of the PPU FTS systems:

- The 2 MW target module design exterior interfaces remain as with the original design.
- No target materials will be considered for the target module other than the original type 316L(N) stainless steel.
- Changing the mercury pump is unnecessary for PPU.
- The mercury pump can be operated at 400 rpm (the original 2 MW design basis speed was 400 rpm).
- The existing spare mercury pump will be modified by SNS operations to be compatible with target gas injection.
- The existing mercury heat exchanger is compatible with PPU gas injection.
- Both the mercury pump overflow tank (OFT) and mercury return pipe gas-liquid separator (GLS) are necessary to mitigate risks associated with high-rate gas injection. Gas injection experience with 1.4 MW targets will continue to be considered up to the time of installation of the GLS and OFT.
- The CMS will be upgraded by SNS operations to ensure reliable 2 MW operation by the scheduled PPU CD-4 date.
- The PBW in use at the time of the PPU will be made of aluminum. Neutronic performance, target systems component heating, and radiation damage rates assume an aluminum PBW. Proton beam scattering is significantly less with aluminum. Neutronics and engineering evaluations will not be duplicated for an Inconel PBW. Evaluating the use of an Inconel PBW under 2 MW/1.3 GeV operation might be considered by SNS operations.
- PPU FTS installation activities will be coordinated with the timing of replacing the IRP from number 2 to number 3. It is preferred that the replacement not occur during the PPU extended outage starting in Q1 FY 2023. PPU outage planning will adjust as the IRP replacement time clarifies.
- PPU will purchase PPU test target #1 (T31 in the October 2019 Target Management Plan). This target will employ swirl bubblers like those planned for PPU target deployment in a modified 1.4 MW target design.
- PPU will also purchase PPU test target #2 (T32 in the October 2019 Target Management Plan). This target will be very close to the final design of the PPU target.
- PPU will purchase three PPU production targets.

The broad scope within FTS systems leads to more detailed assumptions to satisfy this summary. Those will be described in the subsystem sections.

6.4 OVERVIEW OF PPU FTS SYSTEMS EVALUATIONS AND UPGRADES

The FTS systems technical work scope is organized by systems in a manner similar to the existing SNS. The work breakdown structure (WBS) is graphically shown in Figure 6.1. Within each level 3 area are

activities broadly broken down into those associated with evaluating the impact of the higher beam energy and power (which will include specifying required upgrades or operational changes and documentation updates) and upgrades associated with a 2 MW target module and systems supporting target gas injection. There is a related R&D effort on gas injection and efforts to mitigate postulated accidents that lead to mercury escaping the service bay. Gas injection R&D is described in Section 8.

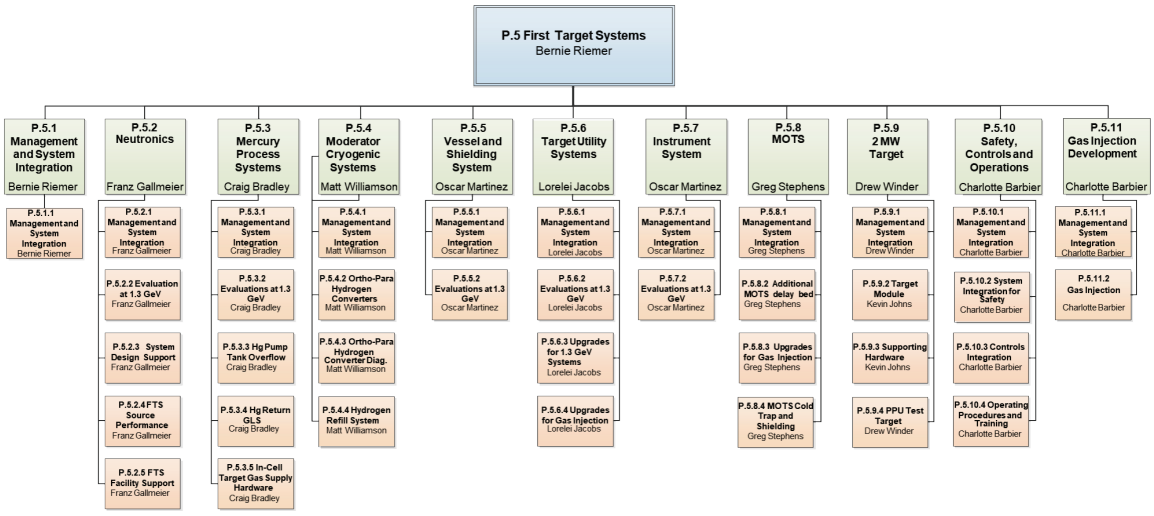

Figure 6.1. FTS systems work breakdown structure.

6.4.1 FTS Systems Level 3 Summary Descriptions

- *Neutronics*—This work scope includes evaluations to determine nuclear heating power deposition, radiation dose, and material damage rates; evaluations of shielding efficacy throughout the FTS monolith and instruments have been performed. Neutronic performance under PPU operation has been estimated. The facility radionuclide inventory for the FTS PPU beam for its extended lifetime to 60 years has been estimated. Neutronics support for design work under other WBS systems has been provided; this will continue through the final design stage. Neutronics performance measurements are planned during project commissioning.

- *Mercury Process Systems*—Evaluations have confirmed there are sufficient engineering and operational margins in the mercury process systems for the PPU beam. A GLS and mercury pump OFT are being provided to accommodate high-flow target gas injection. The mercury pump will be operated at 400 rpm during PPU operation (the pump's original speed) to provide sufficient flow. Hardware will be provided to connect target gas supplies from the connection point on the process bay wall (P.5.6 utilities scope) to the target carriage. Required operational procedure changes will be implemented. The operating temperature of the target carriage has been evaluated with the PPU beam.

- *Moderator Cryogenic Systems*—The PPU scope for moderator cryogenic systems includes the addition of catalyst beds to ensure near 100% parahydrogen in the three hydrogen moderator loops. This upgrade will ensure FTS neutronic performance is consistent throughout operating cycles and as predicted by neutronics analyses, irrespective of time since hydrogen was loaded or power on the target station. Diagnostics will be added to provide online measurement of the orthohydrogen to parahydrogen fractions. Upgrades to the hydrogen refill system will provide the necessary capacity

for the larger hydrogen inventory associated with the new catalyst equipment. Operational procedures have been updated.

- *Reflector Vessel and Monolith Shielding*—These evaluations have ensured there are sufficient engineering, radiation damage, and operational margins in the FTS vessel and monolith shielding systems for the PPU beam and defined upgrades if needed. Hardware upgrades are not required. Evaluations included the ORP and CV. Updated design basis data for the cooling utilities have been provided. Neutronics analysis indicated that at the end of the extended facility lifetime, portions of the ORP will reach 17 dpa, exceeding the original design basis limit of 10 dpa. A justification for increasing the radiation damage limit on the ORP to 20 has been prepared and approved.

- *Target Utility Systems*—These evaluations ensure that there are sufficient engineering and operational margins in the FTS target utility systems for PPU operation and include necessary minor upgrades. Utility changes have been coordinated with the evaluations and needs of other WBS systems. Control set point adjustments may be specified. Operating procedures will be updated. Target utility systems is also responsible for adding high-flow gas supply capabilities as required by the 2.0 MW–capable target. The target gas system is designed to primarily use gas recirculation but will be also capable of once-through gas operation.

- *Instrument Systems*—This evaluation has confirmed there are enough engineering, radiation, and operational margins in FTS instrument systems with the PPU beam. Specifically, this work has been limited to CVIs, especially those in the forward proton beam direction beamlines. The CVIs are part of a credited boundary for mercury vapor containment, so relevant engineering analyses have been updated. Updated heat loads have been provided to target utility systems. Instrument shielding performance has been confirmed as adequate under neutronics work scope.

- *MOTS*—High-flow gas injection is expected to more effectively sweep activated spallation gases out of the mercury process system. The addition of a second carbon delay bed is planned to limit the dose to MOTS equipment and personnel. A skid of larger molecular sieve beds and a second cryogenic cold trap will be added in the MOTS equipment room. A second molecular sieve bed skid is being added in the gold amalgamation room (GAR). Updated operating procedures will be prepared.

- *2 MW Target*—This work scope includes design and delivery of three PPU target modules. The target design incorporates high-flow gas bubblers and a gas injector close to the inner beam entrance window. The fatigue life of the mercury vessel from pulse response was maximized before crediting benefits from gas injection. The water-cooled shroud has minor design differences from the current design, which include closer spacing of cooling channels and the addition of a pressure relief valve that allows for relaxation of a design requirement condition for overpressurization. This WBS also includes the delivery of PPU test target #1—a 1.4 MW design incorporating swirl bubblers for the first time. The second PPU test target, based closely on the production design, is also provided by PPU FTS systems.

- *Safety, Controls, and Operations*—The system crosscutting activities in this WBS are essential to operational readiness for the PPU beam on the FTS. Four positive unreviewed safety issue (USI) findings concerning the FTS were captured in the Preliminary Hazard Analysis Report. A fifth item was subsequently identified that requires limiting the maximum beam power delivered to the FTS; that is being addressed under the P.4 Ring Systems scope. A new sixth item associated with hypothesized migration of the moderator catalyst is being addressed. Hazards associated with high-flow gas injection require an integrated systems approach to completing designs that sufficiently mitigate accident risks and for which safety authorization must be obtained. Documentation of all identified hazards with needed mitigations is well developed for approval by SNS facility safety

personnel and in preparation for the Accelerator Readiness Review process. Controls—whether or not related to gas injection—touch on nearly all FTS systems project scope. The Controls scope within P.5.10 begins with the wiring from the Level 3 WBS sensor or instrument. Local instruments, devices, and sensors are part of the individual P.5 Level 3 scope. Operating procedures and required training will be prepared for SNS operations for the PPU system changes.

- *Gas Injection Development*—Much of the target gas injection R&D had been completed in 2019 under the project WBS element P.7.1. However, some remaining design development tasks were transferred from P.7.1 over to the recently created FTS Systems WBS element P.5.11 with the approval of the DOE Program Manager for PPU. All gas injection R&D and design development is covered under Section 8.1.

There is no PPU work scope for moderators or the IRP. The Neutron Technologies Division of SNS is providing an IRP (#3) that will be fully compatible with PPU beam energy and power.

6.4.2 High-Flow Target Gas Injection

Target gas injection addresses the two fundamental target lifetime vulnerabilities—mercury vessel fatigue and cavitation erosion. Both originate from beam pulse–induced pressure waves. A PPU target will experience 270 million pulses over the minimum lifetime goal of 1,250 hours. The high-flow gas injection envisioned for the mercury target requires work across all FTS systems besides the target module. Mercury process systems, target utility systems, MOTS, safety, controls, and operations all have project scope associated with high-flow gas injection. The plan and basis for SNS target gas injection—from initial steps under SNS operations to maximum deployment—was outlined in the 2016 *Conceptual Design Report: Mercury Target Gas Injection* [1]. Project plans are captured in the PPU *2 MW Target Development Plan* [2] and its addendum [3]. The PPU target and supporting systems design have incorporated developments from PPU R&D, from SNS operations (vis-à-vis the *SNS Target Management Plan* [4] and from the GI3 project [5].

As power increases, the fatigue and cavitation vulnerabilities increase disproportionally, requiring effective countermeasures. Gas injection—in two forms—has excellent prospects to provide substantial life improvement when further developed and deployed in the target. The two forms of gas injection are

- Small gas bubbles injected at high gas flow rates and dispersed throughout the target

- A local region of high gas injection close to the worst area of high cavitation damage, specifically at the middle of the inner beam entrance wall of the mercury vessel, near the wall surface facing the bulk mercury volume

An ideally beneficial small bubble size distribution and volume fraction is difficult to precisely specify. Numerical studies of monodispersed populations indicate smaller bubbles ($R < \sim 150$ μm) are more effective in reducing pressure induced by beam pulse heating [6]. Different behaviors are expected depending on whether the location of interest is within the heated volume or simply nearby. Larger gas fractions are also beneficial. A combination of high gas fraction of solely the smallest bubble sizes appears impractical because of coalescence and other behavior. While the physics in the numerical studies are not comprehensive, fortunately, experimental and operational experiences have provided encouraging results for vessel fatigue and cavitation damage reductions with gas injection.

The Japan Proton Accelerator Research Complex (J-PARC) mercury target uses swirl bubblers at relatively high gas injection rates (ca. 0.5%, as defined by gas rate at standard temperature and pressure normalized by the mercury volume flow rate). Online measurements of the J-PARC target vessel have

demonstrated vibration reduction with a swirl bubbler to about one-third that without bubbler operation (Figure 6.2). Comparable reductions in vessel pulse response stress (and cycles) will greatly improve fatigue life.

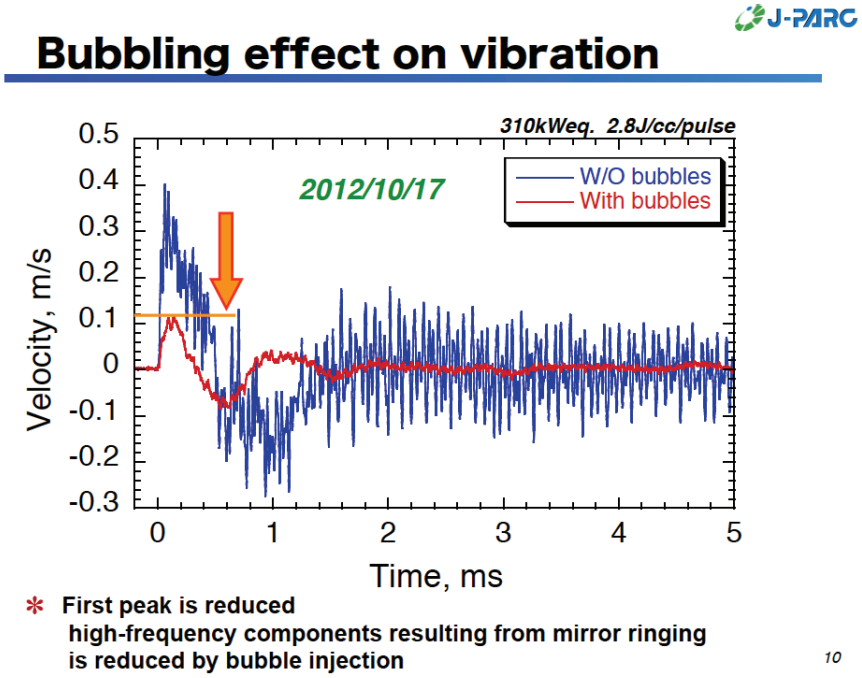

Figure 6.2. Vibration data from Japan Spallation Neutron Source (JSNS) target at J-PARC, illustrating the attenuating effects of gas bubble injection. *Source:* T. Naoe, 2012 SNS-JSNS Collaboration meeting.

The SNS began target gas injection in late 2017 with target T18. The 1.4 MW targets have employed orifice bubblers—arrays of gas injectors with openings of ~10 μm. Achieved gas rates have reached a maximum of 1.7 SLPM to date (~0.16% of mercury flow). Strain measurements capturing the dynamic pulse response of the mercury vessel have shown dramatic reductions with gas injection.

For example, the strain sensor layout on target T24 is shown in Figure 6.3, and strain response data without and with gas injection for sensor "A" (near sensor 1) is shown in Figure 6.4. Sensor A's strain is reduced by roughly 40% with gas injection, and rebound cycles are greatly attenuated.

It is convenient to use "strain range" (maximum–minimum) from measured responses as a rough metric for fatigue life (employed techniques for target design are more sophisticated). Furthermore, it is convenient to define a strain reduction factor as

$$reduction\ factor = \left(1 - \frac{gas\text{-}on\ strain\ range}{gas\text{-}off\ strain\ range}\right).$$

In the T24 target sensor A example, the reduction factor is about 45% at 1.4 MW with 1.7 SLPM gas injection. This level will significantly improve fatigue life in the high-cycles regime. It is nearly 40% at the rate of 0.8 SLPM—an indication of some saturation of the gas injection benefit.

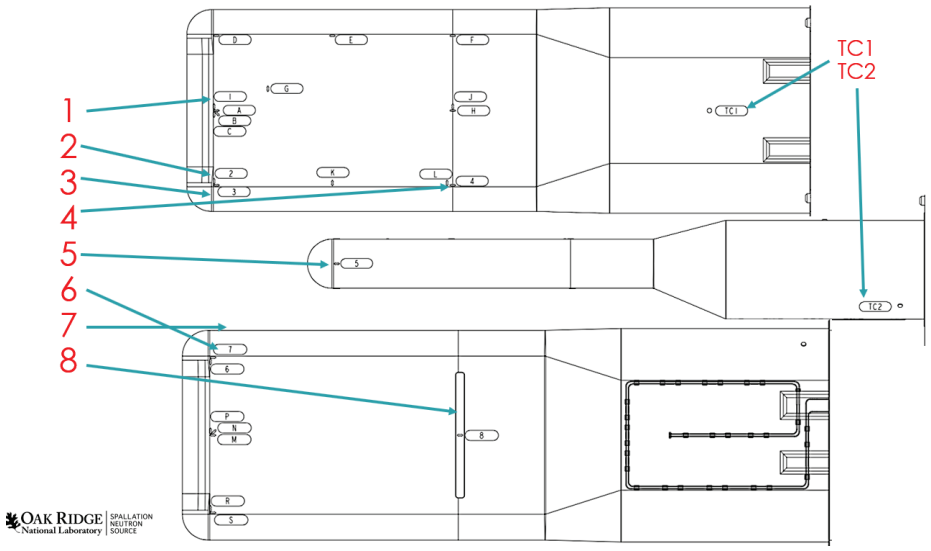

Figure 6.3. Sensor layout on the T24 mercury vessel. Lettered sensors are single-mode (SM) fiber type; numbered sensors are multi-mode (MM) type.

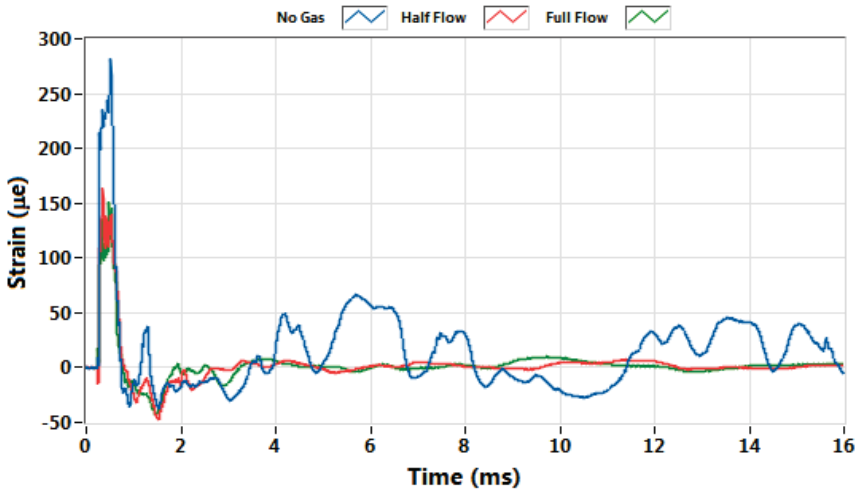

Figure 6.4. Pulse strain responses at sensor A without and with gas injection at 0.8 SLPM (half flow) and 1.7 SLPM (full flow), at pulse intensities equivalent to 1.4 MW operation.

Strain range vs. pulse equivalent power is shown on the left of Figure 6.5 for sensor A on T24. Reduction factors from the set of sensors are compiled for 1.4 MW pulses on the right of Figure 6.5 as a function of distance from the beam entry point on the vessel. Reduction factors farther from that point are greater than at the closest locations. Saturation is not complete—higher flows provided more reduction. Up to 10 SLPM can be accommodated for bubblers under the PPU design approach.

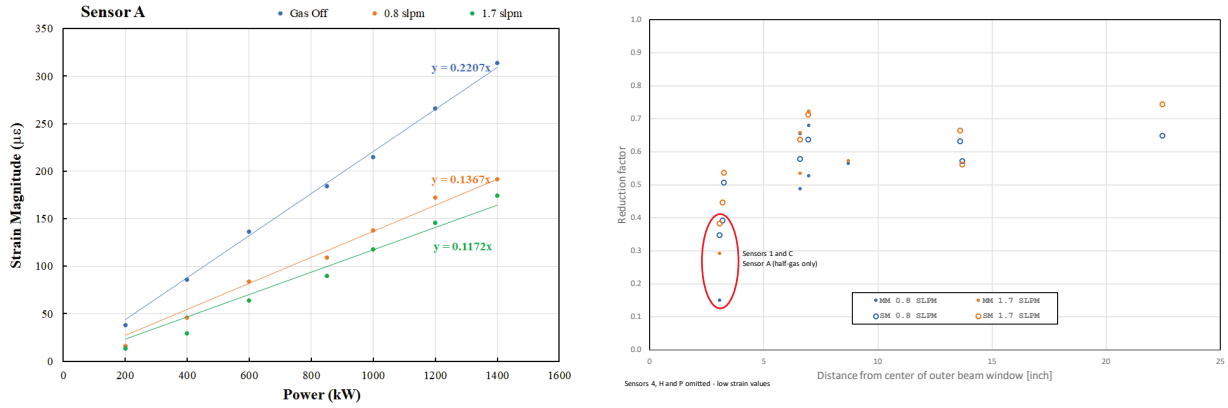

Figure 6.5. Pulse strain response at sensor A vs. equivalent power for gas off, 0.8 and 1.7 SLPM (left). Strain reduction factors plotted vs. sensor distance from the entry point of the beam are shown on the right for the suite of single-mode and multi-mode sensors on T24.

Goals for gas injection at the inner beam window have been adjusted as a result of R&D [Section 8.1] and PPU target design evolution. Direct gas coverage on the wall (a "gas-wall") is no longer considered essential, as was originally envisioned and described in the *Conceptual Design Report* [1]. A zone of relatively high gas volume fraction—bubble sizes unspecified—near the center of the inner window bulk side surface will be established by a nearby injector fed by a dedicated gas supply at up to 10 SLPM. That the injector and supply must be mechanically robust has been emphasized in the design. A bubbly zone in this location has good prospects of further reducing strain at the locations with low reduction seen in T24, i.e., where beam heat deposition is highest, as well as in further reducing cavitation damage of the inner beam wall. Without this injector, experiments have shown the main inlet flows leave this zone relatively low in gas fraction because of the bulk flow patterns.

Strain data with gas injection from 1.4 MW targets have indicated diminishing returns for strain mitigation with increasing gas flows. Extrapolation to 2 MW is problematic, as is extrapolation to substantially higher gas flows envisioned with PPU. Considering the strong desire to exceed the 1,250-hour PPU lifetime goal, and the consequences of high power at the power beam repetition frequency, which might be pursued when the STS begins operation, PPU plans for high gas rate capability are unchanged.

Mitigation of cavitation damage has been demonstrated in SNS targets operated with low levels of gas bubble injection. Figure 6.6 shows target vessel samples cut from target beam windows arranged as if viewed from inside the targets looking into the beam. The extreme left and right samples are outside the incident beam and part of the mercury containment layer. The center three samples are from the inner beam wall. Target T18—the lowest row of samples in Figure 6.6—was the first gas injection target. The T18 inner wall is not fractured, and cavitation damage is less than targets without gas injection. There are some through-holes in the T18 center sample. Those through-holes align with locations of erosion on the outer beam wall (the containment wall)—an indication that protection of the inner wall should be a priority of the PPU design.

Observations of cavitation damage vs. target gas rate provide encouragement that higher rates are more effective in reducing damage. Figure 6.7 presents similar sample images from only jet-flow targets with increasing gas rates. Despite having the highest total energy and average power on target, T-20 suffered the least apparent damage because of its higher gas injection rate.

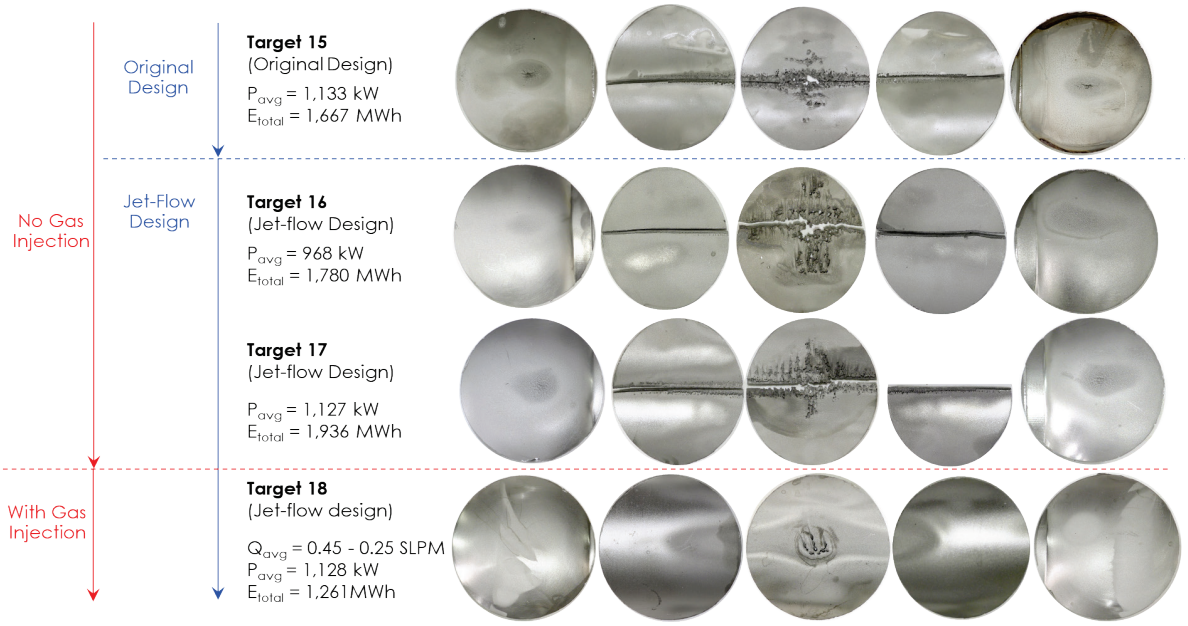

Figure 6.6. Beam window sample surfaces facing bulk mercury from different designs, including the first with gas injection (target 18).

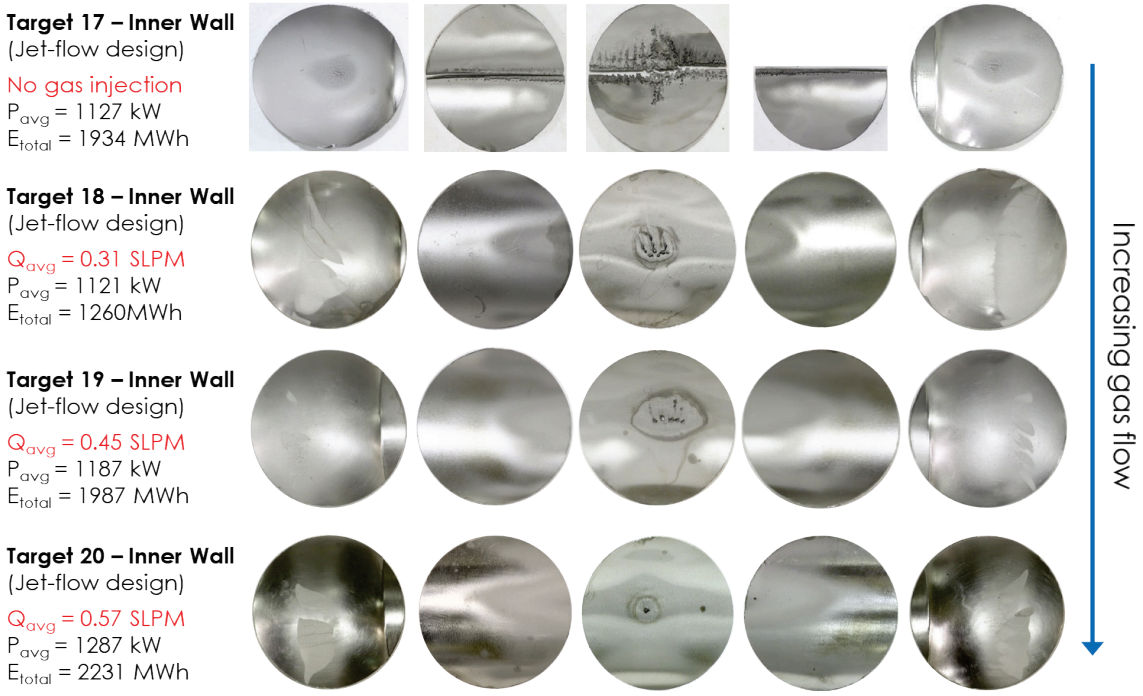

Figure 6.7. Jet-flow target samples illustrating damage vs. gas rate.

Recirculating gas compressors will be used primarily to limit helium consumption. They will be capable of injecting up to 20 SLPM at 60 psig and of lower flow rates at up to 100 psig. The selected location of the compressors is the carbon adsorber room. Once-through gas supply operating capability is also specified for system reliability and flexibility. In recirculating mode, gas can be drawn from either between the room temperature delay beds and the copper oxide bed, or downstream of all MOTS treatment beds before direction to the hot off-gas system.

The target module vent line will be redesigned to ease venting of as much gas as possible within the return channel of the target mounting block. However, additional gas removal is necessary to ensure that the amount of gas flowing to the heat exchanger is of the same order as that in current 1.4 MW operation, i.e., less than 2 SLPM of injected gas. R&D for development of a GLS for the mercury has produced a viable concept that fits within constraints of SNS piping and shielding. Details of the GLS internal design and venting are mature but continue refinement under R&D activities.

A mercury pump OFT has been designed to protect against hypothesized scenarios of liquid mercury overflowing the pump tank and potentially escaping the service bay. Its design and installation are part of the mercury process systems.

The MOTS will be upgraded to handle a steady gas flow rate up to 20 SLPM and a higher transient gas flow rate that could be caused by the release of a large gas pocket in the pump tank. Treatment bed stability, efficacy, and thermal loading have been considered in upgrade plans. A second carbon delay bed will be installed in the GAR to increase the delay of vented spallation hot gases and provide the ability to swap out a carbon canister when necessary.

High-rate target gas injection was a positive USI identified in the *Preliminary Hazard Analysis* [7] issued in 2017. It was further addressed in the PPU *Hazard Analysis Repor*t [8] issued January 2020. A comprehensive approach to addressing this issue, including hardware and controls designs, has progressed through internal reviews. Another off-normal hazard review is planned for late FY 2020.

6.4.3 FINAL DESIGNS AT THE CD-2/3 REVIEW

The following FTS systems equipment will be at final design status at the time of the CD-2/3 review:

- MOTS room temperature delay bed, GAR crane (P.5.8.2)
- 2 MW target (P.5.9)

All other new or upgraded FTS systems equipment is at preliminary design status.

6.4.4 References

1. B. Riemer, *Conceptual Design Report: Mercury Target Gas Injection*, SNS 106010000-TR0132-R00, Oak Ridge National Laboratory, 2016.
2. B. Riemer, *PPU FTS Systems 2 MW Target Development Plan*, PPU-P05-PN0001-R00, Oak Ridge National Laboratory, April 2017.
3. C. Barbier, *Addendum to the PPU 2 MW Target Development Plan*, PPU-P05-PN0001-R01, September 2019.
4. Neutron Science Directorate, *Target Management Plan*, 106010000-PN0005-R07, Oak Ridge National Laboratory, December 2019.

5. P. Rosenblad, *Gas Injection Initial Implementation (GI3) Conceptual Design Review (CDR) Report*, 106010000-DE0004-R00, Oak Ridge National Laboratory, September 2016.
6. K. Okita, S. Takagi, and Y. Matsumoto, "Propagation of pressure waves, caused by a thermal shock, in liquid metals containing gas bubbles," *Journal of Fluid Science and Technology* **3**(1), 116–128, 2008.
7. R. M. Harrington and S. M. Trotter, *Preliminary Hazard Analysis in Support of the Proton Power Upgrade Project*, PPU-P01-ES0001-R00, Oak Ridge National Laboratory, May 2017.
8. *Proton Power Upgrade Project Hazard Analysis Report*, PPUP-103-ES0004-R00, January 2020.

6.5 DETAILED WORK SCOPE DESCRIPTIONS

6.5.1 FTS Neutronics Evaluations and Upgrade Support

6.5.1.1 General Aspects

Most of the components of the SNS FTS were designed for 2.0 MW of 1.0 GeV proton beam power incident to the target. At a constant power of 2.0 MW, increasing the proton energy from 1.0 to 1.3 GeV decreases the proton current from 1.25×10^{16} to 0.96×10^{16} protons/s. The neutron yield per proton on thick high-Z target scaling is approximately linear with the proton beam energy according to Hilscher [1], so the neutron source strength remains unchanged at constant power for the proton energy increase considered here.

Nevertheless, the proton energy increase will cause changes in the particle flux distributions in the target station systems; the proton range (i.e., the distance to which a proton can penetrate into bulk materials and continuously lose energy through ionization until it stops) into the mercury target depth will increase from 45 to 64 cm; the high-energy fraction of the secondary neutron source is more (proton beam) forward directed, causing higher heating power deposition and higher material damage in the forward direction.

Both effects will have an impact on local radiation-induced heating rates, material damage and radiation fields, triggering a reassessment of practically all target station components starting out with neutronics evaluations.

With the availability of mightier computer systems and advances of analysis tools, the SNS target systems can be assessed at a much-refined level compared with the time of the SNS design. On the neutronics side, quantities of interest such as heating rates, material damage rates, and flux fields are nowadays calculated in pixelated 3-dimensional (3D) mesh structures with cubic-millimeter resolution if required. Additionally, these analysis results are generally mapped at the provided resolution into thermal and mechanical analysis workflows. In the past, the spatial dependence of the quantities of interest was obtained as functional dependencies based on bounding-curve analyses results; these overestimated the integral heating badly but often missed peak heating, as estimated heating values were generally averaged over larger spatial zones. The new analysis approach has uncovered some weaknesses in the original engineering designs despite the original generously applied safety factors. The reanalysis efforts for PPU have proved to be a worthwhile undertaking.

New developments of the MCNP6 code allow us to base analyses on CAD-based design models, rather than on neutronics models reconstructed from dimensional information obtained from CAD designs. This new capability was particularly applied to systems of high complexity, such as the mercury target and the IRP and moderators (the latter work was done in support of SNS operations).

The basis for neutronics analyses was the target station configured with an aluminum PBW, which causes smaller proton beam losses to the target, experiences less heating, imposes lower proton beam scattering compared with the original Inconel 718 window design, and has a somewhat longer lifetime. If the decision of using an aluminum beam window were reversed in favor of the Inconel 718 window, the higher proton beam scattering would increase the peak heating deposition in the CV proton flight channel toward the target, the ORP, and the IRP. The increase would impact the peak temperatures and stress levels in the components and impact the ORP lifetime. The level of impact for a Inconel PBW was not quantified in detail.

Furthermore, all analyses of energy deposition assumed an IRP configuration like that of IRP2, which is the heavy-water-cooled IRP variant. Because IRP2 has a lifetime limitation of 28 GWh, owing to the decoupled moderators' neutron-poison burnup, it is expected that IRP2 will be replaced by IRP3 by the time FTS is operated at PPU conditions. The designs of IRP2 and IRP3 are very similar and should have little impact on the analysis outcomes summarized here. As the IRP is a disposable target station component and will be replaced at 3–4 year intervals, the IRP design is not part of the PPU project but is dealt with by SNS operations.

Unless otherwise stated, all neutronics analyses were conducted with the latest Monte Carlo (MC) codes of the MCNP family MCNPX version 2.7 or the MCNP6 code version 6.1, on computing cluster systems, where they were centrally installed, tested, and executed. Activation analyses involved exclusively the CINDER90 transmutation engine and the scripts from the CINDER-1.05 RSICC code package driving multicell analyses with radionuclide production rates and neutron fluxes obtained from MCNP simulations. All the analyses are documented in dedicated reports, which were reviewed by subject matter experts before release and are referenced in the following subsections.

In case neutronics analyses are part of wider engineering analysis workflows and feed into designs of subcomponents, the analysis outcomes are presented and summarized in the dedicated subcomponent chapters. The following sections present the neutronics analysis effort summarizing the major findings of subject areas.

6.5.1.2 Proton Beam Modeling

The requirement for the original SNS 1.0 GeV proton beam on the target was a peak current density of $\leq$0.25 A/m^2 at 2 MW power with 95% of the beam impinging on the target within a footprint of 70×200 mm^2 centered at the target axis [2]. Later, three beam profiles—nominal, overfocused, and underfocused—were generated for target design analyses, with a nominal beam meeting the initial requirements and about 20% higher/lower peak proton current densities for over-/underfocused beam conditions [3].

New proton beam profiles have been generated for the PPU beam condition (2 MW power, 1.3 GeV proton energy) to serve the neutronics analyses. These were based on two million proton tracks simulated by the ORBIT code through the SNS linac, accumulator ring, and proton beam transport to the PBW and the target nose. A first-effort profile providing a peak proton current density of 0.22 A/m^2 at the target nose was deemed too peaked [4] and was subsequently replaced by a set of *preliminary design* nominal, overfocused, and underfocused beam profiles for detailed analyses with beam characteristics as detailed in Table 6.1 [5]. The *preliminary* nominal beam profile thereof was applied in simulations for all target station components going into the final design stage, except for the target module, which employed heating from the final beam profile.

Table 6.1. Proton beam characteristics of nominal, overfocused and underfocused beams applied to target design and neutronics analyses

Cases	*Preliminary* proton beam at 2 MW power Peak current density (A/m^2)		*Final* proton beam at 2 MW power Peak current density (A/m^2)	
	PBW	Target	PBW	Target
PPU underfocused	0.162	0.150	0.167	0.160
PPU nominal	0.202	0.191	0.187	0.181
PPU overfocused	0.223	0.210	0.207	0.203
Nominal FTS [2]	0.251	0.254		

A subsequent set of *final* nominal, overfocused, and underfocused beam profiles has since been generated for the target module final design engineering evaluations [6] The differences are mainly important to target engineering analyses. Some subset of other neutronics evaluations will be revisited with the *final* nominal beam profile and documented at a later date.

6.5.1.3 Shielding Evaluations

All SNS target station and neutron instrument shielding was designed for 2 MW proton beam power at 1 GeV proton energy. A simple hand calculation formula [7] indicates that the dose rates from secondaries of proton interactions at 1.0 and 1.3 GeV at 2 MW power produce only insignificantly higher radiation dose rates for scattering angles of 30°, and lower-but-equal (relative to the incident proton beam direction) or lower dose rates at higher scattering angles [8]. Nevertheless, full-scale radiation transport analyses were employed to verify that the target monolith shielding and the instrument shielding meet the dose rate requirements of 0.25 mrem/h in generally accessible areas, and below 20 rem/h in accident conditions triggering beam shutdown with radiation monitors, as outlined in the SNS Final Safety Assessment Document [9].

The target monolith shielding was verified by the same hybrid MC and discrete ordinates analysis codes (MCNPX and DORT) applied for the original FTS design. The target monolith is accessible only in the angular range of 35–145°. Neutron source terms were generated at forward direction averaging between 20 and 60° with 3D MCNPX analyses and then fed into the DORT code as internal boundary sources of a 2D (R,Z) transport analysis using an HILO2K multigroup cross section with 2 GeV upper energy [10]. The dose rates on the outer surface of the shielding monolith increase slightly but remain below the goal of 0.25 mrem/h.

To verify the neutron beamline shielding analyses, the source terms at the CVI locations (effectively the start locations of the beamline neutron optics) of beamlines BL2 and BL17 for backward-directed beams at 135°, for BL5 at 90°, and for BL9 and BL10 at 35° were reassessed applying the 3D as-built target monolith model to MCNPX simulation with a 1.3 GeV 2MW incident proton beam on target [11]. For BL5, the analyses results were only about 10% higher source intensities across all energies; and for BL9, an indication of 100% higher intensities for energies from 300–800 MeV was seen. As the source terms for BL5 and BL9 exhibited some elevation due to the PPU beam conditions, the shielding analyses for the CNCS and CORELLI instruments occupying BLs 5 and 9, respectively, were repeated, applying the new source terms. For both beamlines, the shielding has been shown adequate for PPU conditions with doses remaining below the goal of 0.25 mrem/h [12][13].

Further shielding analyses were conducted for the coolant process streams of activated water, in particular the water delay and GLS tanks that delay the propagation of water into the basement to eliminate N-16 (decay with 6–7 MeV gamma emission) and remove the radiolysis gases [14]. The workflows used

MCNPX to generate neutron fluxes and high-energy particle radionuclide production rates in water (loop 2 and 3) and the heavy water (loop 4), and CINDER90 to decay the radionuclides in the transport time from the radiation exposure location to the delay and GLS tanks, considering nominal flow velocities. The final transport analyses with source terms of decay gammas and decay neutrons (for loop 4) confirmed that all delay and GLS tanks are well-shielded by high-density concrete thicknesses of 1.45 m and 0.85 m, respectively, with a 0.25 m conservatism in shielding thickness. (to be verified!!)

The shielding of the carbon adsorbers (delay beds)—part of the MOTS providing the decay time for noble isotope off-gases from the mercury loop—was reassessed. It was assumed that, in equilibrium, the produced noble gases are emitted instantly and deliver gamma sources into the carbon bed with a 1-minute delay. At 1.3 GeV of proton energy, the radionuclide mix originating from the proton beam impact is different from the mix for a 1.0 GeV proton-driven system. The 17.2 cm thick radial and 15 cm lid lead shielding on the existing delay bad was shown to be sufficient to achieve dose rates outside the adsorber drum of below 100 mrem/h, as was previously demonstrated for 1.0 GeV operation [15].

In-cell shielding changes are required for PPU modifications to the mercury process loop. Currently, all mercury loop components are shielded by 10 cm thick steel shielding in the target service bay, and this requirement was extended for all PPU modifications of the loop. The mercury GLS was designed to fit under the shielding panels. After beam shutdown, i.e., for target exchange, the shielding panels may be removed. About 135 kg of activated mercury may be trapped in the GLS and would act as an additional source term in the target service bay. The dose rate at 30 cm distance from the GLS was calculated to amount to only 260 rem/h at 6 hours after beam termination [16], which was deemed acceptable considering that a retracted and shielded target would deliver dose rates about 8 times higher [17].

6.5.1.4 Heating Power Deposition

Table 6.2 gives an overview of integral heating power deposition in the target station components. At the same power level, the higher proton beam energy trends to cause higher secondary particle leakage, thus reducing the integral beam heating deposited into the target, and tends to increase the heating slightly in components surrounding the target. Overall, the integral heat deposition in the target station environment is not changing much as already found in pre-CDR scoping studies [18][19].

Table 6.2. Integral heating power deposition into target station components based on 2 MW incident beam power.

Component	Heating (kW)		Heating ratio 1.3-GeVcase/ 1.0-GeVcase
	1.0 GeV case	1.3 GeV case	
PBW module	12.0	10.2	0.850
Target	1252	1155	0.922
Inner reflector plug	296	317	1.071
Outer reflector plug	191	208	1.091
Core vessel	54.6	57.2	1.048
Total	1806	1748	0.968

Similar effects are seen in the heating directly deposited by radiation into the light water of cooling loop 2 (target shroud and PBW), loop 3 (moderator and premoderator water), and the heavy water of loop 4 (IRP, ORP and CV) contributing to radiolysis. Contributions to components exposed to direct proton beam are reduced; however, water heating in surrounding components is increased. Table 6.3 lists the split-up of the contributions for 1.0 and 1.3 GeV beam energy [20][21]. Loop 2–4 contributions are

calculated from prompt radiation in MCNPX calculations, whereas the mercury heat exchanger water is exposed not to prompt radiation but to decay gamma radiation originating from activated mercury.

Table 6.3. Beam power deposited directly into water and heavy water of cooling loops 1-4 based on 2 MW incident beam power.

Zone	Heating (W)		Heating ratio 1.3-GeVcase/ 1.0-GeVcase
	1.0 GeV case	1.3 GeV case	
LOOP1-Mercury heat exchanger	–	9	–
LOOP2-Target-water	6461	6138	0.950
LOOP2-PBW-water	1687	1407	0.834
LOOP3-Moderators	10285	10852	1.055
LOOP4-IRP	30013	31809	1.060
LOOP4-ORP	6632	7228	1.090

Detailed energy deposition calculations with fine spatial resolution were conducted for all target station components except the PBW. The PBW sees lower proton beam current at a constant 2 MW power level and hence lower charged-particle–induced power deposition and lower secondary particle reactions.

Conceptual analyses for the PPU FTS target started out by providing heating power deposition from the present-day design basis FTS beam profile (but at 1.3 GeV proton energy and 2 MW) into an infinite half space of mercury for initial target design analyses [22]. For preliminary and final designs, neutronics delivered detailed heating information to the target and target shroud [23][24][25] for pixel sizes of $2.5\times2.5\times2.5$ mm^2. The analysis models were generated directly from CAD designs, including conical-shape nose designs that include bubble generator, bottom-to-top sweeping mercury flow channels. Analyses were provided for nominal, overfocused, and underfocused proton beams (see Section 6.2.1.2), and analyses for offset nominal beams were also required and delivered. Details are discussed in the target design section. Table 6.4 compares peak incident proton current densities, peak power deposition in steel and mercury, and integral steel and mercury heating for the FTS blue-target design [3], and the preliminary and final PPU target designs. The peak heating rates are reduced by flattening the proton beam profile. With a flatter beam profile, proton current is pushed to outer areas of the target, where a larger fraction of secondary radiation can leak from the target and reduce the integral heating.

Table 6.4. Target vessel heating deposition assuming 2 MW proton beam power.

Quantities	Target designs		
	Conceptual [3]	PPU-preliminary	PPU-final
Peak proton current density (A/m^2)	0.254	0.191	0.181
Peak steel heating (W/cc)	608	504	487
Peak mercury heating (W/cc)	799	787	763
Integral steel heating (kW)	116	120	103
Integral mercury heating (kW)	1105	952	984

Although 1.3 GeV protons incident on the target range out at about a 65 cm depth at (compared with 45 cm for 1.0 GeV), the secondaries produced in nuclear reactions in the target and sprayed into all directions carry some of the energy of the primary beam into the surrounding structure. At higher proton energies, the forward-directed secondaries have higher energies than in the original SNS design and

penetrate deeper into the shielding. Simulations show a factor of 2–3 higher local heat deposition in the ORP around the target insertion port [26]. Similarly, the CV shielding experiences increasing heating around the target carriage of 40% [27]. Being at the most forward direction, the target carriage receives 542 W at 1.3 GeV, which is about 40% higher than with 1.0 GeV [28]. Detailed heating maps are provided for thermal and structural evaluations of the respective components covered in later sections.

The CVI received special attention because they are credited engineering devices to enclose mercury vapor in case of a major target fracture [29]. CVIs are exposed to radiation streaming through the neutron flight channels pointing at the moderators. Single-beam and dual-beam CVIs were investigated for the forward-directed BL8 and 9, and for 90° beamlines BL4 and 5. About a 10% increase in energy deposition is seen by converting from 1.0 to 1.3 GeV beam energy at constant beam power in line with the general finding of increased leakage of secondary radiation at increased beam energy.

The evaluation of the IRP with the PPU beam is not part of the PPU project. However, it must be mentioned here that the impacts of the PPU target redesign with a narrowed nose, which results in higher radiation leakage, was considered in the IRP3 design because it will be the first IRP version impacted by PPU changes [30].

The CV experiences its highest heating rates at the downstream side of the PBW shaft and at the downstream side of the proton flight path toward the target, where 0.59 W/cc and 0.30 W/cc at the respective locations are reported [31] This analysis assumed operation with an aluminum PBW, for which window scattering is reduced by a factor of 3 compared with an Inconel window. A potential switch back to the proven Inconel PBW would strongly impact the heating of this area and require further neutronics and thermal analyses.

6.5.1.5 Radiation-induced Material Damage and Component Lifetime

Radiation-induced material damage calculations in terms of dpa and/or helium implantation in units of helium atoms parts per million material atoms also benefits from the increased granularity. Like energy deposition evaluations, the impact of the PPU increase in proton energy from 1.0 to 1.3 GeV is felt in local variations of material damage. Further, material damage is accumulated over long periods of time. With the PPU extending the life of the FTS from 40 to 60 years, the accumulated material damage was assessed considering the lifetime extension for components that are in service for the life of the facility.

As life-of-facility structures, the ORP, CV, and CVIs were assessed for accumulated material damage. The ORP provides actively cooled steel shielding stacked in a plate arrangement into a cylindrical structure within a SS316 vessel wrapped around the IRP. Horizontal penetrations for flight channels for proton beam delivery and neutron beam extraction, and a port for target insertion, are designed into the ORP. Neutron- and proton-induced dpa production rates were analyzed for 1.0 and 1.3 GeV 2 MW incident beam conditions [32]. Figure 6.8 shows total dpa production rates in the ORP vessel in horizontal and vertical cuts through the ORP center, defining locations A and A’ around the target port and B and B’ around the proton flight path, where dpa production rates were highest. The production rates at these locations are listed in Table 6.5. The dpa production rates in the forward direction increase by 40–60% as the proton energy increases (locations A and A’); but they are essentially unaffected by the energy increase in the backward direction (locations B and B’), assuming a constant power level.

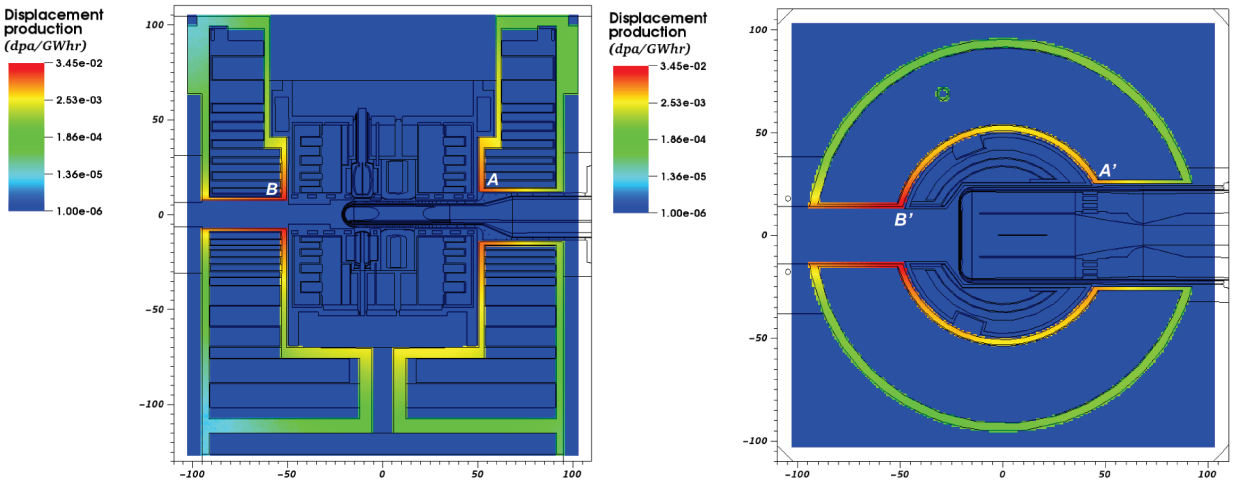

Figure 6.8. Horizonal view (right) and elevation view (left) of dpa production rates in ORP for a 1.3 GeV 2 MW proton beam incident on the target.

Table 6.5. DPA production rates at locations defined in Figure 6.8 for 1.0 and 1.3 GeV 2MW proton beams incident to the target, and accumulated dpa assuming operation at 1.0 GeV for 100 GWh until CY 2026, and at 1.3 GeV for 400 GWh beyond CY2026.

Location	dpa production rates (dpa/GWh)		dpa accumulated in 60 years
	1.0 GeV	1.3 GeV	
A	0.0080	0.0130	6.00
A'	0.0054	0.0073	4.46
B	0.0208	0.0207	10.36
B'	0.0348	0.0345	17.25

Surprisingly, the location of the peak dpa was found to be the downstream section of the proton flight port of the CV and upstream of the target module. This means that neutron backscattering from the target is the main contributor. Over the projected FTS lifetime of 60 years, this location is projected to accumulate 17.25 dpa in radiation damage. This projection considers the material radiation damage incurred over the past 10 years and assumes operation for the next 10 years at 1.4 MW and 1.0 GeV, followed by 40 years of operation at PPU conditions (2.0 MW and 1.3 GeV). This rate exceeds the original design basis limit of 10 dpa and the current administrative limit of 12 dpa for the replaceable target module. For this reason, the dpa limit of ORP was revisited and extended from 10 to 20 dpa considering the local temperatures, stress, and limited load cycling [33].

Previously, the location with the highest dpa was found to be the upstream section of the proton flight channel. For this reason, this location was specifically looked at [31]. As SNS has switched from an Inconel-718 to an Al6061-T6 window, the scattering from the window is reduced by a factor of 3, so that the location of peak dpa production has shifted from the upstream position (near the PBW) to the downstream position (near the target), accumulating 4.4 dpa over 60 years.

Also, the CVIs were reinvestigated for accumulated radiation damage [29]. The dpa production rates (dpa/GWh) in the aluminum windows of the inserts, the parts with the highest exposure, were found to be little affected by the proton energy increase. Despite the lifetime increase, the windows will accumulate at most 3% of the assumed limit of 30–40 dpa.

6.5.1.6 Moderator Performance

The moderator positions are fixed by the viewing ports of the 24 SNS beamlines, so repositioning the moderators with regard to the target monolith coordinates is out of the question. However, positioning the moderators relative to the target nose by changing the target body length is feasible. This approach was investigated in the early stages of the PPU project to see if a performance advantage might be gained. In part, increasing the proton beam energy acts similarly to moving the nose of the target more downstream because at a higher proton energy, the location of peak neutron production is shifted deeper into the target. The result is ~8% performance gains for the coupled moderators in the downstream position [18]. MC simulations were conducted to evaluate the moderator performance by cold and thermal time-averaged brightness metrics for cold and thermal moderators, respectively, with a dedicated PPU proton beam profile [4]. Otherwise the SNS as-built target station model changed the target body length by as much as ±2 cm [34]. Increasing the length by 2 cm decreased the coupled moderator brightness by 5% and increased the decoupled moderator brightness by 2.5%, as shown in Figure 6.9. As the decoupled moderators serve twice as many instruments as the coupled moderators, no overall gains were seen to justify changing the present target length.

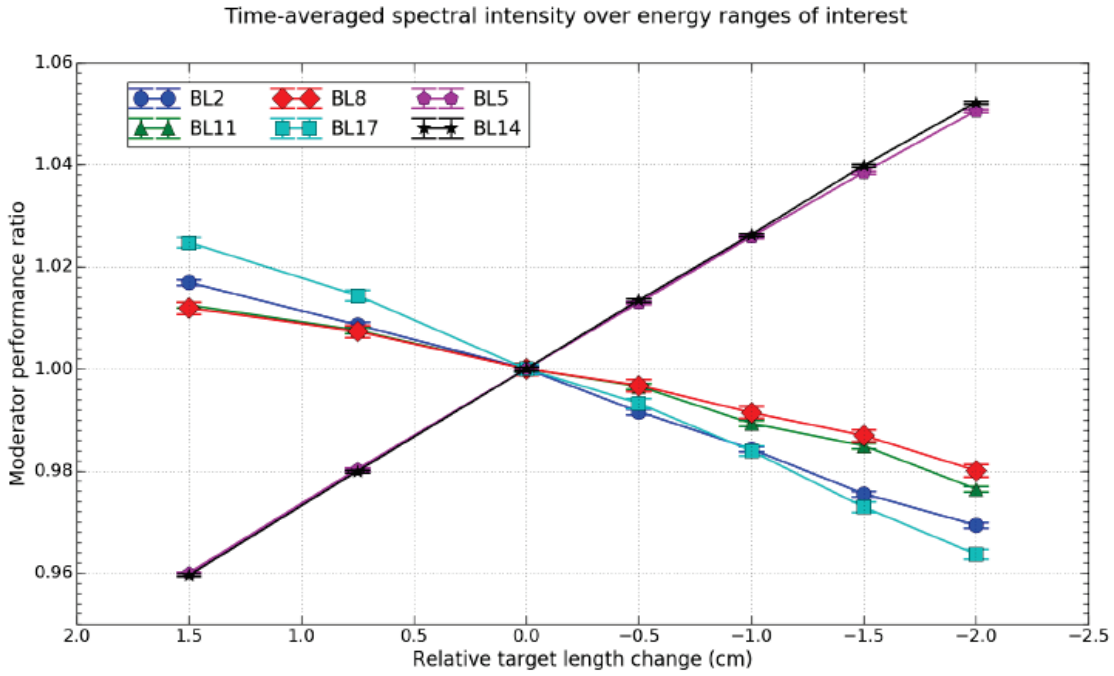

Figure 6.9. Moderator performance changes due to changes in the target body length at fixed target mounting and moderator positions.

Changing the target shape from the so-called 'Blue' 1.4 MW target design to the preliminary PPU target design, which introduces a horizontally narrowed nose, suppresses the overall brightness by about 5% [35]. The final target design recovers about 2.5% of the losses by including a somewhat broadened nose and requiring a vertically more peaked proton beam profile [36].

The PPU strives to reach at least the projected moderator performance reported by Lu for the FTS at 2.0 MW with 1.0 GeV protons [37]. This estimate assumed the hydrogen moderators are fed with 100% para-H_2 and the IRP is cooled with heavy water (D_2O). To ensure this condition is consistently maintained in the moderator, the hydrogen loops require the addition of catalyst devices that are planned as part of the PPU. Gains of 2% and 8% in the time-averaged brightness of the upstream and downstream

moderators, respectively, can be expected if the proton energy is increased from 1 to 1.3 GeV with the same para-H_2 and D_2O conditions applied. The impacts of upgrading the hydrogen loops with catalytic converters and pushing the hydrogen toward the almost full parahydrogen state was discussed with the Neutron Science Division and approved.

Presently, the decoupled hydrogen moderator experiences a measured 20% performance degradation at high-power operation for 3 Å neutron wavelengths, compared with the expected linear scaling with proton power [38]. For shorter-wavelength neutrons, this nonlinearity is less pronounced. This issue is partly being addressed independent of the PPU. The current thinking is that the degradation may be caused by power-induced changes in the orthohydrogen/parahydrogen ratio, and/or the reduction of hydrogen density in the moderator resulting from nuclear heating. If verified, this situation could be remedied by increasing the LH_2 flow or by modifying the internal flow geometry inside the decoupled hydrogen moderator, and in part by applying a catalyst system. No degrading effects have been seen so far in the coupled hydrogen moderators or in the decoupled water moderator.

6.5.1.7 Activation and Spent Component Disposal

The SNS mercury inventory in the target loop is for life-of-facility. Extending the facility life to 60 years and changing the proton beam energy impacts the radionuclide cocktail of the mercury loop. Using the following assumptions—

- a beam history of 60 years
- 10 years of as-delivered beam at 1.0 GeV
- 10 more years of 5000 hours per year at 1.0 GeV and 1.4 MW power
- an added 40 years of history at 5000 hours per year of 1.3 GeV energy and 2 MW power

—the shutdown activity accumulates to 1.67 MCi [39] in 2200 species of radionuclides. That is a slightly lower value than the 1.7 MCi reported [40] in early design analyses for 40 years of operations at 1.0 GeV and 2 MW power for 5000 hours per year. These data were provided to the environmental impact statement update. The earlier calculation did assume a stagnant mercury volume be irradiated and did not account for the dilution effects by the loop that were considered in the later analysis. Radionuclide map and activity levels at shutdown are depicted in Figure 6.10.

The bounding case of the radionuclide inventory was reassessed for 5000 annual hours of beam exposure at 1.3 GeV and 2 MW to investigate its impact for its disposal path [41]. Furthermore, the changes to the activity buildup in water loops 2–4 were studied [42][43][44]. For all water loop analyses, the dispersion of the activity in the loop volume was considered to lower the tritium buildup to at least 50% of the SNS design analysis values.

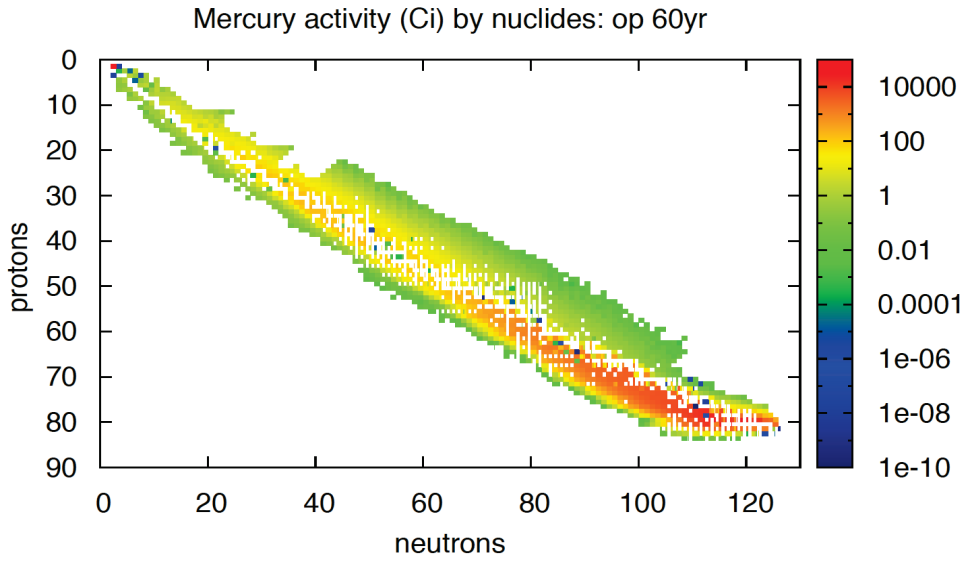

Figure 6.10. Mercury loop radionuclides and their activity at shutdown after 60 years of operation.

6.5.1.8 References

1. D. Hilscher, F. Goldenbaum, U. Jahnke, et al., "Neutron multiplicity distributions for GeV proton induced spallation reactions on thin and thick targets of Pb and U," p. 176 in *Proc. of Int. Workshop on Nuclear Methods for Transmutation of Nuclear Waste*, eds. M. Khankhasayev, H. S. Plendl, and Z. Kurmanov, Dubna, Russia, May 29–31, 1996, World Scientific, Singapore, 1997.
2. F. X. Gallmeier, D. Raparia, "Proton beam profiles at the target and at the beam dumps of the SNS," Fourth International Topical Meeting on Nuclear Applications of Accelerator Technology, Washington, D.C. November 12-15, 2000, American Nuclear Society, pp 240–245, 2000.
3. W. Lu, *Energy Deposition Calculation for the Blue Target*, SNS-106100200-DA0083-R00, Oak Ridge National Laboratory, May 2017.
4. W. Lu, F. X. Gallmeier, and J. A. Holmes, *A Tentative Incident Proton Beam Profile at PBW for the PPU Project*, SNS-106100200-TR0247-R00, Oak Ridge National Laboratory, May 2018.
5. W. Lu, F. X. Gallmeier, and J. A. Holmes, *Preliminary Incident Proton Beam Profiles at PBW for the PPU Project*, SNS-106100200-TR0255-R00, Oak Ridge National Laboratory, August 2018.
6. W. Lu et al., Incident Proton Beam Profiles at PBW for the Final Design of the PPU Project, PPUP-502-TR0003-R00 , Oak Ridge National Laboratory, April 2020.
7. A. H. Sullivan, *A Guide to Radiation and Radioactivity Levels near High Energy Particle Accelerators*, Nuclear Technology Publishing, Ashford, Kent, TN23 1JFW, England, 1992.
8. I. I. Popova, *Influence on Radiation Levels Inside the Klystron Gallery with Beam Energy Increase from 1 GeV to 1.3 GeV*, PUP0-342-TR0001-R00, Oak Ridge National Laboratory, September 2016.
9. *Spallation Neutron Source Final Safety Assessment Document for Proton Facilities*, SNS-102030103-ES0018-R00, Oak Ridge National Laboratory, June 2005.
10. K. Bekar and A. Ibrahim, *Design Analyses of SNS Target Station Biological Shielding Monolith with Proton Power Upgrade*, SNS-106100200-TR0219-R00, Oak Ridge National Laboratory, April 2017.
11. F. X. Gallmeier, *SNS Beamline Shielding Source Terms for Beams with 1.3 GeV incident Proton Energy*, SNS-107030700-DA0007-R00, Oak Ridge National Laboratory, April 2019.

12. F. X. Gallmeier, *Assessment of CNCS Beamline Shielding with PPU Source Term Based on 1.3 GeV Incident Proton Energy*, CNCS-05-70-DA0017-R00, Oak Ridge National Laboratory, June 2019.

13. W. Lu, *Shielding Analysis for CORELLI (BL-9)*, SNS-106100200-DA0063-R01, Oak Ridge National Laboratory, August 2019.

14. F. X. Gallmeier and I. I. Popova, *Target Station Water Loop Delay and Gas-liquid Separator Tank Shielding Analyses for PPU Conditions*, PPUP-502-DA0001-R00, Oak Ridge National Laboratory, October 2018.

15. I. I. Popova, *Shielding Analyses for the Mercury Offgas Carbon Delay Bed for PPU Conditions*, SNS-106100200-DA0103-R00, Oak Ridge National Laboratory, October 2018.

16. F. X. Gallmeier, *Assessment of Dose Rates in the Proximity of Mercury Gas-liquid Separator after Shutdown*, PPUP-502-TR0002-R00, Oak Ridge National Laboratory, February 2019.

17. P. D. Ferguson, *Calculation of Target Vessel Activation and Shield Boot Evaluation*, SNS-106100200-DA0013-R00, Oak Ridge National Laboratory, March 2004.

18. F. X. Gallmeier, *Neutronics Impact of the SNS Proton Energy Upgrade from 1.0 to 1.3 GeV*, SNS-106100200-TR0186-R00, Oak Ridge National Laboratory, January 2011.

19. W. Lu et al., *Impacts of 1.3 GeV Proton Beam on the Energy Deposition of FTS*, SNS-106100200-TR0218-R00, Oak Ridge National Laboratory, 2016.

20. F. X. Gallmeier, *Direct Nuclear Energy Deposition into Liquids of SNS Target Station for PPU Beam Conditions*, PPUP-502-TR0001-R00, Oak Ridge National Laboratory, March 2020)

21. I. I. Popova, *Heat Deposition in the Mercury Heat Exchanger for PPU Conditions*, SNS-106100200-TR0262-R00, Oak Ridge National Laboratory, December 2018.

22. W. Lu, *Energy Deposition Calculation on a Generic Mercury Target*, SNS-106100200-TR-0234-R00, Oak Ridge National Laboratory, August 2017.

23. W. Lu, *Energy Deposition Calculations for the Preliminary Design of the PPU Target*, SNS-106100200-DA0107-R00, Oak Ridge National Laboratory, January 2019.

24. W. Lu, *Energy Deposition Calculations for the Water Cooling Shroud of the PPU Target*, SNS-106100200-DA0108-R00, Oak Ridge National Laboratory, February 2019.

25. W. Lu, *Energy Deposition Calculations for the Final Design of the PPU Target Module*, PPUP-502-DA0002-R00, Oak Ridge National Laboratory, April 2020.

26. W. Lu, *Energy Deposition at the Outer Reflector Plug for 1.3 & 1.0 GeV Proton Beams*, SNS-106100200-TR0251-R00, Oak Ridge National Laboratory, April 2018.

27. W. Lu, *Energy Deposition at the Core Vessel for 1.3 & 1.0 GeV Proton Beams*, SNS-106100200-TR0257-R00, Oak Ridge National Laboratory, September 2018.

28. W. Lu, *Energy Deposition at the Target Carriage for 1.3 & 1.0 GeV Proton Beam*s, SNS-106100200-TR0259-R00, Oak Ridge National Laboratory, September 2018.

29. I. Remec, *Neutronics Assessment of the SNS FTS Core Vessel Inserts for the PPU*, SNS-106100200-DA0098-R00, Oak Ridge National Laboratory, April 2018.

30. W. Lu, *Energy Deposition at IRP3 under PPU Conditions*, SNS-106100200-TR0267-R00, Oak Ridge National Laboratory, August 2019.

31. W. Lu, *Radiation Damage and Energy Deposition along the Proton Flight Path for a 1.3 GeV Proton Beam*, SNS-106100200-TR0260-R00, Oak Ridge National Laboratory, September 2018.

32. W. Lu, *Radiation Damage at the Outer Reflector Plug for 1.3 & 1.0 GeV Proton Beams*, SNS-106100200-TR0258-R00, Oak Ridge National Laboratory, April 2018.
33. D. McClintock, *Review of the Administrative Dose Limit for 316L in the SNS Outer Reflector Plug at the Spallation Neutron Source*, SNS-106030000-TR0001-R00, Oak Ridge National Laboratory March 2019.
34. W. Lu, *Target Vessel Length Optimization for the PPU Project*, SNS-106100200-TR0250-R00, Oak Ridge National Laboratory, May 2018.
35. W. Lu, *Moderator performance Impacts due to PPU Target Preliminary Design* , PPUP-502-TR0004-R00, May 2020
36. W. Lu, *Moderator performance Impacts due to PPU Target Final Design* , PPUP-502-TR0005-R00, May 2020
37. W. Lu, *Moderator Performance of the SNS As-built Configuration*, SNS-106100200-TR0199-R00, Oak Ridge National Laboratory, January 2013.
38. F. X. Gallmeier, *Moderator Performance Measurements Utilizing Instrument Beam Monitors*, SNS-106100200-TR0266-R00, Oak Ridge National Laboratory, March 2019.
39. I. I. Popova, *Radionuclide Inventory for Mercury in the SNS Target Loop for PPU Condition 2 MW with As-delivered Beam History for the First 10 Years of SNS Operations*, SNS-106100200-DA0079-R00, Oak Ridge National Laboratory, November 2017.
40. P. D. Ferguson, *Radionuclide Inventory of the SNS Mercury Target*, SNS-106100200-DA0014-R00, Oak Ridge National Laboratory, July 2005.
41. I. I. Popova, *Target Vessel Activation and Waste Handling for PPU Conditions 1.3 GeV Proton Energy and 2.0 MW Power*, SNS-106100200-DA0080-R00, Oak Ridge National Laboratory, September 2016.
42. I. I. Popova, *Loop 2 Water Activation Estimate for PPU Conditions*, SNS-106100200-TR0261-R00, Oak Ridge National Laboratory, October 2018.
43. I. I. Popova, *Loop 3 Water Activation Estimate for PPU Conditions*, SNS-106100200-TR0248-R01, Oak Ridge National Laboratory, June 2018.
44. I. I. Popova, *Loop 4 Heavy Water Activation Estimate for PPU Conditions*, SNS-106100200-TR0249-R00, Oak Ridge National Laboratory, June 2018.

6.5.2 Mercury Process System Evaluation and Upgrades

6.5.2.1 Scope

The scope of PPU mercury process systems includes the following activities.

- Target carriage evaluations at 1.3 GeV
- Mercury pump OFT
- Mercury return line GLS
- In-cell target gas supply hardware

6.5.2.2 Assumptions

Assumptions include the following:

- Higher proton beam energy (1.3 GeV) will cause higher temperatures in the target carriage.
- Higher helium gas injection rates are necessary to mitigate the effects of higher proton beam power on the target.
- Higher helium gas injection will cause accumulation of helium in the mercury return piping/heat exchanger, and that will displace mercury and cause excessive mercury volume levels in the mercury pump.
- Helium gas can be separated from the flowing mercury in the return piping at a sufficient rate to prevent accumulation in the mercury return piping and heat exchanger.

6.5.2.3 Technical Evaluations

The heat removal capacity of the mercury process system with PPU beam operation is not an issue. The loop heat exchanger and flow capacity were designed for 2 MW, albeit with 1.0 GeV protons. The heating power to be removed is unchanged within the bounds of the original design basis uncertainties.

In any case, thermal-hydraulic assessments were made vs. power, assuming 65% of the beam power is deposited as heat in the mercury, to be removed by the process system. The assessments accounted for the loop and target flow losses in a 1.4 MW configuration (no GLS, jet-flow type target). Heat exchanger mercury and water outlet temperatures are shown vs. beam power in Figure 6.11. A key temperature design criterion is that the mercury exit temperature out of the heat exchanger does not exceed 60°C. This limit is reached at 2.3 MW with the mercury pump running at 350 rpm. It was verified that mercury expansion does not overflow the existing pump volume for power up to 2.8 MW. Increasing the pump speed increases the heat exchanger mercury discharge temperature because of decreased mercury residency time inside the heat exchanger.

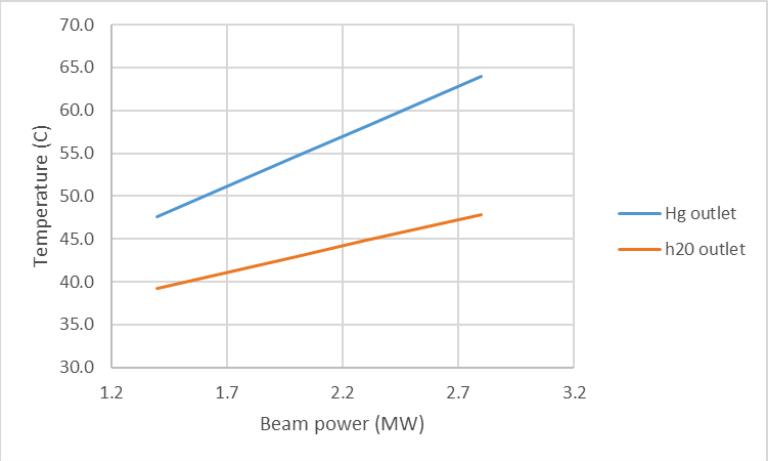

Figure 6.11. Peak mercury and water temperatures vs. beam power at heat exchanger outlets for the pre-PPU process loop and target configuration and 350 rpm mercury pump speed. (C. Barbier, D. Winder).

The designed PPU upgrades will incur a higher pressure drop in the mercury process loop because of the addition of a GLS and features of the PPU mercury vessel. The mercury pump will be operated at 400 rpm—its original design basis speed. Based on the preliminary target design and pressure loss factor of 20 for the GLS, mercury flow with PPU operation is estimated to be a 252 gpm volume flow—less than the 283 gpm under 1.4 MW/350 rpm conditions. The mercury temperature at the heat exchanger outlet will

be lower than the 2 MW/350 rpm pre-PPU loop configuration analysis because of the increased mercury residency time in the heat exchanger. The average mercury temperature out of the target will be higher but within the 90°C limit.

Target carriage operating temperatures have been evaluated for PPU design basis heating (2.0 MW with 1.3 GeV protons) [1]. The PPU evaluation was an update of the original SNS analysis work done with 1.0 GeV proton heating in 2003 using a simplified heating function. Current practices more accurately use mapping from neutronics analyses [2]. Carriage thermal analysis was performed using the finite element method using ANSYS Workbench 18.2 software.

Following the original analysis approach, two boundary condition cases for PPU heating were evaluated related to carriage exterior surfaces inside the tunnel (and inside the target box) during operation.

- Case 1: Natural and forced convection cooling conditions—depending on carriage region
- Case 2: Adiabatic conditions in the region positioned in the cart-liner tunnel during operation

The load case 1 simulated the normal "beam on" condition with forced convection cooling in the cart tunnel from a normally on air supply. The load case 2 simulated the loss of forced convection cooling during operation, a bounding scenario condition. Common to both cases are heat conduction to the carriage rails (fixed at 147°F) and mercury pipe supports (fixed at 140°F inlet pipes and 194°F outlet pipe). Both cases treat the exterior surfaces outside the tunnel adiabatically.

Steady-state temperature results from load cases 1 and 2 f are summarized in Table 6.6 and Figure 6.12 and Figure 6.13. Maximum temperatures of 198°F and 251°F are reached for load cases 1 and 2, respectively. These are approximately 34° higher and 4° higher, respectively, than the corresponding original thermal analysis cases. Temperatures at some other carriage locations are lower, but in general the temperatures are slightly higher with PPU heating. No temperature limiting criteria were defined in the original evaluations. PPU maximum temperatures do not present risk in terms of strength loss or mechanical function for the carriage materials (off-grade carbon steel shielding, 4130 steel, SS316L piping).

Table 6.6. Maximum temperatures in carriage with PPU heating.

Location	Load case 1 (°F)	Load case 2 (°F)
Target shelf	197.7	250.9
Front of carriage	140.5	157.1
Inside surface	134.5	140.6
Rails	147.0	147.0
Shielding between rails	136.7	151.8

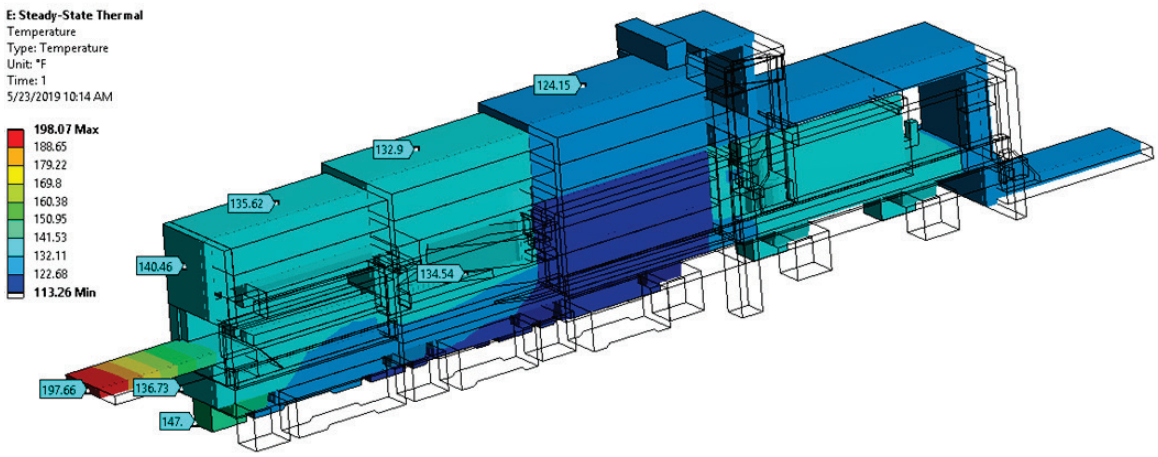

Figure 6.12. Carriage temperature with PPU heating with convection cooling in the tunnel (°F).

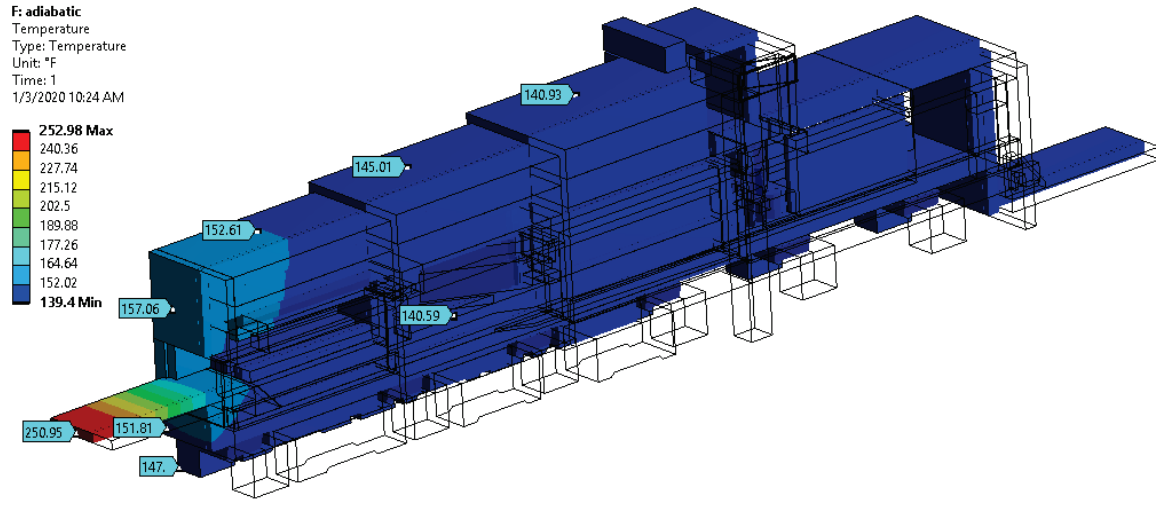

Figure 6.13. Carriage temperature with PPU heating with adiabatic conditions in the tunnel (°F).

6.5.2.4 Technical Design

Mercury pump overflow tank

Higher PPU target gas injection rates bring the potential for more gas accumulation within the mercury loop piping and heat exchanger. This would lead to more mercury displaced from the piping into the mercury pump tank. An unmitigated accident scenario is for the level in the pump tank to increase enough to completely fill it and send liquid mercury out the gas vent line and outside the service bay. The new PPU mercury pump OFT adds extra high-level volume capacity to the pump tank and allows mercury to freely return to the pump tank when the level recedes.

The following are requirements for the design of the mercury pump OFT:

- Provide 40 gal of volume capacity for displaced mercury from the mercury pump tank.
- Allow displaced mercury to return to the mercury loop.
- Provide shielding equivalent to that for the mercury pump—4.5 in. of steel—for the radioactive mercury
- Remotely install OFT and remotely maintain all equipment.
- Provide for gas connections from the mercury pump tank vent nozzle (existing) and the anticipated mercury return GLS vent line (described below)
- Provide gas connection for the loop seal vent line to MOTS (existing)
- Provide level measurement of the amount of mercury in the OFT
- Meet seismic design requirements for SDC-2 per DOE STD-1020-2012

The OFT preliminary design is based on the following assumptions:

- A single level measurement instrument is adequate.
- A servomanipulator and 7.5-ton crane are available for remote installation and maintenance.

Overflow tank description

The OFT is a passive design. It will be located on top of shielding blocks adjacent to the mercury pump and will be connected to the currently unused pump nozzle via a 1.5 in. metal flex hose. Excess mercury can flow freely between the pump tank and the OFT. When the mercury height in the pump tank exceeds the 82% level (mercury pump tank bubbler level instrument TGT_HG:Tnk_LY5121:Lvl), it will begin to flow into the OFT and rise to whatever level the volume requires. As the volume recedes in the pump tank, mercury will flow back into the pump tank from the OFT. The tank and associated piping will be shielded with 4.5 in. steel. A level instrument will provide a measurement of the mercury level in the OFT. The mercury pump OFT is shown in Figure 6.14.

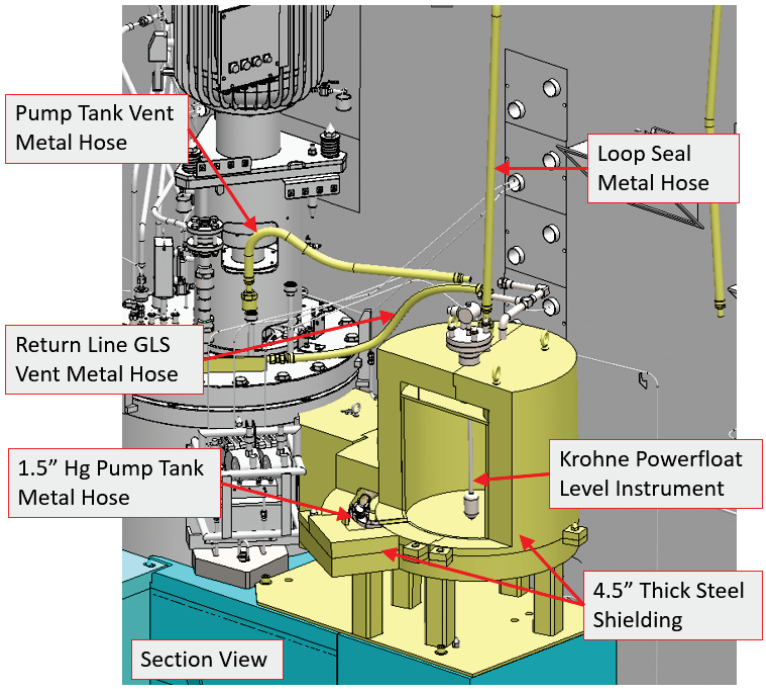

Figure 6.14. Section view of mercury pump overflow tank preliminary design.

The OFT will be vented to the MOTS off-gas system through the existing loop seal flexible metal hose, which presently connects to the mercury pump tank. New vent hoses from the mercury pump tank and the return line GLS will be connected to the top of the OFT. These hoses will provide a path to vent gas from those components and contain liquid mercury if it should be forced through the vent hoses.

A preliminary seismic analysis was performed for the OFT and support stand, including its shielding and the shield blocks underneath it to which the tank will be bolted. The analysis concluded that the existing structure and restraints for the OFT and supporting shield blocks are adequate for the seismic loads to meet the requirements of SDC-2, according to current codes and standards for SNS.

Return line GLS

The mercury return line GLS will remove a high flow rate of target gas before the return mercury reaches the heat exchanger and pump; it will maintain a mercury level in the pump tank equivalent to that under current low rate gas injection without a GLS. This will minimize the potential for displaced mercury in the process piping to send liquid mercury out the gas vent line into the MOTS. The only suitable location for the GLS is the return pipe elbow at the end of the target carriage. The return line GLS will maintain remote disconnect capability for target replacement. Separated gas will be routed to the OFT.

The following are requirements for the design of the mercury return line GLS:

- It will provide 90% removal efficiency for up to 20 SLPM of helium gas from liquid mercury in the return line.
- The GLS must be remotely installed and maintained.
- Installation planning will include removal of the existing 90° elbow connected by a 4-bolt Graylok.
- It shall not significantly interfere with other remote handling operations.
- It will provide for gas connections for the GLS vent line to the OFT hose connection.
- It will prevent liquid mercury from migrating into the helium vent line, or provide shielding for the vent line.
- It will meet seismic design requirements for SDC-2, according to DOE STD-1020-2012.

The return line GLS preliminary design is based on the following assumptions:

- A porous metal filter is adequate to prevent liquid mercury from getting in the helium vent hose.
- A servomanipulator and 7.5-ton crane are available for remote installation and maintenance.

GLS description

The PPU GLS will be installed in place of the existing 6 in. return line pipe elbow at the end of the target carriage. Functionality for routine connection of the GLS to the fixed return pipe during target exchanges will be maintained. The GLS will move with the target carriage during target replacement, just as the existing elbow does. The existing elbow location is shown at the left of Figure 6.15.

The design of the GLS (at the right of Figure 6.15) consists of a 16 in. diameter housing with an internal separator cone that causes the liquid mercury flow to circulate around the outside of the cone before flowing under the cone and out of the GLS. The rotationally enhance buoyancy will cause the gas phase to separate inward and upward. A connection for the gas vent hose will be located at the top centerline of the housing. All GLS components will be fabricated from 316L stainless steel.

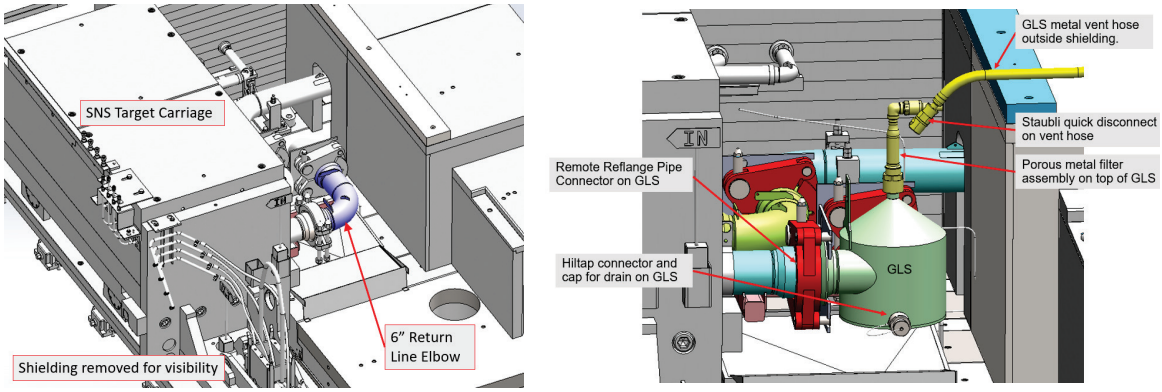

Figure 6.15. Location for the return line GLS preliminary design. Return line GLS preliminary design.

The GLS design includes a method to vent the helium gas from the top of the GLS to the OFT outside of the shielding. A flexible metal vent hose from the GLS will be routed through an opening in a new "spacer" shield block to the OFT. The hose will be supported by a stand attached to the pump tank lid (Figure 6.16).

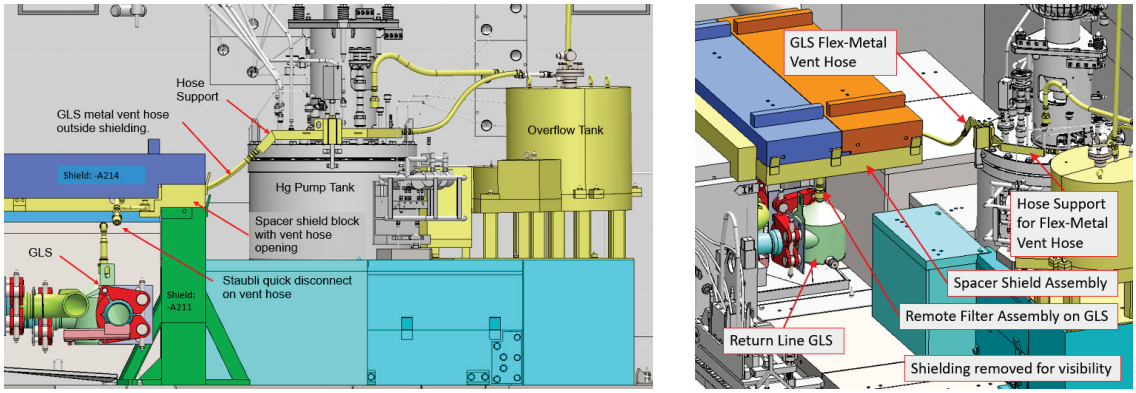

Figure 6.16. Return line GLS and shield blocks preliminary design.

Concerns were identified with regard to two potential issues during an Internal Preliminary Design Review for Safety and Controls (P.5.10):

- Liquid mercury in the GLS vent hose outside of shielding
- Mercury holdup within the GLS housing during the time it is outside of the shielding for target replacement

A porous metal filter is planned to deal with the potential for liquid mercury accumulation in the vent hose. Commercial off-the-shelf filters are currently used, with helium gas injection going into the target module. Tests with standard filters for the GLS application have led to the pursuit of custom-made filters, which will be validated in early 2020.

The GLS housing internal design is driven by R&D on gas separation from the return pipe flow. Space and interface constraints result in a "hold-up" volume of approximately 10 liters of liquid mercury after the mercury loop is drained. So long as the mercury mass is less than 200 kg—which equates to 14.8 liters—no additional credited controls beyond those already in place are needed to mitigate a target

service bay fire. A housing drain with a Hiltap cap is included but is not intended for use during routine target exchanges.

A new stand will support the metal vent hose between the GLS and the OFT. The support stand will be attached to a guidepost on top of the mercury pump and bolted to the top of the pump tank. All components in the GLS preliminary design are designed to be installed and maintained remotely using the remote handling equipment in the target cell.

A preliminary internal design review was conducted for the return line GLS in April of 2019. The design review comments were documented and have been addressed consistent with the current level of completion and the current level of the GLS development testing.

In-cell target gas supply hardware

The PPU in-cell target gas supply hardware will provide the supply flow for the gas wall/bubble zone in the mercury target at its inner beam window. The PPU target will use the existing in-cell supply hardware for its small bubble generators, but new hardware is needed for the gas wall injector. The scope of this design change is the hardware needed to transmit the gas from its supply point at a penetration into the service bay to the new vent line shield block gas supply line in the target carriage.

The following are requirements for the design of the in-cell target gas supply hardware:

- It will provide for up to 10 SLPM of helium gas at a pressure of 100 psig.
- The in-cell target gas supply hardware will be remotely installed and remotely maintained.
- It shall not significantly interfere with other remote handling operations.
- It will connect to the helium supply at the existing helium gas connection at the hot-cell wall.
- It will connect to the Staubli quick-disconnect connector on the new vent line shield block for the target carriage

The in-cell target gas supply hardware preliminary design is based on the following assumptions:

- A new vent line shield block will be installed on the target carriage either before or at the same time as the in-cell target gas supply hardware installation.
- A servomanipulator and 7.5-ton crane will be available for remote installation and maintenance.

In-cell target gas supply hardware description

The design for the SNS PPU in-cell target gas supply hardware is very similar to that for the existing hardware for target bubble injection. The target gas supply hardware is shown in light blue in Figure 6.17.

The gas supply line will be a weldment including ½ in. diameter stainless steel tube and flexible metal hose. The end connection at the candelabra end of the first hose will be a ½ in. female Hiltap connector. The other end connection for the first hose will be a 3/8 in. Staubli valved quick-disconnect. This will connect to a gauge and valve assembly that will be supported on a bracket-mount weldment. A second hose will use a Swagelok connector at one end and another Staubli quick-disconnect connector at the other to connect the gas supply to the vent line shield block connector on the target carriage. The quick-disconnect connectors will allow for the supply hose to be remotely disconnected and reconnected as needed for target replacement operations. The support mount for the valve and the gauge are designed to be remotely handled to hook onto the lift fixture on the dog-house shield to hold the assembly in place during operations.

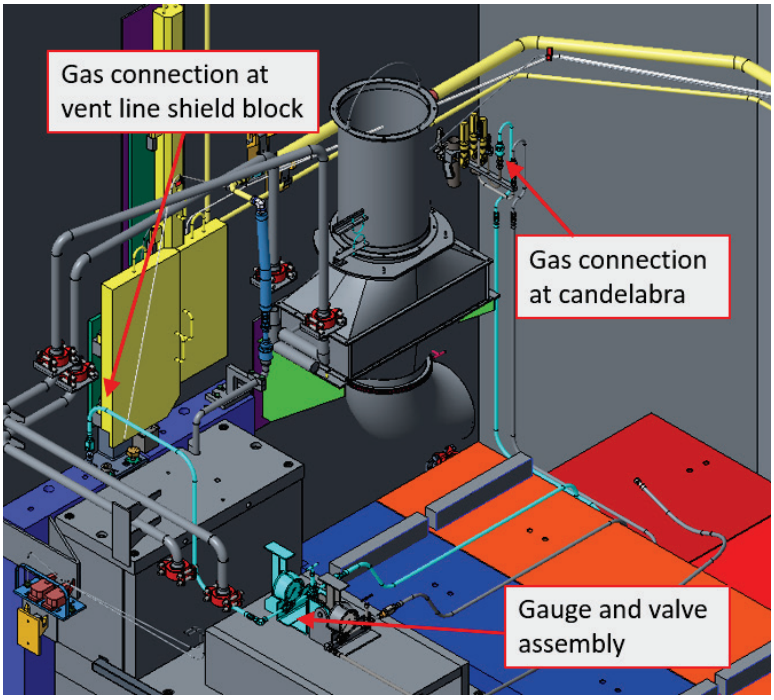

Figure 6.17. Preliminary design for in-cell target gas supply hardware.

A preliminary internal design review was conducted for the in-cell target gas supply hardware in June of 2019. The design review comments were documented and have been addressed consistent with the current level of completion.

6.5.2.5 References

1. O. Martinez, *Heat Transfer Analysis of the SNS Target Carriage Heating for PPU*, SNS-106010102-DA0004-R01, Oak Ridge National Laboratory, January 2020.
2. W. Lu, Energy *Deposition at the Target Carriage for 1.3 & 1.0 GeV Proton Beams*, SNS-106100200-TR0259-R00, Oak Ridge National Laboratory, September 2018.

6.5.3 Moderator Cryogenic Systems Upgrades

6.5.3.1 Scope and Introduction

The term “moderator cryogenic systems” (MCS) refers to the PPU project scope of work to differentiate it from the entire CMS.

The hydrogen in the target CMS comprises ortho- and parahydrogen, the concentrations of which are currently determined by the fluid temperature and by radiolytic conversion rates from para- to orthohydrogen (forward) and ortho- to parahydrogen (backward) by the neutrons incident on the liquid hydrogen.

Normal equilibrium hydrogen at room temperature is 75% orthohydrogen and 25% parahydrogen, which is approximately the concentrations of the hydrogen gas supply to the CMS. When cooled to the CMS operating temperature of 20 K, and without other influencing factors such as neutrons, the hydrogen

undergoes a slow process (days or weeks) by which orthohydrogen is converted to parahydrogen until it reaches its normal equilibrium concentrations of 0.2% orthohydrogen and 99.8% parahydrogen. During normal operation, the conversion rate from ortho- to parahydrogen attributed to temperature only—without a catalyst—is slower than the conversion rate from para- to orthohydrogen by neutrons in the moderator. The neutron conversion causes the orthohydrogen concentration to be much greater than the equilibrium value for 20 K. However, the conversion rate from ortho- to parahydrogen can be changed from many days to seconds by a catalyst. A catalyst speeds up the conversion rate so that approximately 42 L of catalyst (~50 kg of catalyst) will convert 25% to 95% parahydrogen in CMS loop 1 in a once-through pass through the catalyst. However, the mass of the catalyst is a trade-off between the extra volume of hydrogen needed for the catalyst, the heat added to the hydrogen when ortho- converts to parahydrogen, and the rate of conversion for startup, transient, and steady-state performance. The requirements for this catalyst, its rate of conversion, and measurement of the ortho- and parahydrogen concentrations are addressed in subsequent subsections of this section.

The neutronics team strongly argued that maintaining a high parahydrogen fraction (>99%) by the use of a catalyst would provide consistent neutron pulse characteristics for improved resolution regardless of beam power or hydrogen age. Several meetings with Neutron Sciences Division staff and leadership led to concurrence with the catalyst upgrade as part of the PPU [1]. The changes to the process flow diagram are shown in Figure 6.18.

Implementation of catalyst modules requires a redesign of the hydrogen refill system to accommodate the additional hydrogen required. This effort includes replacing the gas control panel and hydrogen gas cylinders. The gas control panel is being replaced because it contains outdated components that are unavailable from suppliers. The current hydrogen gas cylinders are nonstandard cylinders and need to be replaced to provide adequate gas supply for the new catalysts in the CMS.

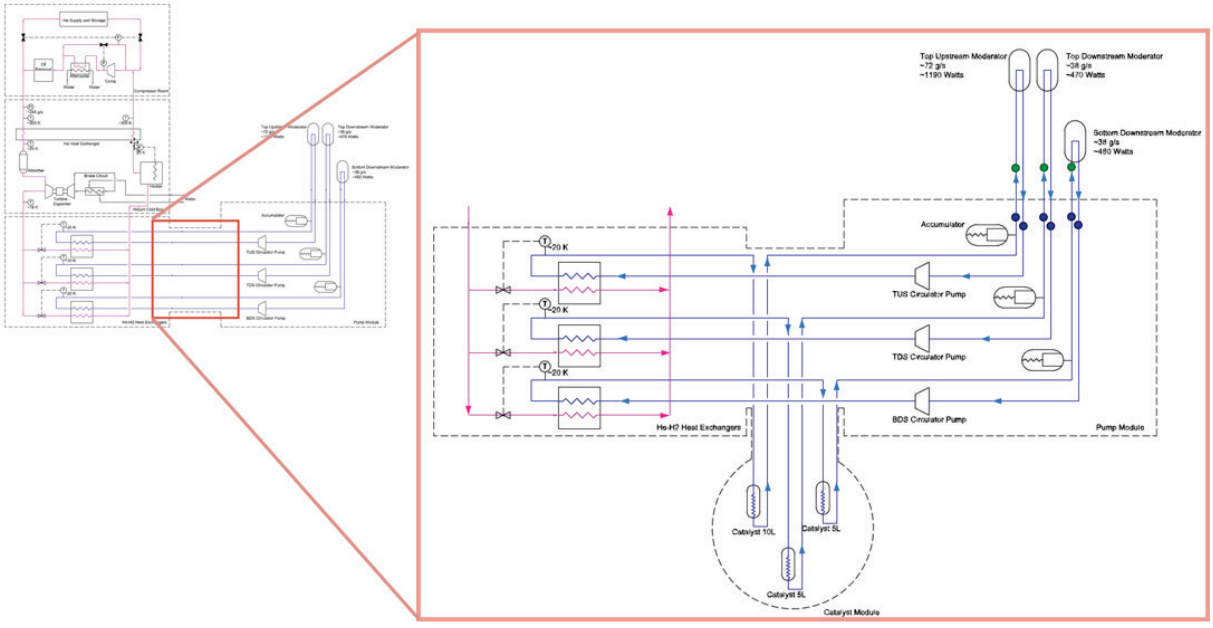

Figure 6.18. Proposed ortho-/para- hydrogen catalyst vessel interfaces with the current CMS configuration.

6.5.3.2 PPU MCS Requirements

The steady-state concentration of parahydrogen during operation shall be maintained above 99% by deployment of catalyst beds in each of the three hydrogen moderator loops.

Online measurement of the ortho- and parahydrogen concentrations will be provided to provide confirmatory measurements and traceability to experiment dates and times if needed.

The hydrogen refill system will be upgraded to accommodate the additional hydrogen mass resulting from the addition of the catalyst hardware. The upgrade shall meet the SNS fire protection requirements and the Final Safety Assessment Document (FSAD) requirements.

Technical design

Catalyst modules will be provided for each of the three CMS hydrogen loops. Figure 6.19 illustrates the proposed location and concept for the CMS ortho-/parahydrogen catalyst vessel assembly that will house these modules and provide interfaces with existing CMS hydrogen loop piping. The vacuum vessel ties into the vacuum volume of the current system using a large tee-in connection. This location also houses the hydrogen process loops that will be rerouted to pass through the catalyst modules before entering the loop accumulators and proceeding to the moderators. Figure 6.20 provides views of the catalyst module concept.

The design of the catalyst modules was influenced by time-proven robust designs deployed at the Japanese Spallation Neutron Source at J-PARC. Redundant and varied materials are included in an effort to guarantee containment of catalyst media during operation. A hypothetical safety risk case is being investigated that posits a mass migration of catalyst toward the moderator vessels housed within the SNS IRP. This investigation also assumes catalyst activation over the course of a typical IRP lifetime (~5 years) and migration of activated catalyst media to the CMS hydrogen utility room. Resulting dose rates from this conservative approach will potentially lead to safety creditation of the CMS catalyst retaining mechanisms.

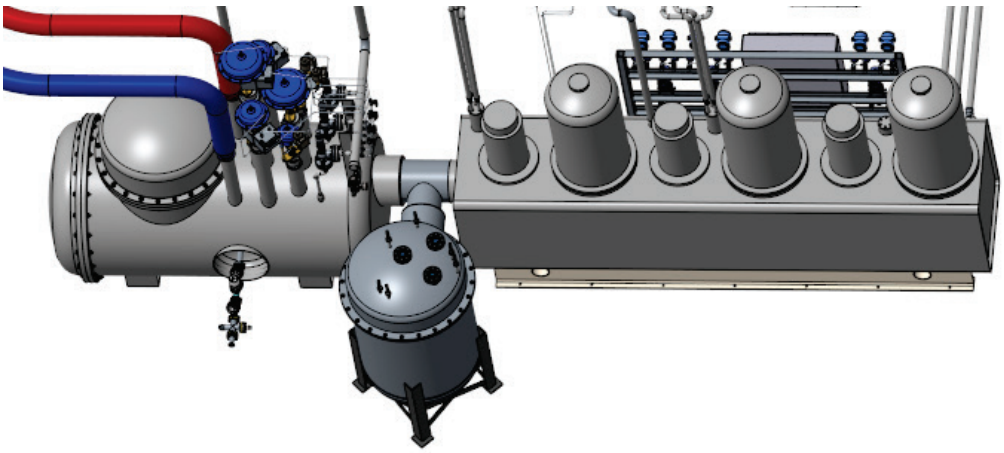

Figure 6.19. Catalyst vacuum vessel shown installed in the existing CMS between the heat exchanger and pump module.

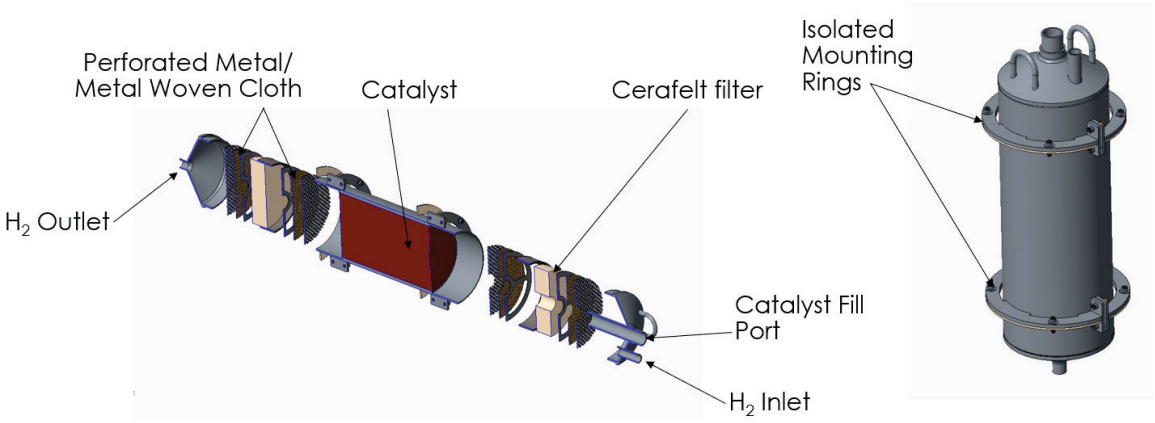

Figure 6.20. Sectional expanded view of the catalyst module design (5L version pictured).

Each moderator loop catalyst upgrade will be instrumented with probes and sensors to measure temperature, pressure and ortho-/parahydrogen fractions. Temperature probes and pressure transducers will be at inlets and outlets of each loop. Laser Raman spectroscopy will directly view into the hydrogen via dual sapphire windows (hydrogen and vacuum boundaries). The temperature sensors and pressure transducers will mimic the units currently used in the CMS, and the SNS testing is being performed to supplement test data from vendors and other institutions to qualify the sapphire windows. Interfacing with these sensors and probes will be done outside the catalyst vessel via six penetrations in the vessel head. Figure 6.21 illustrates the current vacuum vessel and catalyst module designs.

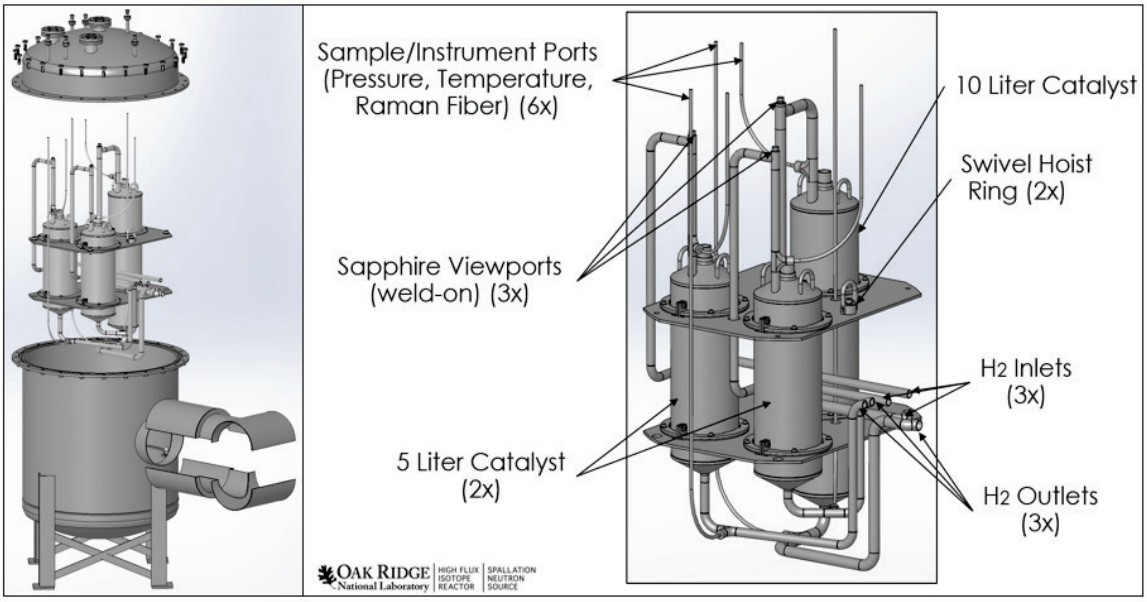

Figure 6.21. Catalyst vacuum vessel assembly (left, exploded view), and catalyst module subassembly (right).

A successful benchtop demonstration of an ortho-parahydrogen diagnostic approach with a through-the-window Raman spectroscopy measurement was achieved. The orthohydrogen fraction within a 2 ml liquid hydrogen sample was measured as the sample relaxed from room-temperature normal hydrogen to

99+% parahydrogen (the sample was catalyzed to speed conversion) during viewing through two sapphire windows. In the benchtop configuration with preexisting components, the minimum orthohydrogen fraction detected was less than 5% compared with the 30% minimum detected with an alternate, immersion-probe–based concept that suffers from a poor signal-to-noise ratio. A sample sapphire diagnostic window and results observed in November 2019 are visible in Figure 6.22. A better laser, spectrometer, and Raman probe is expected to provide orthohydrogen detection to less than 1% under similar test conditions. Testing with the improved components is planned in the summer of 2020.

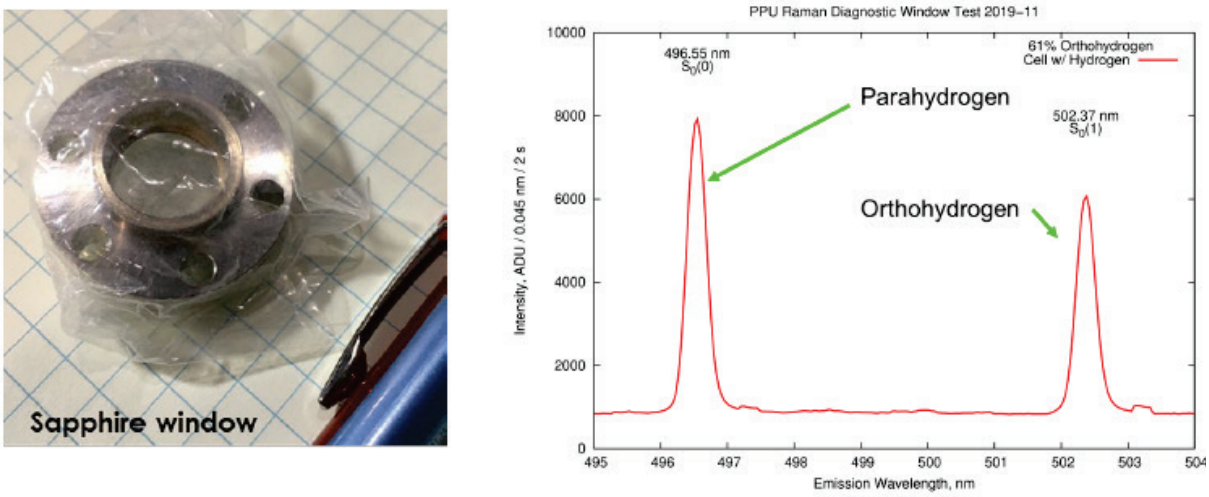

Figure 6.22. Sapphire diagnostic window and successful Raman analyzer output.

The outlook for safety and engineering acceptance of the robustness of the through-windows (commercial sapphire windows) as hydrogen and vacuum boundaries is now positive to the point it has become the primary choice over the fiber immersion-probe. Vendor data and pressure test data from the European Spallation Source at cryogenic temperatures have provided a foundation for confidence. These data will be augmented with ORNL testing of windows being arranged at the Fusion Energy Division facility under SNS design-basis hydrogen pressure and temperature conditions. An overview of the sapphire window test article design is provided in Figure 6.23. Fabrication of this assembly is under way, and testing will begin at the Fusion Energy Pellet Laboratory in May 2020.

Testing will certify the integrity of the sapphire diagnostic windows using helium at CMS operational conditions:

- Temperature ~17 K
- Pressure ~20 bar
- Simulate thermal cycling that occurs typically during CMS warm-up and cool-down
- Simulated thermal analysis to optimize the test procedure to maximize typical SNS operational years

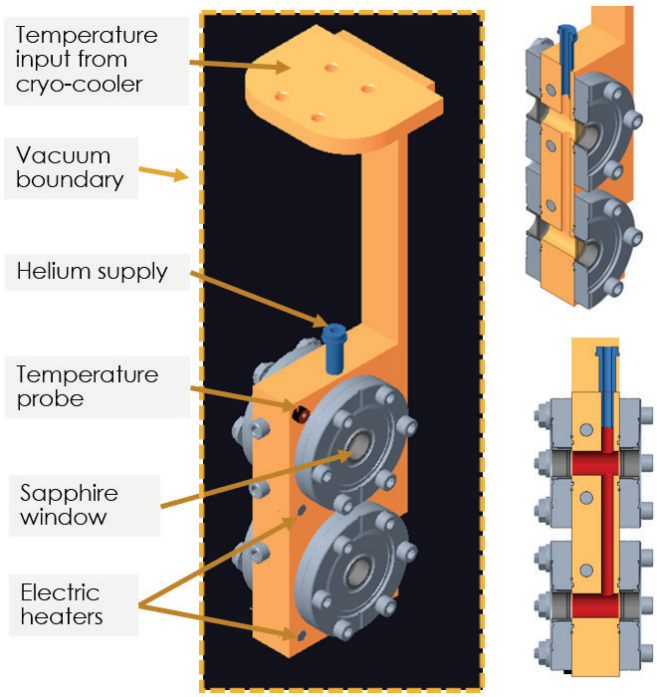

Figure 6.23. Window pressure/temperature integrity test article.

The hydrogen refill system functions to supply research-grade hydrogen, 99.9999% pure, to the CMS at the specified pressure, temperature, and flow. The scope of the redesign of the hydrogen refill system includes replacing the gas control panel and the 12 hydrogen gas cylinders; the latter contain the hydrogen required for the CMS, including the ortho- and parahydrogen catalysts to be added to the CMS. These 12 gas cylinders will be replaced because they are not standard and do not contain adequate hydrogen gas to fill the CMS after the catalysts are installed. The gas control panel is being replaced because it contains outdated components that are unavailable from suppliers and because hydrogen safety for the current panel requires improvements.

The gas panel will be moved from inside to outside Building 8760 to simplify hydrogen safety features including ventilation, gas monitors, and continuous cabinet purges required for equipment inside the building. The 16 new standard-size hydrogen gas cylinders, of equivalent purity to the old ones, will be mounted on skids with headers and isolation valves to simplify connections to the gas panel.

A hydrogen cylinder skid comprises 16 standard-sized cylinders (size 300) delivered at 2400 psig with adequate hydrogen gas to fill the CMS with one skid. The CMS will contain approximately 8 kg of hydrogen, including the catalysts, and a 16-cylinder skid contains approximately 10.6 kg of hydrogen. After filling the CMS, the spent skid will be returned to the gas supplier for a replacement skid. The vendor will deliver the skids with gas purity certifications. SNS proposes to purchase four 16-cylinder skids.

Drawings were completed to locate the gas cylinder skids on the pad outside Building 8760 as shown in Figure 6.24. The skids will include a manifold for all the gas cylinders with a single manual block valve on the outlet of the manifold. This is simpler than the old design for 12 cylinders; it did not include a manifold, so SNS mechanics had to connect each cylinder separately to the gas panel. The hydrogen fittings are tested for leaks, which are more significant for the current panel because the gas cylinders are inside where leaks could create explosive conditions. The current panel requires continuous ventilation

and monitoring, but neither is required for the new systems to be located outside. Leak tests will be performed on the new design, but small hydrogen leaks dissipate quickly and do not create explosive conditions outside.

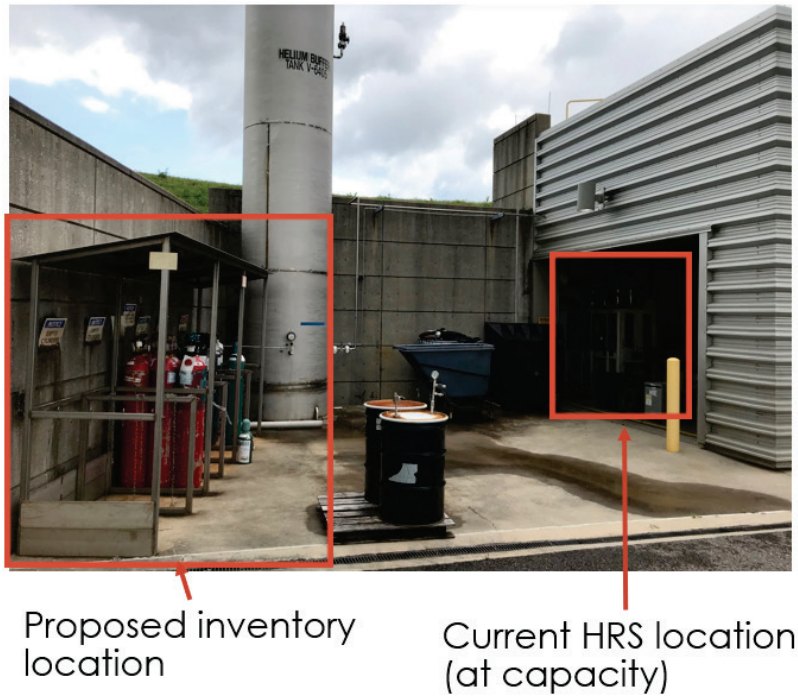

Figure 6.24. Proposed location for expanded hydrogen refill system inventory.

The current gas panel and 12 gas cylinders are mounted in enclosures inside Building 8760. Two of the enclosures are visible in Figure 6.25; the other two are behind them. These enclosures are continuously ventilated and monitored for hydrogen, but the gas monitors are currently not functional. Gas panel and line purging uses evacuation and helium flow to carry the gases out the vent. An ejector creates some vacuum, but it is ineffective creating vacuum in much of the panel. The ejector creates a vacuum of only a few psi below atmospheric pressure and leaves more than two-thirds of the gas in the panel. Most of the gas is removed by helium purging.

The new gas panel will be located outside near the hydrogen gas skids. Because they are not in an enclosure, they do not have to be actively ventilated or monitored for hydrogen. A vent line that releases 15 ft above the panel will vent hydrogen safely to the atmosphere. Components on the panel and other components within 15 ft will be classified Class I, Division 2, Group B. This can be done with commercial components that are passive, which simplifies design and operation.

Panel purging will be accomplished by helium flow that is connected farther upstream than for the current panel. It will purge most of the supply lines and gas panel by forcing residual gases out the vent, and it will make helium back-flow unnecessary. Small sections that are dead-end volumes will be purged by a combination of dilution and purging. Evacuation will not be used. After helium forces air out of the system, hydrogen will be used to purge the helium and leave pure hydrogen in the panel to fill the CMS. Hydrogen will be purged from the panel using helium flow and dilution to get the hydrogen concentration below the lower explosive limit before the panel is opened for maintenance.

Figure 6.25. Current hydrogen enclosures located in Building 8760.

6.5.3.3 References

1. Email from H. Christen of Oak Ridge National Laboratory to B. Riemer of Oak Ridge National Laboratory, Re: PPU scope to add ortho to para catalyst that will affect FTS instruments, November 21, 2018.
2. E. B. Iverson, *Orthohydrogen Production in SNS H2 Moderators for PPU*, PPUP-504-TR0001-R00, Oak Ridge National Laboratory, July 13, 2018.
3. A. Crabtree, *Hydrogen Moderator System Design Criteria Document*, 106020000-DC-0001-R02, Oak Ridge National Laboratory, June 30, 2003.
4. J. A. Eckroth and J. A. Crabtree, *Equivalency Analysis Document for the Conventional Facilities and Equipment that Support the Cryogenic Moderator System*, 108030700-ES0001-R01, Oak Ridge National Laboratory, December 30, 2005.
5. *Spallation Neutron Source Final Safety Assessment Document for Neutron Facilities*, 102030102-ES0016-R05, Sect. 3.3.3, Oak Ridge National Laboratory, September 2011.
6. David Sulfredge, *Hydrogen Line Rupture Analysis*, 106020200-DA-0005-R00, Oak Ridge National Laboratory, June 2003.
7. Email letter from T. McManamy of Oak Ridge National Laboratory to J. Eckroth of Oak Ridge National Laboratory, Re: Increased hydrogen inventory, 106020200-TD0003-R00, April 6, 2006.
8. R. M. Harrington and S. M. Trotter, *Preliminary Hazard Analysis in Support of the Proton Power Upgrade Project*, PPU-P01-ES0001-R00 Sect. 2.9, Oak Ridge National Laboratory, May 2017.

6.5.4 Evaluations of Reflector Vessels, Monolith Shielding, and Core Vessel Insert Systems

This scope verifies there are sufficient engineering, radiation damage, and operational margins in the FTS vessel and monolith shielding systems under PPU operating conditions, and if needed, defines any

necessary utility or operational changes. Vessel and shielding equipment within the FTS monolith were originally designed for 2 MW of 1.0 GeV proton operation. Specific requirements under this WBS include the following:

- Confirm there are sufficient temperature, stress, and operational structural margins in these systems with PPU operation of the FTS.
- Verify all wetted surface remain below boiling.
- Verify aluminum temperatures remain below 130°C to maintain heat treatment temper states.
- Ensure that all pressure/structural components meet the ASME Section VIII, Div. 2 stress criteria [1].
- Justify increasing the administrative radiation damage limit for the ORP.
- Define any needed utility upgrades or operational changes and provide design-basis data to utilities.

Area P.5.5, Vessel and Shielding Systems, covers detailed evaluations of the lower ORP and CV. A previous evaluation of the aluminum PBW with 2 MW 1.0 GeV heating was reviewed, and it was found to have ample margins; 1.3 GeV PBW heating will be lower. Temperatures of the monolith shielding around the CV exterior were estimated along with the CV analysis. Beyond that, no additional evaluations were needed. Figure 6.26 shows a cross section of the monolith, highlighting the evaluated systems.

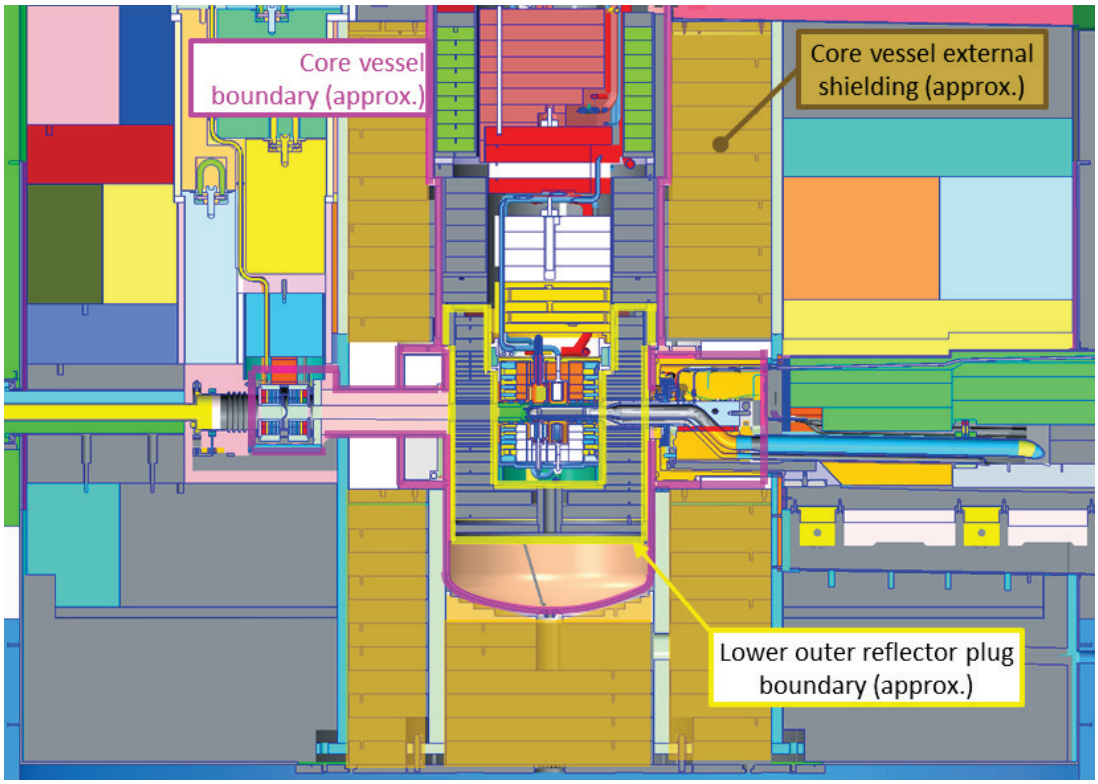

Figure 6.26. Monolith cross section showing evaluated core vessel, core vessel external shielding, and lower ORP systems.

Neutron shutters and shielding beyond the CV external shielding do not require evaluation with PPU beam heating, as they were designed with generous thermal margins. The same is true for the middle and upper portions of the ORP. The design of the IRP with PPU heating is the responsibility of the Neutron Technologies Division.

The lower ORP and CV were evaluated for heating and radiation damage with PPU operation at 1.3 GeV and 2.0 MW to a projected facility lifetime of 60 years. The radiological protection performance of the monolith shielding is covered under P.5.2, Neutronics. Neutronics evaluations of the accumulated radiation damage to the permanent vessel systems with the extended lifetime also determined the lower ORP exceeded the original damage limit of 10 dpa. A justification has been prepared for raising this limit for the lower ORP to 20 dpa [2].

The evaluation of the vessel and shielding systems follows the same evaluation process used during the original design basis. Because of increases in computational power and advancement in analysis software, various improvements were made to the evaluation of the shielding and vessel systems for PPU beam operation. Unlike the original design-basis evaluation, which used a spherical heating model for energy deposition, PPU energy deposition was characterized by fully mapped energy deposition on the vessel and shielding systems. Additionally, millions of elements and nodes were used in the computational fluid dynamics (CFD) and structural models, which increased the fidelity and resolution of the results.

Initial neutronics analysis showed that, in general, the heat deposition in the vessel and monolith shielding systems from a 1.3 GeV proton beam will be comparable to that from the 1.0 GeV beam. However, local increases in heat deposition by up to a factor of three in the regions surrounding the target transition and rear body are indicated, which required more detailed analysis. Higher local heating along the proton beam port of the CV has also been revealed, leading to thorough evaluation of thermal-hydraulics and thermal stress.

6.5.4.1 Proton Beam Window

The existing aluminum PBW design is the baseline for operation with PPU beam. Further evaluation was unnecessary for the aluminum PBW and its associated shielding because of a 30% reduction in heat deposition compared with the baseline case of 2 MW at 1.0 GeV and high safety factors for the window components and weld. Water temperatures in the aluminum PBW are shown in Figure 6.27; the maximum temperature is estimated to be 52°C with 2 MW of 1.0 GeV proton beam heating.

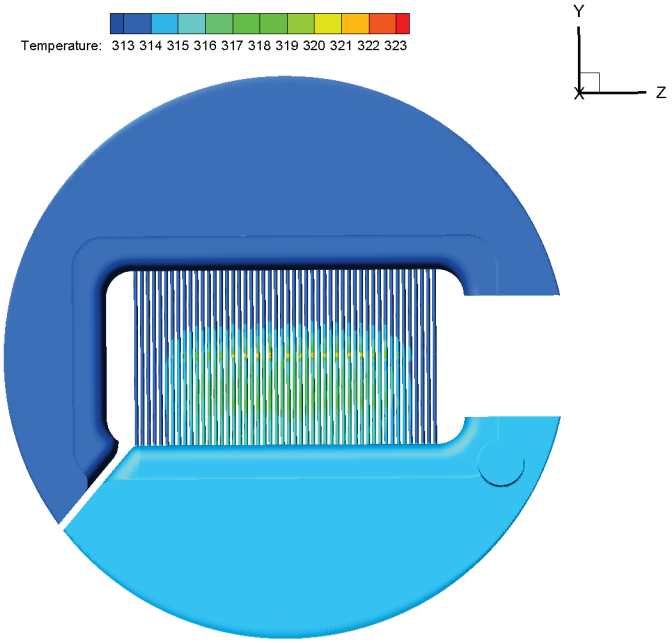

Figure 6.27. Aluminum PBW water temperature (in K) for 2 MW 1.0 GeV proton beam (C. Barbier).

6.5.4.2 Outer Reflector Plug

The total heat load deposited on the lower ORP from PPU operation will be 208 kW on the structure and 7 kW in the heavy water coolant. CFD thermal analysis [3] of the ORP indicated a maximum structure temperature of 114°C at the neutron port 4-5-6 tube block (106040103M8E8700A004-3) and a maximum temperature of about 112°C on the target port weldment (106030102M8E8700A020-1), as seen in Figure 6.28. The main and secondary coolant flows are 50 and 30 gpm, respectively, at 35 psia. Coolant wetted surfaces are below these maximum structure temperatures. The boiling point of the heavy water coolant at 35 psia is 126.2°C. There is no risk of boiling in the lower ORP.

The ORP temperature results from the CFD/conjugate heat transfer analysis were imported as input into a thermal-structural analysis model [4]. The finite element model was generated in ANSYS and the assembly was evaluated for the PPU beam operation load case. The design criteria are based on the "design by analysis" approach of the *ASME Boiler and Pressure Vessel Code* (BPVC), Section VIII, Division 2. The allowable stresses are based on the von Mises theory; processed finite element results were compared with the ASME stress allowables for primary, bending, and peak stress categories. All stresses with PPU beam conditions are within allowable values. The peak stress under thermal loading is 342 MPa at the proton beam port, as shown in Figure 6.29. This is close to but does not exceed the secondary stress limit of 345 MPa.

Neutronics analysis [5] projected the maximum integrated radiation dose at a location around the target port of the ORP to reach 17.25 dpa because of the increased damage rate and 20 year facility lifetime extension. A justification for increasing the original design basis limit of 10 dpa was developed [1] that concluded there are no issues with increasing the ORP dose limit to 20 dpa with regard to material strength.

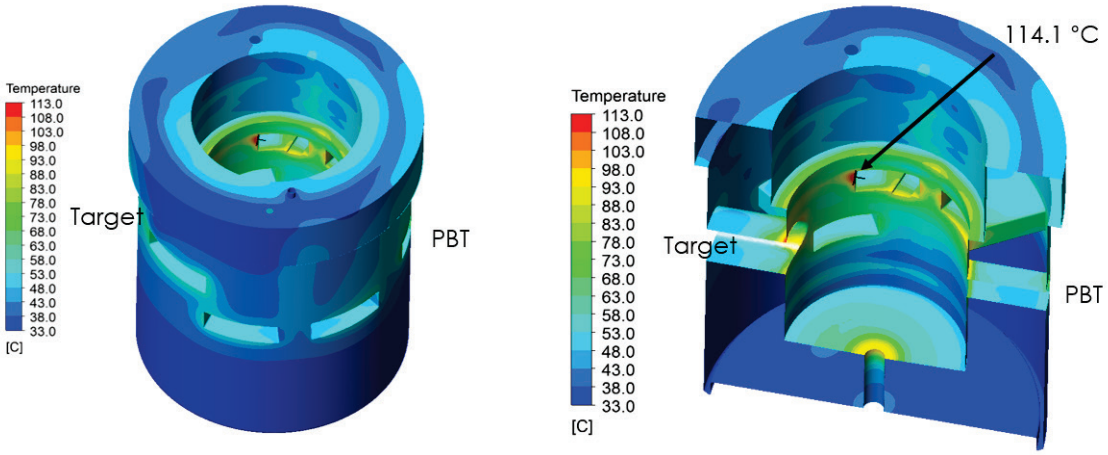

Figure 6.28. Temperatures in the ORP PPU beam operation.

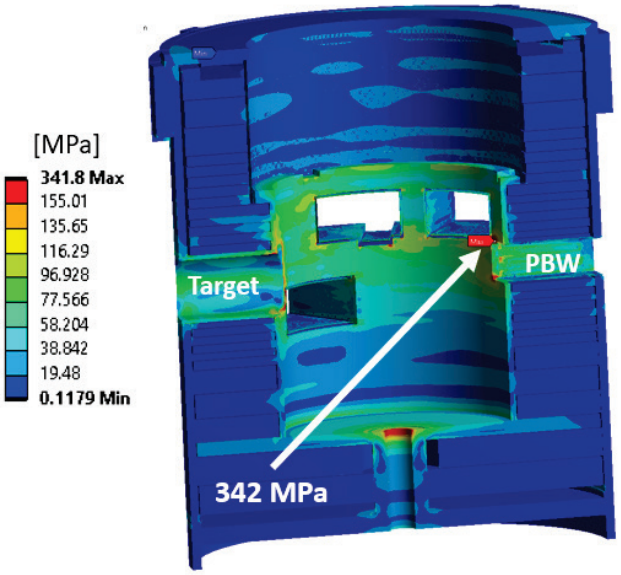

Figure 6.29. Von Mises stress of the lower outer reflector plug for 1.3 GeV, 2.0 MW proton beam.

The impact of a high dose (here, between 10 and 20 dpa) on thermal conductivity was considered as a result of a recommendation at the CD-3b review in June 2019. The reduction in thermal conductivity for SS316L in this range could not be found in the literature but was assessed to be minor considering the complete lack of data in this dose range for the commonly used SS316L in nuclear applications. Thermal analyses were repeated with a postulated uniform 20% reduction in thermal conductivity to provide an imperfect assessment of the potential impact. The maximum temperature in the lower ORP rose to 141°C. Thermal stress was similarly reevaluated with the peak van Mises stress increasing to 454 MPa.

The peak stress from the reduced thermal conductivity condition exceeds the ASME allowable secondary stress limit based upon minimum strength data for SS316L. The as-built material strengths for specific

ORP components where the maximum stress occurs was then found from project records. Using the actual strengths from the material's certified mill test report, a significantly higher secondary allowable stress level of 482 MPa was obtained.

6.5.4.3 Core Vessel

The total PPU heat load deposited in the CV structure is 55 kW; the heat load is 2.46 kW in the heavy water coolant. CFD and conjugate heat transfer analysis resulted in a maximum structure temperature of 111°C near the neutron port 4-5-6 tube block [6]. The temperatures are shown on a half of the CV in Figure 6.30. The largest heating rate occurs in the proton beam port because it is close to the direct path of the 2 MW, 1.3 GeV beam. However, the proton beam port has enough cooling to maintain the wetted steel surfaces at temperatures below 94°C.

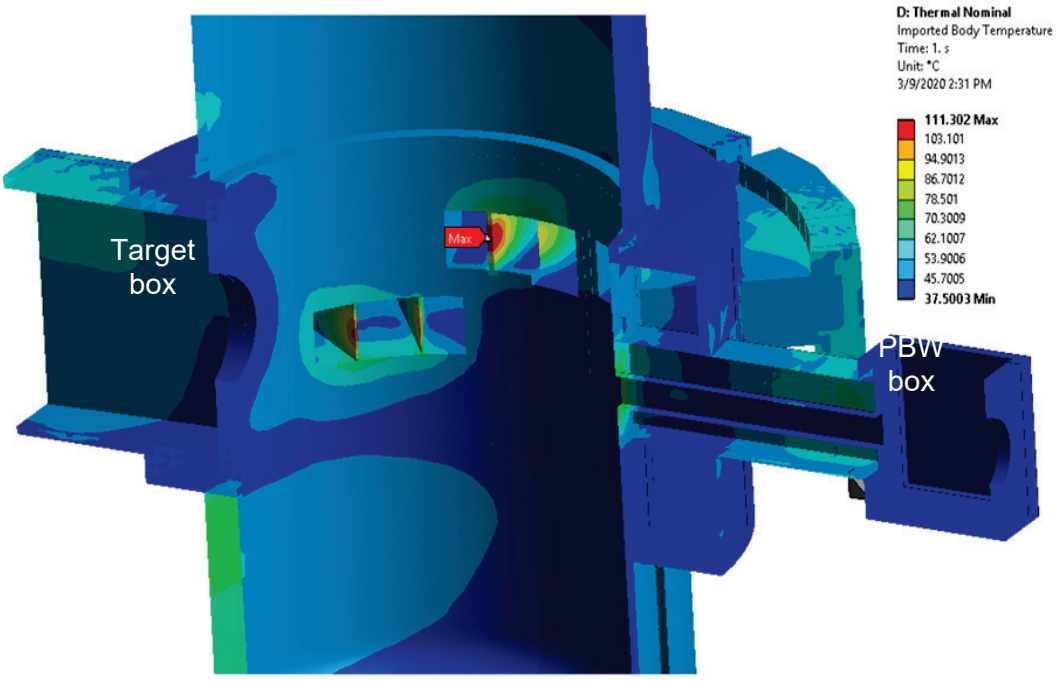

Figure 6.30. Core vessel temperature with PPU beam operation.

CV temperatures were imported into a new thermal structural analysis finite element model developed with ANSYS [7]. The normal PPU beam operation load case was evaluated (e.g., temperatures, gravity, coolant pressure). Stresses were categorized and compared with the ASME BPVC allowable values based on the design-by-analysis approach, Section VIII, Division 2. The maximum von Mises stress in the CV is 245 MPa, within the secondary stress limit of 345 MPa. CV stress profiles are shown in Figure 6.31.

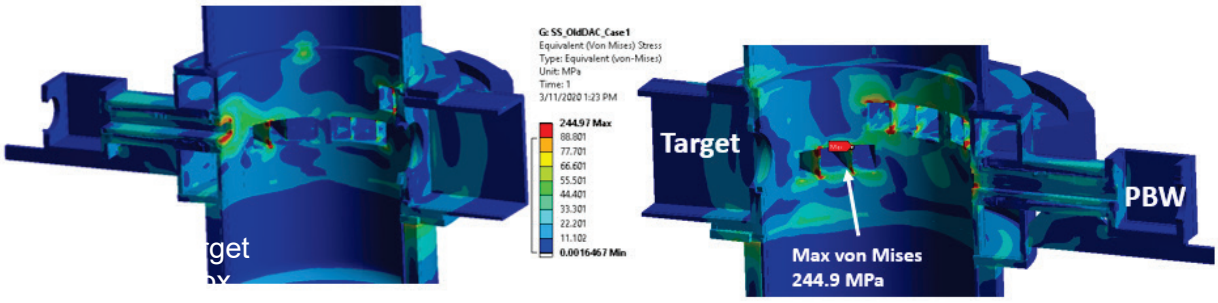

Figure 6.31. Von Mises stress of the lower outer reflector plug for 1.3 GeV, 2.0 MW proton beam.

The total projected radiation dose to the CV is not projected to exceed the original design basis of a 10 dpa administrative limit even after the extension in facility lifetime and use of 1.3 GeV protons. In any case, thermal and thermal structural evaluations of the CV were revisited under a postulated 20% reduction in vessel wall thermal conductivity similar to the approach used for the ORP. The maximum CV temperature increases to 123°C under this conservative assumption. The maximum stress increases to 262 MPa.

6.5.4.4 Core Vessel Inserts

CVIs were evaluated to determine the thermal and structural response of the inserts when subjected to normal PPU beam heating loads. Four CVIs were considered: CVI-4, CVI-9, CVI-10, and CVI-11; they are located as shown in Figure 6.32. The neutronic heating power [8] was mapped to thermal–structural finite element models and evaluated with ANSYS software. The CVIs are light water–cooled with a 1.5 gpm flow at an inlet temperature of 26.7°C [9][10][11]. The total heat load deposited on the CVIs from the PPU beam ranged from a minimum of 334 W for CVI-10 to a maximum of 479 W for CVI-11.

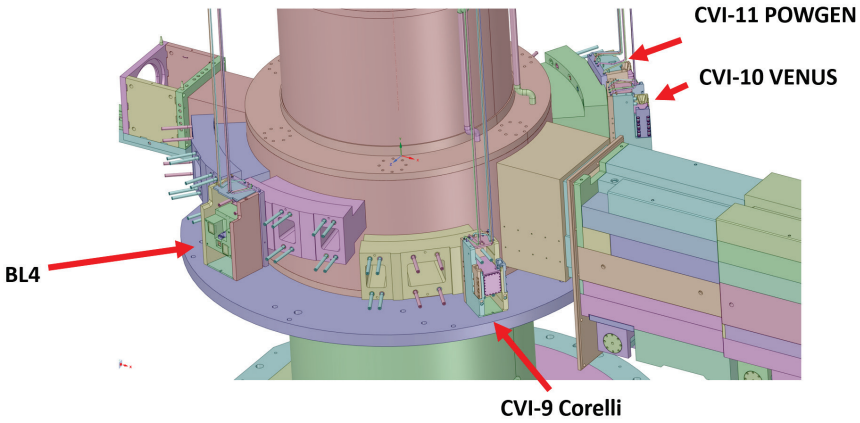

Figure 6.32. Core vessel inserts evaluated with PPU operation.

The CVI temperatures were determined with the mapped nuclear heating, convection cooling to ambient outside helium environment (CV interior), forced convection due to the coolant channels, and conduction heat transfer conditions at mounting interfaces. The steady-state temperatures are shown in Figure 6.33. The maximum temperature was 81°C in CVI-10, which, uniquely, contains a collimator inside the alignment block with a helium gap. The helium gap acts as a poor conduction medium, and the energy in

the collimator is essentially trapped, resulting in a higher peak temperature compared with other CVIs. Overall, no steel or aluminum temperatures approach CVI design criteria limits.

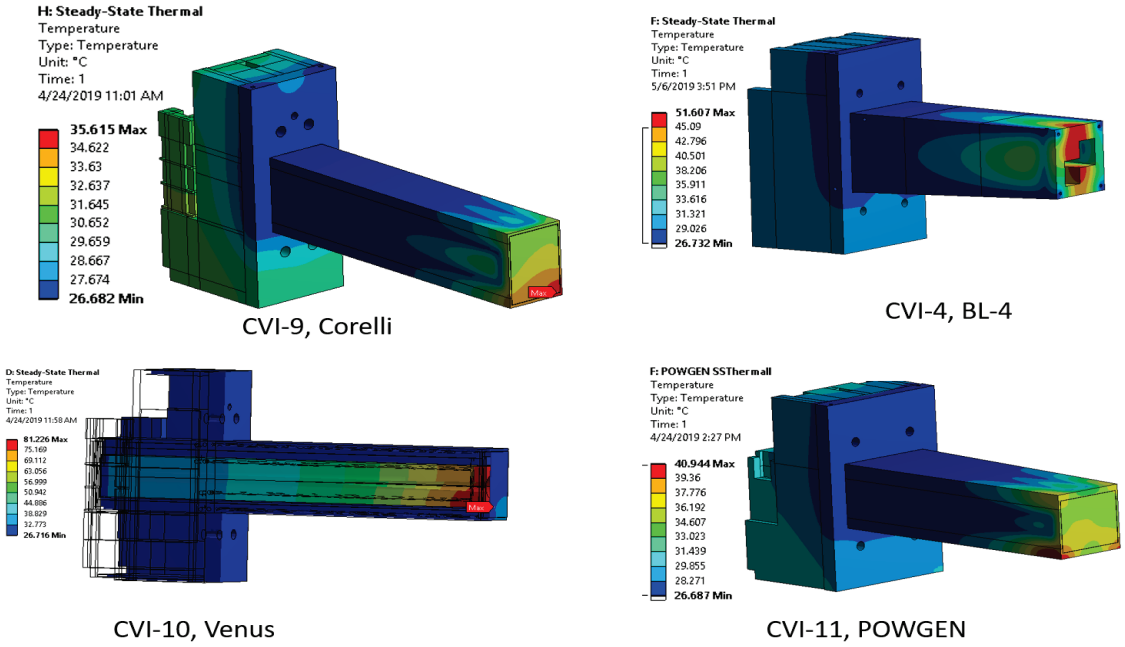

Figure 6.33. Core vessel insert temperatures under PPU beam operation.

CV stress results were similarly categorized and evaluated against ASME BPVC design-by-analysis criteria [12]. The maximum von Mises stress for the CVIs was low—78 MPa—and all stress limits were satisfied (Figure 6.34). The CVI thermal fatigue life is exceedingly large.

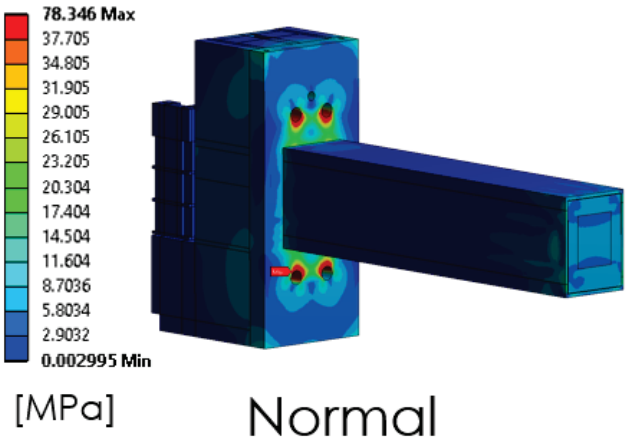

Figure 6.34. Von Mises stress in CVI-9 under normal PPU operation.

6.5.4.5 Fatigue Life Evaluations

The lower ORP, CV, and CVIs were evaluated for total fatigue life as a result of PPU thermal cycles. The austenitic stainless steel S-N curve [13] and the components' alternating stresses were used to calculate the fatigue lifetime. Historically, the frequency of beam trips has been averaging 4.39 trips per day since 2013. The fatigue assessments concluded that PPU beam trips will not cause fatigue issues because the allowed number of cycles of 245,000 at 172 MPa alternating stress (342/2) corresponds to 260 years for the ORP (assuming 200 days operation per year). The CV estimated thermal cycles are 133,000 cycles, corresponding to nearly 1400 years. The CVIs have an essentially infinite fatigue life of 100 million years.

Fatigue lives were also evaluated for the lower ORP and CV with thermal stresses resulting from the postulated 20% reduced thermal conductivity from radiation damage. The nominal ASME fatigue design curve was still employed. Figure 6.35 shows the fatigue life for nominal and radiation-damaged thermal conductivity for the ORP (left) and CV (right). The fatigue life for a radiation-damaged CV is reduced from 1382 years to 1070 years, and for the lower ORP, it is reduced from 260 years to 71 years.

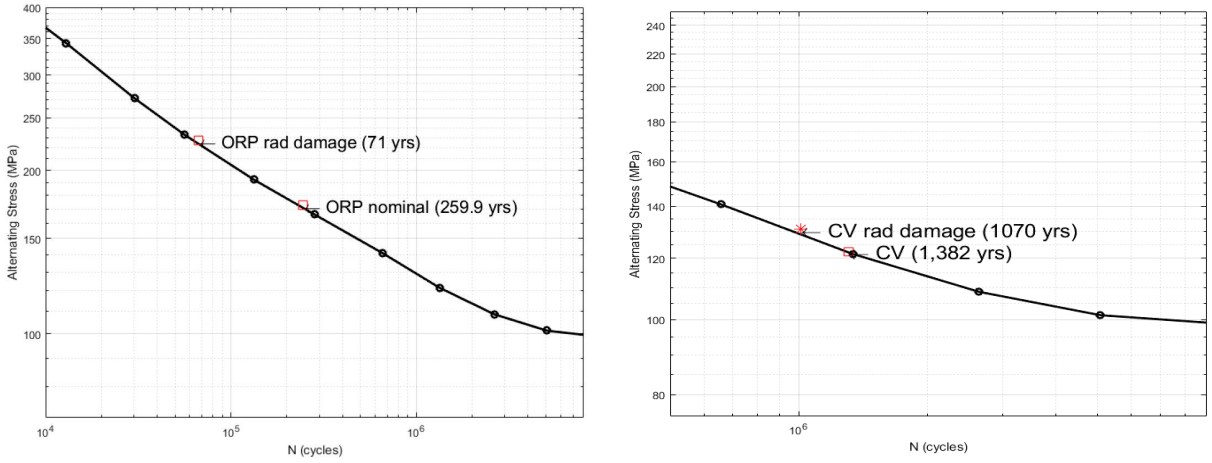

Figure 6.35. Left: ORP fatigue life with alternating PPU thermal stress with nominal thermal conductivity temperatures. Right: The fatigue lifetimes for the CV.

6.5.4.6 References

1. ASME International, *2017 ASME Boiler Pressure Vessel Code,* Section VIII, Division 2, American Society of Mechanical Engineers, New York, 2017.
2. D. McClintock, *Review of the Administrative Dose Limit for 316L in the SNS Outer Reflector Plug at the Spallation Neutron Source*, 106030000-TR0001-R00, March 2019.
3. C. Barbier, *Thermal Analysis of the Lower Outer Reflector Plug for a 1.3GeV 2MW Proton Beam*, SNS-106030102-DA0004-R00, Oak Ridge National Laboratory, October 2018.
4. O. Martinez, *Lower Outer Reflector Plug Structural Analysis with PPU Beam Operation*, PPU-505-DA001-R01, Oak Ridge National Laboratory, March 2018.
5. W. Lu, Radiation Damage at the Outer Reflector Plug for 1.3 & 1.0 GeV Proton Beams, SNS-106100200-TR0258-R00, Oak Ridge National Laboratory, April 2018.

6. V. Rao, *Simulation of Conjugate Heat Transfer in the Core Vessel*, SNS-106040100-DA0017-R00, Oak Ridge National Laboratory, April 2020

7. O. Martinez, *Core Vessel Structural Analysis with PPU Beam Operation*, PPUP-505-DA0002-R00, Oak Ridge National Laboratory, April 2020.

8. I. Remec, *Neutronics Assessment of the SNS FTS Core Vessel Inserts for the PPU*, SNS-106100200DA0098-R00, Oak Ridge National Laboratory, April 2018.

9. J. Bailey, *Thermal Analysis for BL4 Core Vessel Insert*, SNS-107050600-DA0001, Oak Ridge National Laboratory, October 2004.

10. *Thermal Analysis of the 06td SANS Diffractometer Core Vessel Insert and Guide*, SNS-107080600-DA0005-R00, Oak Ridge National Laboratory, July 2003.

11. P. Strons, *Thermal Analysis of the Core Vessel Inserts*, SNS-107030600-DA0005, Oak Ridge National Laboratory, August 2002.

12. O. Martinez, *Core Vessel Insert Thermal & Structural Analysis with PPU Beam Operation*, PPUP-507-DA0001-R00, Oak Ridge National Laboratory, August 2019.

13. ASME International, *2017 ASME Boiler Pressure Vessel Code*, "Fatigue Evaluations Including Environmental Effects, Case N-792, Section II, Division I," American Society of Mechanical Engineers, New York, 2017.

6.5.5 Target Utility Systems Evaluations and Upgrades

Scope

This work scope is to ensure there are sufficient engineering, radiation shielding, and operational margins in the FTS target utility systems for reliable operation with the PPU beam over the extended FTS lifetime and to install necessary upgrades. Coordination with other FTS systems is integral to assessing reliable system performance. Those systems will provide new utility requirements for PPU operation, if any issues are found. Evaluations will consist of review of design basis documents (e.g., design and analysis calculations) and comparison with operational data from current operations as needed.

The PPU target gas injection supply falls within the target utility upgrade scope. Two independent supplies will be provided—one for target small bubble generators and one for gas wall injection at the target nose. The primary mode of target gas injection will be via recirculation. Capability for once-through gas injection will also be provided.

For reference, the target utilities systems include the following:

- Target primary water loops 1, 2, 3 and 4
  - Water loop 1—Mercury heat exchanger
  - Water loop 2—Target water-cooled shroud and PBW
  - Water loop 3—Moderators, shutters, and CVIs
  - Water loop 4—Reflector plugs (heavy water)

- Secondary water loops
  - Deionized water loop
  - Chilled deionized loop cooling
  - Sensible chilled water loop
  - Tower water (within Building 8700)
  - Chilled water (within Building 8700)

- Helium gas distribution
- Nitrogen gas distribution

Requirements

- Evaluate each cooling loop for readiness for PPU operation, incorporating original design-basis information, operational experience, and evaluations of PPU heat loads provided from the other FTS systems areas.

- Update utility systems design basis documentation to reflect the evaluations performed and recommended changes to the utility systems to accommodate PPU operation.

- Specify updated utility systems set points for PPU operation.

- Provide two independent target helium gas injection supplies, with variable flow and pressure within required limits.
  - The primary mode is gas recirculation.
  - The secondary mode is once-through.

- Provide upgrades to existing utility systems to assure adequate performance under PPU operation

Assumptions for target utility systems

- Hot off-gas recombination and recycle will be implemented for water loop 4 independent of the PPU.
- Operational improvements to gas panel 9 will be implemented before the PPU.
- Additional heavy water to support the IRP (IRP3) will be procured by SNS operations before installation of IRP3

6.5.5.1 Evaluations of Target Utility Systems at 1.3 GeV

Primary target cooling loops

Target utility systems were originally designed to be 2.0 MW–capable with 1.0 GeV protons at a 60 Hz pulse repetition rate. The original design basis for each of the primary water loops has been compared with updated neutronics, CFD, and thermal models for the individual components of the target system. Table 6.7 is a summary table showing the pressure drops, heat loads, and energy deposited in the cooling water (for radiolysis calculations) of each component [1][2][3][4][6][7][8][9].

The original design-basis values noted in Table 6.7 include heat added by the loop 3 trim heater and original safety factors that are not shown. Instead of the original design factors, it includes the calculated new PPU design factors; these, when applied to the new PPU design baseline values (without design factors), result in the original design basis energy distribution values. The original total of active cooling loads with original design factors was 2,504,722 W; the new PPU design basis total of active cooling heat loads without a design factor is 1,743,083 W, resulting in a calculated overall PPU design factor of ~1.44.

Table 6.7. Original design basis vs. PPU design baseline.

2MW									
Target systems energy deposition	**Dist.**	**PPU design baseline w/o design factor**	**Calculation basis for design heat, energy in water, and pressure drop**	**Notes on design baseline**	**New PPU design factor**	**Original design basis**	**Original and PPU design basis flow**	**Energy in water**	**Component ΔP**
		Watts				**Watts**	**GPM**	**Watts**	**PSI**
TOTAL		**1,829,301**				**2,590,940**			
Target systems active cooling	**95.3%**	**1,743,083**				**2,504,722**			
Light water station 1		**1,072,500**				**1,540,071**		**9.2**	
Mercury Heat Exchanger		1,072,500	SNS-106100200-DA0107-R00 total heat, SNS-106100200-TR0262 for energy in water		1.44	1,540,071	**400**	9.2	7.5
Light water station 2		**67,960**				**130,000**	**80**	**7,545**	
Target Shroud/Seal Flange/Shielding		57,760	SNS-106100200-DA0108-R00; PPUP-502-TR0001-R00; 106010101-DA0048-R00		1.56	90,000	50	6,138	9.6
PBW and Up/Down Shields		10,200	Franz Sept. 2019 PDR presentation; PPUP-502-TR0001-R00; 106040200-DA0004-R00		3.92	40,000	30	1,407	4.3
Light water station 3		**42,483**				**72,649**	**58.7**	**10,455**	
Inner Inserts – 12 Single-Channel		4,373	PPUP-507-DA0001-R00, 1016100200-DA0098-R00 + 2/3/20 email from Igor Remec		4.79	20,967	18	5	5
Inner Inserts – 6 Multi-Channel		3,014			6.96	20,967	9	9	5
Ambient Moderator (BU)		19,613	SNS-10630101-DA0005-R01		0.65	12,804	15.85	10,441	3.89
Coupled Cryogenic Moderator (BD)		10,849			1.22	13.277	15.85		0.576
Transfer Line to Moderators				Included in moderator loads					
Trim Heater		4,634			1.00	4.634			
Heavy water station 4		**560,140**				**755,002**	**263**	**39,979**	
Lower Inner Top Reflector		114,500	SNS-10630101-DA0005-R01		1.53	175,251	60	30,002	8.0
Bottom Reflector		114,500			1.53	175,251	60		11.3
Top Beam Tube		28,700			1.48	42,528	15		10.74
Bottom Beam Tube		28,600			1.49	42,528	15		7.94
Intermediate Inner		13,300	Assumed same as 1 GeV original design spherical model		1.19	15,827	8.1	270	0.17
Outer Plug Lower		93,900	SNS-106030102-DA0004-R00; PPUP-502-TR0001-R00	The bottom and lower portions of the lower outer plugs are cooled in series	1.17	109,480	30	7,228	0.32
Bottom		110,500			1.13	124,950	50		0.65
Intermediate Outer		1,140	Assumed same as 1 GeV original design spherical model		1.19	1,357	1.6	19	0.02
Vessel Wall, TGT Port Box, PWB Box		55,000	SNS-106100200-TR0257-R00	Target port box, vessel wall and PBW box cooled in series	1.23	67,830	23	2,460	17.45
Air-cooled components	**0.4%**	7,700	Agrees with FIDP 9/14/01	~ 1996 estimate that 1.8% of 1 MW removed from shielding ≅ 18,000 W	1.00	7,700			
Binding energy	**4.3%**	78,518	~ 1996 estimate that 3.9% of 1 MW is binding energy ≅ 39,259 W		1.00	**78,518**			

Table 6.7 shows that while some individual components (i.e., moderators) have an increased heat load relative to the original cooling loop design basis, each individual loop heat load—as well as the overall heat load produced from the 2.0 MW beam at 1.3 GeV—is reduced from the original design basis.

To address the revised technical component pressure drops at the analyzed cooling water flow rates, all primary loop flow control valves were evaluated for resulting operating ranges and were determined to be suitable for operation at 2.0 MW and 1.3 GeV. The remaining information required to complete the documentation of the analysis of the primary cooling loops is a reference document for the heat load in the PBW.

Table 6.8 provides the calculated heat load data summarized by water loop for both the original 1.0 GeV design and the PPU 1.3 GeV/IRP3 design. For both design cases, total heat load values do not include the added heat associated with the loop 3 trim heater and do not have a safety factor applied. The predicted PPU energy distribution is lower in each primary loop than in the original design, and therefore can be accommodated by the existing primary cooling loop designs.

Table 6.8. Summary of target system cooling loop heat loads and radiolysis design basis.

	Total heat load, W		Nuclear heating of water, W	
Cooling loop	**IRP3 1.3 GeV**	**Original 1 GeV**	**IRP3 1.3 GeV**	**Original 1 GeV**
1. Mercury exchanger	1,072,500	1,400,000	9	Not quantified
2. Target shroud/PBW	67,960	124,116	7,545	17,465
3. Moderators/inserts	37,849	46,602	10,455	9,193
4. Reflector plugs	560,140	658,045	39,979	31,470
Total loops 1–4	1,738,449	2,228,763		

Table 6.8 also summarizes the energy deposited in the water in each water loop. The energy deposited in the water (provided by neutronics analysis and represented as total wattage) is used to calculate the radiolytic gas production from the breakdown of the water. The total energy deposited in the water for loops 3 and 4 is higher than in the original design basis, and it is lower for loop 2. The installed purge and gas handling hardware was designed to cover a wide range and can accommodate both the lower and higher radiolytic gas generation rates that are predicted to result from the PPU energy deposition in the individual water loops.

Refer to document PPU-103-ES0003-R01 [10] for additional details regarding impact on radiological emissions.

Based on these analyses, the original primary cooling loop designs are capable of handling the heat load produced at 2.0 MW and 1.3 GeV.

Secondary cooling loops

Given that the individual primary loop heat loads and the overall target heat load are lower than the original SNS 1.0 GeV design values, and the original secondary system designs were based on the higher loads, the original secondary loop designs are capable of handling the PPU loads. However, a review of operating data suggests that the pressure profile in the tower water system within Building 8700 (the Target Building) has changed since the system was installed, and some individual components are still being evaluated.

The only anticipated upgrade to the target utility systems is the replacement of a temperature control valve in the tower water cooling loop 1. Maintenance was recently performed on the heat exchanger that provides the control parameter (loop 1 outlet temperature) for the temperature control valve. The control valve position is automatically adjusted to maintain this outlet temperature. Final evaluations and recommendations for the temperature control valve are expected to be complete by the CD 2/ 3 review.

Section 6.5.9.6 covers the helium gas injection and gas recirculation components of the PPU project.

6.5.5.2 Helium Gas Injection Modifications for PPU

The actual required gas rate and pressure to the target will be determined by R&D. The maximum envisioned total gas rate is 20 SLPM. The maximum envisioned pressure is 100 psig. Recirculating gas will be the primary means of gas supply to the target, with a once-through supply backup/supplement capability. Along with the 2.0 MW–capable target gas injection work scope, the specific performance requirements, installation, and safety approvals will be achieved for new gas injection supply equipment. PPU target gas utilities will build upon anticipated progress from the operations-supported GI3 project.

The existing gas panel 9 can supply helium at up to 10 SLPM to the target bubblers. A new gas panel 10 will be installed to supply helium at up to 10 SLPM to the target wall at 100 psig, for a total combined helium flow of up to 20 SLPM. Gas panel 10 will be installed in the high bay, next to gas panel 9, and will have the same hardware as panel 9. The method of controlling the gas flow to both the target bubblers and the target wall is still under evaluation. The two options being considered are a cascade control scheme using a pressure controller, and a mass flow controller. These options are being evaluated as part of an off-normal analysis in April 2020. Once a control scheme is selected, it will be implemented for both gas panels.

For additional details on control scheme, refer to the SNS technical document *Mercury Target Gas Injection System Process Control System Description* [11].

6.5.5.3 Preliminary Gas Recirculation Design

A recirculating gas compressor is planned for long-term target gas injection to conserve helium and reduce the stack emission potential. The gas recirculation system will use two separate compressor trains. Each train will have two compressors, with one compressor acting as an installed spare. One train will supply recirculated gas to the target bubblers and the second will supply recirculated gas to the target wall. These compressors will have the option of using either compressor speed or suction throttling as the variable to control the flow rate of the gas. This will allow operators to have flexibility in reaching the desired flow conditions.

The gas recirculation system will have two tie-in options to the MOTS. One will be upstream of the CuO beds, located in the carbon adsorber room, and the second will be downstream of the cryogenic adsorber, which is located in the MOTS room. This arrangement will provide operational flexibility for the recirculation of the gas. The recirculation gas can be sent back to the target wall and bubblers with or without full off-gas treatment through MOTS.

The gas injection system (panels 9 and 10 and the recirculation system) will have the capability to provide either once-through gas or recirculation gas. Safety interlocks have been designed to ensure that only one of these configurations (once-through or recirculation) can be in operation at any given time. Additional safety interlocks are included to ensure that the total helium supply to the target does not exceed 20 SLPM. For additional details, refer to the document *Mercury Target Gas Injection System Process Control System Description* [11].

A molecular sieve skid will be used with the gas recirculation system and will be installed in the GAR. The molecular sieve skid will remove water vapor from the gas stream. During the recirculation operating mode, water intrusion into the system could build up, potentially freezing in either the mercury vapor condenser or the cryogenic charcoal bed in the MOTS. Water vapor freezing in either location has the potential to impact operation of the target system.

Most of the gas recirculation system (e.g., compressors, instrumentation) will be installed in the carbon adsorber room. The gas lines that feed the target wall and bubblers from the compressors will travel through the basement utility vault, up the vertical chase, through the delay tank cavities, and to the target service bay through the repurposed target shroud spare water line. The recirculating gas lines are routed through areas that are exhausted by either the secondary confinement exhaust or the primary confinement exhaust system. Figure 6.36 shows an overview of the gas piping path.

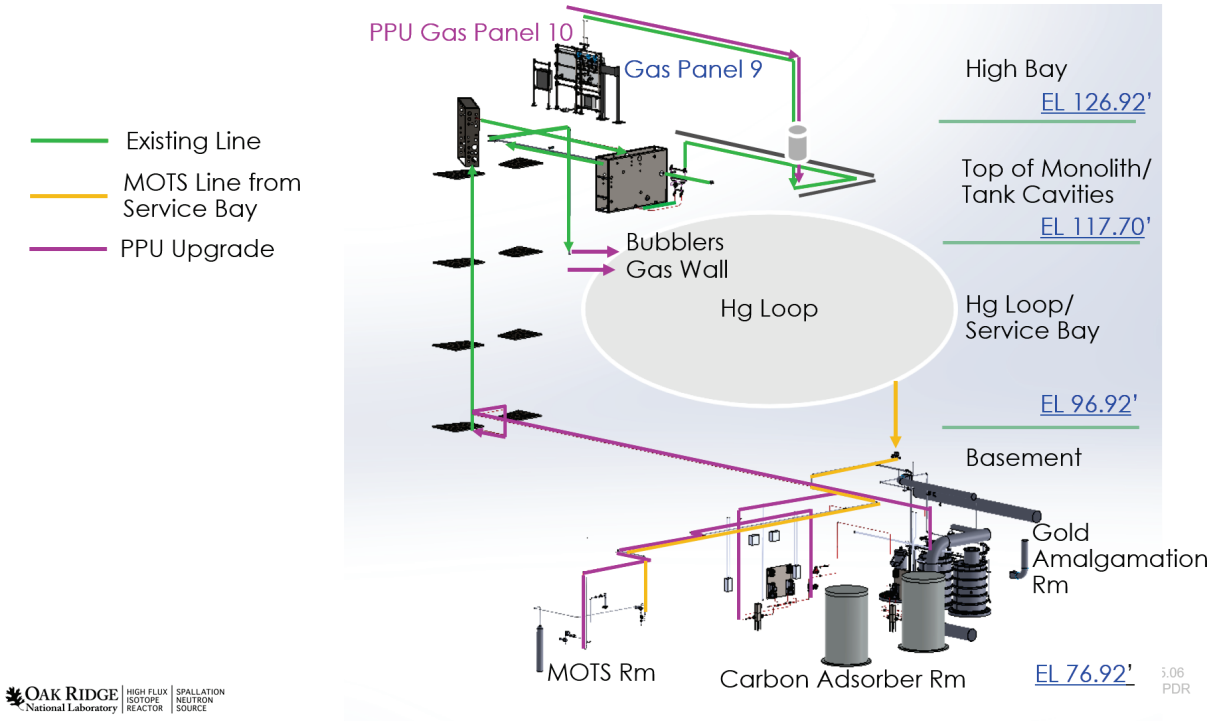

Figure 6.36. Overview of pipe path for the target gas recirculation system.

Additional radiation monitors are being installed in the carbon adsorber room to monitor the newly installed gas lines and equipment. These monitors will also help detect any changes to the radiation dose rate as the gas flow rate to the MOTS fluctuates with the overall gas injection rate. Dose rates from the gas line may necessitate shielding of components and lines.

The gas recirculation system will require an electrical upgrade. This upgrade will include the installation of a new 480 V distribution panel, a 480/208 transformer, and conduit and wiring to loads and instruments. The electrical installation will require pulling power from the instrumentation floor of the target building into the basement.

Figure 6.37 depicts the compressors that feed recycled helium to the target wall.

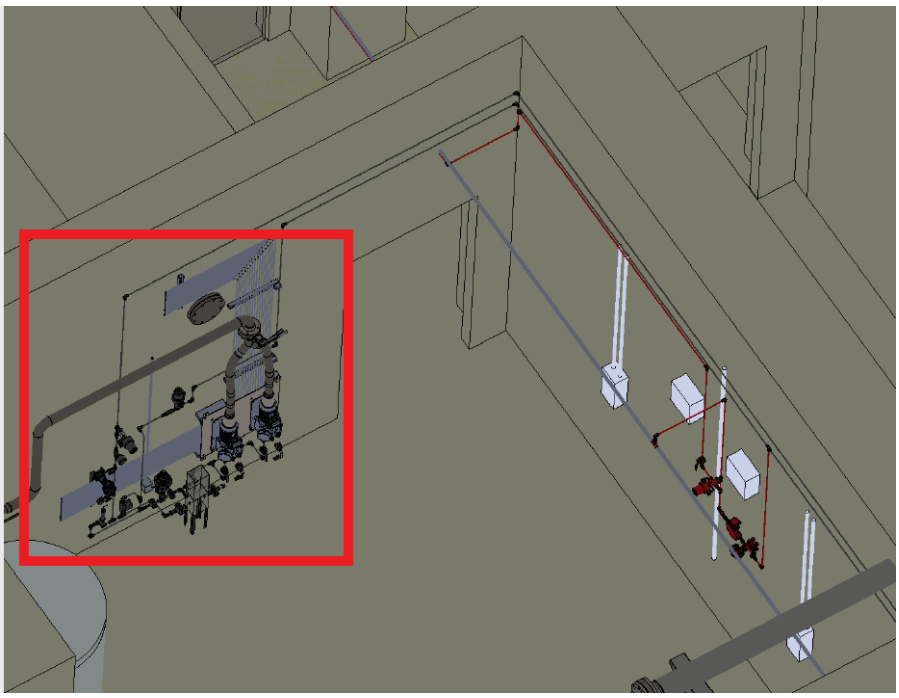

Figure 6.37. Target wall compressors.

Figure 6.38 depicts the compressors that feed recycled helium to the target bubbler.

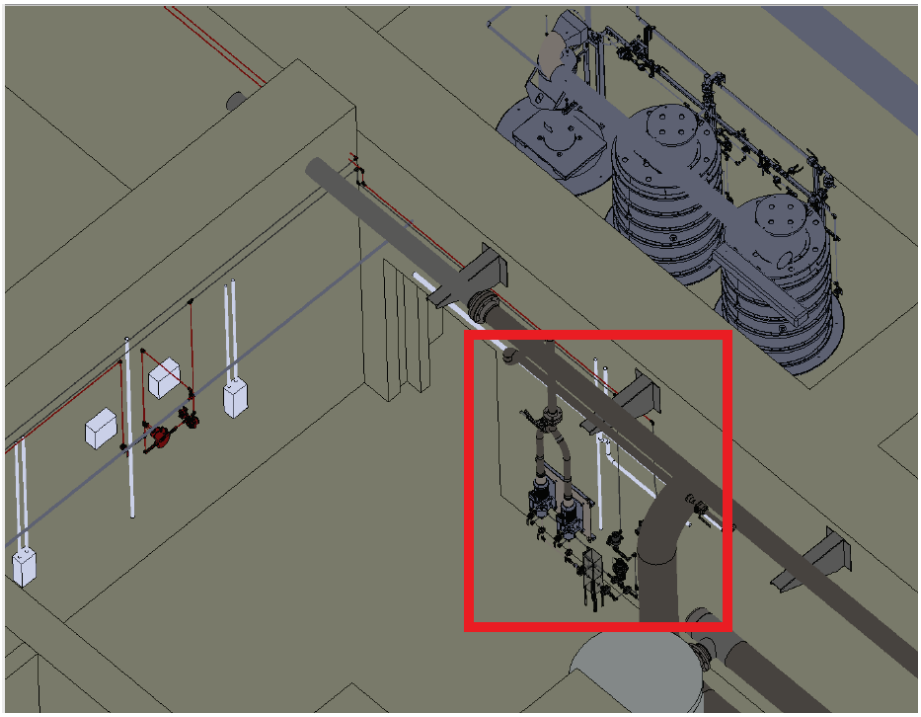

Figure 6.38. Target bubbler compressors.

A preliminary block flow diagram of the modifications for PPU is shown in Figure 6.39.

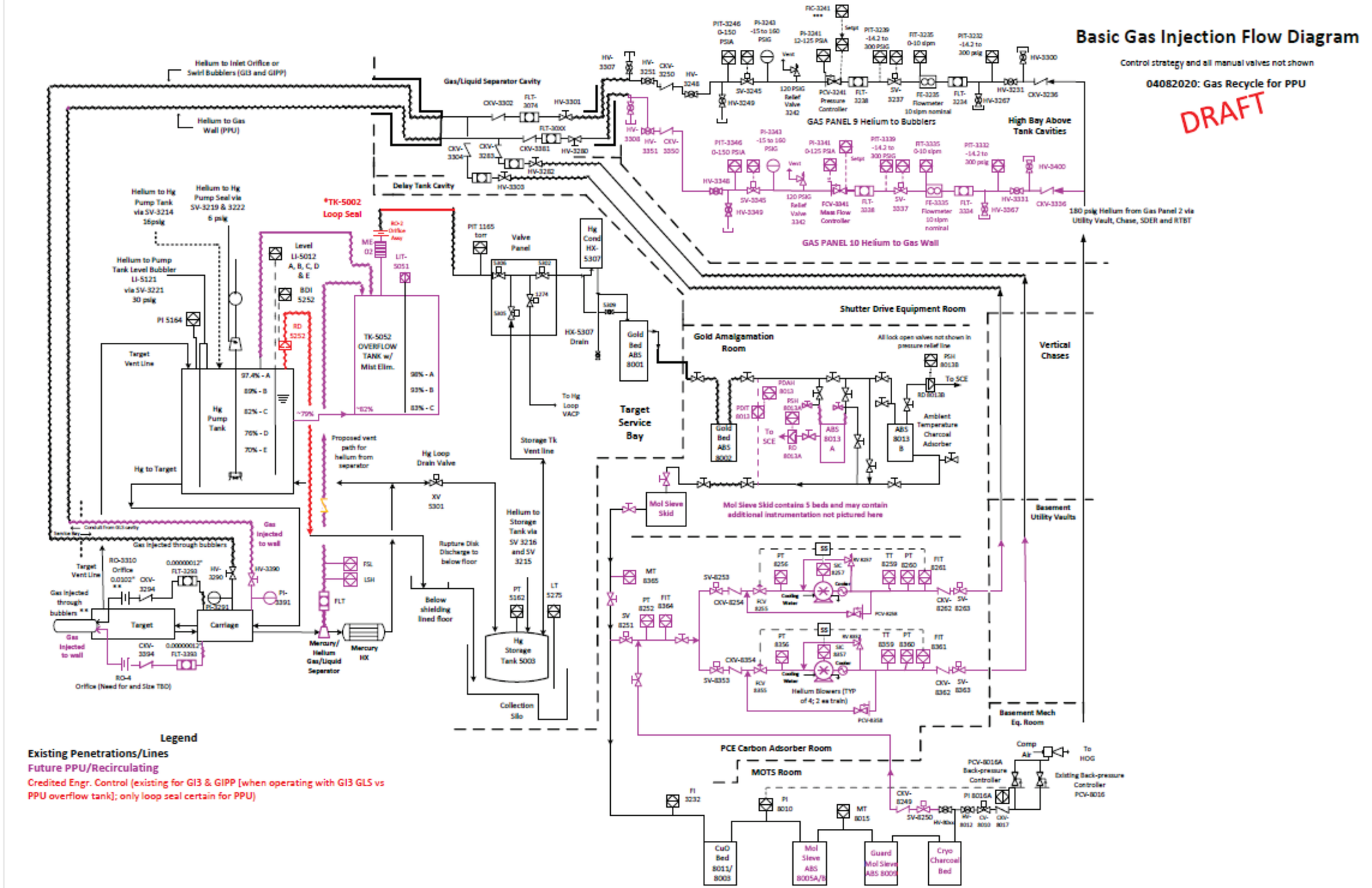

Figure 6.39. Basic gas injection flow diagram.

Completion of P.5.6 design is expected in FY 2021.

6.5.5.4 References

1. I. Popova, *Heat Deposition in the Mercury Hear Exchanger for PPU Conditions*, SNS-106100200-TR0262-R00, Oak Ridge National Laboratory, December 2018.
2. *Direct Nuclear Energy Deposition into Liquids of SNS Target Station for PPU Beam Conditions*, PPUP-502-TR0001-R00, Oak Ridge National Laboratory, July 2018.
3. E. Dominguez-Ontiveros, *Thermal Computational Fluid Dynamics (CFD) Analysis of the Lower Inner Reflector Plug 3 (IRP-3) of the First Target Station (FTS) at SNS*, SNS-10630101-DA0005-R01, Oak Ridge National Laboratory, June 2019.
4. O. Martinez, *Core Vessel Insert Thermal Structural Analysis with PPU Beam Operation*, PPUP-507-DA0001-R00, Oak Ridge National Laboratory, April 2019.
5. I. Remec, *Neutronics Assessment of the SNS FTS Core Vessel Inserts for the PPU*, SNS-106100200-DA0098-R00, PPUP-507-DA0001-R00, Oak Ridge National Laboratory, April 2018.
6. D. McClintock, *Review of the Administrative Dose Limit for 316L in the SNS Outer Reflector Plug at the Spallation Neutron Source*, SNS-106100200-TR0251-R00, Oak Ridge National Laboratory, March 2019.
7. W. Lu, *Energy Deposition at the Core Vessel for 1.3 & 1.0 GeV Proton Beams*, SNS-106100200-TR0257-R00, Oak Ridge National Laboratory, September 2018.
8. C. Barbier, *Thermal Analysis of the Lower Outer Reflector Plug for a 1.3GeV 2MW Proton Beam*, SNS-106030102-DA0004-R00, Oak Ridge National Laboratory, October 2018.
9. C. Barbier, *Thermal-Hydraulic Analysis of the Aluminum Proton Beam Window and Assembly Design Analysis Calculations (DAC)*, SNS-106040200-DA0004-R00, Oak Ridge National Laboratory, March 2016.
10. *Radiological Emissions Associated with the PPU Project at the Spallation Neutron Source*, PPU-103-ES0003-R01, Oak Ridge National Laboratory, October 2019.
11. *Mercury Target Gas Injection System Process Control System Description*, SNS-106060000-TD0006-R03, Oak Ridge National Laboratory, In progress.

6.5.6 MOTS Upgrades

6.5.6.1 Scope and Introduction

The purpose of the MOTS is to remove mercury vapor, tritium, noble gases, and spallation products from the helium vent stream from the mercury process system. The system comprises the mercury condenser and a gold amalgamation bed in the target service bay (TSB); a second gold amalgamation bed and ambient-temperature carbon adsorber in the GAR; and two copper oxide reactors, two molecular sieve beds, a guard molecular sieve bed, and two cryogenic carbon adsorbers in the MOTS room.

A simplified diagram of the MOTS with PPU upgrade scope outlined in red is shown in Figure 6.40. ABS-8013A and shielding, the GAR crane, and the CuO reactor shielding design are complete. The mercury condenser (Hg Cond in the figure) in the MOTS exhaust train serves to reduce the amount of mercury vapor entrained in the target system off-gas stream. A dedicated refrigerator cools the process flow to condense mercury vapor into droplets, which are collected and periodically returned to the mercury system. The two gold amalgamation units contain Al_2O_3 pellets impregnated with gold (1.6%

Au) for removal of any remaining mercury vapor. The ambient-temperature carbon adsorber inside the GAR provides delay/retention capacity of noble and spallation gases to minimize the dose rates outside the GAR. Copper oxide reactors convert elemental tritium into tritiated water, which is captured in the molecular sieve beds. The guard molecular sieve bed captures moisture escaping the upstream sieve bed, in the event it becomes saturated, to prevent the downstream cryogenic carbon adsorber from plugging. The cryogenic carbon adsorber captures the remaining noble gases and spallation products and prevents their release to the environment. The MOTS discharges treated gas to the hot off-gas system (HOG in the figure).

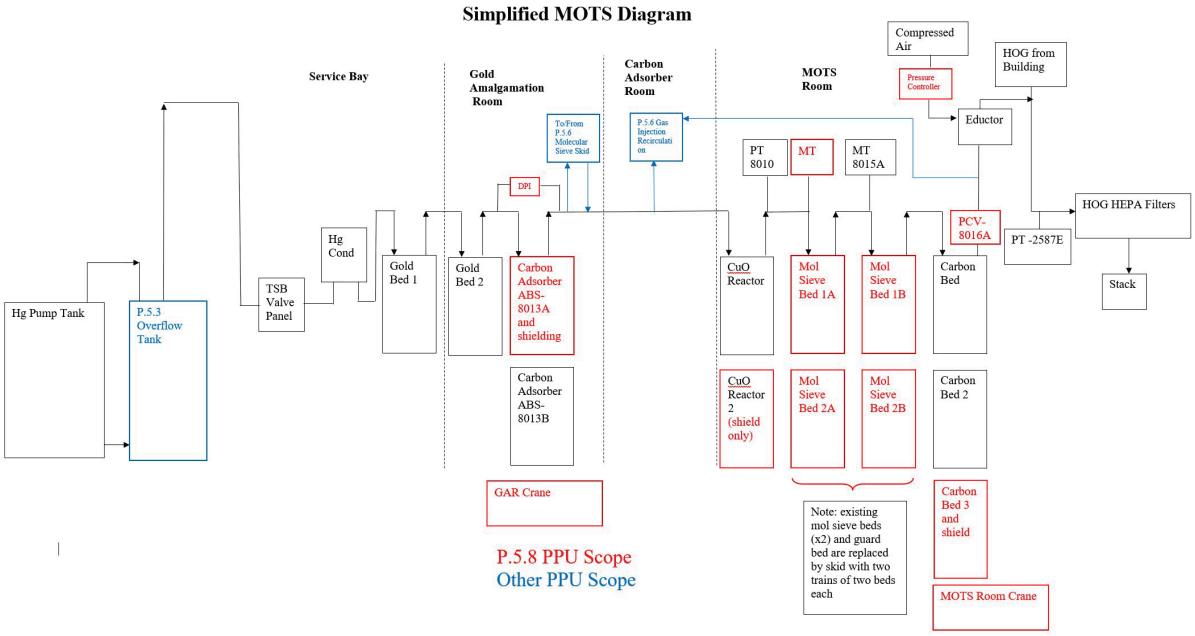

Figure 6.40. Simplified MOTS diagram with PPU scope outlined in red.

6.5.6.2 Requirements

The following are the MOTS process design criteria/requirements for the 2 MW, 1.3 GeV beam:

- Maintain the ability to treat once-through helium gas up to 10 SLPM to both the target bubblers and target wall (a total of up to 20 SLPM) without plugging the cold trap.
- Maintain MOTS operating pressure between 12.5 and 14.7 psia,
- Maintain mercury pump tank head space operating pressure unchanged from current values in once-through mode (<16 psia PAHH),
- Modify MOTS set points, indications, and controls to incorporate operation of the gas injection recirculating compressors (TBD),
- Maintain temperature of the cryogenic carbon adsorber at <115 K (the freezing point of krypton is 116.6K) at 20 SLPM to maintain system efficiency and stay within the limits of the site air permit.

- *Radiological Emissions Associated with the PPU Project at the Spallation Neutron Source (PPU-103-ES0003, R00)* [1] concludes that PPU modifications will not require a permit to construct or pre-notification to the Environmental Protection Agency or Tennessee Department of Environmental and Conservation. Maintaining the current efficiency of MOTS is assumed and is therefore a requirement for P.5.8.

6.5.6.3 Assumptions

MOTS modifications for the PPU are based on the following assumptions:

- Steady helium gas injection flow capability of up to 20 SLPM.
- 2.0 MW, 1.3 GeV proton beam.
- The GI3 project is complete with the following equipment designed, procured, fabricated, and installed (achieved November 2017):
  - The first shielded carbon delay bed in MOTS for noble gas adsorption is installed in the GAR.
  - Piping and piping supports for the carbon delay bed will include connections for a second delay bed.
  - The MOTS vent line GLS is in place to prevent mercury from entering the target service bay gas valve panel because of gas injection to the mercury process loop.
  - A low-flow, once-through gas supply panel with the ability to monitor and control helium flow via EPICS is installed.
  - Features to prevent mobilization of MOTS bed media by high-rate gas flows associated with expanding trapped gas bubbles (e.g., restricting orifice, surge suppression tank) are in place, or there is verification that mobilization is impossible under PPU steady or transient gas rates.

- The following documentation, procedures, and training materials are updated:
  - Design basis documents, including the FSAD. Accelerator Safety Envelope (ASE), and Operational Envelope.
  - Operation Procedure Manual procedures.
  - Piping and instrumentation diagrams.
  - Target operation shift technical training materials and qualification standard.

6.5.6.4 Technical Design

The PPU MOTS scope includes the addition of a second ambient-temperature carbon delay bed and related shielding inside the GAR (Figure 6.41). The first one was installed as part of the GI3 effort. High-rate target gas injection with the PPU will add to the radioactive gas flow rate and likely the specific radioactivity that eventually reaches MOTS. The second delay bed will ensure dose rates to workers and equipment in the MOTS equipment room and nearby areas will be maintained at acceptable levels. It also provides the ability to swap out or regenerate one delay bed canister while maintaining MOTS operation. An electric monorail crane in the GAR (Figure 6.42) will be constructed to provide a safe means to install/remove the shield blocks for the delay beds. A differential pressure transmitter and new moisture transmitter will also be included in the GAR installation to monitor for plugging and in-leakage to the system. The designs for the additional MOTS delay bed, shielding, and monorail crane are complete [2][3].

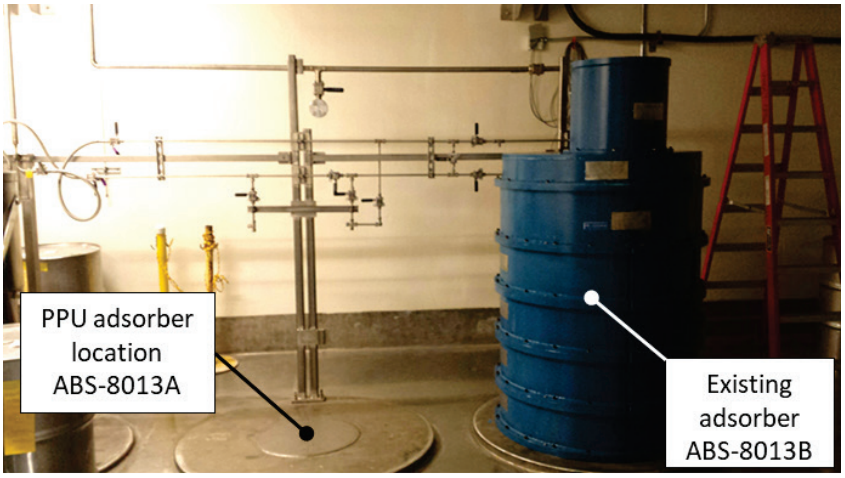

Figure 6.41. The PPU ambient temperature carbon adsorber will be placed next to the existing unit inside the gold amalgamation room.

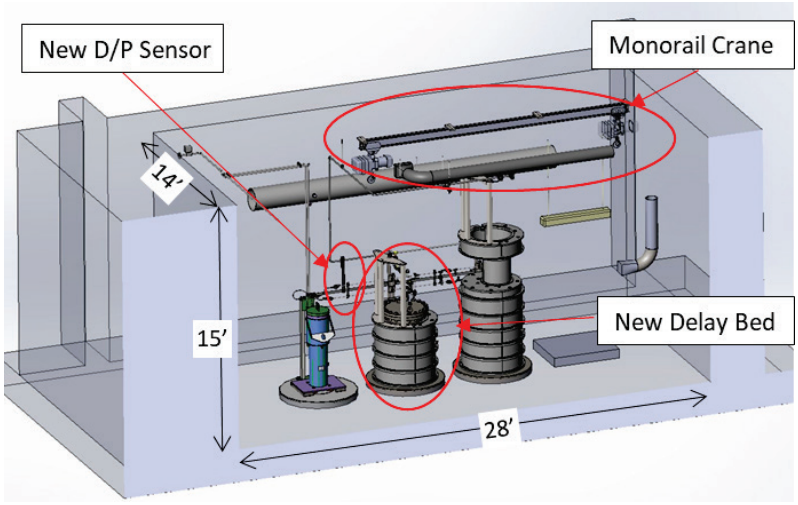

Figure 6.42. Gold amalgamation room equipment layout.

Other upgrades to the MOTS have been identified to improve operational reliability under high gas flow conditions. An additional cryogenic carbon adsorber assembly and shielding will be provided (Figure 6.43). Full redundancy is needed because of the more frequent maintenance expected with PPU high-flow gas injection and the long decay times associated with carbon adsorber cold head maintenance. A manual monorail crane is included in the design to provide a safe means to install/remove the shield blocks for maintenance. Two thermocouples will be included for monitoring the performance of the cold head. The design of the additional cryogenic carbon adsorber leverages the existing design of ABS-8012 [4].

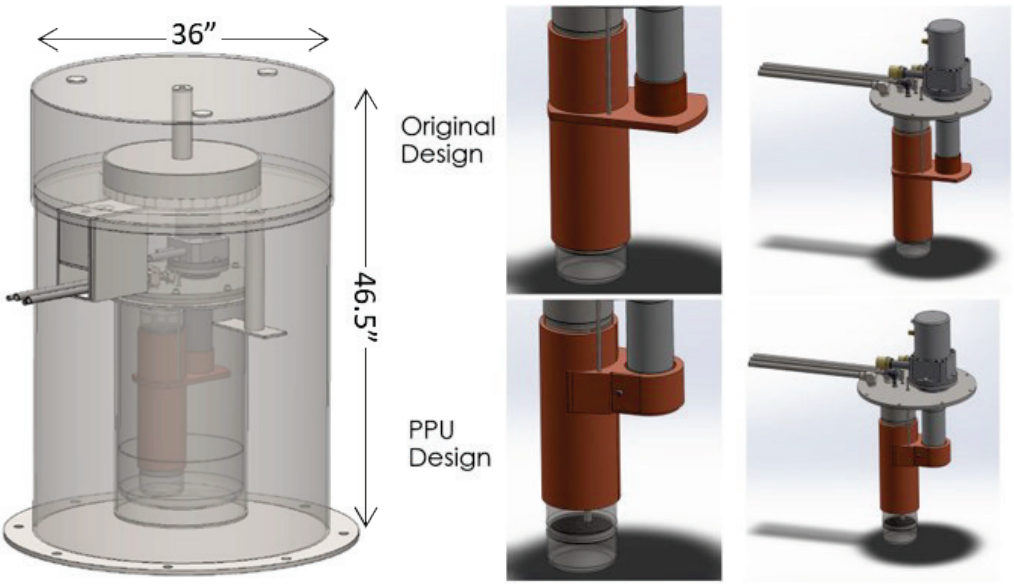

Figure 6.43. Additional cryogenic carbon adsorber assembly preliminary design.

However, thermal analysis of the design indicated, and testing confirmed, that improvements are needed to increase the thermal capacity of the cryogenic adsorber in order to maintain temperatures below the freezing point of krypton (116.6 K) with the increased heat load of 20 SLPM [5][6]. The modifications include these:

- Increasing the heat transfer surface between the cold head and thermal plate
- Adding a regenerative heat exchanger to cool incoming gases
- Vacuum jacketing the outgoing gas line to the regenerative heat exchanger
- Modifications for better brazing of the thermal sleeve

The existing molecular sieve beds and their glove box will be replaced with much larger units (Figure 6.44) to provide the required residence time at 20 SLPM [7]. A total of five units, including shielding, will be provided. The layout in the MOTS equipment room is shown in Figure 6.45. The configuration will be two trains of two molecular sieve beds each for operational reliability. These units will require heaters, temperature indications, and controls for regeneration of the media. A new moisture transmitter will be included in the design to monitor system performance. The fifth bed will be used to capture the exhaust of the regenerated units and will be replaced periodically. The addition of the new molecular sieve beds and shielding will require the removal of the existing MOTS glove box, which also houses one of two existing copper oxide reactors. A shield housing for the reactor is also included in the MOTS PPU scope. Because the CuO reactors are identical, the design for the existing shielding will be used and is complete [8].

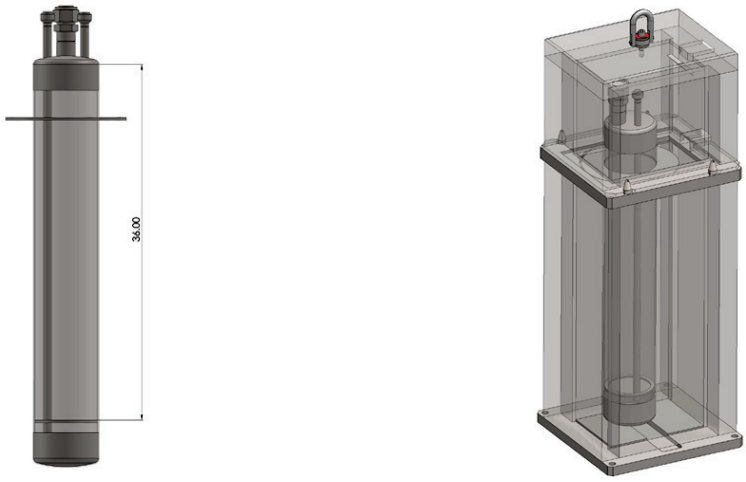

Figure 6.44. Molecular sieve bed (left) and shielding (right) preliminary design.

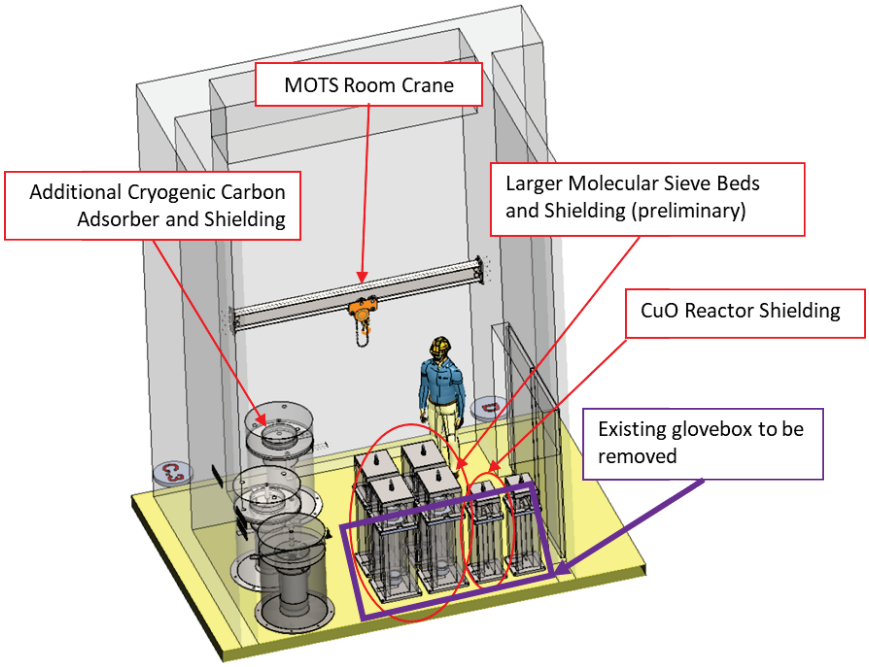

Figure 6.45. MOTS equipment room layout.

A pressure controller will be included to control MOTS pressure automatically in either once-through or recycle modes of target gas injection. The pressure controller will allow operators to control the system from EPICS instead of locally operating a manual regulator. MOTS set points, indications, and controls will be modified to integrate with operation of the gas injection recirculating compressors.

The PPU FTS systems work scope for MOTS includes the design, fabrication, installation, commissioning, and documentation updates necessary to complete these goals to ensure safe and reliable operation with high-rate gas injection. Table 6.9 lists design reviews and test results to date for P.5.8.

Table 6.9. P.5.8 progress to date.

P.5.8 scope	Date	Reference
Gold amalgamation room crane FDR	October 2018	PPUP-508-DE0001-R00 *Final Design Review Report: Gold Amalgamation Room Monorail Crane*
MOTS flow testing with beam off	February 2019	108030700-TR0011-R00 *Characterization of Mercury Off-gas Treatment System at Higher Gas Flow Rates with Beam Off Test Report*
Mercury condenser evaluation	February 2019	SNS-106010000-TR0143-R00 *Mercury Vapor Condenser Efficiency Testing at Flow Rates Elevated due to Bubble Injection*
Delay bed and shielding FDR	April 2019	PPUP-508-DE0002-R00 *Final Design Review Report: MOTS Ambient Temperature Carbon Adsorber ABS-8013A and Shielding*
P.5.8 Internal PDR	September 2019	PPU-508-DE0003-R00 *Mercury Off-gas Treatment System Internal Preliminary Design Review Report*
MOTS molecular sieve bed sizing	October 2019	PPU-508-DC0001-R00 MOTS *Molecular Sieve Bed Sizing Determination*
Cryogenic carbon adsorber design analysis	October 2019	PPUP-508-TD0001, R00 *Technical Review of Cold Adsorber Design*
MOTS flow testing with beam on	Completed February 2020	PPUP-508-TR0001, R00 *Characterization of the Mercury Off-gas Treatment System at Higher Gas Flow Rates with Beam On*

6.5.6.5 References

1. S. Trotter, *Radiological Emissions Associated with the PPU Project at the Spallation Neutron Source*, PPU-103-ES0003-R00, October 2019.
2. G. Stephens, *Final Design Review Report: MOTS Ambient Temperature Carbon Adsorber ABS-8013A and Shielding*, PPUP-508-DE0002-R00, April 2019.
3. G. Stephens, *Final Design Review Report: Gold Amalgamation Room Monorail Crane*, PPUP-508-DE0001-R00, October 2018
4. ABS-8012 and Shielding Mechanical Drawings, 108030700-M8U-8700-A023 to -A029.
5. B. Degraff, *Technical Review of Cold Adsorber Design*, PPUP-508-TD0001-R00, October 2019.
6. G. Stephens, *Characterization of the Mercury Off-gas Treatment System at Higher Gas Flow Rates with Beam On*, PPUP-508-TR0001-R00, March 2020.
7. D. Montierth, *MOTS Molecular Sieve Bed Sizing Determination*, PPU-508-DC0001-R00, October 2019.
8. CuO Reactor Shielding Drawings, 108030700-J8U-8700-A353 and -A354.

6.5.7 2.0 MW Target Module Design

6.5.7.1 Scope

A state-of-the-art target vessel design capable of operating at 2.0 MW will be provided for the PPU. The scope includes a redesigned target vessel, modifications to the water-cooled shroud, and hardware that interfaces the target to the carriage. Changes to the IRP, mercury process system, and carriage drive are

not in the 5.9 scope; thus, their interfaces with the target module will remain the same as the current interfaces. The target lifetime requirement is a minimum 1250 h, which is four target vessels per year.

Three 2.0 MW targets will be fabricated for use by the project. In addition, the scope includes two additional test targets that provide early feedback on new design features in the 2.0 MW targets. These targets will be operated before the 2.0 MW targets.

6.5.7.2 Requirements

The 2.0 MW target module shall meet the requirements of the 2 MW Target Module Design Specification, 106010101-TS0006, which includes the following:

- Provide continuous operation up to 1250 hours or more at 2 MW, 1.3 GeV, and 60 Hz.
- Is evaluated to and meets the requirements of *Structural Design Criteria for SNS Target Modules*, 106010101-DC0001
- Interface with existing structures including but not limited to the target carriage, core vessel, and IRP.
- Provide a secondary boundary to contain any mercury leaks from the inner mercury vessel and a method of detection for the leaks.
- Maintain the ability to replace targets using remote handling.

6.5.7.3 Assumptions

The following assumptions were made in designing and evaluating the target module.

- 2 MW and 1.3 GeV beam are within limits as defined in in the case load tables in Section 6.5.7.4 and as provided by Neutronics for final beam profile cases.
- Mercury pump operates at up to 400 rpm, which is vendor's maximum recommended operating speed, and adequate cooling of mercury is provided by the heat exchanger.
- Two helium lines are supplied to the target module which can provide up to a combined 20 SLPM at 100 psig. GLS and mercury overflow tank are installed to allow operation at these gas injection rates.
- Higher-volume gas injection provides strain reduction to meet expected fatigue criteria.

6.5.7.4 Technical Design

Figure 6.46 illustrates an exploded view of the PPU target. The bolt-on shroud encapsulates the target forward of the flange protecting the IRP from mercury leaks. There is a small volume between the target vessel and BOS called the "interstitial space." If a target or bolt-on shroud leaks before the end of a run cycle, it will be captured within the interstitial space where it will be sensed by leak detectors. The PPU target will deploy new features such as a tapered front-body and swirl bubblers to achieve reliable operation at 2.0 MW.

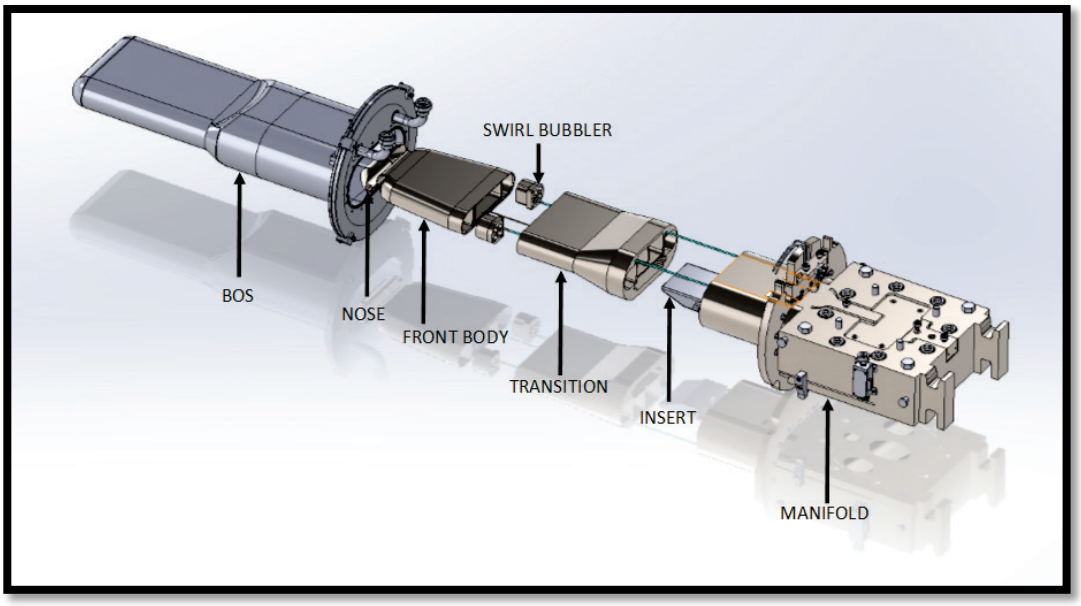

Figure 6.46. Exploded view of target assembly.

The PPU will increase beam power from 1.4 MW to 2.0 MW and beam energy from 1.0 GeV to 1.3 GeV. The 43% increase in power will increase the pressure pulse, which is generated when the proton beam strikes the liquid mercury in the target vessel. The peak pressure in the mercury will rise from 25 MPa to 34 MPa, significantly increasing the burden on the 316L stainless steel target vessel. Operational experience and the latest analysis techniques will be used to develop a target design fit for 2.0 MW operation.

The intense pressure within the mercury damages the target in two significant ways. Cavitating mercury erodes the stainless-steel vessel, and the 60 Hz cyclic pulse can initiate a crack in the vessel from high cycle fatigue. The proton beam also heats up the target vessel, which can lead to high thermal stresses. Periodically, a beam trip will occur, and the vessel will cool down again, leading to additional fatigue damage from thermal cycles. Both types of damage can lead to a target failure. To date, 8 of the 24 targets operated have developed leaks from either fatigue or cavitation damage. Targets that fail prematurely disrupt the facility run cycle that provides scheduled neutron availability to users. Therefore, target reliability is both a project and facility priority that must be met.

Target vessel analysis is evolving as the latest software matures and provides new capabilities not available before. Target design and analysis is complex and cannot be tested anywhere outside of operation. Therefore, analysis techniques are always evolving and using the latest methods available. Targets today must meet the same design requirements as targets of the past but use new, more advanced tools to do so.

The material model, which simulates the pressure pulse generated by the short proton pulse, has not been changed. With gas injection, predicting the dynamic response of the target vessel is further complicated. Strain measurements at the beginnings of run cycles are carried out to build a database that can be used to better understand this two-phase relationship.

The water-cooled shroud, which was originally designed for 2.0 MW at 1.0 GeV, needs little modification to operate at 2.0 MW and 1.3 GeV. The increased energy will deposit the protons deeper into the target,

thus heating the shroud further back than before. Figure 6.47 shows cooling water temperature with PPU beam operation on the front portion of the current water-cooled shroud design. The water pressure is high enough that boiling is not possible.

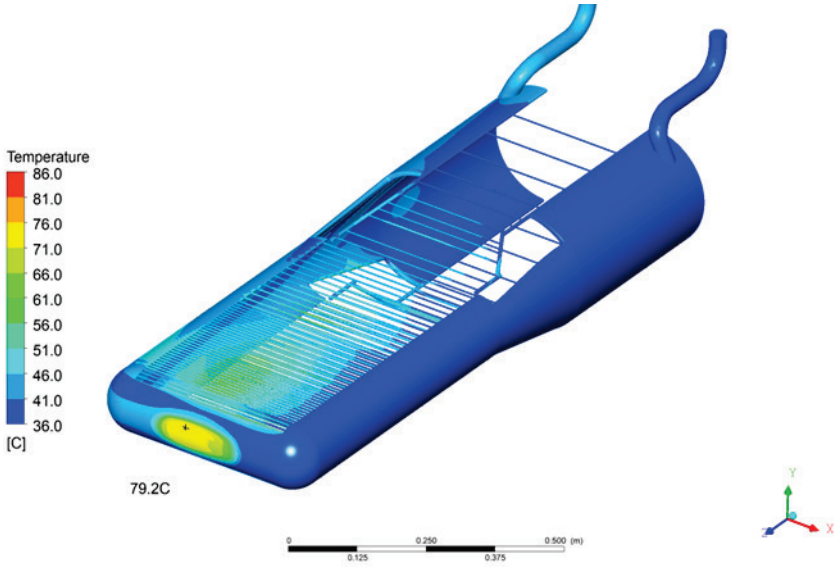

Figure 6.47. Target shroud water temperature using 2 MW PPU beam heating on the 1.4 MW jet-flow target. The PPU WCS design has minor changes affecting upper and lower coolant passages (C. Barbier).

Because of the deeper penetration of the 1.3 GeV beam heating, more cooling channels were added to remove the heat further back in the shroud, as shown in Figure 6.48.

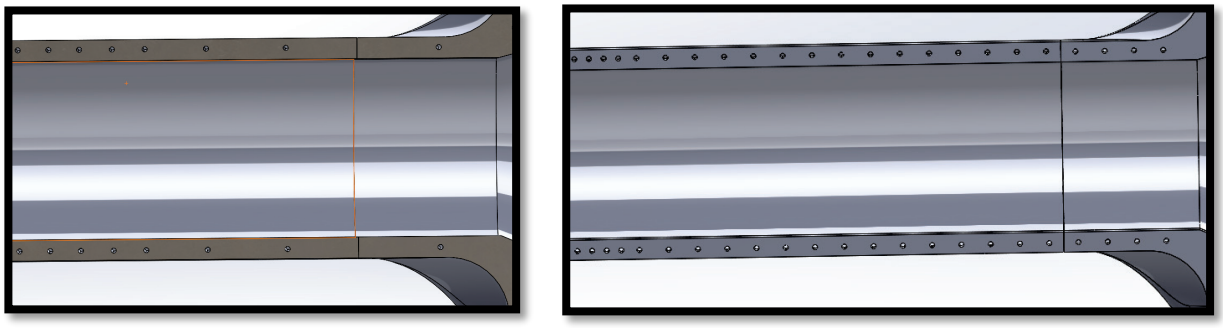

Figure 6.48. (L) Current water-cooled shroud cooling channels; (R) PPU water-cooled shroud target channels.

The water-cooled shroud has steel temperatures under the 200°C limit, as specified in the design specification. All primary and secondary stresses meet the code requirements. Fatigue is analyzed only for thermal cycles, because the proton pulse does not generate a significant pressure pulse in the cooling water as it does in mercury. Thermal cycles are evaluated to 10,000 cycles. All cases for the water-cooled shroud have a thermal fatigue life greater than 1.5 M. Load cases for the water-cooled shroud are listed in Table 6.10.

Table 6.10. Water-cooled shroud load cases.

Case	Loads / Beam	Shroud weight	H_2O weight	H_2O pressure (psia)	Interstitial (psia)	Core vessel (psia)	Incident heating	Thermal cycle
	Water-cooled shroud-normal operation							
1	Nominal	X	X	46.3 (mapped	14.7	14.7	X	X
2	Nom-6 mm up	X	X	46.3 (mapped	14.7	14.7	X	X
3	Nom-6 mm down	X	X	46.3 (mapped	14.7	14.7	X	X
4	Overfocused	X	X	46.3 (mapped	14.7	14.7	X	X
5	Underfocused	X	X	46.3 (mapped	14.7	14.7	X	X
6	Side-4 mm	X	X	46.3 (mapped	14.7	14.7	X	X
7	No beam	X	X	46.3 (mapped	14.7	14.7	X	X
	Abnormal operation							
8	Nominal-IRP vacuum	X	X	46.3 (mapped)	14.7	0	X	X
9	Nominal-HWP	X	X	67.5	14.7	14.7	X	X
10	Nominal-LWP	X	X	30	14.7	14.7	X	X
11	Leak	X	X	46.3 (mapped)	45	14.7	X	X
	Test and installation conditions							
12	Water passage test-P	X		102.7	14.7	14.7		
13	Interstitial test-P	X		14.7	65.4	14.7		
14	Interstitial test-H	X	X	14.7	71.1	14.7		
15	Interstitial vacuum test	X		14.7	0	14.7		
16	Maximum allowable working pressure	X		14.7	60	14.7		

The target vessel design poses many challenges to be addressed to operate at 2.0 MW and 1.3 GeV. The heat load increases thermal stresses, and the higher-pressure pulse will lead to a reduction in fatigue life and more cavitating mercury. New design features and gas injection will be needed to mitigate these challenges.

Figure 6.49 shows a cut view of the 2 MW target design. The cool mercury will be supplied via two bulk supply channels similar to that of the currently operating targets. The mercury will then pass through the swirl bubbler, which will be bolted into the back of the front body; there, it will be injected with small helium gas bubbles. The bolted design of the swirl bubblers allows them to be installed after the front-body-to-transition electron beam weld. This approach preserves accessibility during the welding for beam blockers and film for nondestructive examination after the weld is complete.

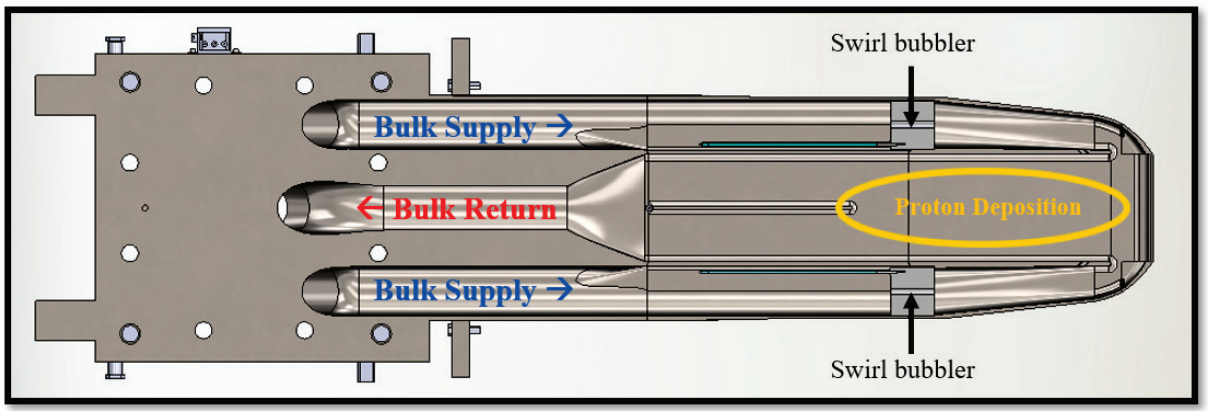

Figure 6.49. Plan section view of target module.

The front body of the target will be tapered forward of the swirl bubbler. The taper will increase the shear flow of mercury around the front corner of the target to provide mitigation of cavitation erosion compared with low shear flow. Targets T12 and T13 failed from cavitiation erosion in the front corners. The taper also will benefit the structural response of the target, which has no center baffle like the current targets. The center baffle was removed in the front body and moved to the transition so that it is located behind the high-energy-deposition zone in the front body of the target. Compared with the preliminary design, the final design shown has a less aggressive taper to reduce manufacturing challenges and to accommodate the swirl bubblers.

Gas injection is needed to reach the minimum 1250 hour target lifetime to withstand pulse fatigue loading under PPU beam operation. Gas injection acts as a cushion for the intense pressure pulse geneterated from the proton beam. The small bubbles can react quickly to the pressure change, thus reducing cavitation and fatigue damage. Current targets have seen a large reduction in caviation damage during post-iradiation examination of target modules. Large reductions in strain have also been measured using the strain gauges mounted to the outside of the target module. To date, target gas injection has not surpassed 2 SLPM. PPU tarets will inject up to 20 SLPM.

The PPU target will use swirl bubblers (Figure 6.50) to inject small helium gas bubbles into the mercury. This is a change from the current method using orifice bubblers. SNS orifice bubblers have consistently shown a repeatable trend of degraded flow rate over the operating cycle. J-PARC has been using swirl bubblers successfully for gas injection into its liquid mercury targets. Swirl bubblers will satisfy the requirement for sustained, reliable gas injection rates over the entire operation cycle. Compared with orifice bubblers, gas flow control is more flexible with swirl bubblers.

The PPU target module will also supply gas to the nose of the target where the energy deposition is greatest via a supply tube (1/8 in. OD) through the jet flow. The inner beam window has been a region of cavitation damage, leading to window fracture and disturbance of window cooling flow. This local gas injection provides gas near the region of interest while keeping supply hardware out of the beam path to avoid high thermal stresses. The increased gas fraction will further reduce the impact of the damaging pressure pulse. Figure 6.51 shows a cut view of the nose region of the target where the gas will be supplied. The exact geometry of the tube end injection tip is being developed through R&D. When R&D is complete, results and recommendations for the nozzle geometry will be defined in the document SNS-106010104-TR0001.

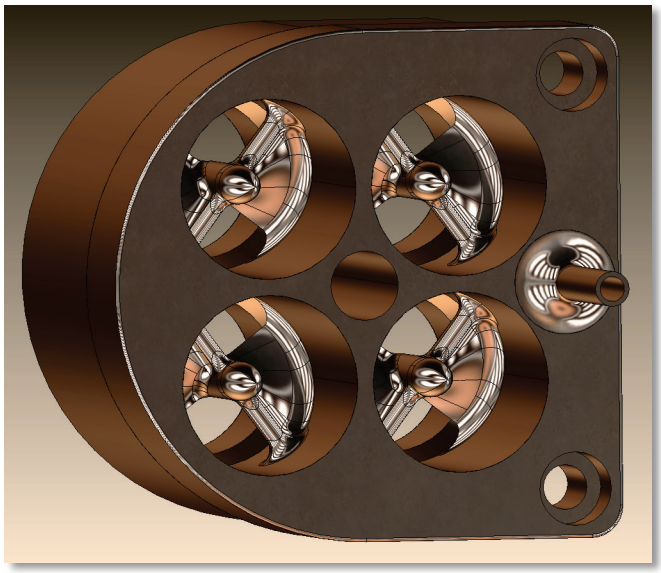

Figure 6.50. Swirl bubbler for the PPU target: 4-unit, 2-vane configuration.

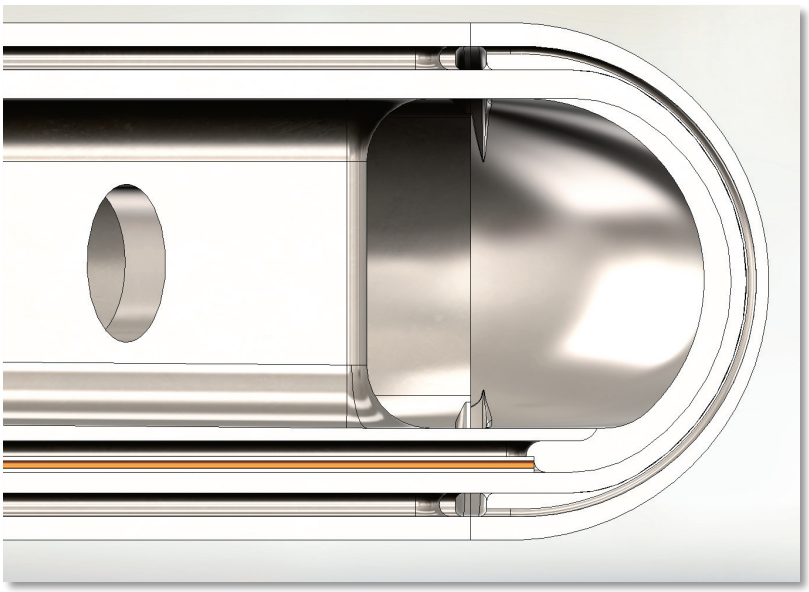

Figure 6.51. Elevation section view of target front end showing the gas supply tube (orange) to the inner beam window base.

After the preliminary design of the target module was evaluated, there was an optimization period during which many design iterations were analyzed with one goal: reduce thermal stress without sacrificing fatigue life. The PPU target will have thicker welds than the current targets to withstand the increased pressure pulse. The front body welds were increased from 1/8 in. to 3/16 in. and show a comparable life estimate to that of the current jet-flow targets operated at 1.4 MW. The thickness of the inner window and its welds were also increased to delay cavitation erosion through the window and improve the fatigue

lives of window ribs. A tapered diving board was implemented to mitigate a modal response near 60 Hz while reducing thermal stresses in the jet-flow ribs.

The transition section of the target module has been redesigned to improve its manufacturability. Current targets supply mercury to the jet flow from supply passages by diverting mercury from the bulk supplies, as shown in Figure 6.52. This is a complicated geometry for manufacturers to fabricate. The PPU target will supply the jet flow from the window flow supply, eliminating the complex bulk supply geometry. The PPU target will use a bolted-in transition insert that distributes the mercury between the window flow and jet flow. The insert will eliminate complex machining in the large transition segment.

The manifold section of the target underwent only minor changes. The interface to the target carriage and and utility connnections are unchanged. The manifold burst disk was removed and replaced with a check valve with 4 psig breaking pressure to vent leaked mercury or water from the intersitial space. Gas routing hardware will be below the top surface of the manifold to prevent any damage from remote handling and allow for greater visibility for remote handlers.

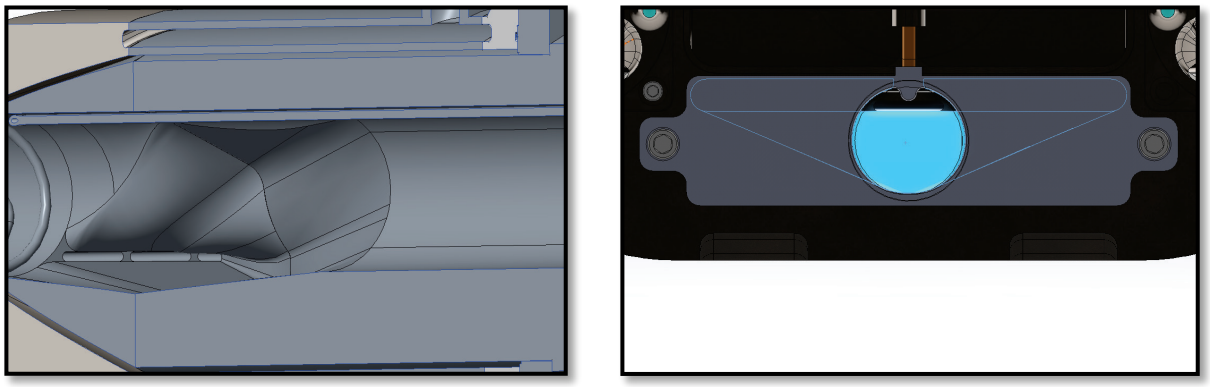

Figure 6.52. (L) Current jet-flow supply; (R) PPU jet-flow supply.

Load cases for the mercury vessel are listed in Table 6.11.

Table 6.11. Target mercury vessel load cases.

Case	Beam \ Loads	Target weight	Mercury weight	Mercury pressure	Interstitial (psia)	Incident heating	Thermal cycle	Pulse cycle
				Mercury vessel—normal operation				
1	Nominal	X	X	@400 rpm	14.7	X	X	X
2	Nom-6 mm up	X	X	@400 rpm	14.7	X	X	X
3	Nom-6 mm down	X	X	@400 rpm	14.7	X	X	X
4	Overfocused	X	X	@400 rpm	14.7	X	X	X
5	Underfocused	X	X	@400 rpm	14.7	X	X	X
6	Nom-4 mm side	X	X	@400 rpm	14.7	X	X	X
7	No beam	X	X	@0 rpm	14.7			
				Abnormal operation				
8	Nominal	X	X	@280 rpm	14.7	X	X	X
9	Nominal	X	X	@350 rpm	14.7	X	X	X
10	Gas layer	X	X	@400 rpm	14.7	X	X	X
				Test and installation conditions				
11	Mercury cavity pressure test	X		74.7	14.7			

The maximum wetted surface temperature in the mercury vessel for the nominal beam case is 192°C, which is below the 200°C limit. Figure 6.53 shows the mapped temperatures of the internal wetted surface for the target module.

Stress results are much improved over the prelimary design. Stress levels are comparable to current 1.4 MW targets, which gives confidence in moving forward with the current design. All primary stresses from the weight of the vessel and mercury, along with the internal pump pressure, meet the design criteria.

Figure 6.54 shows regions of high thermal stress in the front body. The ribs of the target have the most vessel material in the energy deposition zone, which leads to higher thermal stresses. Table 6.12 illustrates that the nominal, overfocused, and underfocused cases meet the design criteria before linearization. The 6-mm up and 6-mm down cases are slighly over the limit of 345 MPa but drop to within the limit when linearized to extract peak stresses that contribute to fatigue.

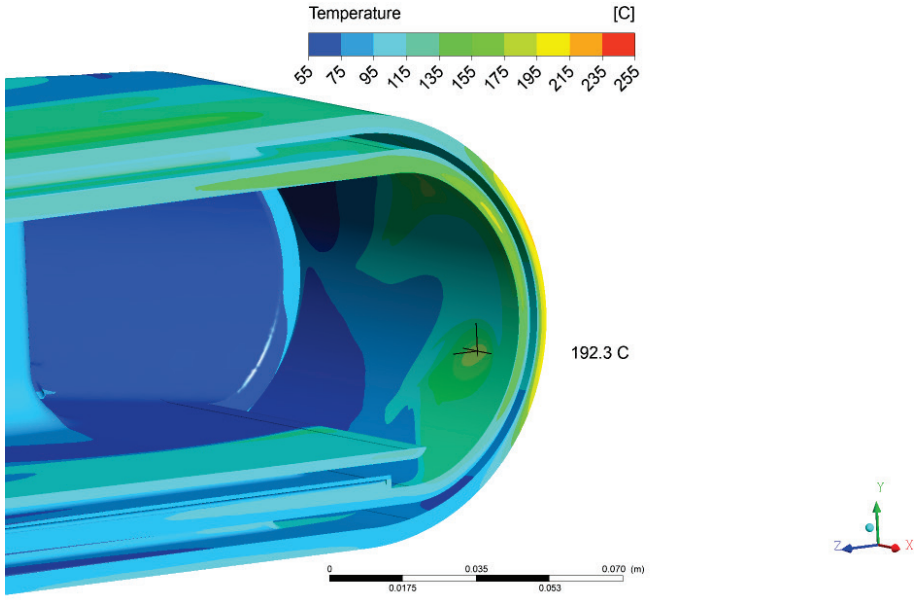

Figure 6.53. Target module wetted surface temperature contour—nominal beam.

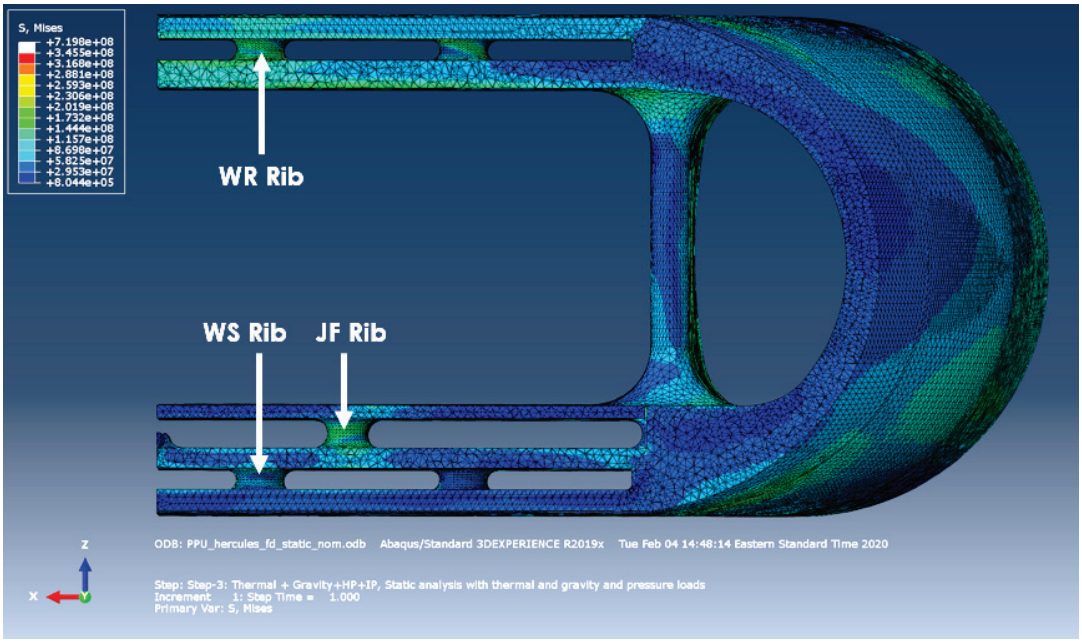

Figure 6.54. Target module static stress contour—nominal beam.

Table 6.12. Target module maximum stress values.

	Nominal	Up	Down	Over	Under
JF rib	215	152	403	175	272
WS rib	146	111	160	136	170
WR rib	258	398	251	239	270
Outer window	250	283	283	267	248
Inner window	242	409	203	219	283
Ellipse	302	290	317	277	334

The target module is evaluated for fatigue to assess its ability to operate for the minimum lifetime of 1250 hours. Over that lifetime, the vessel will experience more than 270 million pulses. The design basis for thermal cycles is for up to 10,000 cycles—a conservative number based upon present-day operating experience.

For all thermal load cases, the target module exceeds the 10,000 thermal cycle limit. Figure 6.55 shows the predicted pulse fatigue life at the lowest-life regions. The jet-flow rib has a minimum life prediction of 1.5 million cycles. This is well below the expected lifetime operation of 270 million cycles. Because of conservatism, material modeling, and other factors, fatigue life predictions have always been low. The best way to gauge whether the target is suitable for operation is to compare it with a current target that has operated successfully. The best operating target to date is the jet-flow target. The jet flow target has a minumum predicted fatigue life of 1.7 million cycles at 1.4 W. This life prediction is very comparable to what the PPU target is achieving.

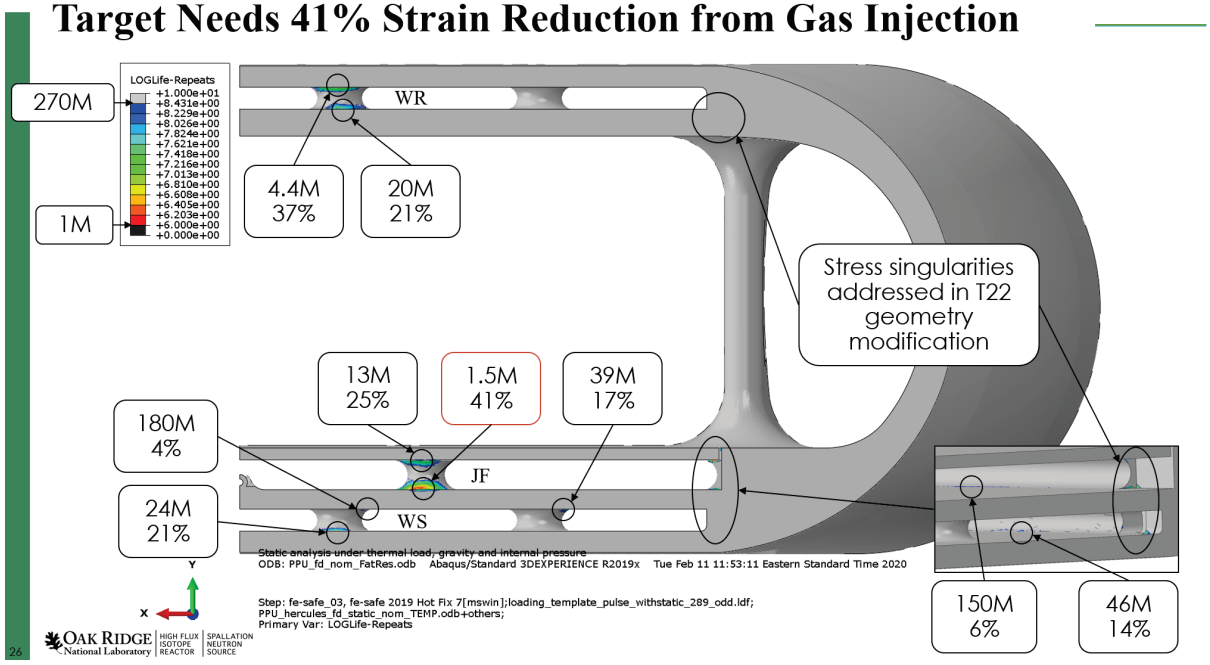

Figure 6.55. Target predicted fatigue life and required strain reduction.

The analysis also predicts how much strain reduction from gas injection is needed to meet the 270 million pulse cycle requirement. For the PPU target, a strain reduction of about 40% is needed from gas injection. The swirl bubblers and nose injection aim to provide a high void fraction of gas in the high energy deposition zone to achieve this. Current targets that have injected no more than 2 SLPM have seen a greater than 40% strain reduction in certain areas. The PPU target will be capable of injecting up to 20 SLPM with the goal of higher strain reduction more broadly across the target vessel.

The PPU 2 MW target is based upon the best available design practices, R&D, modeling, and simulation techniques, and it incorporates years of operational and fabrication experience. Design features differ from the 1.4 MW design while conforming with the same interfaces and constraints. The design approach has emphaized maximizing the fatigue life against beam pulse loading. Gas injection is essential for reducing pulse stress and cavitation erosion. Experience to date indicates the needed levels of pulse stress reduction are achievable. The PPU gas injection upgrades provide the largest possible gains in target pulse fatigue life and cavitation erosion mitigation. The overall design has excellent prospects for exceeding the minimum target lifetime of 1250 hours at 2 MW.

6.5.8 Safety, Controls, and Operations

6.5.8.1 Scope

The crosscutting activities of safety, controls, and operations are essential to operational readiness for PPU beam on the FTS. Four of the five USIs identified in the PPU Preliminary Hazard Analysis [1] fall within FTS systems:

- Increased beam particle energy from 1 GeV to 1.3 GeV—effect on target spallation product inventory

- Increased beam particle energy from 1 GeV to 1.3 GeV—effect on target CV component heat distribution

- Injection of helium into the circulating target mercury in the target module to control the rate of cavitation erosion of the target module

- Increased hydrogen inventory of the target ORP due to the proposed installation of a catalytic conversion stage to convert orthohydrogen into parahydrogen

Two additional issues were identified during design development activities:

- Inadvertently generating a 2.8 MW beam and training it onto the first target for an indefinite period
- Potential transport of the catalyst from the para-ortho converter

Each USI was evaluated, and more details can be found in the Hazard Analysis report [2]. The following were findings:

- 1.3 GeV particle energy causes higher unmitigated accident consequences due to increased spallation product inventory at end-of-facility-life but does not require additional credited controls. Existing multiple levels of safety make mitigated consequences negligible.

- 1.3 GeV particle energy impacts on the CV and CVIs were analyzed. Heat transfer and structural analysis were performed and demonstrated the adequacy of the design for 2 MW, 1.3 GeV [3][4][5].

- The increased hydrogen inventory of the target CMS does not need additional credited controls.

- A safety credited control must be in place to limit the power on the target. The scope was added to the PPU scope.

- The potential transport of the catalyst from the para-/orthohydrogen converter could be addressed with a robust design.

Hazards associated with target gas injection (third bullet item above) require an integrated systems approach to developing designs, controls, and operating procedures that sufficiently mitigate accident risks and for which safety authorization must be obtained. Relevant systems include mercury process systems, target utility systems, the MOTS, and the 2 MW target. Their controls for gas injection are in addition to existing control functions. Ensuring safe operation of gas injection must consider interactions between new and existing controls. Current experience with gas injection in the target is leveraged [6]. Over the past 3 years, it has been observed that higher gas injection rate did not lead to higher dose rates in the GAR or above the mercury pump. Gas accumulation is found to be linear with gas injection rate (see Figure 6.56), and no transient behavior related to gas injection in the target has been observed yet. The current approach for gas injection safety for PPU is to demonstrate that the OFT is large enough to address any transient related to gas injection in the target [7][8].

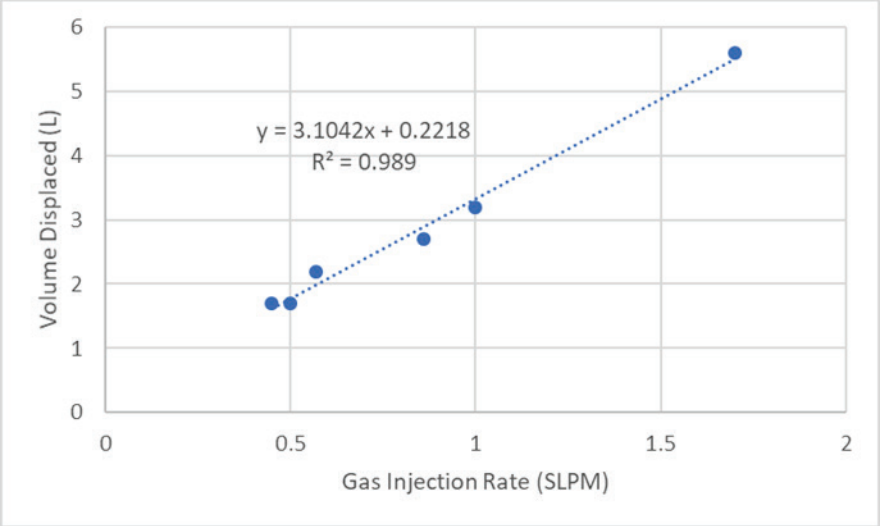

Figure 6.56. Amount of mercury displaced in the pump tank as a function of the gas injection rate.

Safety authorization begins in the design process and culminates with a positive outcome from an accelerator readiness review (ARR) and authorization from the DOE Field Office. Several crucial steps are to be completed in between, for example, updates to the FSAD and ASE. These require coordination, interaction, and iteration with PPU control account managers and operations staff; responsibility for this coordination falls within this work scope area.

Controls touch on nearly all of the FTS systems project scope. Safety, Controls and Operations first responsibility is to evaluate all the hazards related to PPU FTS upgrades. Its second responsibility include PLC controller hardware, PLC logic, EPICS integration (database, screens, alarms, archiving) and controls enclosures or racks to house control equipment. The installation, functional testing, and full integration to verify proper operations using EPICS will be performed once all field equipment installation, wiring and software deployment is complete. The cable design, installation, termination, and cable/connector material cost from PLCs to field devices will be included in the Safety, Controls and Operations. The Controls documentation will include design requirements documentation, PLC enclosure layout drawings, detailed I/O wiring to field instrumentation drawings, integration testing procedures, and functional system design (FSD) documents.

Commissioning with and without beam will be developed to demonstrate the ability of the FTS to operate at 2 MW, 1.3 GeV with up to 20 SLPM gas injection in the target.

Similarly, operating procedures and required training updates will be made ready for new and modified systems installed for the PPU. This work scope will ensure that operator training for these systems is prepared. The procedures and training will be needed for operation authorization.

6.5.8.2 Requirements

The controls developed for PPU FTS must integrate to the current FTS controls seamlessly. All the designs (PLC cabinets, electrical wiring, layouts) and software implementation (EPICS) must be documented using the same protocol used at SNS. Similarly, all the safety documents, procedures, and training documentations must follow the same template as current documentations at SNS.

6.5.8.3 References

1. R. M. Harrington and S. M. Trotter, *Preliminary Hazard Analysis in Support of the Proton Power Upgrade Project*, PPU-P01-ES0001-R00, Oak Ridge National Laboratory, May 2017.
2. R. M. Harrington and S. M. Trotter, *Proton Power Upgrade Project Hazard Analysis Report*, PPUP-103-ES0004-R00, Oak Ridge National Laboratory, January 2020.
3. O. Martinez, *Core Vessel Structural Analysis with PPU Beam Operation*, PPUP-505-DA0002-R00, Oak Ridge National Laboratory, April 2020.
4. O. Martinez, *Core Vessel Insert Thermal & Structural Analysis with PPU Beam Operation*, PPUP-507-DA0001-R00, Oak Ridge National Laboratory, August 2019.
5. V. Rao, *Simulation of Conjugate Heat Transfer in the Core Vessel*, SNS-106040100-DA0017-R00, Oak Ridge National Laboratory, April 2020
6. C. Barbier, *Gas Injection Impact on the Mercury Process Loop*, SNS-106010201-TR0001-R00, Oak Ridge National Laboratory, 2020.
7. C. Barbier, *Estimation of the Maximum Potential Gas Accumulation Volume in the SNS Mercury Loop*, SNS-10610200-TR0007-R00, Oak Ridge National Laboratory, 2019.
8. C. Barbier, *Adequacy of the Overflow Tank to Address Large Gas Injection Rate in the Target*, SNS-106010200-DA0018-R00, Oak Ridge National Laboratory, 2019.

7. CONVENTIONAL FACILITIES

The Conventional Facilities (CF) WBS element provides the new buildings and associated utilities that will support the technical equipment required for the PPU project. There are two major scope elements for CF: the klystron gallery and the ring-to-target-beam transport (RTBT) stub. An additional scope element is the EPICS controls for the new klystron gallery heating, ventilating, and air-conditioning (HVAC) unit and deionized (DI) water cooling system.

7.1 KLYSTRON GALLERY (FINAL DESIGN)

The CF scope of work for the PPU in the klystron gallery area consists of new construction and existing facility modifications. The radio frequency (RF) and Cryo level 2 WBS elements cover the installation of technical equipment in the klystron gallery and the linac, which is required to increase the proton beam energy. The CF provides the new building and the distribution of utilities needed for the technical equipment. CF also provides the EPICS controls for the new HVAC unit and DI water cooling system. A high-level view of the klystron gallery project area is shown in Figure 7.1. Figure 7.2 depicts the construction area and adjacent operational areas.

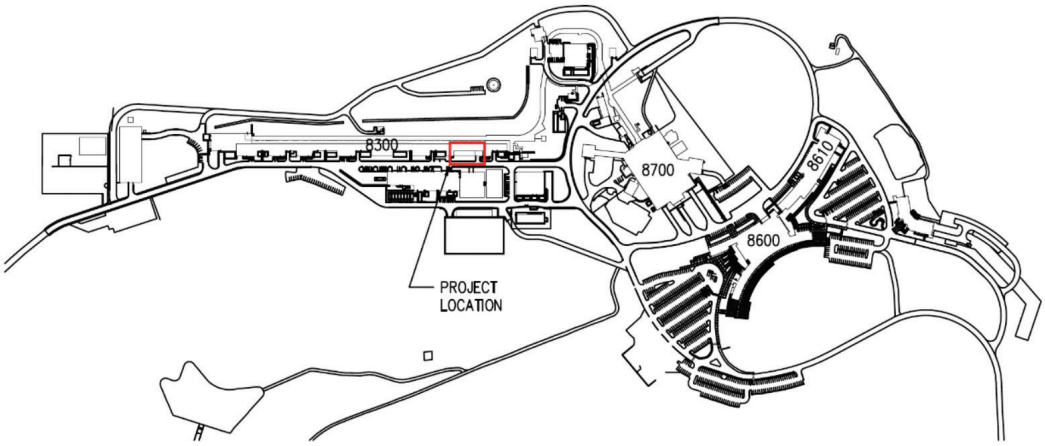

Figure 7.1. SNS campus map with detailed insert of the klystron gallery conventional facility activity.

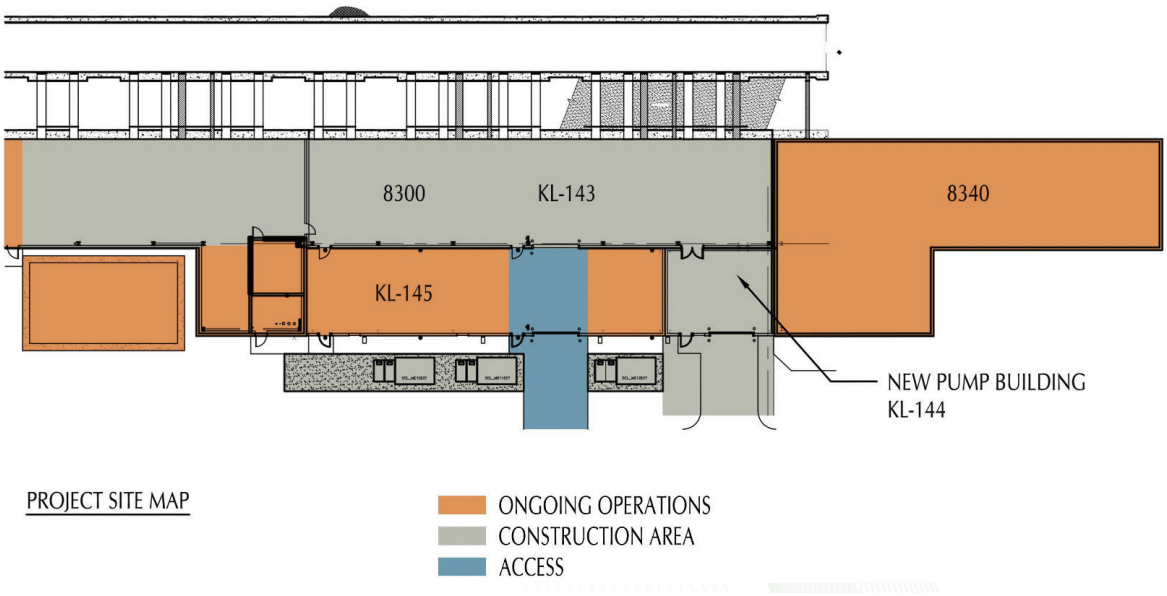

Figure 7.2. Relationship of construction areas to operating areas including access to construction.

7.1.1 Klystron Gallery New Construction

7.1.1.1 New Pump Building

A new pump building (KL-144) will be constructed to house the new DI water cooling loop for the accelerator equipment. The approximately 25 ft by 25 ft building will be between the east end of the existing klystron gallery buildout (KL-145) and the west side of the high-energy beam transport (HEBT) service building (8340).

Structural systems and site improvements

The new pump building (KL-144) will be a steel frame structure with a metal deck roof (International Building Code Type II construction). The foundation will be a reinforced concrete slab with thickened edges. The structure is designed to meet Natural Phenomena Design Category NDC-2 requirements for wind and seismic activity. In addition to a 20 psf live load (LL), the roof is designed for a 50 psf collateral load. The floor slab is designed for an LL of 500 psf and will have floor drains and a sump.

Two isolated concrete foundations will be installed within the room for the DI water pumps/motors.

A new driveway will be installed from Los Alamos Drive to a rollup door in the pump building. A sidewalk will also be connected to the new man door.

Building enclosure systems

The pump room building siding will be a flat-faced insulated metal panel to match the adjacent klystron gallery buildout previously completed. Special transitional expansion pieces are required to interface with the deep rib panel of the HEBT service building. Matching louvers will be provided for ventilation.

The roof system will include a corrugated metal deck with insulation board and a built-up roof to match the existing klystron gallery roof. The roof system will be a Factory Mutual Global Class 1–approved

type and will meet UL Class A fire exposure requirements. Gutters and downspouts will provide drainage from the roof. Expansion joints between the new pump building and adjacent buildings will be provided.

New double doors will be cut into the south wall of the klystron gallery (KL-143) to provide interior access into the new pump building (KL-144). The existing single man door will be removed and infilled with siding panels to match the existing door. A 3 ft by 7 ft man door in the south wall of the pump building will provide access to the building and egress to the exterior. A 12 ft by 12 ft overhead door will also be provided in the south wall.

The concrete slab-on-grade will receive an epoxy sealer for dust control and durability. There will be a floor drain and a sump within the room.

Life safety requirements

The new pump building (KL-144) will be separated from the HEBT service building (HS-102) by a UL-listed 2 hour rated partition. Egress will be provided directly to the outside via the man door in the south wall in compliance with National Fire Protection Association (NFPA) 101, *Life Safety Code*. Access to this exit from the klystron gallery (KL-143) through the new pump building (KL-144) will be provided.

Mechanical systems

The new pump building (KL-144) will be protected from freezing by a thermostat-controlled unit heater and ventilated by an exhaust fan.

Tower water (supply and return) lines will be provided to cool the new DI water system. The tower water lines will be installed from the adjacent HEBT service building (8340).

A process waste sump and associated pumps and piping will be installed to dispose of liquids from floor drains and other influent sources.

A process water line for makeup water will be routed to the DI water system.

A new accelerator cooling water DI system will be installed including pumps, heat exchangers, and water treatment systems.

Fire protection systems

Sprinklers

Sprinkler piping will be extended from the existing klystron gallery buildout (KL-145) to the pump building (KL-144). The occupancy hazard classification is Ordinary Hazard Group 2 (0.20 gpm over 3,000 ft^2), and the sprinkler system design will comply with NFPA 13, *Standard for the Installation of Sprinkler Systems*. Seismic bracing for the sprinklers will be provided. Installation of seismic bracing will be in accordance with NFPA 13.

Fire alarm

A new very early smoke detection apparatus (VESDA) system will be installed in the new pump building (KL-144). The fire alarm notification circuit in the existing klystron gallery buildout (KL-145) building will be extended into the new pump building (KL-144). A manual pull station will be provided at the new pump building (KL-144) exit door.

Electrical systems

Power, lighting, and communications will be provided for the new pump building (KL-144). Circuits will be routed from panels/racks in the existing klystron gallery. Emergency light units and exit signs for the new pump building (KL-144) will be routed from existing emergency power panels in the klystron gallery. Light fixtures and exit signs will use LED-type illumination. Lightning protection will be extended to the new pump building (KL-144) from the existing klystron gallery system.

7.1.1.2 New Electrical Distribution

The addition of new high-power RF equipment and three high-voltage converter modulators (HVCMs) and operation of the HEBT-ring-RTBT magnets at higher current will significantly increase the SNS site electrical load. To support new klystron gallery electrical loads, concrete pads for three new 1500 kVA transformers will be installed just south of the gallery buildout (KL-145). The additional RF and the installed transformers will support the new HVCMs on a one-to-one basis. A fourth concrete pad and associated conduit stub-outs will be installed for future equipment.

Three new 13.8 kV interrupter switches will be installed (one on each pad) to isolate the modulator power supplies from the electrical distribution system.

Underground duct banks will be provided from existing manhole M20 to the new pad-mounted interrupter switches. A new 13.8 kV feeder will be routed through manhole M20 to HEBT switch 3014-82. The CF scope for the new electrical distribution ends at the primary of the interrupter switch. The remaining electrical distribution is part of the RF scope. The switches will be closely coupled with cabling/buses to the transformers. Secondary cabling from the transformers will be fed through underground conduits into the existing klystron gallery buildout (KL-145).

7.1.2 Klystron Gallery Existing Facility Modifications

Modifications in the east end of the existing klystron gallery are required to support the new accelerator equipment. The CF utilities (mechanical, electrical, fire protection) will be installed in the klystron gallery.

7.1.2.1 Mechanical Systems

The section of the klystron gallery with new accelerator equipment will be heated and cooled with a rooftop-mounted chilled-water and heated-water HVAC unit. The air will be strategically distributed to technical equipment loads by overhead galvanized ductwork. The cooling capacity of the HVAC unit was selected to be 100 tons and 30,000 cfm.

Chilled water lines will be constructed to the new HVAC unit from the HEBT service building (Building 8340).

Heating water lines will be constructed to the new HVAC unit from existing piping located nearby in the klystron gallery.

Compressed air lines for utility air have been previously installed.

The new DI water supply and return piping in the klystron gallery will be constructed from the new pump building through transmitter cooling carts (RF WBS provided) to tie-in points for technical equipment connections.

Condensate from the rooftop HVAC unit will be routed to the storm drain.

7.1.2.2 Fire Protection Systems

Sprinklers

The existing sprinkler system in the east end of the klystron gallery (KL-143) is in compliance with NFPA 13, *Standard for the Installation of Sprinkler Systems*. Additional sprinkler heads will be provided under new ductwork greater than 4 ft wide.

Fire alarm

VESDA units will be installed in the east end of the klystron gallery (KL-143) building. Existing spot smoke detectors in the klystron gallery (KL-143) will be removed. Area notification appliances will be relocated as required for proper coverage requirements.

7.1.2.3 Electrical Systems

Existing switchgear for the klystron gallery (KL-143) will supply power to new panels for technical equipment supporting systems, e.g., vacuum, controls, diagnostics, cooling loops.

Power will be provided for the new HVAC unit to be installed on the roof of the klystron gallery (KL-143).

New cable trays will be installed to distribute the power and communications cabling throughout the klystron gallery (KL-143) and buildout area (KL-145).

Existing lighting fixtures in the klystron gallery will be removed and new LED fixtures installed to accommodate the new technical equipment.

Communications for voice and data will be provided for phones and network connections.

7.1.2.4 Controls

The new HVAC unit and DI water cooling system with associated piping systems instrumentation will require new controls. These controls will follow the existing model for SNS CF controls, which are implemented using SNS standard Allen Bradley programmable logic controllers and I/O modules integrated with the SNS EPICS. The SNS Controls Group developed the required controls design, drawings, sequences, ladder logic, test plan, and EPICS input-output controller database. Operator interfaces, alarms, and archived data for this system will be configured using SNS standard EPICS tools.

7.2 RTBT STUB (FINAL DESIGN)

The RTBT stub will be an attachment to the existing RTBT tunnel, which houses the proton beam that serves the FTS. The stub is to be located at the juncture where the proton beam will be split when the STS is built, forming a second proton beam line directed to the STS through the future ring-to-second target-transport (RTST) tunnel. The RTBT stub is to be constructed during an extended shutdown of the SNS required by the PPU to perform upgrades in the target building and ring and installation of cryomodules and related RF systems. This scope is included in the PPU to enable construction of the STS, including the RTST tunnel, without requiring an additional prolonged shutdown of the FTS during the STS

construction period. This strategy should reduce the overall beam downtime from the PPU and STS projects. Figures 7.3–7.6 give an overview of the RTBT stub configuration and location.

Construction of the RTBT stub is scheduled to begin in the last quarter of calendar year 2022, coinciding with a planned extended shutdown of the proton beam line beginning in December 2022. Construction of the RTBT stub within a 6 month beam shutdown period is considered feasible using extended work hours; however, some portions of the stub project will be constructed both before and after the beam shutdown period to minimize the impact on operations.

The RTBT stub length selection was based on a study that considered key design requirements. The important considerations included providing sufficient shielding, facilitating future continuation of the tunnel construction, reasonable site slopes, revised storm drainage, and minimizing constraints on the future STS site plan.

Figure 7.3. Aerial view of the Spallation Neutron Source campus. Yellow highlighting indicates the project area.

Figure 7.4. Aerial view of SNS. The RTBT stub project location is highlighted in yellow.

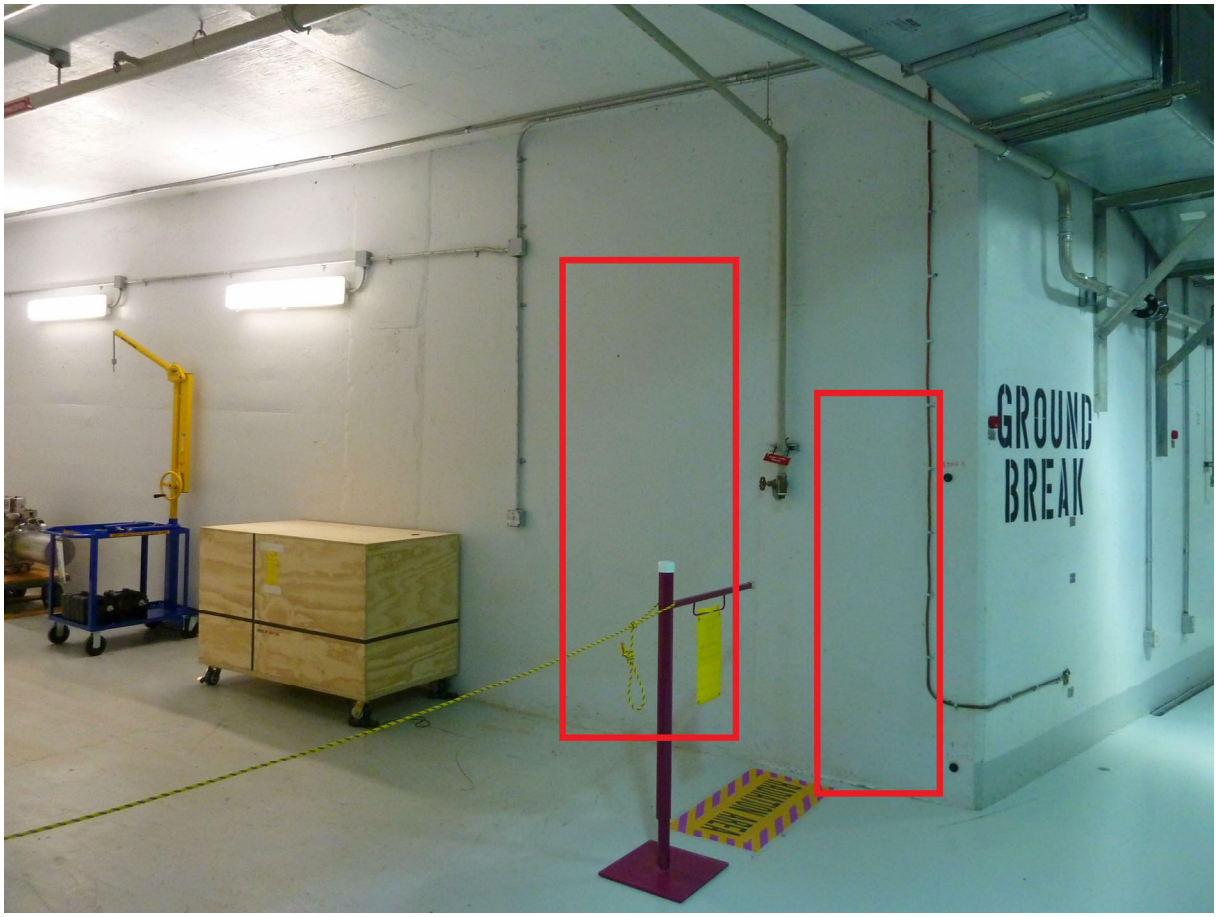

Figure 7.5. Existing RTBT tunnel and truck access tunnel looking toward the stub. The left opening depicted by red rectangle will be for personnel and equipment access and the right opening is for the future proton beam.

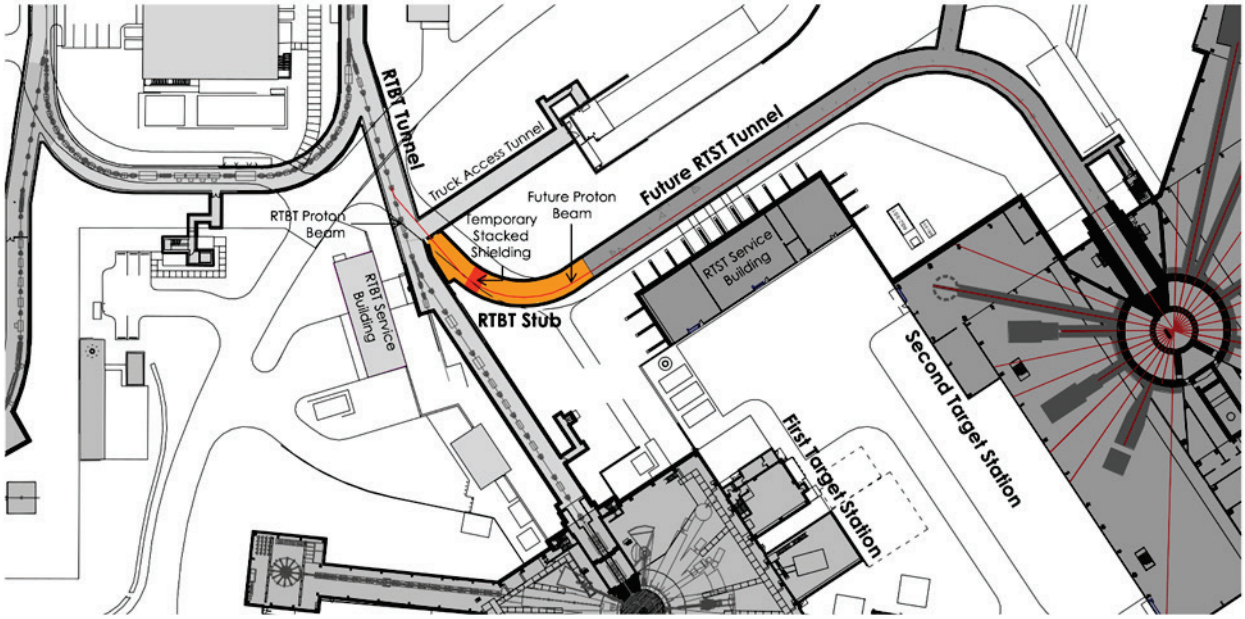

Figure 7.6. Overall RTBT stub configuration.

7.2.1 Shielding Requirements

Shielding calculations, performed as part of part of the SNS project, show that 18 ft and 6 in. of concrete and soil shielding is required from the inside of the RTBT tunnel concrete to the ground surface. This material is necessary to provide sufficient shielding to meet DOE requirements for radiation exposure to personnel on the berm during high-beam-loss conditions and during a postulated beam spill accident and to accommodate operating beam losses. Neutronics studies performed for PPU beam configuration have confirmed that shielding of 18 ft and 6 in. is adequate.

A temporary stacked shield wall and associated PPS equipment will be provided by the ring WBS to allow entry into the RTBT stub downstream of the shielding during FTS operation. The interlaced shielding blocks, totaling about 18 ft thick, will be located as close to the RTBT tunnel as possible while maintaining sufficient earth shielding between the RTBT tunnel and the RTBT stub. The temporary shielding will be removed as part of the STS project.

7.2.2 Civil/Geotechnical

The geotechnical and structural stabilities of the existing RTBT tunnel, proposed RTBT stub, and future RTST tunnel are critically important design concerns closely related to the alignment and performance of the proton beam. The existing earthen berm that covers the RTBT tunnel is around 16 ft thick. A geotechnical exploration and geotechnical report were incorporated into the structural design to ensure that the existing tunnel would not be damaged during construction and that neither the existing nor new tunnel would suffer excessive settlement. Various foundation systems were explored, and a soil-supported system was chosen.

Site grading associated with this project will require that existing Building 8940 (Carpenter and Paint Shop) be demolished.

Figure 7.7 shows an overview of the site after final grading and the existing underground utilities, and Figure 7.8 indicates the present elevation configuration.

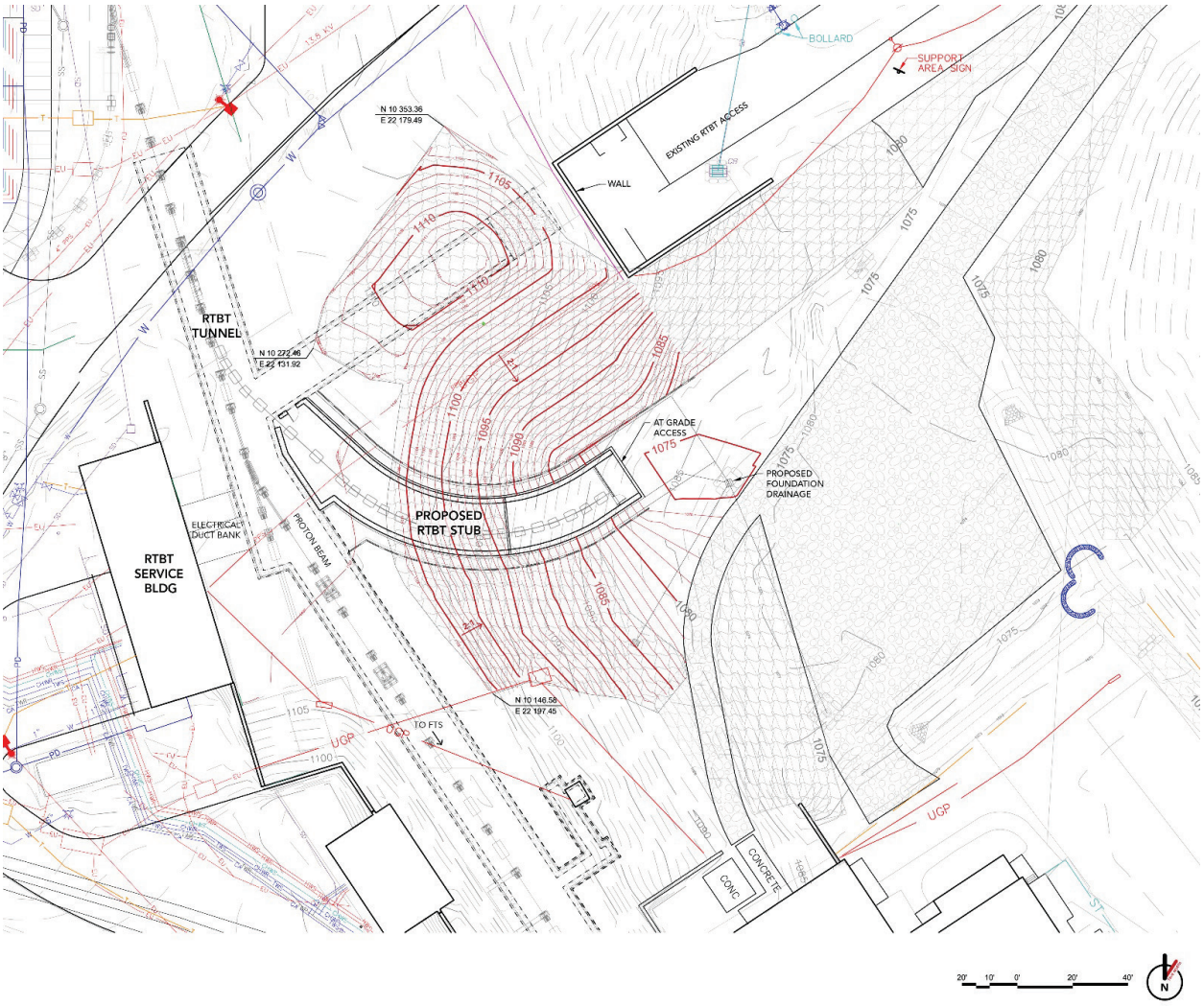

Figure 7.7. Backfill plan and new site drainage.

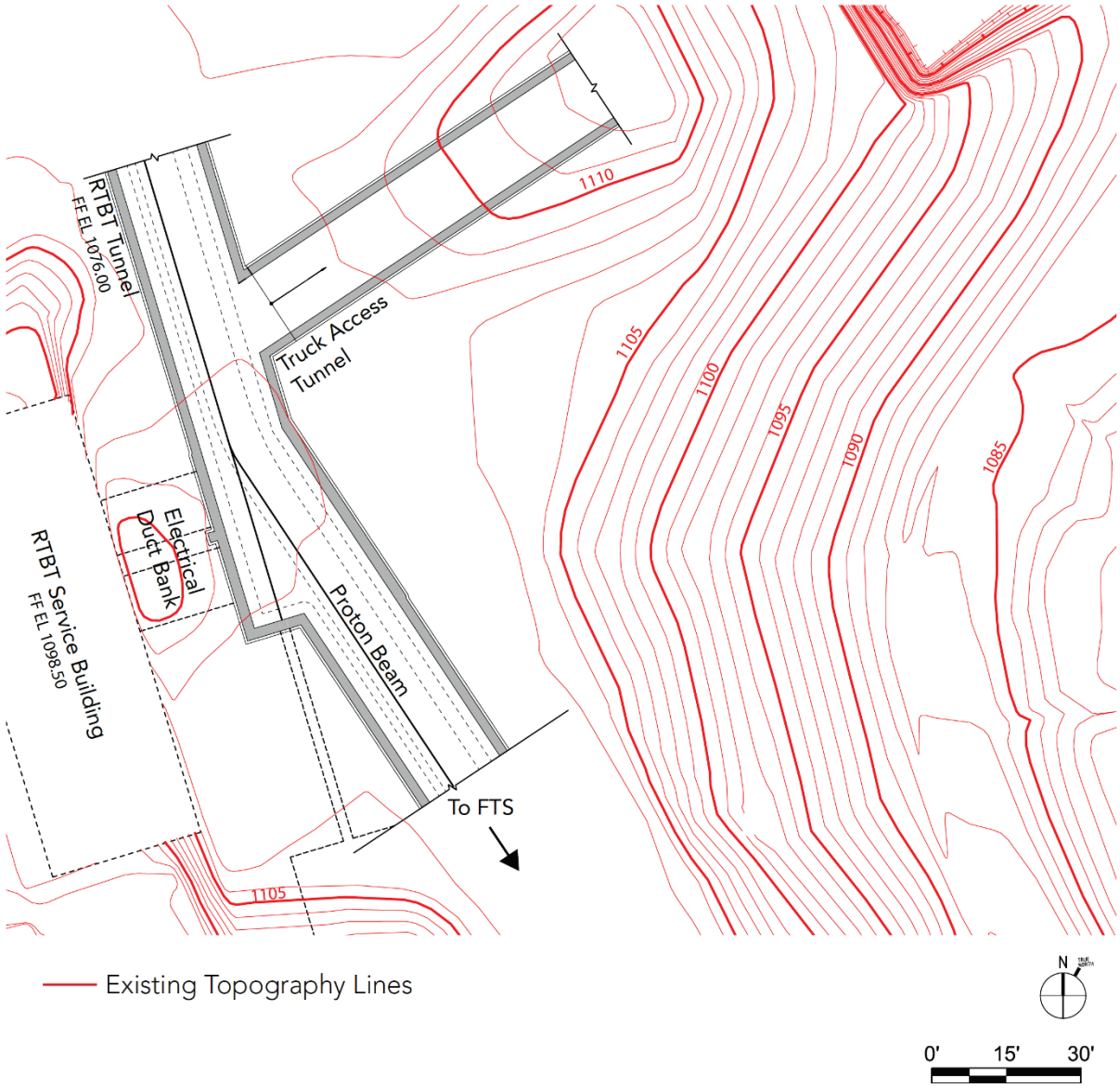

Figure 7.8. The existing RTBT tunnel with existing grades indicated.

The RTBT stub construction will be performed in a step-by-step process, as described in the following paragraphs. Each phase number represents a construction step.

Phase 0: Pre-shutdown

Site work staging and initial excavation for the RTBT stub will start before the shutdown. Any site work outside of the minimum shielding dimension will be started and logistically developed up to that standoff location. The existing fencing in the work area will be removed. Building 8940 will be demolished prior to the shutdown by a demolition contractor. The contractor will mobilize and start the submittal review and approval process and start multiple procurements to ensure material is on hand to allow construction to begin as soon as the SNS shutdown starts.

Phase 1: Initial stub excavation

Phase 1 begins immediately after the start of the extended beam outage. Existing liner and liner header pipe and drains in areas affected by excavation will be removed. The Personnel Protection System (PPS) conduit to the RTBT truck tunnel in the excavation area will be removed after the wiring is disconnected. The contractor will use exploratory trenching and a potholing methodology to locate existing structures during excavation to avoid damage to existing structures. Excavation down to existing tunnels will remove only the soil needed to tie into the existing RTBT and RTBT truck tunnels to minimize the amount of soil that must be disturbed and to stabilize during construction. Shotcrete will be installed to act as temporary erosion control cover over disturbed soil during construction to prevent environmental issues and minimize impacts on the construction schedule caused by precipitation. Storm drains, area drains, and French drains shall be installed to manage water in the construction zone (Figure 7.9).

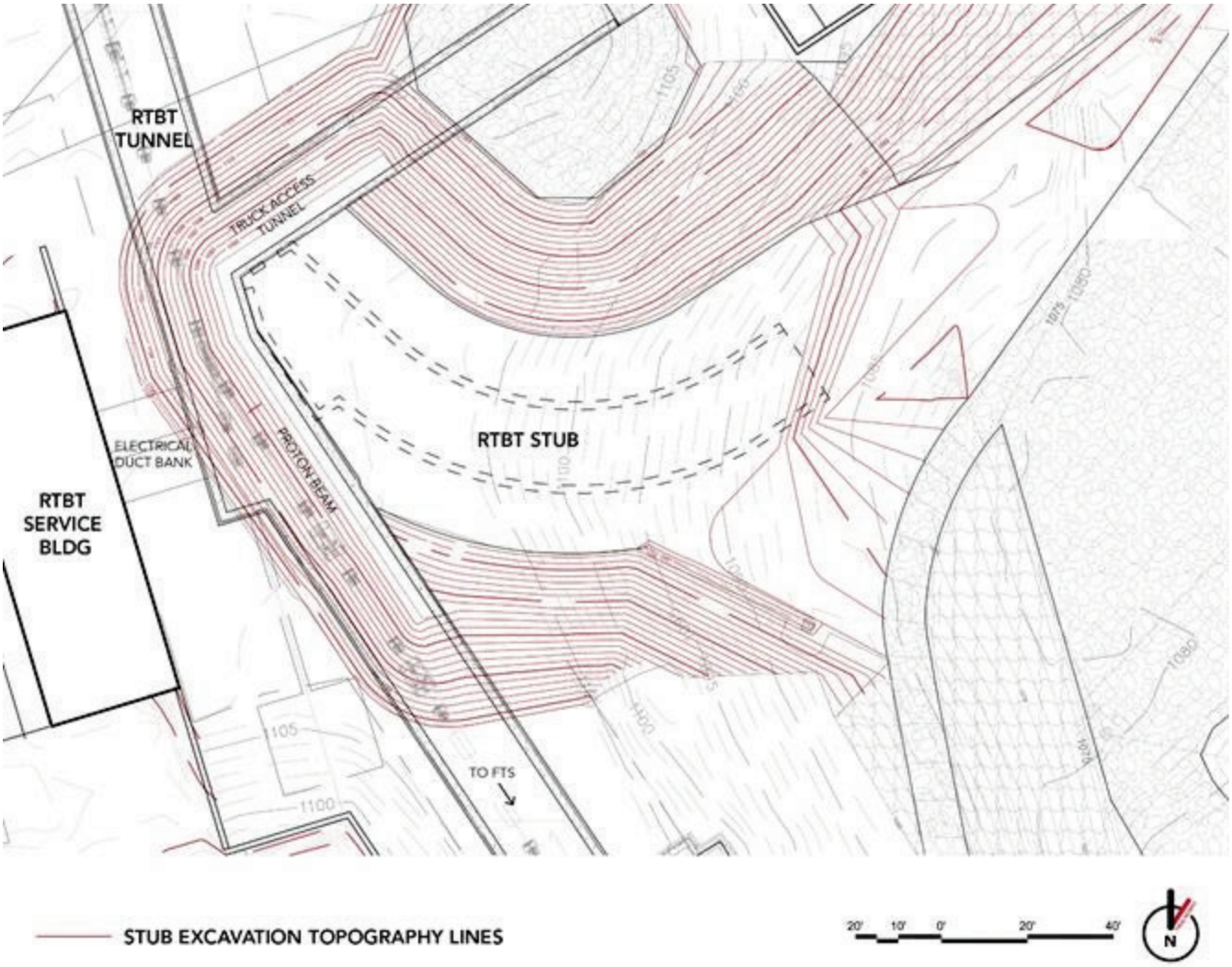

Figure 7.9. Initial stub excavation plan – Phase 1.

Phase 2: Final excavation and stub construction

The remaining excavation to grade for the new tunnel will be performed, sheet piles and foundation will be installed, and changes to the water collection and management features will be made to fully stabilize

the site before beginning construction of new tunnel. These features are intended to minimize the amount of soil to be disturbed and the impact of inclement weather on construction. The cast-in-place concrete structures forming the floor/foundation, the walls, and then the roof will proceed. After waterproofing the tunnel, two openings will be cut into the existing tunnels for the future beamline and for access. The mechanical, electrical and fire protection systems will be installed, and the temporary shielding will be built across the stub (in ring WBS) to allow the future tunnel extension work to proceed up to this point before an additional beam shutdown is required. A temporary wall with a secure access door will finish the tunnel stub end (Figure 7.10).

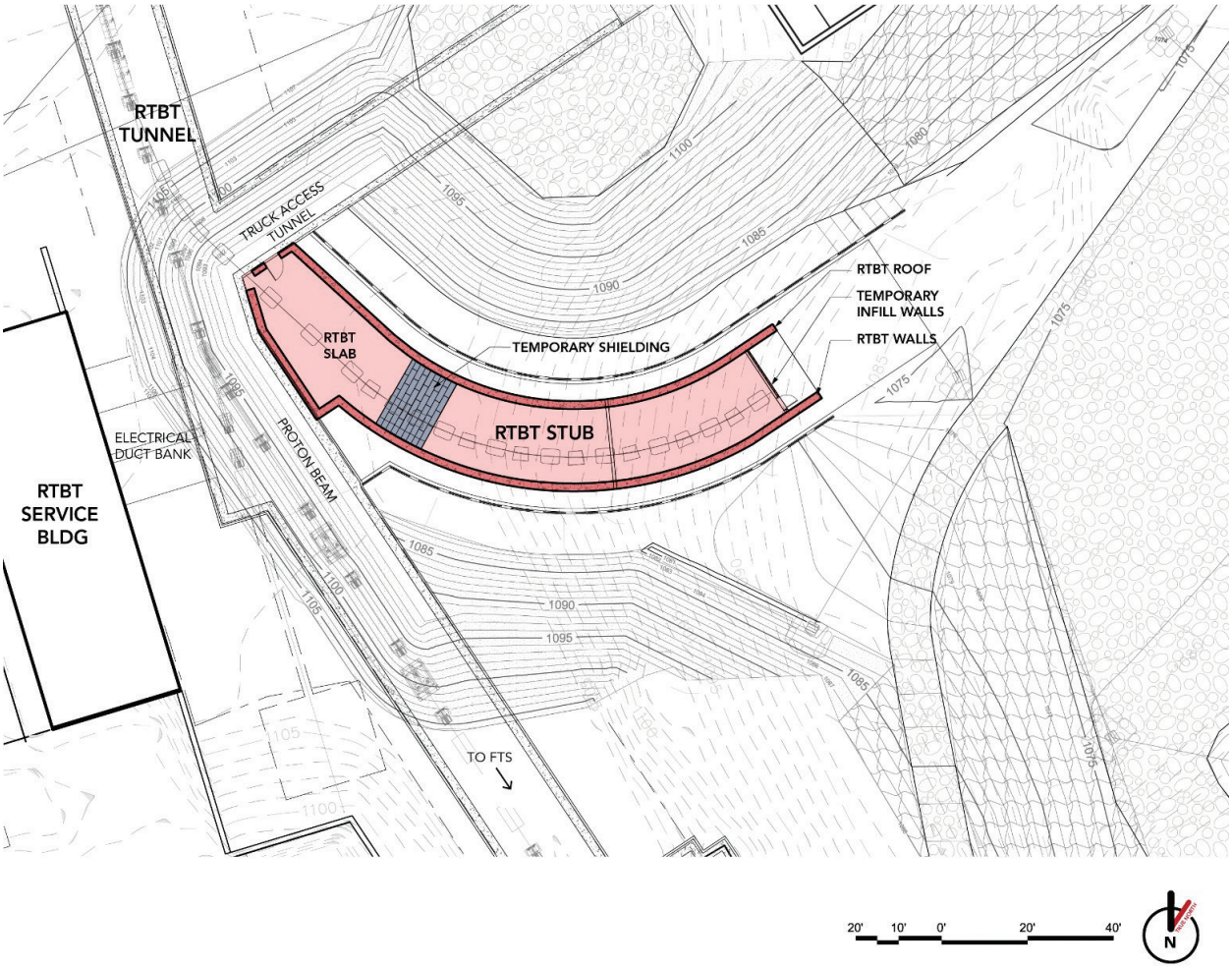

Figure 7.10. Stub construction plan—Phase 2.

Phase 3: Final grading

Once the concrete tunnel has cured to an adequate level of strength and the tunnel stub waterproofing work is completed, backfilling will proceed. The portion of the stub closest to the RTBT tunnel will have full earth shielding, with the grade sloping downward. This grading configuration will allow east tunnel end access and proper water drainage to the south, as shown in Figures 7.11 and 7.12. The displaced portion of the geomembrane over the existing tunnel will be replaced, along with a small portion at the west end of the stub.

See Section 7.2.3 for a discussion of the earth shielding required at the end of the PPU project.

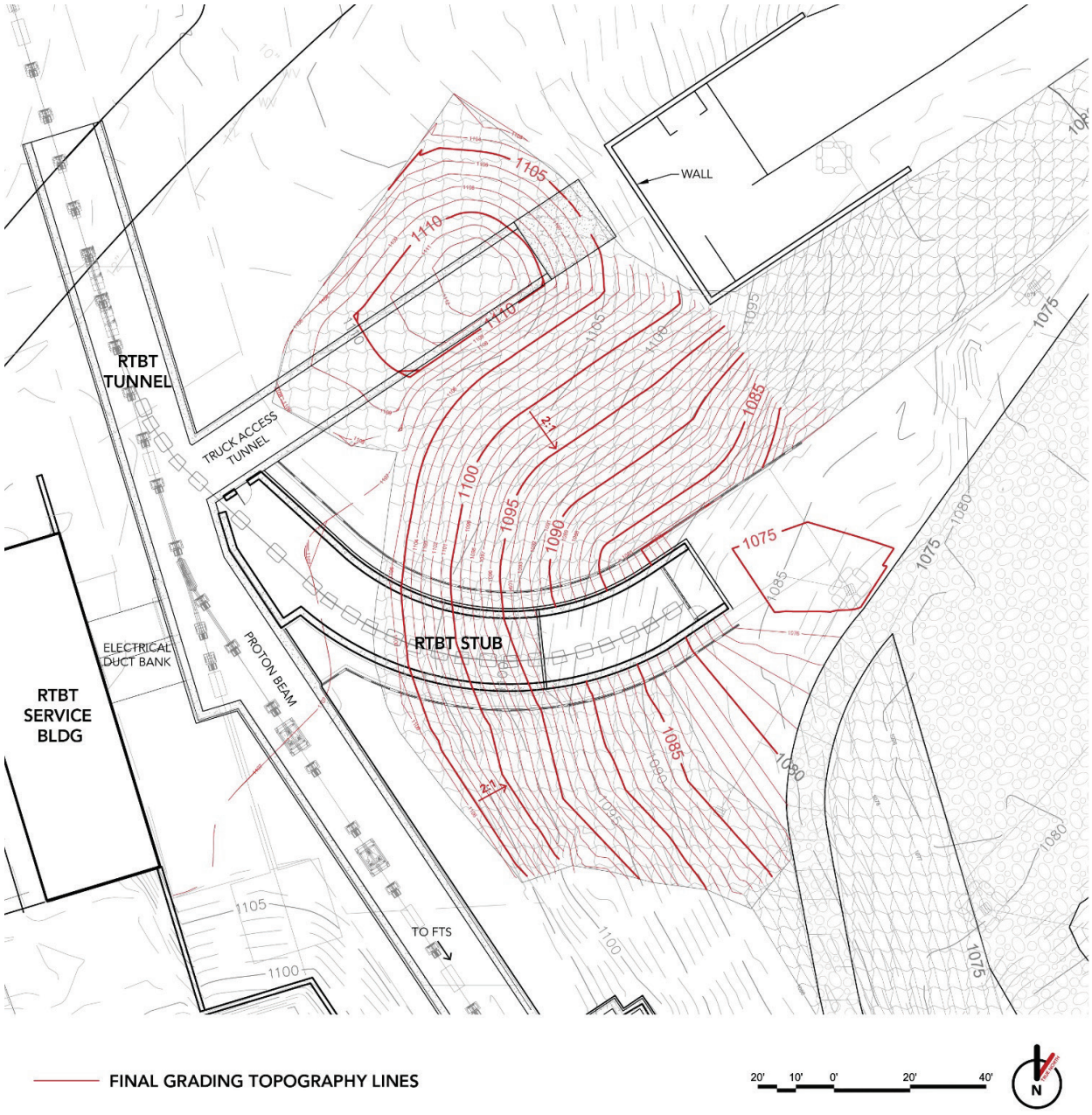

Figure 7.11. Final grading plan—Phase 3.

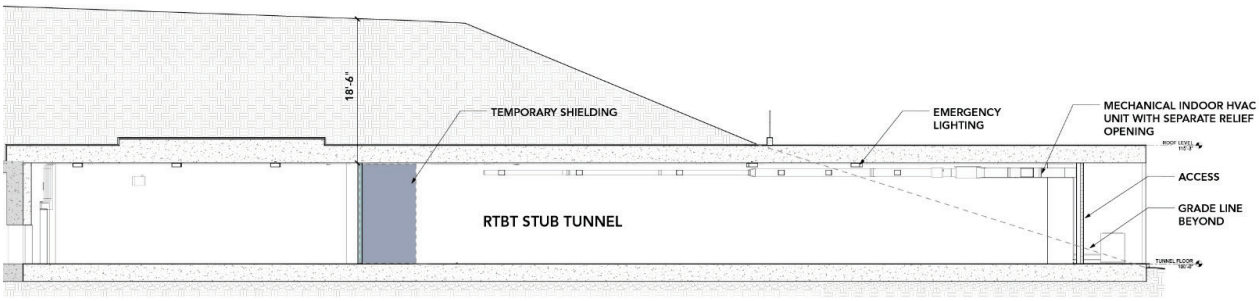

Figure 7.12. Elevation view of tunnel after final grading.

7.2.3 Architectural/Structural

The RTBT stub is a 2,600 gross square foot concrete tunnel structure similar to the existing RTBT tunnel. It will be constructed to enable the completion of the RTST tunnel as part of the STS project. At completion of the RTBT stub construction, the stub will be primarily below grade with at-grade access. It will not house any accelerator components as part of the PPU.

The section configuration for the structural connection is depicted in Figure 7.13. It will require removal of two sections of tunnel walls to allow the transition of the proton beam into the adjacent RTBT stub and to provide personnel and equipment access to the tunnel. The 5 ft high opening for the proton beam and utilities will have sufficient clearance to allow a beam pipe and flanges to be installed. The personnel and equipment access opening will be 4 ft wide by 8 ft high.

The new RTBT stub building will be reinforced concrete (International Building Code Type 1B construction).

The new stub and the impacted existing tunnel will be waterproofed, and a geomembrane will be installed that is compatible with the existing system. Foundation drains matching existing RTBT tunnel foundation drains will be provided for the new tunnel.

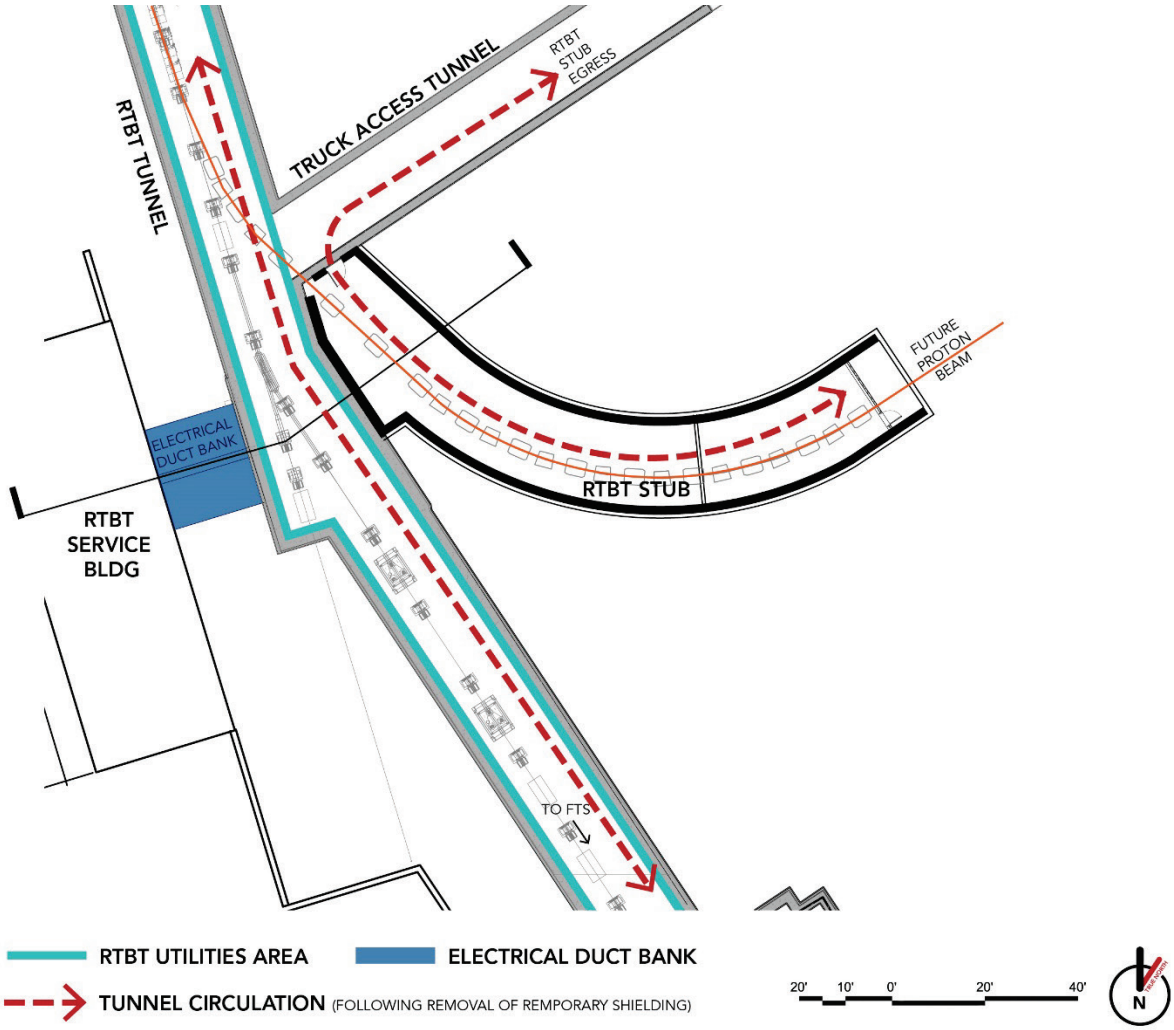

RTBT SERVICE BUILDING, RTBT TUNNEL AND RTBT STUB CROSS SECTION

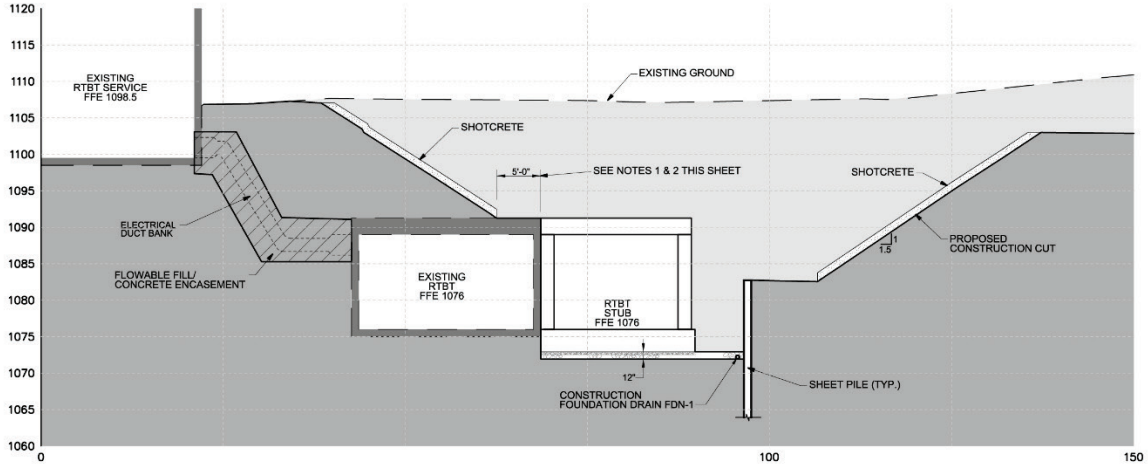

Figure 7.13. RTBT stub structural connection plan.

7.2.4 Electrical

Electrical utilities to serve the RTBT stub will be minimal and will include ambient lighting, convenience receptacles for portable equipment, and power for the HVAC unit. The source of power will be extended from the existing RTBT tunnel.

The 277 V light fixtures will be industrial, weatherproof LED work lights switched ON/OFF at the entry to the stub. A 20 ft-candle illumination level, on average, will be provided within the tunnel. The switch will have a pilot light to indicate lights ON or OFF. Normal and emergency power for the lights will be provided from existing light fixtures in the RTBT tunnel.

The tunnel will have several 120 V convenience receptacles. Power for the convenience receptacles will come from an existing circuit inside the RTBT tunnel. The HVAC system will be 480 V, 3 phase. A local disconnect will be provided for the HVAC unit. The power for the HVAC will be routed from panel RS-1P1, located in the RTBT service building. An existing spare conduit will be used to route the power between the RTBT service building and the RTBT tunnel.

7.2.5 Mechanical

An HVAC unit will be installed to provide temperature control, circulate air, and minimize moisture. The unit will be installed on the floor slab near the end of the stub. A duct will be routed inside the stub to provide outside air in the tunnel and provide a slightly positive pressure. The HVAC unit will be controlled and monitored by EPICS.

A fan will be installed in the portion of the RTBT stub west of the shield wall to improve circulation in this section of the tunnel. This part of the stub is connected to the temperature-conditioned RTBT by two openings that have wire mesh closures.

7.2.6 Site Utilities

The approximate locations of existing utilities within the limits of the proposed stub are shown in Figure 7.7. The only existing site utility within the limits of the stub construction is a PPS circuit extending from the RTBT access tunnel area to the RTBT service building and then to the RTBT tunnel access stair. The PPS line will be removed for construction and reinstalled and certified after grading is complete. Outside the construction limits but nearby to the south of the stub area is high-voltage underground power cabling in duct banks that serve the Target Building.

New French drains, foundation drains, and area drains will be installed to manage stormwater. A new stormwater diversion ditch will be constructed to accommodate drainage from the reconfigured site.

7.2.7 Life Safety

The east section of the new RTBT stub building will be separated from the RTBT tunnel by noncombustible stacked shielding. Exit access east of the stacked shielding will be provided directly to the outside via a man door in the east wall of the RTBT stub in compliance with NFPA 101, *Life Safety Code*. Exit access west of the stacked shielding will be provided via the existing RTBT truck access tunnel (RTBT-01) and the existing RTBT emergency egress ladderway (RT-103).

Fire protection systems

Sprinklers

No sprinklers are required.

Heat detectors

Heat detectors will be installed and connected to the existing system.

Fire alarm

The fire alarm notification circuit in the existing RTBT truck access tunnel (RTBT-01) will be extended into the new RTBT stub building. A manual pull station will be provided at the east exit door.

Fire extinguisher

A 10 lb ABC dry chemical fire extinguisher and cabinet will be provided at the east exit of the RTBT stub.

7.2.8 STS Interfaces

The STS project will install the new utility distribution required for the future RTST beam line. The STS project will also install the crane in the tunnel; the PPU will install only roof embeds to facilitate the future crane installation.

7.3 ASSUMPTIONS

During subsequent PPU phases, it is anticipated that the following assumptions, which may impact project scope or design approach, will be further evaluated.

7.3.1 Klystron Gallery Assumptions

No new HVAC equipment is required for the existing RF equipment running at higher power. It is assumed the existing klystron gallery may need to run at a slightly higher temperature, and any equipment temperature issues will be addressed separately from the PPU by localized cooling and ongoing operational improvements.

There is no CF scope for the remainder of the klystron gallery.

There will be no other work in the klystron gallery (KL-143) for the duration of the CF construction.

7.3.2 RTBT Stub Assumptions

An average amount of adverse weather will be encountered.

8. RESEARCH AND DEVELOPMENT

This work scope covers the development of high-flow gas injection for maximum mitigation of cavitation erosion and reduction of beam pulse–induced fatigue stress in the target vessel. It does not include scope associated with orifice bubblers, injected gas rates ≤1 SLPM, or once-through gas supply associated with the ongoing gas injection initial implementation (GI3) effort. Included are development of high-gas-rate bubblers and protective gas walls; also included is gas removal development to ensure safe and efficient mercury process loop operation. Operation of any test facilities and the documentation of results are covered in this effort. The R&D scope is working along area P5 progress: some scope was added to address specific safety concerns. The R&D consists of experiments with water at the Thermal Hydraulics Laboratory (THL) and experiments with mercury at the Target Test Facility (TTF). In parallel, computational fluid dynamics (CFD) simulations are performed to support the R&D.

8.1 PROTOTYPICAL TARGET FOR WATER AND MERCURY

Prototypical targets for water and mercury were designed and will be used to investigate

- Updated swirl bubbler design (slightly smaller units with only two vanes)
- Gas layer interaction with bulk flow
- Gas layer interaction with small bubbles

Both targets were designed based on the preliminary design of the 2 MW target (“Eridanus”) and have the following features:

- No center baffle
- Tapered nose
- Holes in the side baffles to disturb the recirculation region
- Modular diving board to accommodate new designs from the target team

From the gas-wall-layer experiments (G-WaLE), it became clear that the implementation of the gas layer will be challenging in the SNS target. Even if the R&D effort can develop a gas injection strategy that provides the desired performance, its implementation in a real target may be challenged by thermal stresses and fatigue. The R&D and target team agreed that a convenient method of injecting gas will be to inject from the tip of the diving board. To accommodate this approach, the prototypical target designs are such that the diving board can be swapped so that a configuration close to the final design can be tested at the end of the R&D effort.

The so-called visual target for the water experiments is shown in Figure 8.1. All the outside surfaces are flat to limit optical distortion during particle image velocimetry (PIV) measurements or other visualization measurement techniques. To facilitate the fabrication, the target was divided into 4 in. blocks that could be made from 4 in. thick acrylic sheet (the thickest available at the time). The window flow is omitted, compared with the real target, because it does not affect the main flow and omitting it makes visualization easier. The following are the key features of this target:

- Several holes were made in the flanges for pressure measurements and to insert a borescope just downstream of the bubblers.

- The 3D printed diving board can be replaced to allow different gas layer strategies.

- An individual inlet for each jet-flow channel allows evaluation of the impact of flow distribution on the gas layer.

- The acrylic nose can be swapped with a stainless steel one to investigate the impact of the gas layer on heat transfer (Figure 8.2).

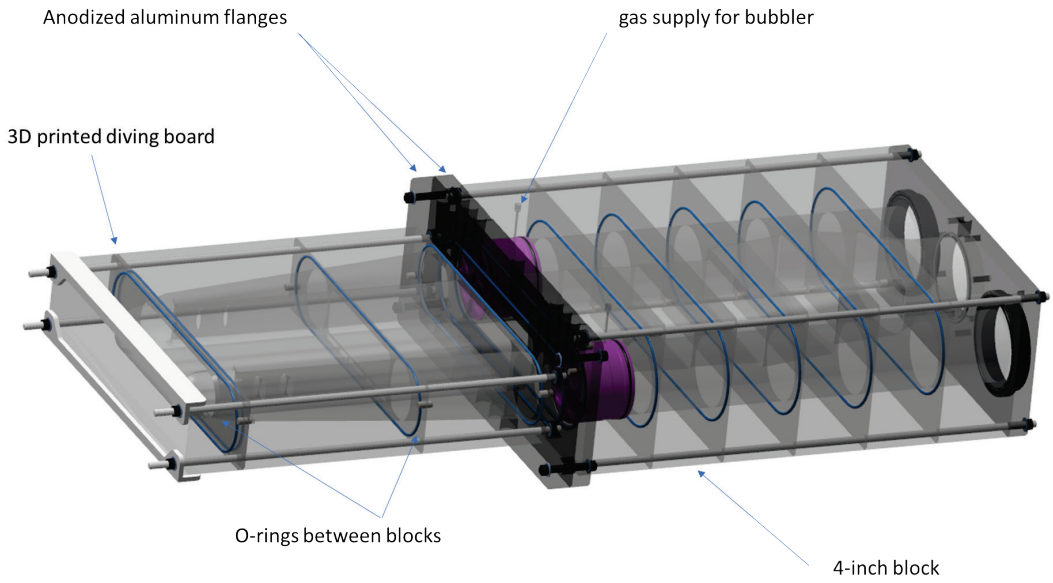

Figure 8.1. Three-dimensional view of the visual target with swirl bubbler (purple parts).

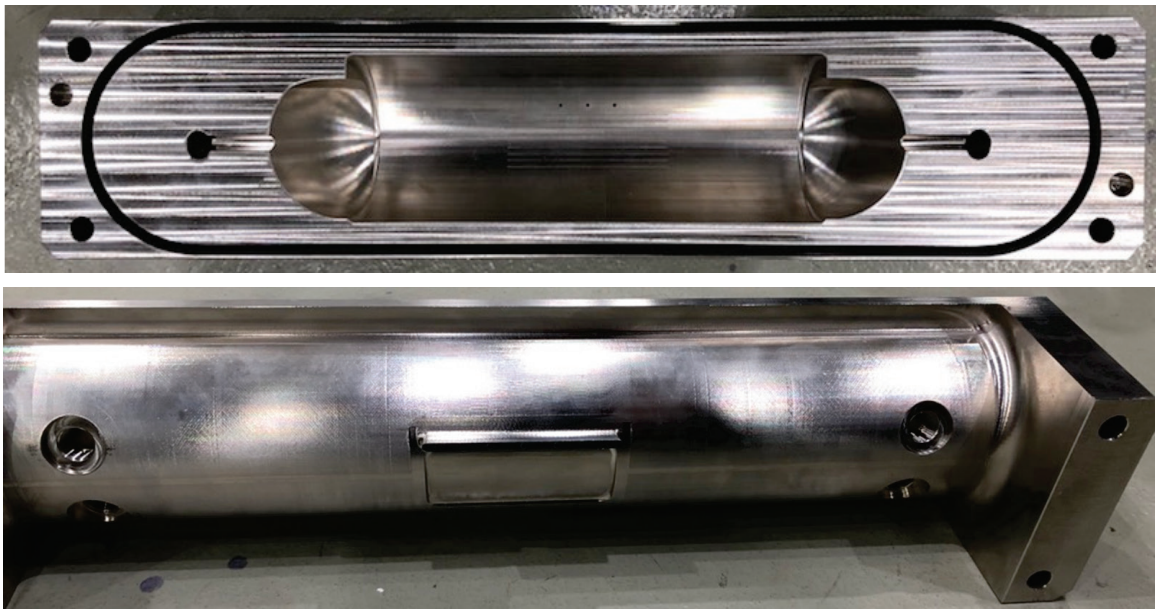

Figure 8.2. Stainless steel nose for the visual target for the heat transfer experiments.

The target was received at the end of February 2019, but an additional aluminum flange had to be designed because two acrylic blocks were not matching (see Figure 8.3). Experiments started during summer 2019.

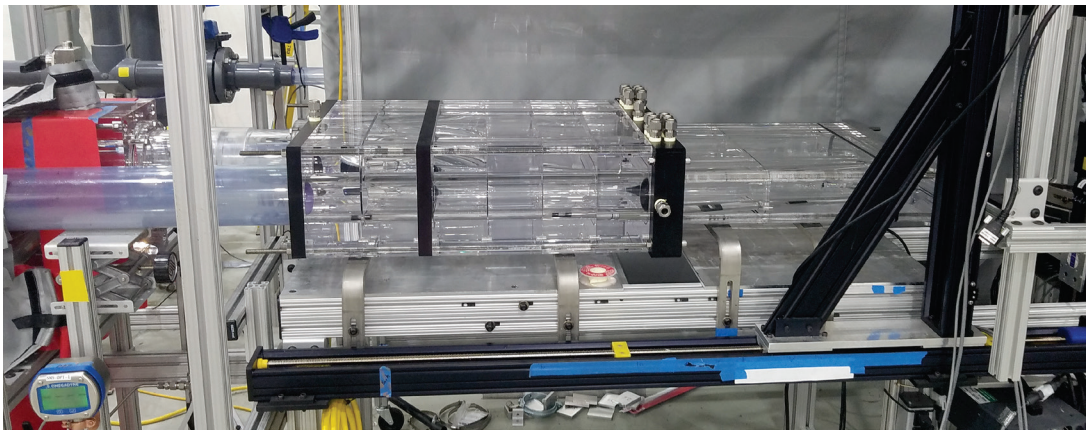

Figure 8.3. Visual target installed at THL with the extra aluminum flange.

The first series of experiments were focused on determining the size distribution of the bubbles generated by the swirl bubbler. Results are presented in the following section. In addition, PIV measurements were performed, in which the flow is seeded with tracer particles that are illuminated with a laser sheet. The laser is pulsed twice, at very short durations, and a synchronized camera captures two frames (Figure 8.4, left). The frames are then split into smaller interrogation areas, and the corresponding displacement vector for each window area is determined using cross-correlation techniques. Each pair of pictures provides an instantaneous flow field that is then averaged (Figure 8.4, right). PIV measurements were performed at several locations and compared with simulation results. A good match was found between the simulations and the experiments (Figure 8.5).

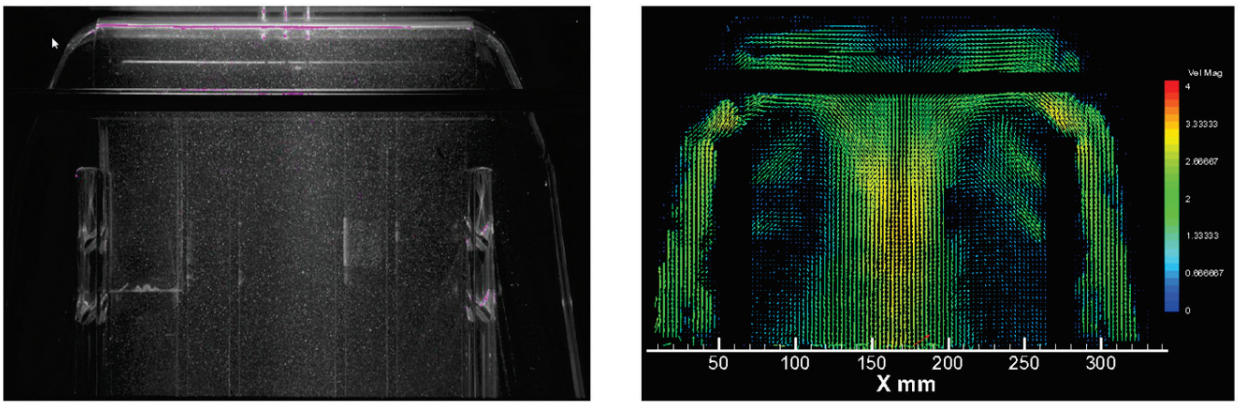

Figure 8.4. Unprocessed PIV picture (left) and measured velocity field averaged over 200 instantaneous flow fields (right).

The design of the TTF target, shown in Figure 8.6, has the following key features:

- A 1 in. vent line at the elbow to remove as much gas as possible at the target
- Several acrylic windows at the top to visualize the bubbles and investigate how the gas layer evolves past the nose
- A flat acrylic nose to limit optical distortion that will be used for the gas layer and for measuring bubble sizes

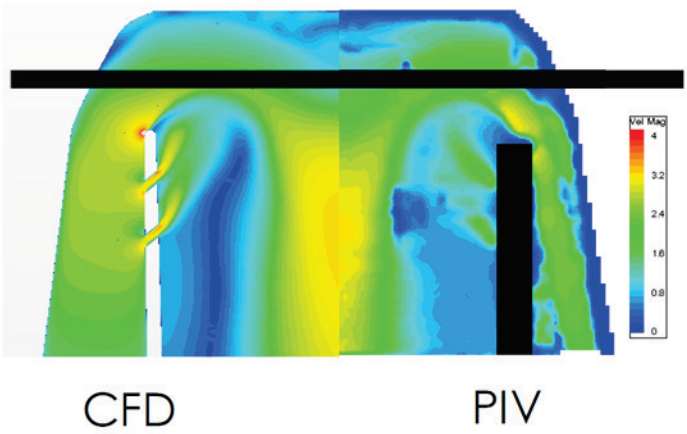

Figure 8.5. Comparison of the simulations (left) and the PIV measurements (right).

- A modular diving board and gas injection (see Figure 8.7)
- A stainless steel nose similar to the visual target to investigate the impact of the gas layer on heat transfer at the nose

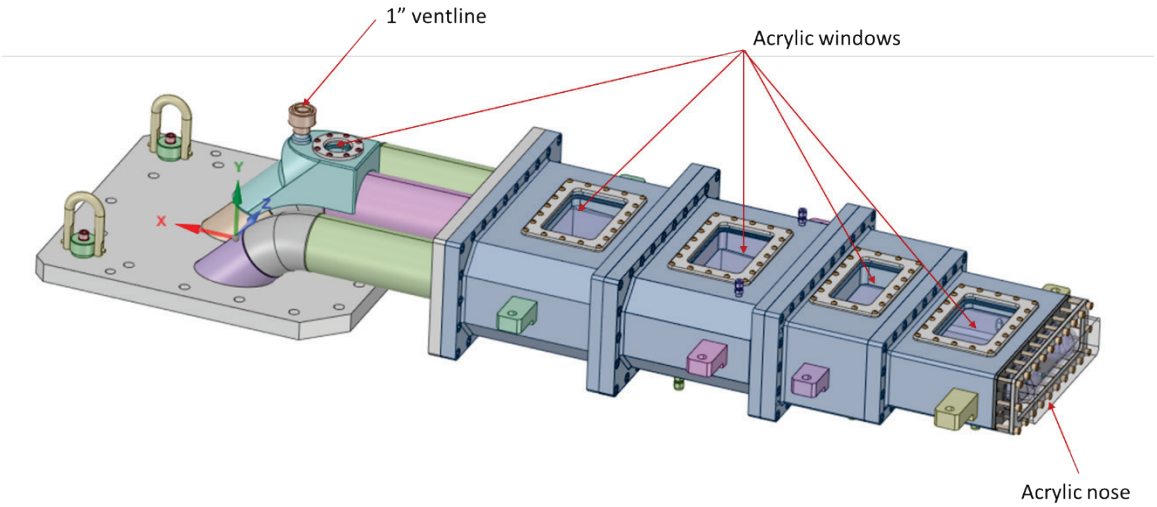

Figure 8.6. Three-dimensional view of the Eridanus target for TTF.

The design of the target was completed in May 2019, and the purchase order was released in early August 2019. The fabrication is late in the schedule, and SNS staff are working closely with the vendor to avoid further delay in the delivery (currently planned for early June 2020).

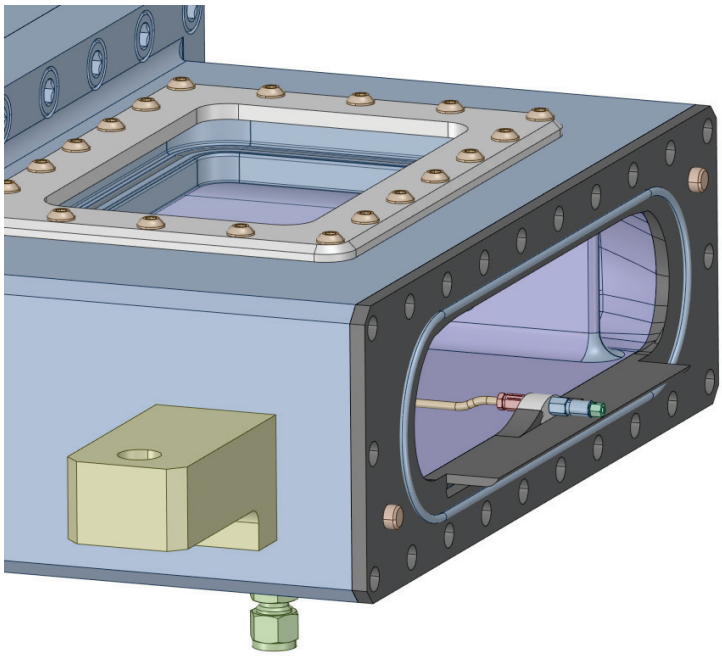

Figure 8.7. Details of the quick-connect for the gas wall.

8.2 SMALL GAS BUBBLE INJECTION

During the past 2 years, small bubbles of helium have been injected into the mercury target using 50–60 small orifices (8–12 μm diameter) with a backpressure of 100 psig (choked flow condition). The bubbles generated by these bubblers have proved to be very efficient at reducing cavitation damage [1]. However, the bubblers clog during operation, causing their flow rates to decrease with time. In addition, they have proved to be troublesome to fabricate: special care must be taken to make sure the orifices do not become clogged during the welding processes, shipping, and storage. Because of all these disadvantages, the PPU plans to use a swirl bubbler, a gas injection method similar to the one implemented at Japan–Proton Accelerator Research Complex (J-PARC) (see Figure 8.8, left). Leveraging ORNL's collaboration with J-PARC, a prototype was fabricated and tested in water and mercury [2] (see Figure 8.9). In water, the most frequent bubble diameter range was 150–200 μm, which should translate to a 100–135 μm diameter in mercury because mercury is more highly turbulent. However, the experiments in mercury exhibited even smaller bubbles than those predicted in theory, possibly because of the measurement technique (see Barbier et al. [2] for more details) or further bubble breakdown due to high turbulence. Figure 8.10 shows the bubble size distribution for a large gas injection rate: it was found that the bubble size was independent of the gas injection rate, as predicted by theory. From this series of measurements in water and mercury, it was concluded that the swirl bubbler could generate large numbers of bubbles with diameters of less than 300 μm. According to Futakawa et al. [3], such small bubbles would be very efficient in mitigating the pressure wave.

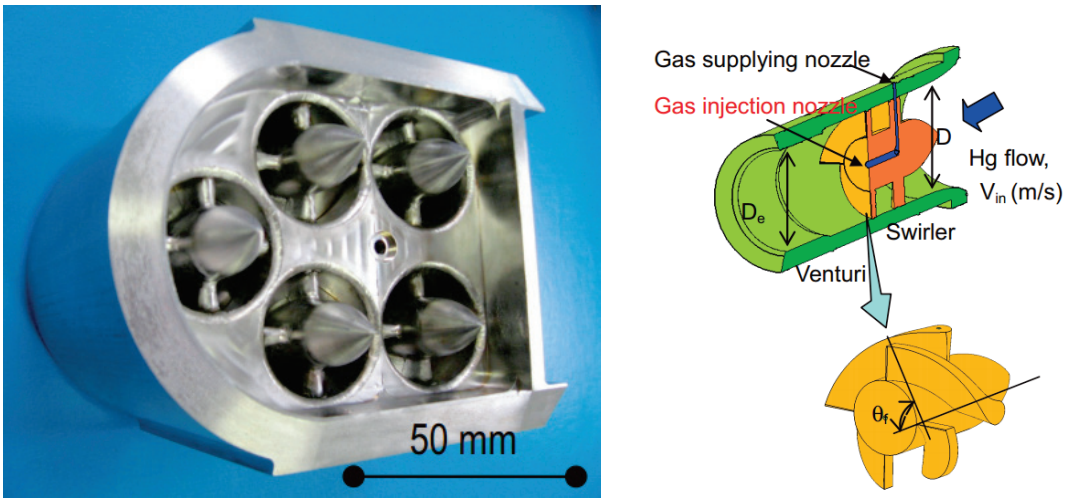

Figure 8.8 Picture of the swirl bubblers assembly used at J-PARC (left) and schematic of the cross-section of a single swirl bubbler (right).

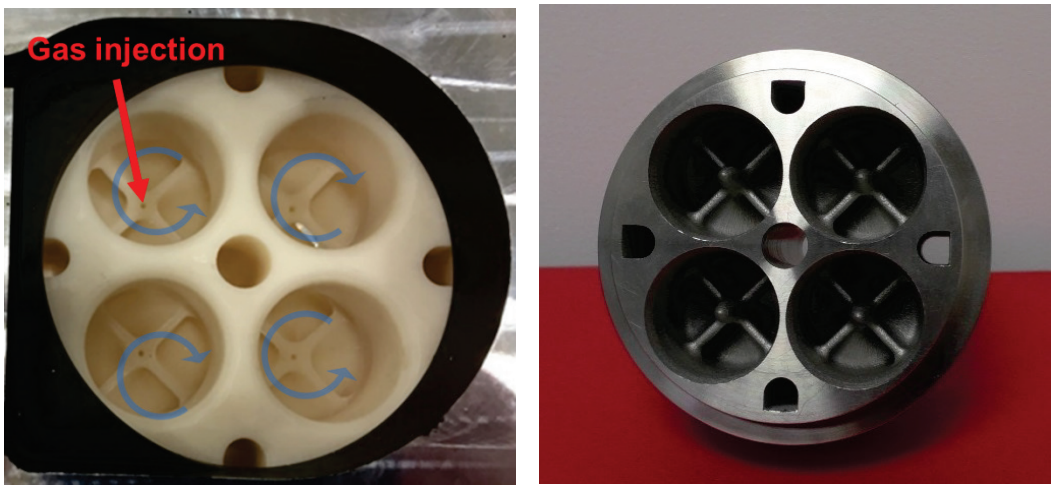

Figure 8.9. Pictures of the back of the swirl bubbler tested in the water target (left) and of the 3D printed stainless swirl bubbler tested at TTF in the mercury.

with the swirl bubbler at 400 rpm.

SNS operations has requested that we provide a better understanding of the difference in the bubble size generated by the current SNS bubbler (the inlet orifice bubbler, IOB) and the swirl bubbler. To do so, we used the visual jet-flow target that was built 2 years ago and installed an IOB with 18 micron orifices on one side and a swirl bubbler on the other side (see Figure 8.11). The flow rate was set up at 106 gpm on each bulk inlet. A slightly higher pressure drop was observed across the IOB, 2.75 psi, vs. 2.50 psi for the swirl bubbler. Figure 8.12 shows pictures from the nose with both bubblers at the same gas injection rate, 69 sccm. Qualitatively, the bubble sizes are similar. A more accurate measurement was performed just downstream from the bubblers (see Figure 8.11), where image analysis was performed to accurately measure the bubble size. The results are shown in Figure 8.13. It was found that both bubblers mainly generated bubbles of less than 600 μm diameter. However, their bubble size distributions were quite different: the swirl bubbler generated more small bubbles, less than 400 μm in diameter, whereas the bubble size distribution from the IOB was flatter.

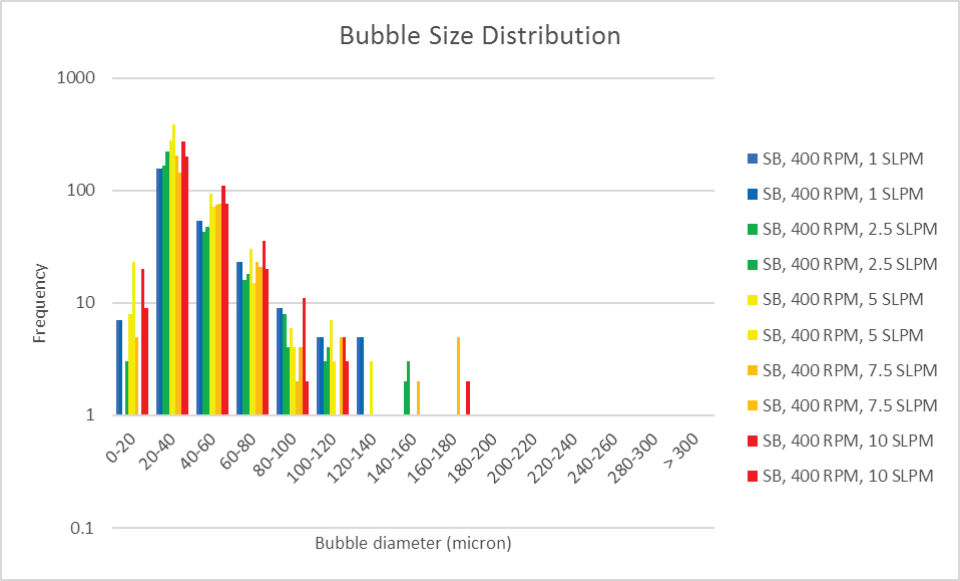

Figure 8.10. Bubble size distribution for several gas injection rates obtained.

Note that the IOB performance decreased rapidly with time; after 2 days in the water, it was completely clogged. This underlines again the limitation of the IOB design: the orifices can easily be clogged. In addition, an IOB with 18 µm orifices was fabricated for the TTF target (original design) and was tested so that further comparisons can be performed in the future (Figure 8.14). Rather than use a pitot tube device to measure the bubble size, the top acrylic window was used; the measurements were more challenging, since the bubbles are small and move relatively fast (1 m/s), but they were much less ambiguous. Note that this IOB design provides at most 3.6 SLPM, which is still a much lower rate than the 10 SLPM required by PPU. Future measurements with swirl bubblers will be compared with this baseline to ensure that the bubble size generated remains similar. At present, we are confident that the swirl bubbler can provide bubbles of a similar size to those generated by the IOB while providing a more reliable gas injection rate.

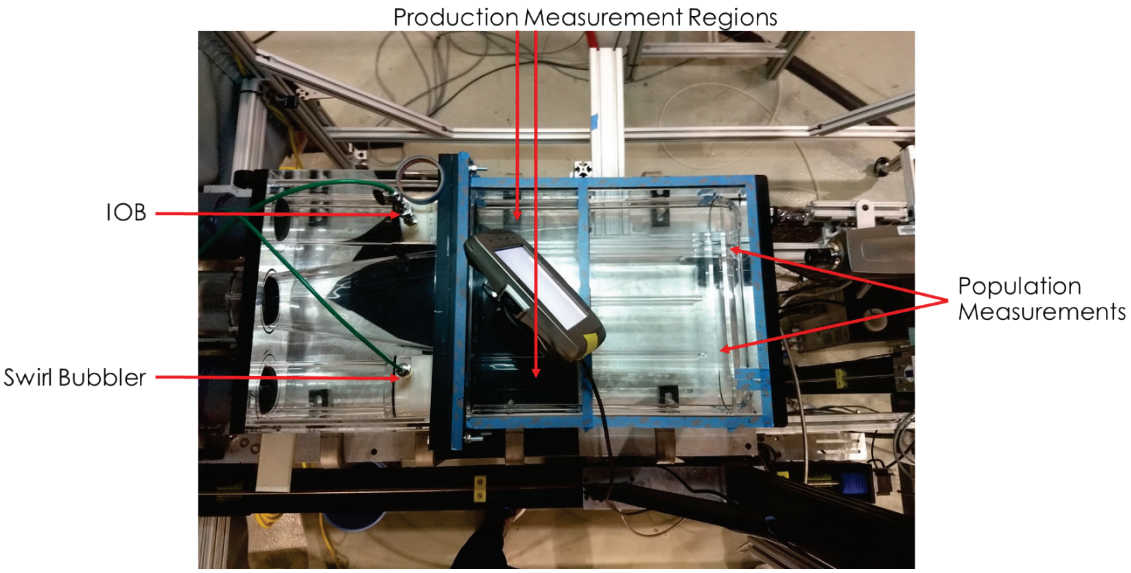

Figure 8.11. IOB vs. swirl bubbler in the visual jet-flow target.

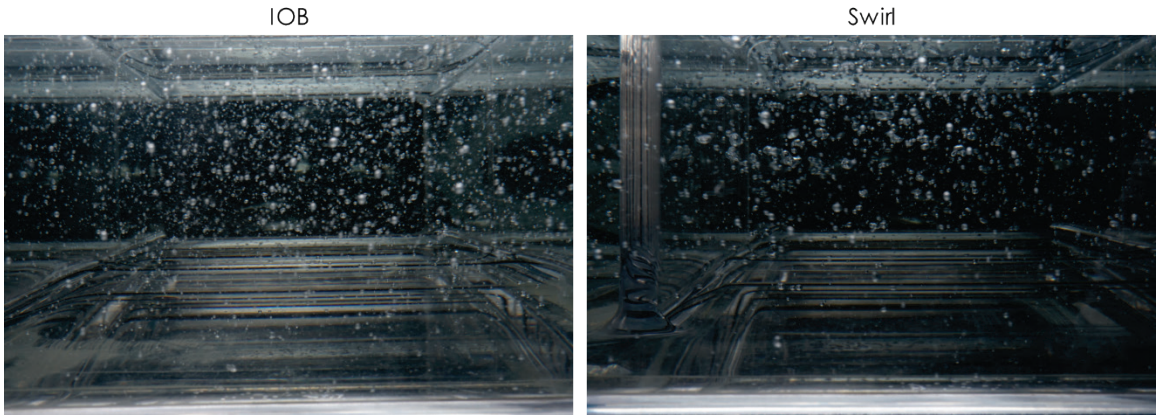

Figure 8.12. View from the nose of the bubbles generated by the IOB (left) and by the swirl bubbler (right).

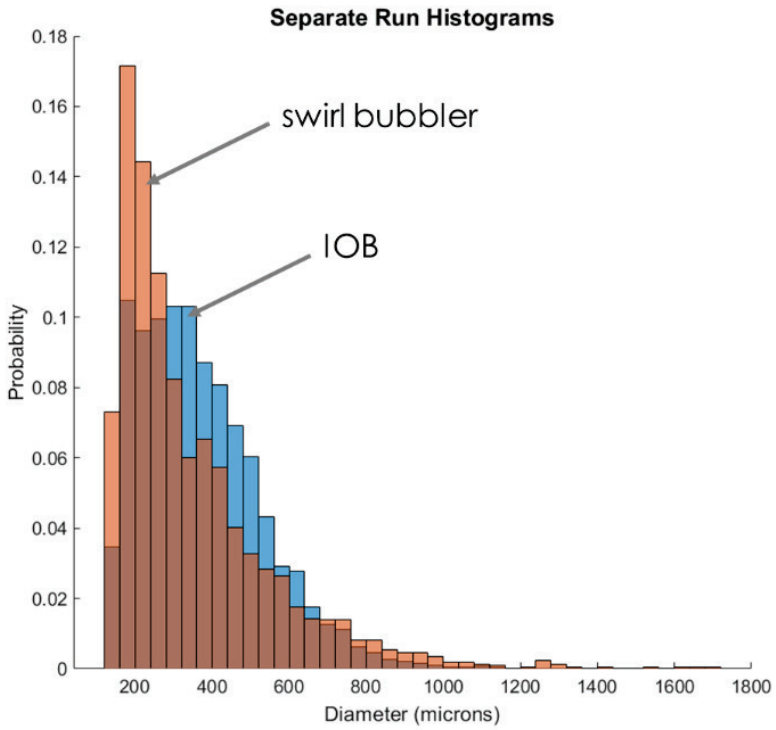

Figure 8.13. Superimposed bubble size distribution for the IOB and the swirl bubbler (experiments in water).

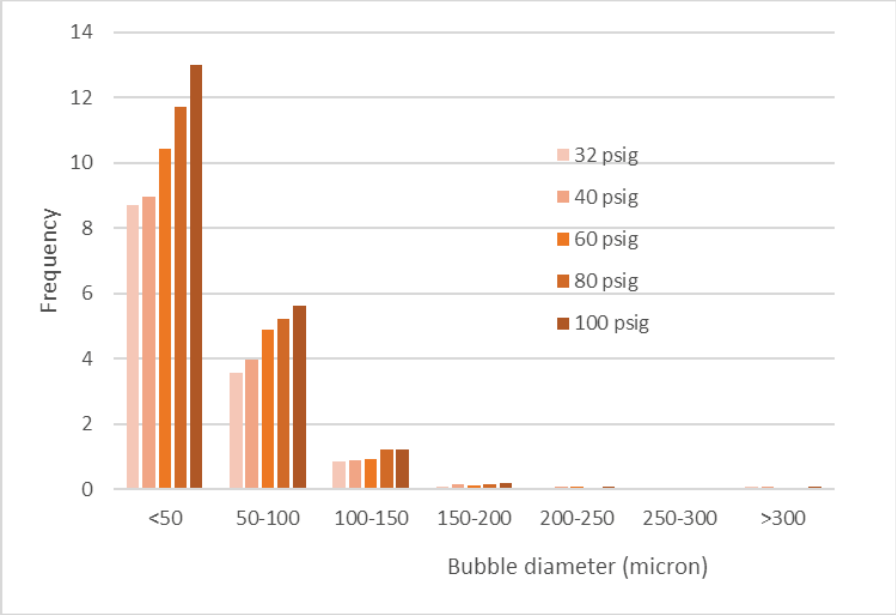

Figure 8.14. Bubble size distribution measured with the IOB with 18 μm orifices at TTF (experiments in mercury).

8.3 PROTECTIVE GAS LAYER

With the PPU beam on the mercury target, a protective gas layer needs to be implemented on the inner window wall of the target to ensure maximum mitigation of vessel erosion in addition to the mitigation that will be provided by small gas bubble injection. Three approaches have been investigated at SNS for establishing a gas layer [4] [5] [6]:

- Free gas layer: gas is injected locally on the inside of the target wall with no structural modification.
- Surface-modified gas layer: surface is textured to enhance gas layer attachment at the wall.
- Porous wall gas layer: a porous material is used to distribute gas across the vulnerable wall.

Establishing a free gas layer to cover the whole nose section was found to be challenging in the original target design. However, in the new jet-flow target design (see Figure 8.15), the jet flow will help stabilize the gas layer and enable better results. The textured surface approach gave very promising results, but uncertainty remains with regard to the mercury's surface wetting behavior on the steel vessel wall in a real SNS target environment versus the experiment. The wetting behavior could switch from nonwetting to wetting, which would degrade the gas wall coverage. Furthermore, the textured features present some risk of being fatigue stress risers. Uncertainties remain regarding the porous media, too, as there is no indication that the material will last in the beam and allow proper cooling of the window. Consequently, the free gas layer method will be the main approach pursued. Fortunately, in-beam experiments with a gas wall indicate that less-than-perfect gas wall coverage can still be highly effective [7].

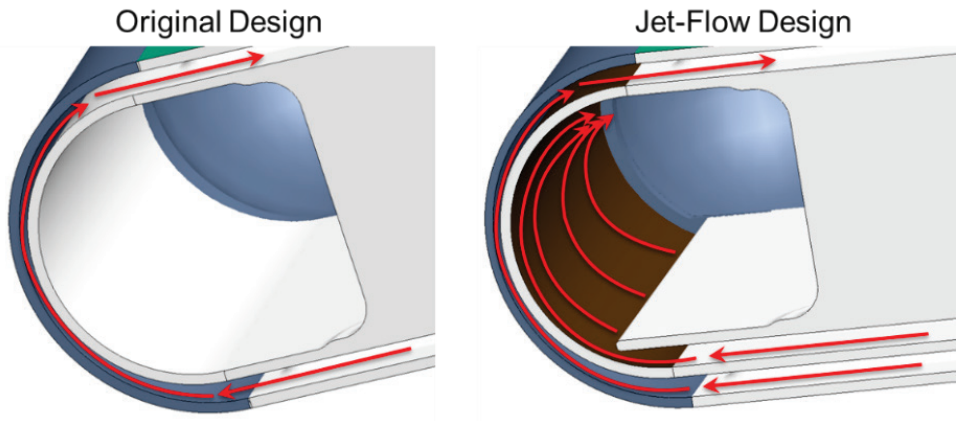

Figure 8.15. Schematic of the original and jet-flow target designs and their associated flow patterns.

First, experiments were performed using water as a surrogate working fluid in an acrylic test section. This type of setup aimed to provide optical access to the test section from different perspectives. As a first approximation, only the jet-flow was considered, and gas was injected at the base of the jet-flow (see Figure 8.16). For the water experiments, compressed air was used as the working gas. Satisfying gas coverage was obtained and matched relatively well with CFD simulations (see Figure 8.17).

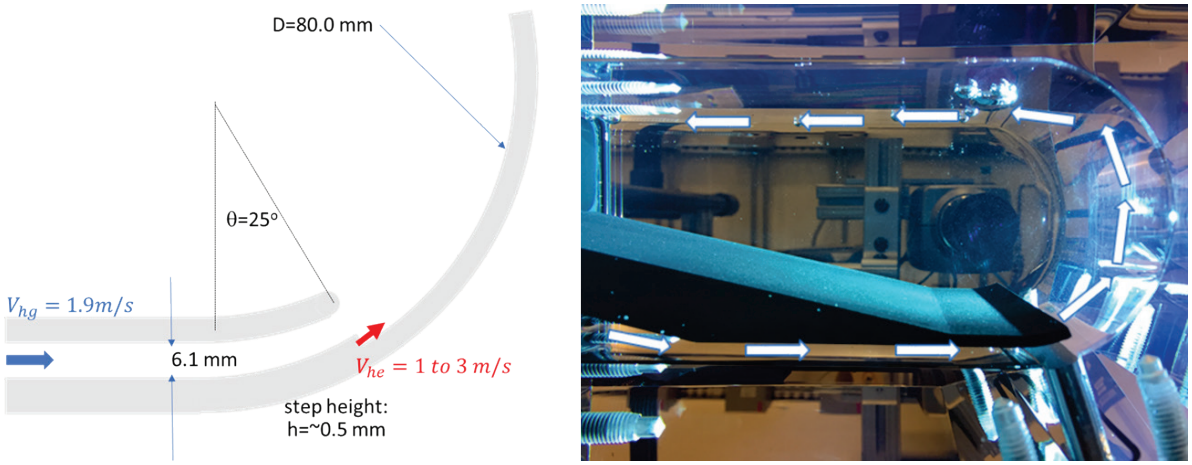

Figure 8.16. Schematic with key dimensions and picture of the water experiments.

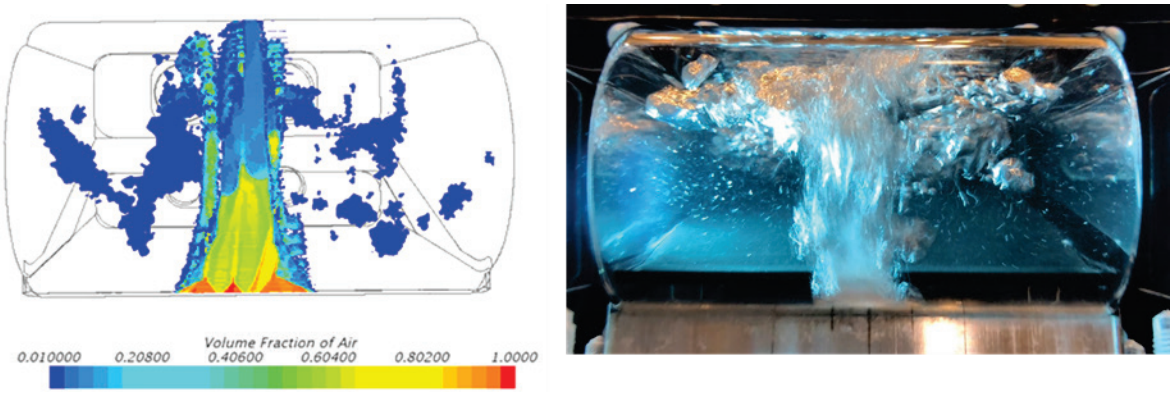

Figure 8.17. Comparison of the fluid simulations with the experiments at 1.9 m/s.

A similar setup was then built for the TTF to run experiments with mercury. Figure 8.18 shows the test section for the G-WaLE. All the results can be found in Weinmeister et al. [8]; only the main results are reported here. It was found that injecting just below the diving board, as illustrated in Figure 8.18, did not provide the desired results. Contrary to the experiments in water, the buoyancy force was much stronger and caused the gas layer to peel off the wall much earlier in mercury. Much better results were achieved when the gas injection was moved closer to the center of the nose (about 1/3 of the total height, see Figure 8.19). For that case, much better coverage was achieved (see Figure 8.20). Implementing such a solution will be challenging: the gas injection will be performed in the beam region and will be subjected to strong energy deposition while being pulsed at 60 Hz with a pressure wave.

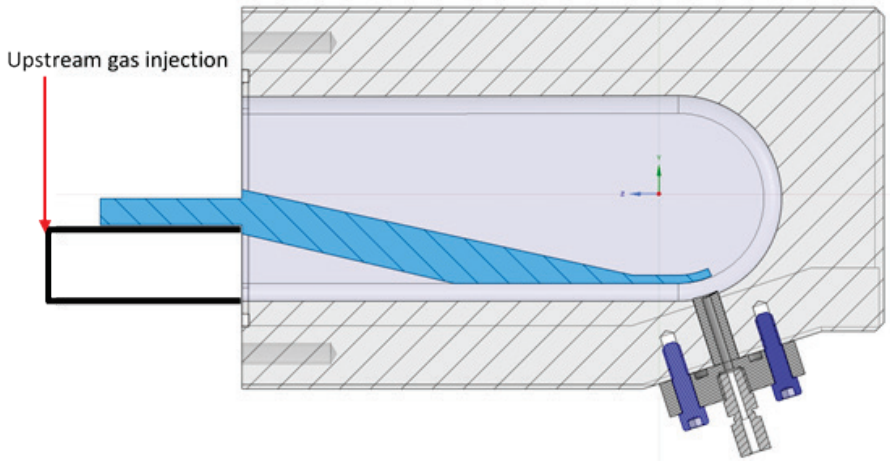

Figure 8.18. Right cross-sectional view of gas wall layer experiments (G-WaLE).

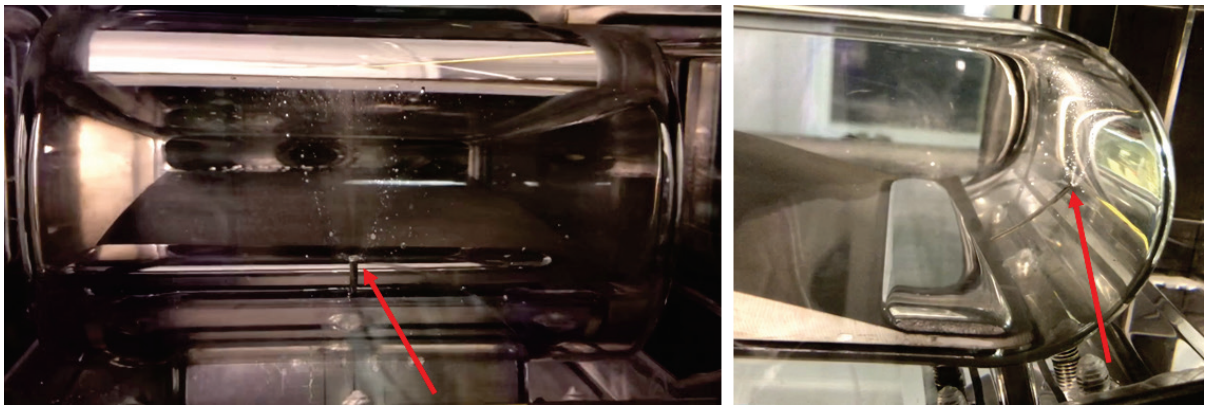

Figure 8.19. Front (left) and side (right) views of the tube insert.

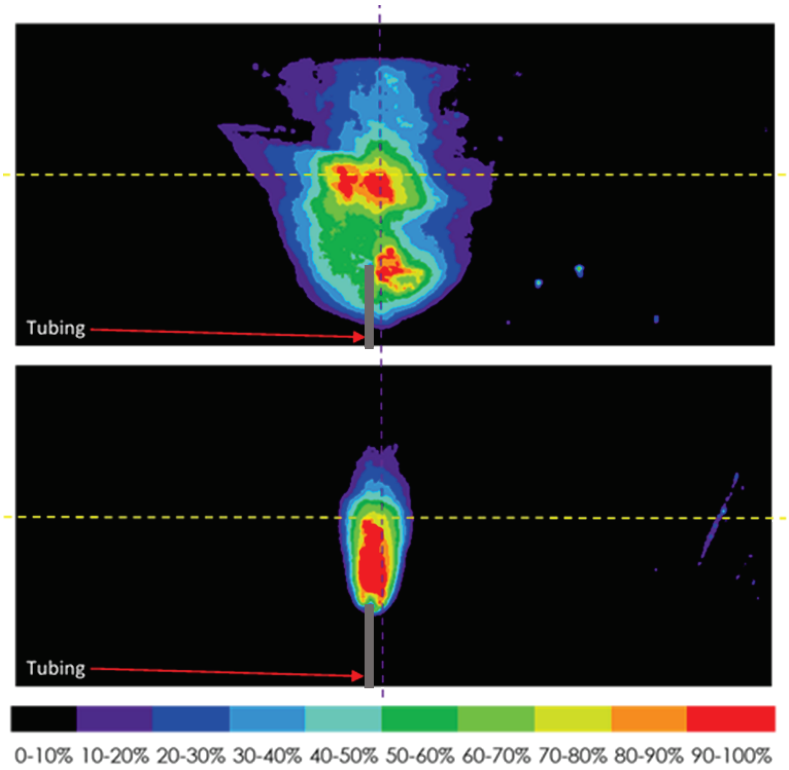

Figure 8.20. Time-averaged gas wall coverage contours for the single nozzle gas injection close to the nose centerline for two flow conditions: V_{Hg}=0.52 m/s and Q_{He} = 14.4 SLPM (top, and V_{Hg}=1.11 m/s and Q_{He} = 5.8 SLPM (bottom).

Gas layer implementation was investigated with the visual target. First, gas was injected close to the region of interest as suggested by the findings of G-WaLE. The results found that the bulk flow caused most of the gas layer to be peeled off the wall very quickly (see Figure 8.21): the bulk flow momentum was too large and the gas pocket was breaking along the flow streamlines. Gas injection under the diving board is currently being investigated.

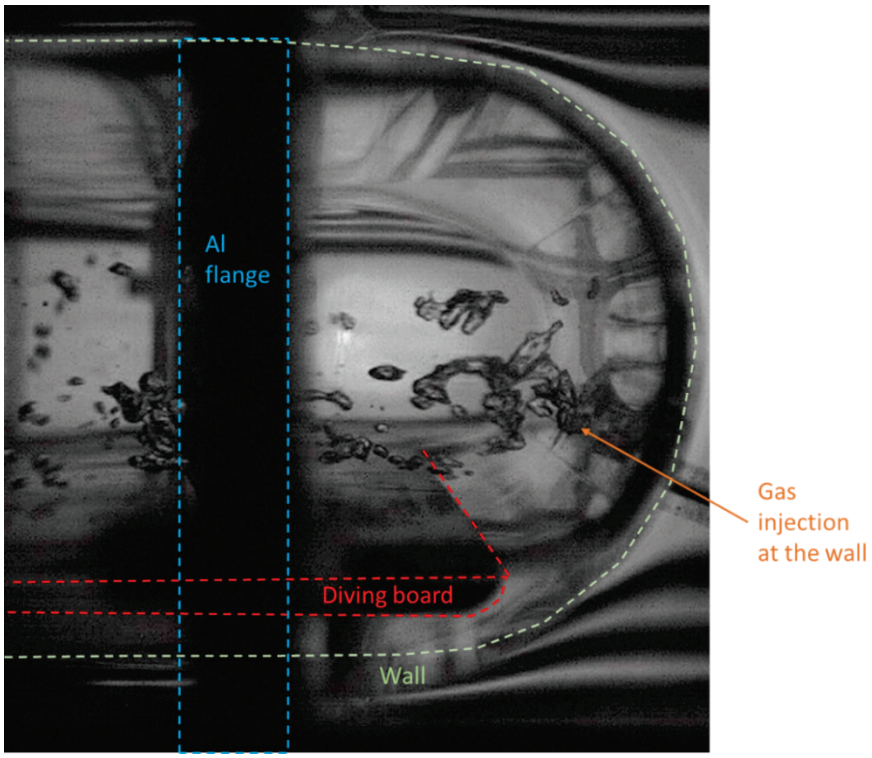

Figure 8.21. Gas layer with injection at the wall near the region of interest with the presence of bulk flow.

8.4 GAS REMOVAL IN THE SNS MERCURY LOOP

One of the main concerns regarding gas injection in the SNS loop is the potential for gas accumulation in the process piping and heat exchanger, which could displace enough liquid mercury to overflow the pump tank. Since October 2017, gas has been injected in the mercury target at different gas injection rates. It has been found that gas accumulation increases as the gas injection flow rate increases (see Table 8.1). Keeping only the data points with a pump speed of 350 rpm from Table 8.1, gas accumulation was found to be almost linear with the gas injection rate (see Figure 8.22). Extrapolating the injection rate to 20 SLPM, a gas accumulation volume of 62.3 L was found, which could be accommodated by the current mercury loop but could pose a problem during a pump trip event. As mentioned previously, a gas-liquid separator (GLS) will be installed to remove the excess gas.

Table 8.1. Amount of volume of mercury displaced with gas injection. The mercury flow rate is estimated via DP measurements.

Date	Target	Design	Gas injection rate (SLPM)	DP (psid)	Q_{Hg} (gpm)	Volume displaced (L)
10/25/2017	T18	Jet-Flow	0.45	35.3	250	1.7L
12/20/2017	T18	Jet-Flow	0.25	22.3	203	3.8L
05/14/2018	T19	Jet-Flow	0.40–0.57	34.8	255	2.2L
08/20/2018	T20	Jet-Flow	0.50	34.4	258	1.7L
01/11/2019	T21	Original	0.86	30.0	293	2.7L
06/20/2019	T22	Blue	1.0	30.1	290	3.2L
10/29/2019	T24	Jet-Flow	1.7	34.3	259	5.6L

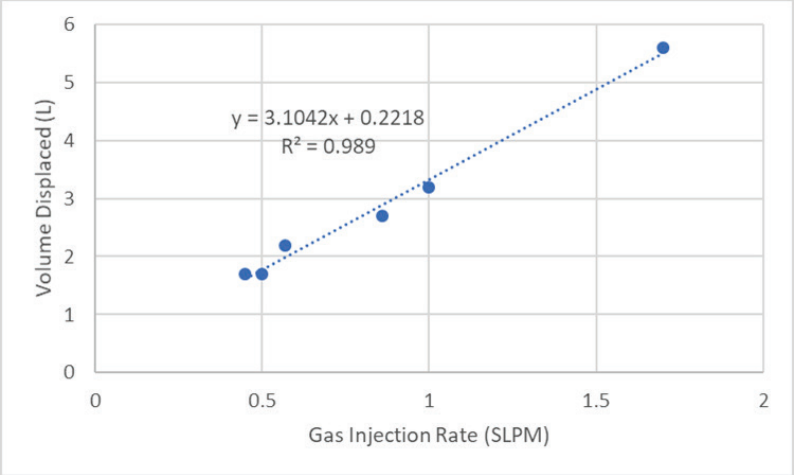

Figure 8.22. Gas accumulation vs. gas injection at 350 rpm.

The R&D effort provided the overall design for the GLS. Because of the spatial constraints and the GLS location, a custom GLS had to be developed. The fluid enters the GLS and swirls around a cone. The gas accumulates on the top and center as a result of gravity and centrifugal force. Meanwhile, the liquid mercury is sucked in at the base of the cone and redirected toward the outlet. Figure 8.23 shows the flow pattern on the GLS prototype that will be built for the TTF. CFD simulations have been extensively used to improve the design of the GLS prototypes. Most simulations used ANSYS Fluent with a polyhedral hexcore mesh, and some supplemental simulations were performed using Star-CCM+ on a polyhedral mesh. The simulations currently used for design are incompressible, single-phase simulations using the realizable k-epsilon turbulence model. Close attention is paid to the streamlines of the velocity and residence time (see Figure 8.24). The velocity must be low enough to prevent additional bubble breakup, which causes smaller bubbles to be re-entrained with the flow. Higher residence times favor bubble coalescence, which creates more buoyant bubbles. The following are the findings:

- The pressure drop is strongly correlated with the area of the gap between the bottom of the GLS and the base of the cone. It can be controlled by the gap height, number of gaps, and gap width.
- The pressure at the GLS vent line is close to the pressure at the inlet pressure.
- Partially filling the cone to create a smooth transition slightly reduces the pressure drop.
- Based on single-phase streamlines, efficiency is expected to decrease in a GLS with a higher bottom to reduce mercury holdup.
- Adding a baffle to force the flow to rotate around the cone increases the pressure drop and causes nonuniform suction at the cone base.
- A larger headspace above the cone reduces turbulent forces where gas bubbles accumulate without increasing pressure drop.
- Realizable k-epsilon turbulence models accurately capture turbulent forces where gas is present; i.e., full seven-equation Reynolds stress models are not needed.

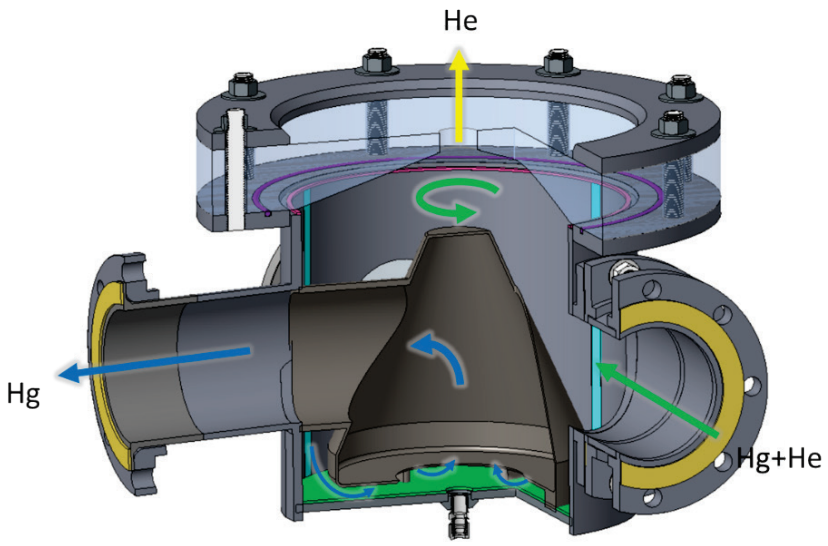

Figure 8.23. Flow patterns in the GLS.

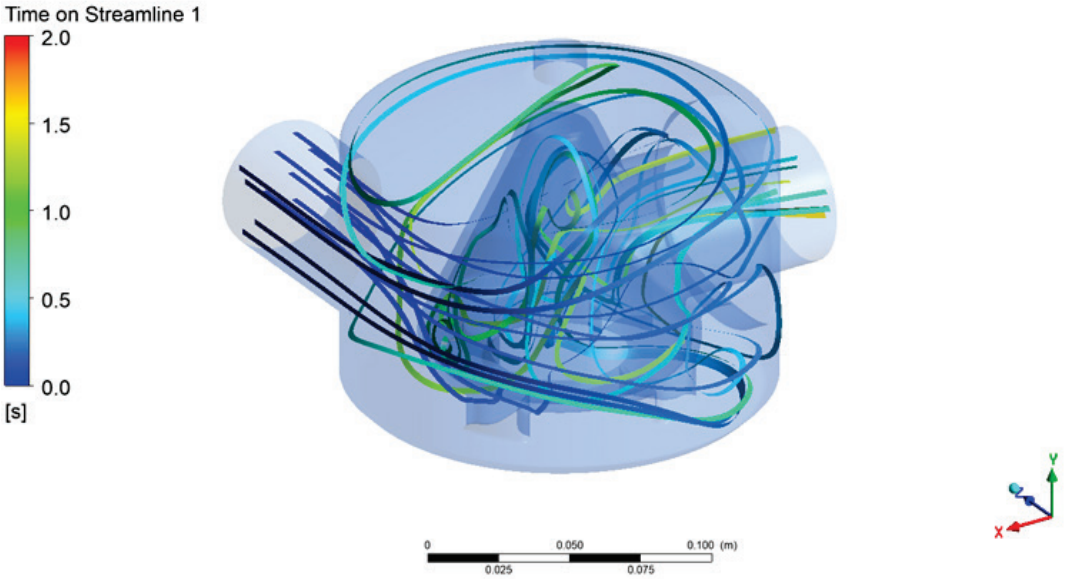

Figure 8.24 Streamlines for the water GLS colored with residence time.

A prototype 1/3-scale GLS was built for testing in the THL using acrylic for the outer housing and a cone additively manufactured using stereolithography. The outer housing was made of acrylic for visual interrogation of the flow, and the base was made using additive processes to speed turnaround time on design iterations if needed. A view of the installed configuration is shown in Figure 8.25. Pressure drops and multiphase testing were performed to validate the CFD results. Results showed that the prototype met the design requirement of greater than 90% gas removal efficiency at typical SNS operating velocities (0.85 m/s) and gas volume fractions (0.8%). Although the results are promising, testing in mercury is needed: the higher Reynolds number is expected to lower the efficiency, whereas the increased buoyancy force and the higher surface tension of mercury/helium pair will improve efficiency.

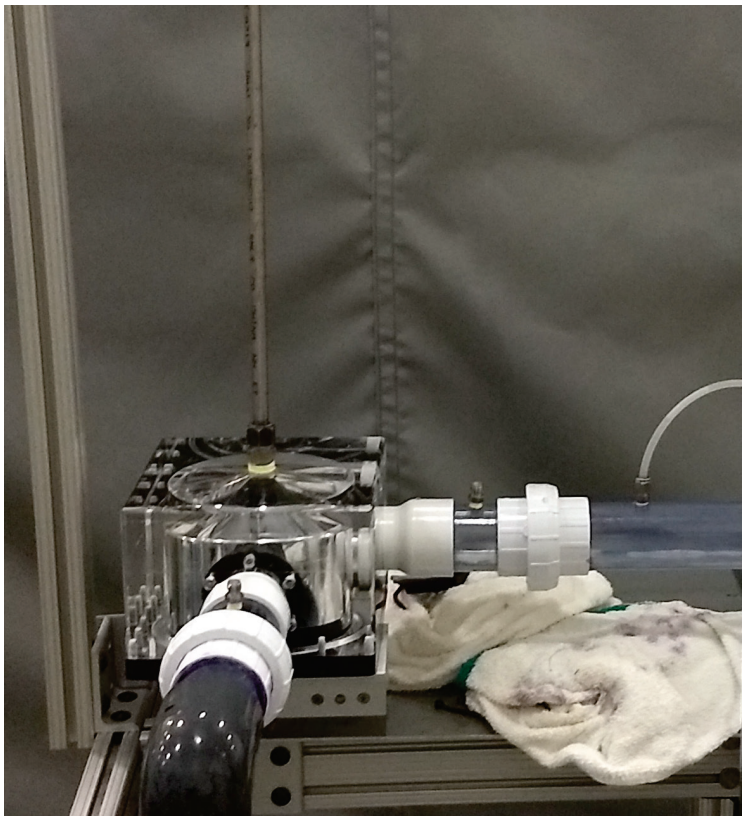

Figure 8.25. Water GLS prototype as tested.

The TTF GLS prototype is based on the water prototype geometry, as satisfactory results were obtained. The design specifications for the TTF GLS were the following (see Figure 8.23):

- Pressure loss factor of less than 20 based on 6 in. pipe
- Possibility of replacing the cone
- Acrylic side view port
- Acrylic top

To test the GLS, the TTF loop was modified to be more prototypical of the SNS loop. Figure 8.26 shows a comparison between the SNS and TTF mercury process loop. The main difference is the lack of a heat exchanger at the TTF. One key parameter in measuring the efficiency of the GLS is the gas distribution at the GLS inlet. To ensure the inlet condition was as realistic as possible, the TTF piping was modified so that the succession of the elbows upstream from the GLS was exactly the same (Figure 8.27). In addition, the 3 ft drop downstream of the GLS was included. Several view ports were also installed to monitor the gas accumulation upstream of the GLS. The TTF piping upgrade was completed on October 2018. TTF GLS fabrication started in May 2019, and installation was complete in October 2019 (Figure 8.28).

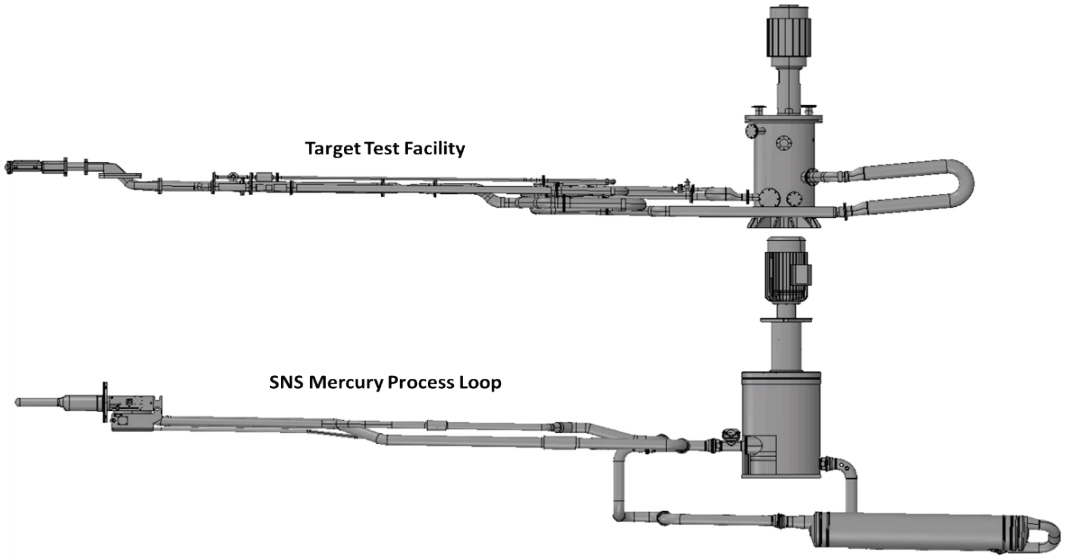

Figure 8.26. Comparison of SNS and original TTF mercury process loop.

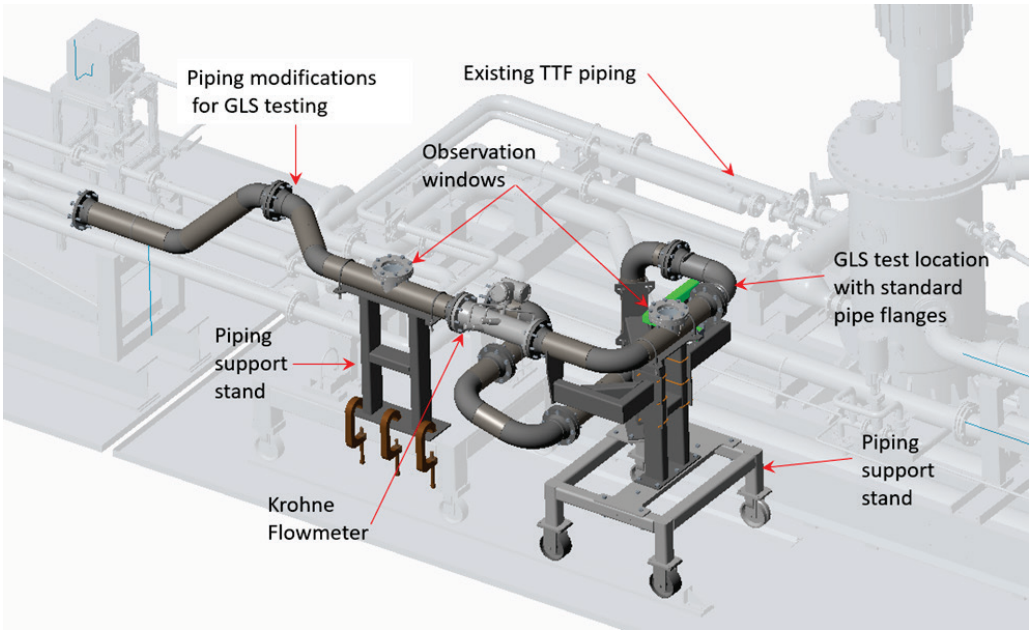

Figure 8.27. TTF piping upgrade.

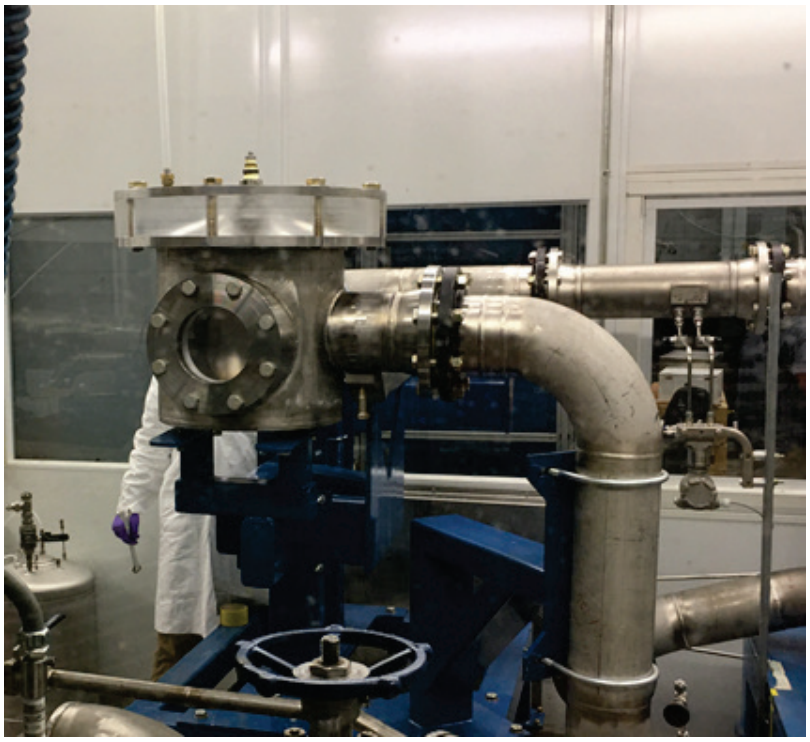

Figure 8.28. Prototypical GLS installed at TTF.

The GLS has been characterized for gas injection from 0 to 20 SLPM and mercury flow rates ranging from 230 to 270 gpm (nominal operating flow rate is 250 gpm). Results are presented in Figure 8.29. For all flow rates, efficiencies above 80% were observed. The best results were observed for the nominal flow rate, for which efficiencies above 90% were observed for all gas injection rate. At 270 gpm, the efficiency was degraded because the gas was introduced into the GLS as smaller bubbles and thus was more easily entrained with the mercury flow. However, as gas injection increased, the efficiency also increased and exceeded 90%. At 230 gpm, the efficiencies were very good up to 12.5 SLPM, then decreased as gas injection increased, suggesting a change in the multiphase flow regime.

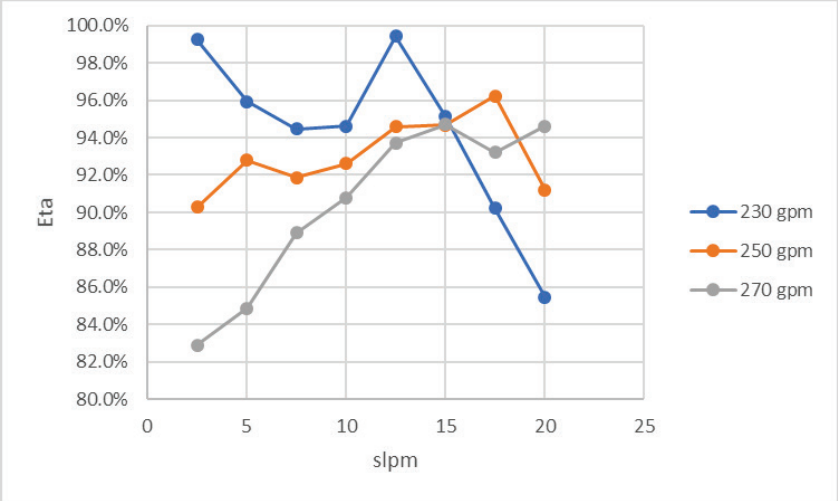

Figure 8.29. GLS efficiency (eta) for different helium gas injection rates for three mercury flow rates.

Following the preliminary design review of the Safety and Controls WBS, the following scope was added to the GLS R&D effort:

- Limit the amount of mercury holdup in the GLS after draining.
- Keep the mercury under the shielding at the GLS vent line.

Figure 8.30 shows an example of a cone design investigated to address the first recommendation. CFD simulations suggest that the efficiency will not be as good as the original design (Figure 8.23). The new cone insert is expected to be delivered at the end of May 2020.

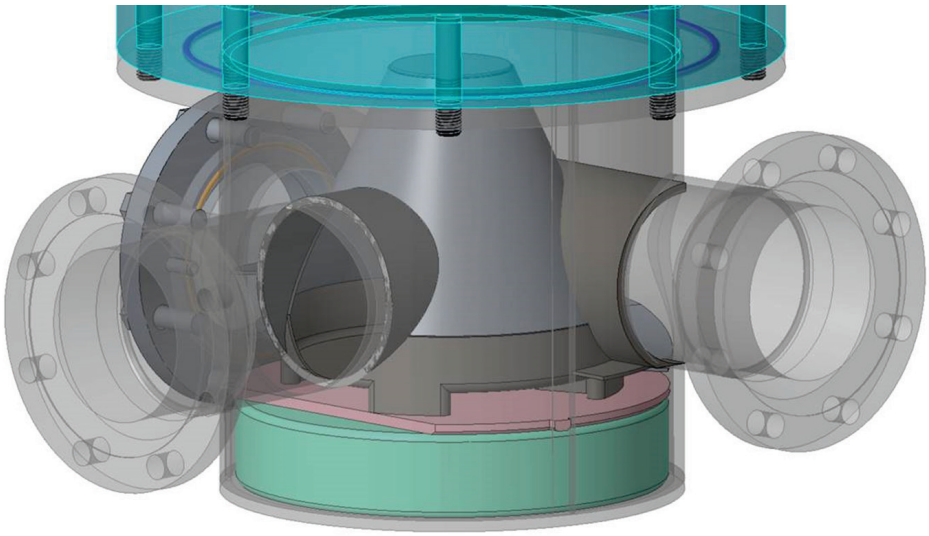

Figure 8.30. Modification of the cone assembly to reduce mercury holdup in the TTF GLS.

To address the second recommendation, we are considering adding a porous filter at the GLS vent line that will hold the mercury while letting the gas vent. For a first test performed on the water loop, a filter was assembled using a combination of different porous media. After several trial and error runs, a combination of Scotch-Brite and Fiberglass insulation class 1 and 3 was efficient at reducing the mercury column at the vent line (from 36 in. to 5 in.) while still letting the gas vent (see Figure 8.31). However, the solution found for water may not be applicable for mercury: the wetting properties of mercury are very different from those of water. It was thus decided to build a stand-alone mercury test stand that will allow testing of different kinds of porous filters.

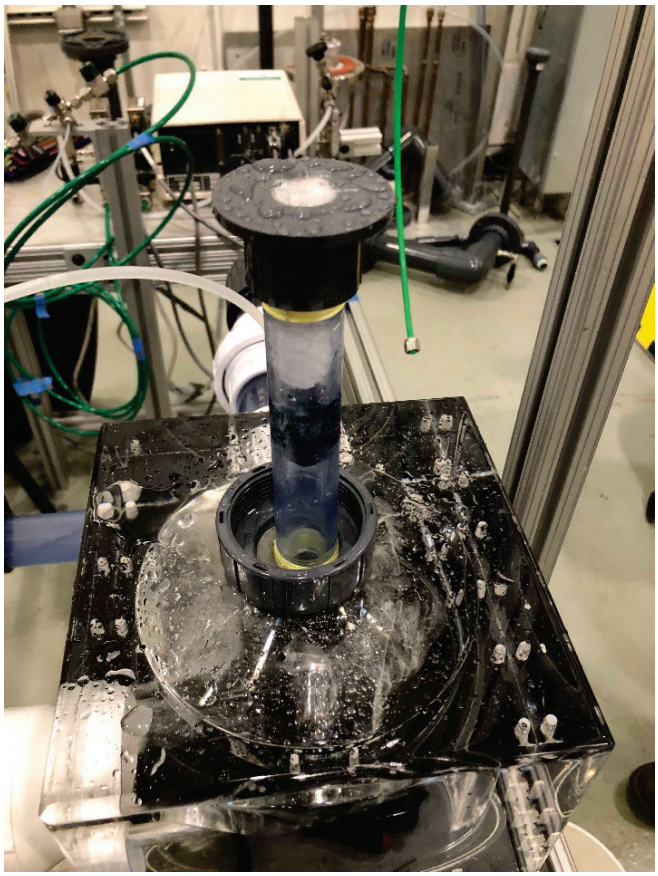

Figure 8.31. Water GLS with porous filter in the vent line.

The TTF filter media test stand is connected to the main mercury loop so that it can be easily be filled from the loop and drained back into it. The filter media are tested on a test section, as shown in Figure 8.32 and Figure 8.33. A first series of measurements are performed in which only mercury is pushed through the filter media to determine how much pressure the filter can withstand. Then gas is injected upstream of the filter to check whether the filter can hold the mercury while letting the helium flow. The first filters that will be tested are two Mott filters:

- GasShield diffuser
- POU-10 (similar to the one tested in Barbier [9])

The GasShield was not capable of holding more than 25 psig, whereas the POU-10 demonstrated its capability to hold up to 45 psig (40 psig with coflowing gas). The POU-10 would work at SNS, but a higher margin of maximum pressure at which it can operate is desired. Thus, two filters were custom-made by Mott and were tested in April 2020. The custom-made filters did not perform as well as POU-10 and so POU-10 is the filter of choice for the GLS. With the current GLS design, the pressure at the filter is expected to be about 30 psig. To ensure the POU-10 is indeed suitable, it will be tested with co-flowing gas for several days (ongoing experiments).

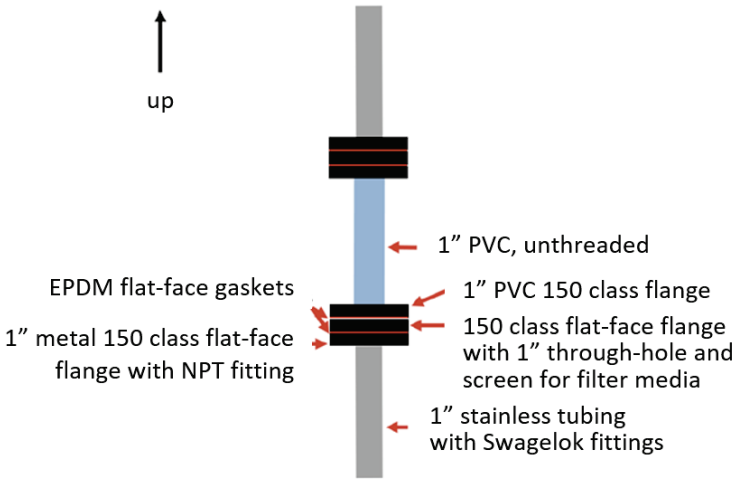

Figure 8.32. Details of the test section of the filter media test stand.

Figure 8.33. Filter media test stand installed inside TTF. Note the test section has been removed.

8.5 GAS-COMPATIBLE FLOW METERS

After some research, two potential gas-compatible flowmeters were identified: a V-cone flowmeter from McCrometer and a magnetic flow sensor from Schneider Electric (Figure 8.34). The V-cone flowmeter was installed in spring 2019 and some preliminary measurements were performed at up to 3.6 SLPM. The preliminary results suggest that the flowmeter reading is noisier than the readings for the venturi installed at TTF (±3% of the mean value compared with ±0.8% with the venturi). When gas injection was increased to 10 SLPM, the flow was found to be stratified upstream of the flowmeter; thus, neither flowmeter is suitable for measuring the flow in such a regime. The results were compiled in a report [10], and the scope related to the flowmeter fabrication and installation at SNS was removed.

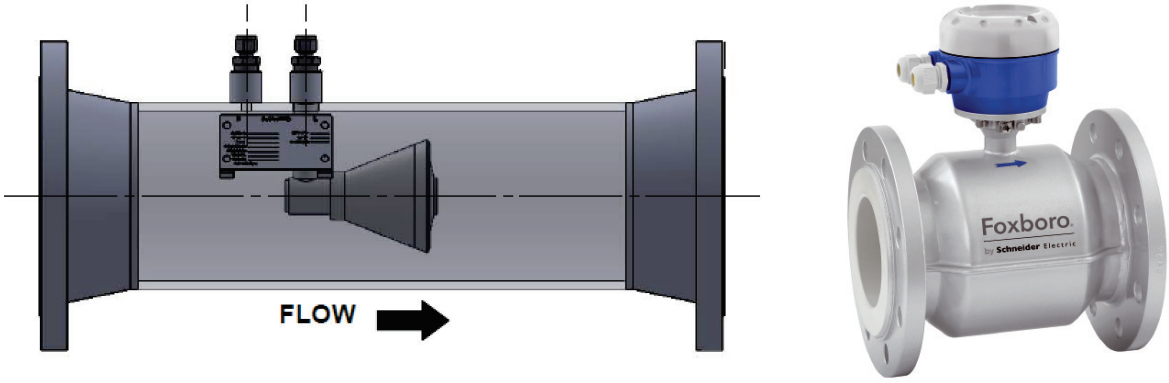

Figure 8.34. V-cone flowmeter from McCrometer (left) and magnetic flow sensor from Schneider Electric (right).

8.6 GAS RECIRCULATION

The diaphragm compressor from KNF Process Pumps was tested over 300 days without problems and is the preferred choice for recirculating gas. The setup was modified to be similar to the gas recirculation system planned at SNS (Figure 8.35). The compressor setup delivered satisfying results (Figure 8.36 and Figure 8.37): the setup can deliver up to almost 9 SLPM, and either the equilibar pressure or the pump speed can be used to regulate the mass flow rate.

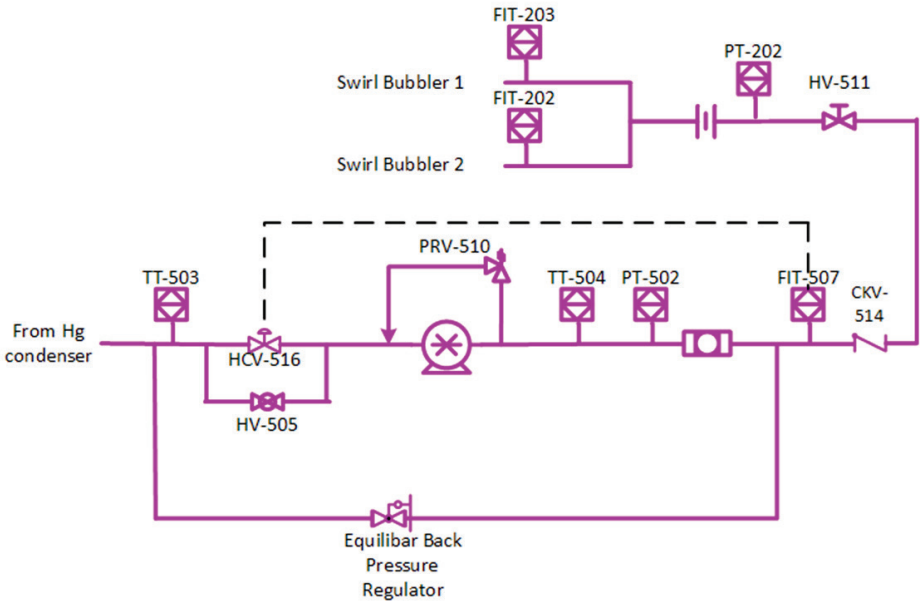

Figure 8.35. Helium gas recirculation test configuration.

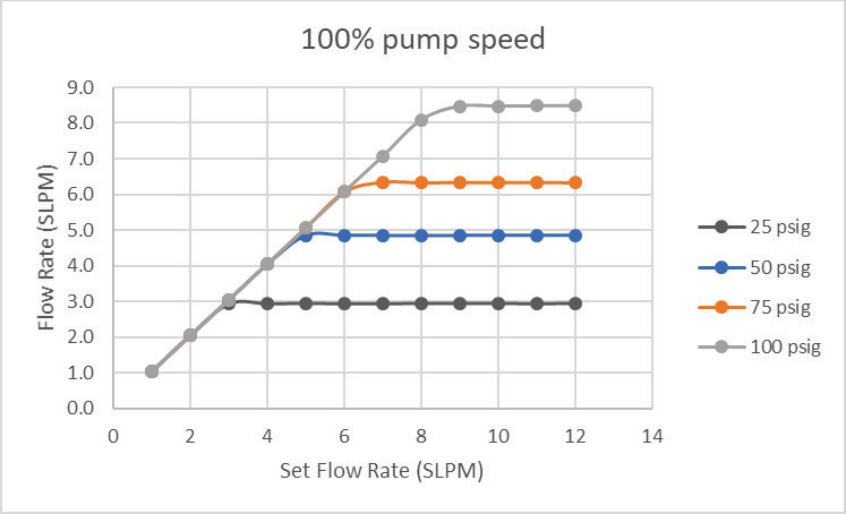

Figure 8.36. Mass flow rate for different set pressure at the equilibar with the compressor running at 100% speed.

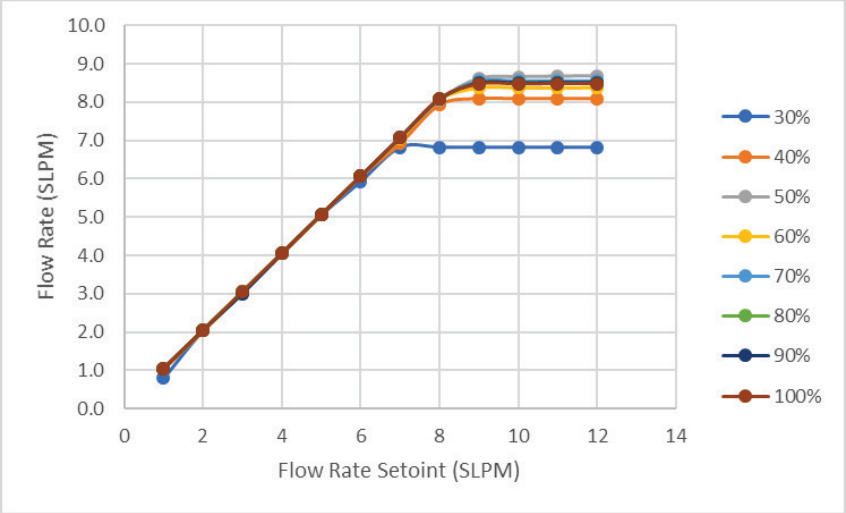

Figure 8.37. Mass flow rate for different compressor speed with the equilibar pressure set at 100 psi.

8.7 SINGLE BUBBLE COLLAPSE

After CD-1, a collaboration was started with professor Eric Johnsen of the University of Michigan. The University of Michigan has a unique code for the high-fidelity computation of a single bubble collapse. Since CD-1, Michigan has developing an equation-of-state (EOS) for mercury, performing bubble collapse near a rigid wall and confined in a channel. Some discretionary time was obtained to run the code on supercomputers at the Oak Ridge Leadership Computing Facility (>3M core-hours on EOS) and the Argonne Leadership Computing Facility (1M core-hours on Theta). The main findings were the following:

- A suitable EOS was developed for mercury, but the high liquid-vapor density ratio caused instabilities in the University of Michigan code. To obtain a better understanding, simulations with different ratios were performed to determine the differences and similarities between the dynamics and wall pressure of bubble collapse in mercury vs. water.

- A series of single bubble collapses near a single wall were performed to determine the maximum pressure at the wall. A scaling law was developed and will be submitted to a peer-reviewed scientific journal.

- A series of single bubble collapses in a channel were performed to determine the maximum pressure at the wall. It was found that if a bubble is too strictly confined, then the maximum pressure at the wall increases. This is a key result: if cavitation erosion is observed at higher power in the target window flow, then a simple solution could be to increase the channel gap.

The next series of simulations will investigate the impact of a local shear flow on the maximum pressure experienced at the wall.

8.8 REFERENCES

1. W. Blokland, Y. Liu, M. Wendel, and D. Winder, *Measurements of the Effects of Gas Injection into SNS Target T18*, 106010101-TR0043, Oak Ridge National Laboratory, 2018.

2. C. Barbier, E. Dominguez-Ontiveros, and R. Sangrey, "Small bubbles generation with swirl bubblers for SNS target," in *ASME 2018 5th Joint US-European Fluids Engineering Division Summer Meeting*, Montreal, Canada, 2018.

3. M. Futakawa, K. Hiroyuki, H. Shoichi, et al., "Mitigation technologies for damage induced by pressure waves in high-power mercury spallation neutron sources (II)—Bubbling effect to reduce pressure wave," *Journal of Nuclear Science and Technology* **45**(10), 1041–1048, 2008.

4. D. Felde, B. Riemer, and M. Wendel, "Development of a gas layer to mitigate cavitation damage in liquid mercury spallation targets," *Journal of Nuclear Materials* **377**, 155–161, 2008.

5. M. Wendel, D. Felde, B. Riemer, et al., "Progress in creating stabilized gas layers in flowing liquid mercury," in *ASMEFluids Engineering Division Summer Meeting* (collocated with the Heat Transfer, Energy Sustainability, and 3rd Energy Nanotechnology Conferences), Jacksonville, Florida, August 10–14, 2008.

6. M. Wendel, D. Felde, A. Abdou, and B. Riemer, "Update on progress in creating stabilized gas layers in flowing liquid mercury," in *ASME 2009 Fluids Engineering Division Summer Meeting*, Vail, Colorado, August 2–5, 2009.

7. J. Haines, B. Riemer, D. Felde, et al., "Summary of cavitation erosion investigations for the SNS mercury target," *Journal of Nuclear Materials*, **343**(1–3), 58–69, 2005.

8. J. Weinmeister, E. Dominguez-Ontiveros, and C. Barbier, *Gas Wall Layer Experiments (G-WaLE)—Preliminary Results*, PPUP-701-TR0001-R00, Oak Ridge National Laboratory, 2018.

9. C. Barbier, *Porous Filter Testing as a Check-Valve Role*, SNS-106010101-TR0034-R00, Oak Ridge National Laboratory, 2017.

10. C. Barbier, *Gas Compatible Flowmeter for the Mercury Loop Process*, 106010405-TR0001-R00, Oak Ridge National Laboratory, 2020.

9. ENVIRONMENT, SAFETY, HEALTH, AND QUALITY ASSURANCE

9.1 INTRODUCTION AND OVERVIEW

The current operating facility, SNS, is fully integrated into the ORNL management systems. The PPU is an extension of the capabilities of the SNS, with no new significant hazards associated with the upgrade. The ORNL institutional safety programs as promulgated through the Standards-Based Management System (SBMS) provide protection from common industrial and laboratory hazards. The "SNS Integrated Safety Management (ISM) Plan," included in the *Spallation Neutron Source Environment, Safety, and Health Plan*, documents the overall approach to the environment, safety, health, and quality (ESH&Q) of the project. The ISM plan and annual updates have been submitted to DOE, and independent internal and external assessments of the program have been conducted. These reviews found the approach to, and implementation of, ESH&Q requirements throughout the project to be appropriate for an effort of this magnitude, risk, and visibility. Commitment to excellence in ESH&Q is a constant goal at all levels of the SNS, and improvements are sought on a continual basis. ISM is implemented through the ORNL SBMS.

ORNL is committed to the protection of workers, visitors, the public, and the environment. Consistent with its prime contract, UT-Battelle LLC, as operator of ORNL, maintains an Environmental Management System Description, a Quality Assurance Program Plan, and an Integrated Safety Management System/Worker Safety and Health Program Description. These programs implement the applicable requirements of DOE O 436.1, *Departmental Sustainability*, 10 CFR 830 Subpart A, *Quality Assurance Requirements*, DOE 414.1D, *Quality Assurance*, and 10 CFR 851, *Worker Safety and Health Program*, respectively.

To support a robust Contractor Assurance System (CAS) and provide reasonable assurance that objectives are accomplished, and systems and controls are effective and efficient, the laboratory maintains compliance with three internationally recognized standards.

- International Organization for Standardization (ISO) 14001:2015, *Environmental Management Systems* (certified by an external organization)

- ISO 9001:2015, *Quality Management Systems* (compliance is verified with an annual lab-wide assessment)

- Occupational Health and Safety Assessment Series (OHSAS) 18001:2007, *Occupational Health and Safety Systems* (certified by an external organization)

ORNL's ESH&Q policies, either directly or via contractual flow-down documents, are applicable to all employees, subcontractors, users, research visitors, students, and suppliers. Fundamental drivers are delineated in ORNL's SBMS. Within SBMS, ESH&Q is described at the highest level in the following management systems.

- SBMS Management System Description: Worker Safety and Health
- SBMS Management System Description: Environmental
- SBMS Management System Description: Quality.

Descriptions of programs that flow down from these management systems go into more detail and contain policy statements. These program descriptions are organized according to the overarching set of requirements for each system and include the following.

- SBMS Program Description: Worker Safety and Health Program [(OHSAS) 18001:2007, *Occupational Health and Safety Systems*]

- SBMS Program Description: ISO 14001:2015, *Environmental Management System*

- SBMS Program Description: Quality Assurance Program (DOE O 414.1D, *Quality Assurance*, which is implemented through ISO 9001:2015 Quality Management Systems)

Each program description references applicable SBMS procedures that provide the next level of detail for that program and are at the lab-wide policy level. At the next level, each organization maintains procedures that continue to flow down these policies to the directorate, division, organization, and process levels.

9.2 HAZARD ANALYSIS REPORT

The potential hazards associated with operation of the SNS are evaluated in two documents, the *Final Safety Assessment Document for Proton Facilities* (FSAD-PF, 102030103-ES0018-R02) and the *Final Safety Assessment Document for Neutron Facilities* (FSAD-NF, 102030102-ES0016-R03). The FSAD-NF focuses only on those hazards associated with operations in the target facility, while the FSAD-PF covers the remainder of the accelerator facility footprint. Both documents focus on those hazards specific to accelerators, relying on institutional programs, such as those described in SBMS, to safely manage standard industrial hazards. Accelerator-specific hazards include prompt ionizing radiation due to beam production and radionuclides stemming from beam activation, including both direct radiation and potential dose due to uptake following a release. Potential releases of radionuclides from various initiators are evaluated, including fire, explosion, confinement failure, and natural phenomena such as an earthquake. Accelerator-specific hazards that pose a significant risk are mitigated using credited engineered controls and/or credited administrative controls.

The SNS Accelerator Safety Envelope (ASE) incorporates the results of both the FSAD-PF and FSAD-NF into a single document that provides the operational limitations and credited controls essential to safe operation of the SNS.

The Hazard Analysis Report (HAR, PPUP-103-ES0004-R00) for the Proton Power Upgrade Project (PPUP) is based on the application of the existing unreviewed safety issue (USI) process at SNS. Changes planned to be implemented as part of the PPUP were evaluated by subject matter experts (SMEs) familiar with the existing FSAD-PF and FSAD-NF. Specific impacts on the existing safety analysis were identified and evaluated using guidance from the USI process to determine if such changes could result in a significant increase in risk associated with operation of the SNS. In those cases where increased risk was identified, credited controls were designated to reduce the risk to an acceptable level.

SNS operations are presently authorized for 2 MW of beam on target at a particle energy of 1.0 GeV. Operations following completion of the PPUP will remain within the 2 MW limit, but additional analysis was required to evaluate increasing the particle energy to 1.3 GeV and its potential effect on the safety analysis. Sections 2 and 3 of the HAR focus on specific aspects of this analysis: target spallation product inventory and target core vessel component heat distribution. The increased beam energy combined with the anticipated throughput of the radio frequency quadrupole following the PPUP is expected to make the accelerator capable of delivering up to 2.8 MW of proton beam. Beam power in excess of 2 MW is being made available to support the anticipated construction of the STS, but consideration is given to the possibility of directing beam in excess of 2 MW to the FTS, as described in Section 7. The ASE also provides a limit on the power that can be deposited in the ring injection dump. Conservative estimations of the potential heat load on the ring injection dump during 2 MW operation potentially exceed this limit,

so Section 4 of the HAR considers increasing the ASE limit for the ring injection dump from 150 kW to 200 kW. To support target module performance, especially at high beam powers, the PPUP includes upgrades to significantly increase the amount of helium gas injection in the target mercury. Initial implementation of target gas injection required additional credited controls, so Section 5 of the HAR evaluates the need for credited controls to support increased injection of helium into the target mercury. Finally, Section 6 of the HAR evaluates potential safety concerns associated with catalytic beds being installed in the cryogenic moderator system to improve the neutronic performance of the moderators, especially soon after cooldown.

Although the modifications associated with the PPUP introduce hazards not previously evaluated in the FSADs, the overall risk associated with operation of the SNS is not significantly changed. The hazards requiring evaluation are similar in nature to existing hazards and, once mitigated by credited controls, do not significantly increase the residual risk associated with SNS operations. The impacts of the PPUP are limited in scope, but the safety analysis documented in the FSAD-PF and FSAD-NF will need to be revised to document the additional safety analysis being performed as part of the HAR. A revision to the SNS ASE will also be required to implement credited controls identified in the HAR. Accelerator Readiness Reviews (ARRs) will be performed as appropriate throughout the construction and commissioning phases of the PPUP to verify that the procedures and hardware are in place and ready to support operations consistent with the FSADs and ASE.

9.3 ENVIRONMENTAL PROTECTION

An environmental assessment was performed via guidelines outlined in the National Environmental Policy Act of 1969. The assessment revealed that the PPU is covered under DOE/EIS0247, *Final Environmental Impact Statement Construction and Operation of the SNS*.

Planning for the disposition of materials for the PPU has begun, along with establishing the disposition pathway. Estimated costs have been established and will be finalized as the project nears realization. All disposition pathways shall follow the current DOE environmental policy at the time of generation. All waste characterization shall follow the appropriate ORNL Transportation and Waste Management Division procedures. The Research Accelerator Division of the Neutron Sciences Directorate (NScD) shall be responsible for the disposal costs.

9.4 ESH AND QUALITY MANAGEMENT

The PPUP is committed to planning and conducting its activities in a manner that preserves the safety of the workers, the public, and the environment. The project has a dedicated ESH&Q team lead who is part of NScD management and oversees the PPU ESH&Q function. As part of this function, there are dedicated safety and health professionals, environmental professionals, and a quality representative (QR), with two additional QRs available as needed. Each participates in design reviews and design meetings and routinely consults with staff to ensure the integration of safety and quality throughout design, planning, and implementation phases. Including ESH&Q staff from across NScD in the design and implementation phases will help ensure a smooth transition to the operation phases of the project.

9.5 INTEGRATION OF SAFETY AND QUALITY INTO DESIGN FEATURES

Design and development of technical assemblies for the PPUP have been reviewed in accordance with the PPU design review process. Design reviews are performed to confirm and substantiate that the proposed design will achieve its desired outcome. Review ensures that appropriate safeguards have been incorporated, appropriate codes and standards have been used, and materials, processes, and qualified parts have been addressed appropriately. Final design reviews confirm that all analyses have been

properly documented and reviewed, in accordance with the PPU Quality Assurance Plan (QAP). Procurement and quality assurance (QA) requirements are also verified at this stage. ESH&Q representatives are standing members of all design reviews held. Other SMEs are added as appropriate. Design elements that integrate safety and quality into the assembly, installation, maintenance, and operation of these assemblies are defined early and incorporated, taking into consideration input from the ESH&Q personnel and SMEs as appropriate.

9.6 CODES AND STANDARDS

Consistent with DOE regulation 10 CFR 851, Worker Safety and Health Program, *the requirement for adherence to specialized codes and standards is verified through a defined PPUP design review process, which includes a check to verify that appropriate codes and standards have been used. At the time of final design approval, the applicable versions of codes and standards will be identified. Because the PPUP spans several years, using the code or standard that is either required or is most current at the time of final design for the individual components or work activity ensures compliance of an overall system while avoiding rework of items.*

9.7 DESIGN REVIEWS

The PPU design review process adheres to the SBMS subject area Engineering Design, which defines the PPU process of evaluating systems and component designs to determine their adequacy in meeting PPU performance, safety, and operational objectives. This process, which implements the laboratory-level SBMS procedure *Design Facilities, Systems and Components*, defines a graded approach to determine the appropriate scope and level of formality and approval for a design review. The SBMS documentation is flowed down to the internal SNS design procedure SNS-OPM 9.A-3 RAD *System, Structure, Component or Software Change Procedure* with the graded approach for PPUP being spelled out in PPUP-103-QA0002 *PPU Graded Approach*. Grading is based on the potential consequence of a failure in the implementation of the design along with other factors such as financial, operational, and ES&H consequences, at a minimum, of a design failure. Within PPUP, this graded approach is carried out for all designs greater than $150K (and any additional assemblies less than $150K but deemed important enough by applicable design personnel to go through this process). The procedure applies to designs for new systems and components and modifications to existing systems or components to be installed as part of the PPUP. This includes mechanical, pressure, cryogenic, electrical, safety, software, conventional construction, PPU facility modifications, and shielding systems and components. The procedure is used for designs created by internal or external parties. Depending on the complexity and potential impact on the PPUP, internal and external panels and SMEs may be included in the review.

From the outset, the safety of the components is evaluated as the components are designed. When assembled and installed, the components are inspected by appropriate personnel involved in the design. Comments and guidance from each of these reviews provide input to the iterative process of safety design and procedures improvement.

9.7.1 Natural Phenomena Hazards Mitigation

The SNS facilities are categorized as Performance Category (PC)-2 or PC-1, as shown by Table 9.1, and are evaluated for all applicable natural phenomena threats in accordance with DOE-STD-1020-94, *Natural Phenomena Hazards Design and Evaluation Criteria for Department of Energy Facilities*. DOE-STD-1020-94 requires the evaluation of flooding, high winds and tornadoes, and earthquakes. Categorization of structures is governed by DOE-STD-1021-93.

9.7.1.1 Flooding

The site is atop Chestnut Ridge and thus is not within a floodplain. Widespread flooding is not likely for a ridgetop site location several hundred feet above the valley floor.

9.7.1.2 Local Precipitation

In accordance with the applicable PC designation (see Table 9.1), each structure's roof and building drainage are required to endure design-basis precipitation. The Chestnut Ridge site is graded to prevent undesired water accumulation, and a site retention basin is provided to control rainwater drainage from Chestnut Ridge.

DOE-STD-1020-94 specifies the evaluation of snow loads in accordance with applicable building codes and standards. Therefore, snow loads on the SNS roofs are evaluated in accordance with American Society of Civil Engineers (ASCE) 7-95, *Minimum Design Loads for Buildings and Other Structures*, using an importance factor of 1.2. For the SNS site, the ground snow load from ASCE 7-95 is 10 lb/ft^2, which is not limiting compared with other design loads.

Table 9.1. Classification of structures.

Building/feature	Performance category[a]	Code of record[e,f]
Front End Building	PC-2	Standard Building Code (SBC)
Linac tunnel	PC-2[b]	SBC
Klystron Building	PC-2	SBC
HEBT tunnel	PC-2	SBC
Ring tunnel	PC-2	SBC
RTBT tunnel	PC-2	SBC
Target Building	PC-2	SBC
Ring Service Building	PC-1[c]	SBC
RTBT Service Building	PC-1	SBC
Beam dumps	PC-2	SBC
Central Helium (He) Liquefier Building	PC-1	SBC
RF cavity reconditioning and test buildings	PC-1	SBC
Central Utilities Building	PC-1	SBC
Central Laboratory and Office (CLO) Building	PC-1	SBC
Site[d]	PC-1	SBC

[a]PC designation based on requirements of DOE-STD-1021-93
[b]PC-2 is based on cost and mission considerations; Importance Factor = 1.25. Peer review of design is required.
[c]PC-1 is essentially life safety; Importance Factor = 1.0.
[d]Site included miscellaneous foundations (e.g., switchyards) and structures (e.g., conduit banks and piping tunnels).
[e]Wind loads defined per ASCE 7-95
[f]Seismic accelerations determined per Uniform Building Code (UBC)-97.

9.7.1.3 Winds

Wind design and evaluation criteria for DOE facilities are specified in DOE-STD-1020-94 and ASCE 7-95. The minimum wind design criteria for SNS are given in Table 9.2 (see Table 9.1 for building PC designations).

Table 9.2. Wind design criteria for SNS.

Performance category (PC)	1	2
Hazard annual probability of exceedance	2×10^{-2}	2×10^{-2}
Peak mph wind speed at 10 m height	90	90
Importance factor	1.0	1.07
Atmospheric pressure change	NA	NA
Missile criteria	NA	NA

9.7.1.4 Seismic Activity

Seismic design and evaluation criteria for DOE facilities are specified in DOE-STD-1020-94. The seismic hazard levels and amplified response spectra have been determined for the SNS site in accordance with DOE-STD-1022-94, *Natural Phenomena Hazards Site Characterization Criteria.*

9.7.2 External Manmade Threats

There are no nearby industrial facilities or other manmade hazards that present a hazard to the SNS site. The Center for Nanophase Material Sciences facility is located adjacent to the SNS Central Lab and Office Building, but it does not involve energetic processes or hazards that could threaten the SNS facilities. Major airports are more than 10 miles away from the SNS site; for example, McGee Tyson Airport, the only major airport in the area, is located about 18 miles to the southeast, in Blount County, Tennessee.

9.7.3 Nearby Facilities

Three major installations are located within several miles of the SNS: the East Tennessee Technology Park, previously known as K-25; the Y-12 National Security Complex; and ORNL.

9.7.4 Wildfires

Because of the location of the SNS site in a forested area, a fire analysis was done, consistent with the requirements and guidelines of National Fire Protection Association (NFPA) 299 to determine the wildfire risk to Chestnut Ridge. The risk assessment, conducted in accordance with the guidelines of Table A-3-2 (a) of NFPA 299, indicates that the risk from a wildfire is a low hazard. The site fire hazards analysis (FHA) contains the detailed analysis. The analysis assumes that administrative controls are in place and implemented in accordance with NFPA 299 to maintain a minimum 30 ft defensible space to protect all SNS buildings and equipment from the effects of a wildfire. The results indicate that no additional physical fire protection features beyond those required by this analysis (and those specified in each SNS building FHA) are needed to maintain a low hazard rating.

9.7.5 Environmental Analyses

The environmental impact analyses for the SNS are documented in the site's *Final Environmental Impact Statement.* A supplemental analysis was filed to describe potential impacts of the project change to a superconducting linac early in calendar year 2000. PPU introduces no additional impacts.

9.8 QUALITY ASSURANCE

The QA requirements for the PPUP are flowed down from DOE O 414.1D, *Quality Assurance,* which is implemented through ISO 9001:2015. The highest-level requirements are spelled out in applicable SBMS sections, which are interpreted at the SNS directorate level via the SNS Quality Assurance Manual (QAM). The PPU Quality Assurance Plan (QAP) adds details specific to the PPUP for applicable sections. Additional requirements and guidance are taken from DOE Order 413.3B, *Program and Project Management for the Acquisition of Capital Assets*, and DOE G 413,3-2, *Quality Assurance Guide for Project Management*. Lab conformance is verified by the laboratory assessment program, internal management reviews, and annual surveillance and internal audits performed by laboratory personnel. The implementation of the project QA program is supported by experienced quality professionals who have the requisite experience, training, and certifications, such as those provided by the American Society for Quality. Project QA personnel assist project personnel in performing visits to vendor facilities and reporting and resolving vendor nonconformances. Project QA personnel also evaluate the QA programs of other DOE laboratories providing items and services to PPUP (i.e., partner laboratories) and assist in correcting potential weaknesses. The overall flow of the PPUP process involving QA is described in Figure 9.1.

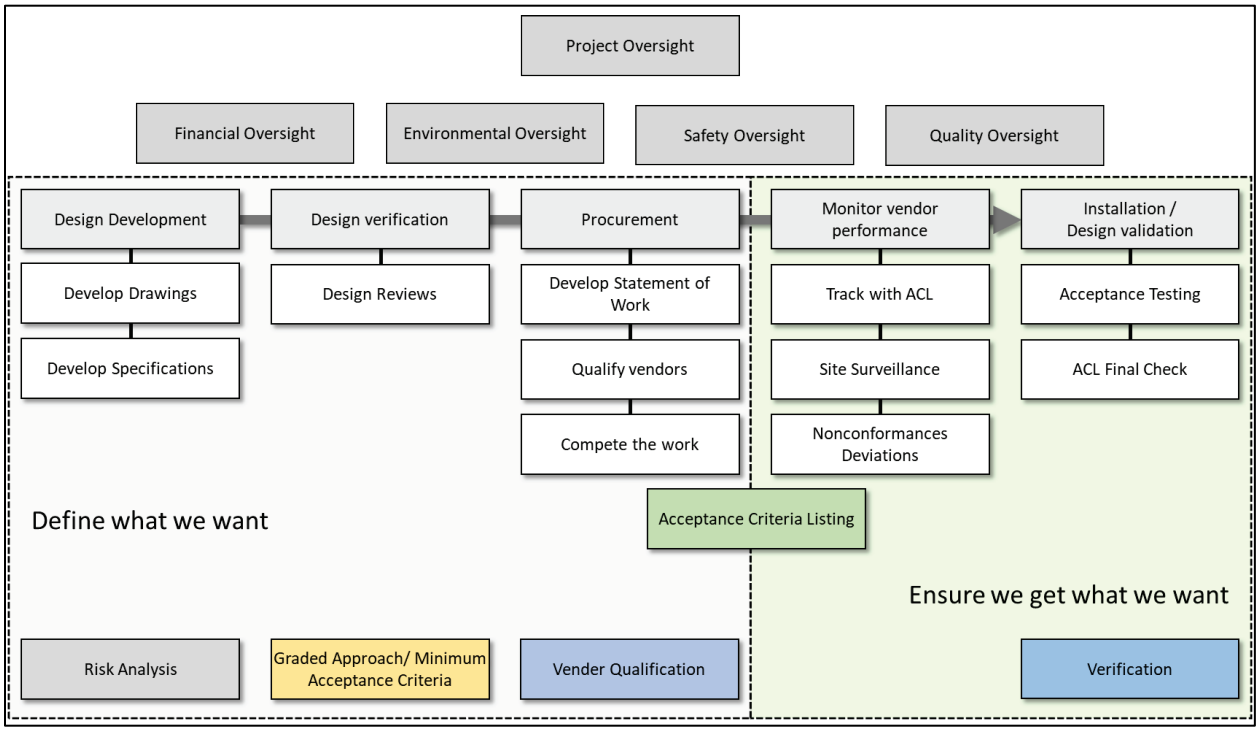

Figure 9.1. PPU Project QA Flow: basic phases, sub-phases and tools.

9.9 PPU PROJECT QA FLOW

9.9.1 Design

During the design development and verification phases, three primary QA tools used are the risk analysis, graded approach, and acceptance criteria listing (ACL). The risk analysis within PPUP is conducted primarily through a design failure modes and effects analysis, which helps in determining areas that might require more rigor. The graded approach determines a grade for the design/procurement that sets the level of rigor for each of the phases, including determining the acceptance criteria.

The PPUP uses ACL (developed according to PPU procedure SNS-QA-P03 *SNS Determination of Acceptance Criteria Procedure*), which specifies the minimum requirements that need to be met by each vendor as part of the acceptance of a procured item. These criteria can include test verifications carried out during manufacture (including onsite verification), factory acceptance tests, and onsite installation tests, all of which are recorded on an ACL for Grade 1 and 2 level designs and on an equivalent for Grade 3 designs.

9.9.2 Procurement

The QA staff are involved in the procurement process by participating in procurement readiness reviews for each PPUP procurement, along with helping to determine the acceptability of vendors' QA programs. QA staff are also tasked with going to vendor sites for assessments, witnessed tests, and so on.

9.9.3 Monitor Vendor Performance

Monitoring of vendor performance relies upon the ACL to track work done by vendors and ensure that all criteria are provided by the vendor, including documentation. Site surveillances, nonconformances, and deviations are part of this as well and are also tracked on the ACL and include QA involvement.

9.9.4 Installation/Design Validation

As part of the determination of acceptance criteria and the grade chosen, the vendor may be asked to provide a factory acceptance test and/or an installation test along with a shipping plan. These are verified and/or witnessed by SNS personnel and tracked on the ACL. After the ACL has been completed with all items received adequately, it can be closed out.

10. COST AND SCHEDULE

10.1 WBS STRUCTURE

A Work Breakdown Structure (WBS) was developed to create a logical breakdown of the PPU work scope by major systems and components. The WBS encompasses all the required work scope of the PPU project. The WBS at Level 3 is shown in Figure 10.1.

The WBS is supported by a detailed WBS Dictionary, which defines the scope of work and major deliverables for each element. The WBS and WBS Dictionary are under configuration control, and changes are made according to the PPU Baseline Change Control Plan.

10.2 SCHEDULE

A detailed project schedule has been developed by decomposing each node of the WBS into discrete activities representing all project work, including R&D, design, procurement, fabrication, construction, installation, and testing. The schedule also includes level-of-effort support activities and milestones and is completely logic driven and resource loaded.

The schedule has incorporated the SNS outage schedule into the plan. Activities within the schedule are optimized and planned to best fit the outages. In addition, the PPU project team works closely with the Operations staff to ensure accurate communication of changes to the planned outages and adjustments as necessary to meet the PPU project needs.

The project duration includes 42 months of schedule float, including 12 months for potential COVID-19 impacts. The actual and planned PPU Critical Decision (CD) milestone dates are shown in Table 10.1.

Table 10.1. Proton Power Upgrade Critical Decision actual and planned milestones.

Major Milestones		Scheduled
CD-0	Approve Mission Need	Jan 2009 (A)
CD-1	Approve Alternative Selection and Cost Range	Apr 2018 (A)
CD-3a	Approve Long Lead Procurements	Oct 2018 (A)
CD-3b	Approve Long Lead Procurements	Sep 2019 (A)
CD-2/3	Approve Performance Baseline and Start of Construction	Q4 FY 2020
CD-4	Approve Project Completion	Q4 FY 2028

At CD-2, the project will establish a Performance Measurement Baseline (PMB), and the baseline schedule will be under configuration control.

10.3 COST

The initial cost range of the PPU project is $184 million to $320 million, with a current point estimated Total Project Cost of $271.6 million. The cost estimate includes ~40% contingency. The Budget at Completion at WBS Level 2 is shown in Table 10.2.

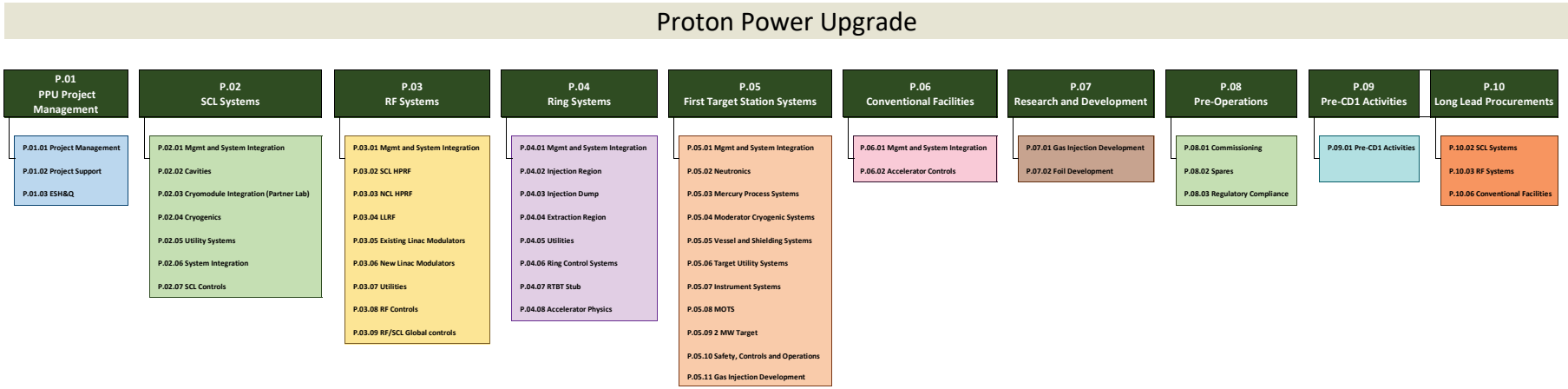

Figure 10.1. Level 3 Work Breakdown Structure for the Proton Power Upgrade.

Table 10.2. Proton Power Upgrade project cost estimate ($k).

WBS	Actual costs (March 2020)	Estimate to Complete (ETC)	Budget at Completion
P.1 Project Management	$ 4,113	$ 17,970	$ 22,082
P.2 Super-Conducting Linac Systems	$ 4,243	$ 16,250	$ 20,493
P.3 RF Systems	$ 8,369	$ 32,397	$ 40,767
P.4 Ring Systems	$ 4,321	$ 13,698	$ 18,019
P.5 First Target Station Systems	$ 6,956	$ 28,079	$ 35,035
P.6 Conventional Facilities	$ 2,328	$ 8,656	$ 10,983
P.7 R&D (OPC)	$ 2,223	$ 186	$ 2,409
P.8 Pre-Ops (OPC)	$ 32	$ 1,094	$ 1,126
P.9 Pre-CD-1 Activities (OPC)	$ 7,250	$ -	$ 7,250
P.10 Long Lead Procurements	$ 12,011	$ 38,213	$ 50,439
	$ 51,846	**$ 156,543**	**$ 208,604**
	Total contingency (40% of ETC)		$ 62,963
	Total Project Cost		**$ 271,567**

The Notional Budget Authority profile generated from the logic-driven, resource-loaded schedule is shown in Table 10.3.

Table 10.3. Notional Budget Authority profile.

	FY16	FY17	FY18	FY19	FY20	FY21	FY22	FY23	FY24	FY25	Total
Notional Funding Profile ($M)	4.1	6.7	36.0	60.0	60.0	45.0	25.0	17.0	13.0	4.8	271.6

The detailed, bottom-up cost estimate was developed based upon the schedule activities and provides a Basis of Estimate for each activity and resource cost. The Basis of Estimate document also captures all systematic estimate assumptions, such as escalation, labor rates, and overheads.

The quantities and durations are largely based upon the actual experience of the engineers, scientists, and technicians who currently operate and maintain the SNS accelerator, target, and conventional facilities. Additionally, the majority of the estimated procurements are based upon recent purchases, vendor quotes, and vendor budgetary estimates.

The Total Project Cost includes contingency derived from the analysis of the project risk register and estimate uncertainty, which is identified within the project schedule.

The project scope that is related to the approved long lead procurements (WBS P.10) is under configuration control, and any changes to the technical, cost or schedule scope require a Project Change Request to be processed and approved. At CD-2, the project will establish a PMB and the full cost estimate will be under configuration control.